Technical Physics, Vol. 48, No. 8, 2003, pp. 1001–1008. Translated from Zhurnal Tekhnicheskoĭ Fiziki, Vol. 73, No. 8, 2003, pp. 62–70.

SOLIDS

Perturbation Evolution at a Metal–Metal Interface Subjected to an Oblique Shock Wave: Supersonic Velocity of the Point of Contact

O. B. Drennov, A. L. Mikhaĭlov, P. N. Nizovtsev, and V. A. Raevskiĭ

All-Russia Research Institute of Experimental Physics, Russian Federal Nuclear Center, Sarov, Nizhni Novgorod oblast, 607190 Russia

e-mail: root@gdd.vniief.ru

Received December 30, 2002

Abstract—The perturbation evolution at the interface between identical metals (metal plates) that is exposed to high-speed oblique shock waves is observed experimentally for the first time (the waves are attached to the point of contact, so that a cumulative jet cannot form). The experiments are numerically simulated by the two-dimensional Lagrange method. An elastoplastic model where the dynamic yield strength is a function of material state parameters is employed. An analytical technique to treat instability development under given loading conditions is suggested. High strains produce a high-temperature zone near the interface (thermal softening zone). A short-lived shear flow with a high velocity gradient depending on the angle and velocity of plate collision is observed. In this zone, the shear modulus and the yield strength are appreciably lower than under normal conditions, which favors instability development. *© 2003 MAIK "Nauka/Interperiodica".*

INTRODUCTION

High dynamic pressure in metals may be produced by oblique shock loading. Under these conditions, the specimen is subjected to the normal and tangential components of stress and velocity [1, 2].

Oblique collision of metal layers (one way of loading by oblique shock waves) generates intense shear strains in the contact zone, heats up the surface layers of the metals considerably, and produces cumulative jets [1, 3]. These effects distort the shape of the metal–metal interface, causing both regular and asymmetrically distorted waves to arise, and may even produce molten layers of mixed composition. In a number of cases, the specimens rigidly adhere to each other [1, 4].

To date, the subsonic conditions of oblique collision, $v_c < C_0$ (where v_c is the velocity of the point of contact and C_0 is the sound velocity in a given material), have been extensively studied. Under these loading conditions, a cumulative jet is continuously formed if the pressure near the collision point exceeds the metal strength [1, 5].

Collision at $v_c > C_0$ is described in a way similar to a supersonic flow past a wedge [2]. If the angle of collision is constant (γ = const, where γ is an analogue of the wedge angle), there exists a critical value v_{cr} of the velocity v_c. When $C_0 \le v_c \le v_{cr}$, detached oblique shock waves appear in the flow. In going through the wave front, the supersonic flow becomes subsonic. Both flows arrive at the point of collision with a subsonic velocity (the fixed and movable plates are in the coordinate system related to this point), and a cumulative jet forms in the collision zone. With $v_c > v_{cr}$, attached oblique shock waves set up at the point of contact. They turn the flows through angles that, taken together, add up to γ. The jet does not form in this case. It is believed [1, 5] that perturbations at the metal–metal interface are also hardly probable in this situation, since their basic source, a cumulative jet, is absent.

The state of the interface under the supersonic loading regime is little understood.

EXPERIMENTAL

Our experiments were carried out by the following scheme (Fig. 1). Plate *3* is rigidly mounted on massive steel support *4*. Movable plate (striker) *2* is fixed over plate *3* at an angle α to it. The movable plate is set in motion by explosion products of blasting explosive *1* (the pentaerythritol tetranitrate (PETN)–based plasticized explosive with $\rho = 1.51$ g/cm^3 and $D = 7.8$ mm/μs or the octogen-based plasticized explosive with $\rho = 1.86$ g/cm^3 and $D = 8.75$ mm/μs), in which a plane gliding detonation wave is generated. The minimal gap h between the plates is taken such that the movable plate has a uniform velocity prior to collision: $h_{min} \ge (3–5)\delta_{str}$, where δ_{str} is the striker thickness [6]. To prevent spalling in the striker, thin spacer *5* made of a low-acoustic-impedance material is inserted between the striker and explosive. The spacer does not influence the velocity and symmetry of the striker motion [7].

Oblique collision is characterized by the following parameters: D, the rate of explosive detonation; W, the

1063-7842/03/4808-1001$24.00 © 2003 MAIK "Nauka/Interperiodica"

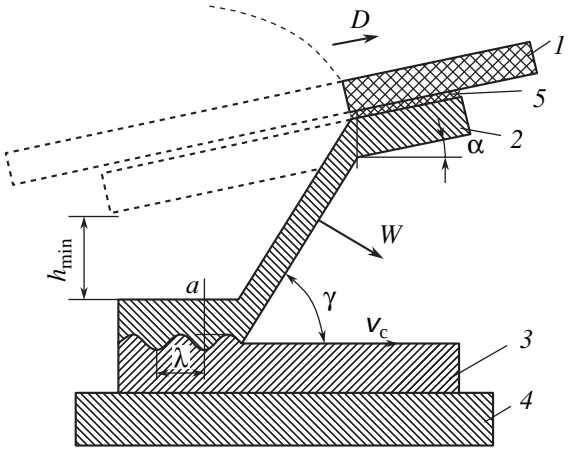

Fig. 1. Experimental scheme.

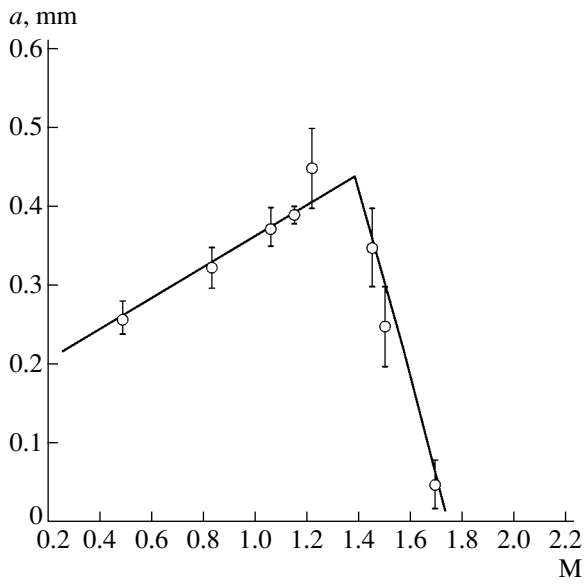

Fig. 2. Perturbation amplitude a at the AMTs–AMTs interface vs. Mach number for $\gamma \approx 13.5° = \text{const}$.

striker velocity; α, the initial inclination of the striker; γ, the angle at which the plates collide; v_c, the velocity of the point of contact; and a and λ, the amplitude and wavelength of arising perturbations (Fig. 1).

After dynamic loading, the plates were trapped by a porous layer. Fragments for preparing microsections were cut from the central parts of the plates (which typically measure 100 × 60 × 4 mm). Figure 2 plots the perturbation amplitude a at the boundary between two contacting plates (made of AMTs aluminum alloy) vs. Mach number v_c/C_0 [8]. The perturbation amplitude a (rather than the perturbation wavelength λ) was taken as an independent variable, because, as a grows, the contact boundary may take the form of turbulently mixed melts of both materials (Fig. 3, AMTs layer). The value of λ becomes uncertain under these conditions. The choice of a as an independent variable provides hydrodynamic similarity upon comparing the perturbation amplitudes at the interface between various (including dissimilar) metals.

The ascending portion of the curve $a = f(\text{M})$ reflects the jet formation conditions at the point of contact (subsonic flow). The increase in the velocity v_c causes the loading pressure and plastic shear strain rate in the contact zone to grow. A large shear of the metal is involved in the jet, and the perturbation amplitude increases. At $v_c \approx v_{cr}$ (the attachment of shock waves to the point of contact), when the jet formation regime changes to the jet-free regime of oblique collision, the perturbation amplitude reaches a maximum.

The transition to the jet-free regime of plate collision means the virtually instantaneous termination of the perturbation evolution (the basic source of perturbations disappears). Accordingly, the curve $a = f(\text{M})$ must terminate abruptly and fall to $a = 0$ at the point $a = a_{max}$. However, in our experiments, the perturbation amplitude falls monotonically with a further increase in the velocity of the point of contact ($v_c > v_{cr}$). The drop from

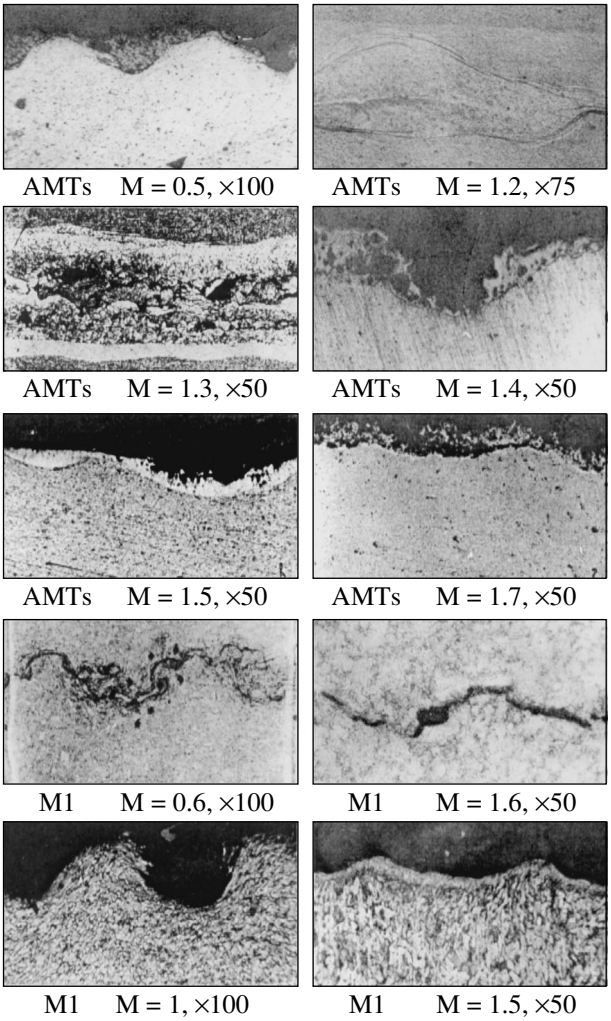

Fig. 3. Micrographs of the contact boundary after fast oblique collision.

$a = a_{max}$ to $a = 0$ is observed in the Mach number interval $1.40 < M \le 1.75$. Such behavior is observed for the first time.

Similar experiments were carried out with another pair of materials (copper and steel; Fig. 3), and they gave similar results. In this case (the materials are similar in physicochemical properties but differ in strength), the perturbation amplitude is greater for the softer material at the same Mach numbers, although the Mach number range (ΔM) of perturbation existence in the supersonic regime ($a_{max} > a > 0$) for the softer material is narrower.

Figure 3 shows the sections of the specimens when observed under a microscope. Here, perturbations at the interface are apparently caused by development of Kelvin–Helmholtz instability due to the tangential discontinuity of the velocities at the boundary between the initially fixed and movable plates, which are in different thermodynamic states.

Behind the front of the oblique shock wave, the materials glide over each other. The temperature of the front grows. The relative gliding of the materials along the interface results in intense shear strains, and the contacting surfaces melt. Kelvin–Helmholtz instability continues developing, enhancing perturbations at the interface between two identical metals. The oblique shock wave front generates initial oscillating perturbations.

ANALYSIS

The problem of perturbations at the interface between metals under oblique collision is hard to solve theoretically. The presence of high strains and a high-temperature zone near the interface makes it difficult to use the small perturbation method and simple models of shear strength. Yet an analytical solution that simulates the situation with Kelvin–Helmholtz instability in strong media might be helpful in elucidating the physics of the process and testing numerical solution techniques. To date, the solutions have been obtained for a perfect fluid [9, 10] and a viscous medium [11]. Of interest also is the development of small perturbations in the case when a perfect fluid glides over the surface of a strong metal. This case resembles the situation where a metal glides over another metal whose surface layer has undergone thermal softening.

(1) Perfect elastic medium. Let a perfect fluid of thickness H and density ρ occupy the upper half-space $y > 0$ and move in the x direction with a velocity U_0. The lower half-space $y < 0$ is occupied by a perfectly elastic incompressible material where transverse waves move with a velocity C. The interface experiences small harmonic perturbations

$$\xi(x) = \xi_0 \exp(iKx).$$

In the case of small perturbations, the equations for velocity in the upper half-space has the form [10]

$$\begin{cases} \dfrac{\partial U_x}{\partial t} + U_0 \dfrac{\partial U_x}{\partial x} + \rho^{-1} \dfrac{\partial P}{\partial x} = 0 \\ \dfrac{\partial U_y}{\partial t} + U_0 \dfrac{\partial U_y}{\partial x} + \rho^{-1} \dfrac{\partial P}{\partial y} = 0, \end{cases} \tag{1}$$

where U_x and U_y are velocity perturbations related to interface perturbations and P is pressure perturbation.

Since the equations of motion in an elastic medium are convenient to write for Lagrangean coordinates instead of velocity, we will represent Eqs. (1) in terms of perturbations of the coordinates X and Y. Small perturbations of coordinates are related to velocities as

$$\begin{cases} U_x = \dfrac{\partial X}{\partial t} + U_0 \dfrac{\partial X}{\partial x} \\ U_y = \dfrac{\partial Y}{\partial t} + U_0 \dfrac{\partial Y}{\partial x}. \end{cases} \tag{2}$$

The Euler equations then take the form

$$\begin{cases} \dfrac{\partial^2 X}{\partial t^2} + 2U_0 \dfrac{\partial^2 X}{\partial x \partial t} + U_0^2 \dfrac{\partial^2 X}{\partial x^2} + \rho^{-1} \dfrac{\partial P}{\partial x} = 0 \\ \dfrac{\partial^2 Y}{\partial t^2} + 2U_0 \dfrac{\partial^2 Y}{\partial x \partial t} + U_0^2 \dfrac{\partial^2 Y}{\partial x^2} + \rho^{-1} \dfrac{\partial P}{\partial Y} = 0. \end{cases} \tag{3}$$

Equations (3) are supplemented by the continuity equation for the incompressible medium

$$\frac{\partial X}{\partial x} + \frac{\partial Y}{\partial y} = 0. \tag{4}$$

For the lower half-space, the equations of motion appear as

$$\begin{cases} \dfrac{\partial^2 X'}{\partial t^2} + \rho^{-1} \dfrac{\partial P'}{\partial x} = C^2 \left(\dfrac{\partial^2 X'}{\partial x^2} + \dfrac{\partial^2 X'}{\partial y^2} \right) \\ \dfrac{\partial^2 Y'}{\partial t^2} + \rho^{-1} \dfrac{\partial P'}{\partial y} = C^2 \left(\dfrac{\partial^2 Y'}{\partial x^2} + \dfrac{\partial^2 Y'}{\partial y^2} \right). \end{cases} \tag{5}$$

Here, the primed quantities refer to the lower medium. The continuity equation does not differ from (4). The boundary conditions are as follows.

(1) At a height H, vertical displacements are absent:

$$Y(x, H, t) = 0; \tag{6}$$

(2) at the interface ($y = 0$), displacements along the OY axis in both half-spaces coincide:

$$Y(x, 0, t) = Y'(x, 0, t); \tag{7}$$

(3) for the stress normal to the interface, we similarly have

$$P(x, 0, t) = P'(x, 0, t) - 2\rho C^2 \partial Y'(x, 0, t)/\partial y; \tag{8}$$

(4) at $y \longrightarrow -\infty$,

$$X'(x, y, t) \longrightarrow 0, \quad Y'(x, y, t) \longrightarrow 0; \tag{9}$$

(5) at the interface, the shear stress is absent:

$$\rho C^2\left(\frac{\partial X'}{\partial y} + \frac{\partial Y'}{\partial x}\right)\Bigg|_{y=0} = 0. \tag{10}$$

A solution for the upper half-space will be sought in the form

$$\begin{cases} X = -i\exp[i(Kx - \omega t)][A\exp(-Ky) - B\exp(Ky)] \\ Y = \exp[i(Kx - \omega t)][A\exp(-Ky) + B\exp(Ky)], \end{cases}$$

which provides the fulfillment of continuity equation (4). In view of boundary condition (5), we have

$$\begin{cases} X = -iA\exp[i(Kx - \omega t)] \\ \times[\exp(-Ky) + \exp(Ky - 2KH)], \\ Y = A\exp[i(Kx - \omega t)][\exp(-Ky) - \exp(Ky - 2KH)]. \end{cases} \tag{11}$$

The pressure in the upper half-space is found from equation (3):

$$P = -\frac{A\rho(\omega - U_0K)^2}{K}\exp[i(Kx - \omega t)] \times[\exp(-Ky) + \exp(Ky - 2KH)]. \tag{12}$$

For the elastic (lower) half-space, we find, in view of boundary condition (9), a solution to Eq. (4) in the form

$$\begin{cases} X = i\exp[i(Kx - \omega t)]\left[B\exp(Ky) + \frac{DK}{n}\exp(ny)\right] \\ Y = \exp[i(Kx - \omega t)]\left[B\exp(Ky) + \frac{DK}{n}\exp(ny)\right], \end{cases} \tag{13}$$

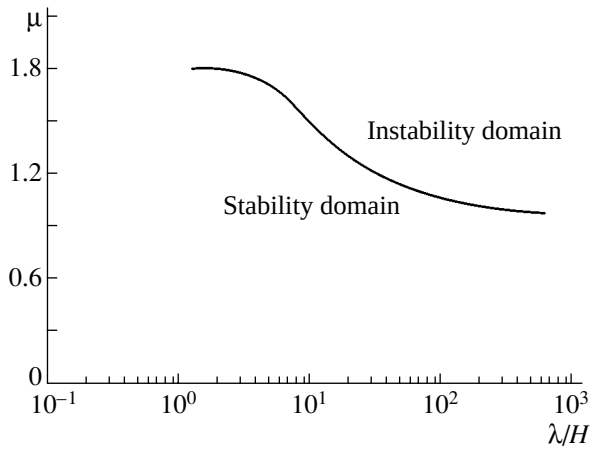

Fig. 4. Critical Mach number vs. relative wavelength $\lambda/H = 2\pi/(KH)$.

$$P = -\frac{B\rho\omega^2}{K}\exp[i(Kx - \omega t)]\exp(Ky), \tag{14}$$

$$n^2 = K^2 - \left(\frac{\omega}{C}\right)^2. \tag{15}$$

Substituting Eqs. (11)–(15) into boundary conditions (6)–(10) yields a homogeneous linear equation for the constants *A*, *B*, and *D*. The compatibility condition for this system is the equation

$$[(\omega^2 - 2(KC)^2)^2 - 4K^3C^4n]\tanh(KH) + \omega^2(\omega - KU_0)^2 = 0. \tag{16}$$

In the notation $\nu = \omega/KC$ and $\mu = U_0/C$, (16) can be transformed into

$$[(\nu^2 - 2)^2 - 4\sqrt{1 - \nu^2}]\tanh(KH) + \nu^2(\nu - \mu)^2 = 0. \tag{17}$$

From (17), it follows that each value of $KH = 2\pi H/\lambda$ can be assigned a maximum value of μ for which Eq. (17) has real roots ν. Real ν correspond to a stable solution that describes the propagation of waves over the elastic half-space. At $\mu > \mu_{cr}(KH)$, only exponentially growing solutions exist; that is the interface becomes unstable. The dependence of μ_{cr} on the relative perturbation wavelength is demonstrated in Fig. 2.

As follows from Fig. 4, the interface is absolutely unstable for any perturbation wavelength if $\mu > 1.8$. For $0.92 < \mu < 1.8$, there is a critical relative wavelength $(\lambda/H)_{cr}$ bounding the stability range from above. In this case, all harmonics for which $\lambda > \lambda_{cr}$ are unstable. However, harmonics with wavelengths close to λ_{cr} ($\lambda_{max} \geq \lambda_{cr}$) are the fastest. The perturbation increment Im(ν) as a function of the relative wavelength λ/H is shown in Fig. 5 for various μ.

In the stability range $\mu < 0.92$, two oppositely traveling waves arise. Their amplitude is given by

$$\xi(x, t) = \cos(Kx \pm \nu Ct).$$

For perfect fluid ($C = 0$, $\mu = \infty$), the solution to Eq. (16) is

$$\omega = \frac{KU}{1 + \tanh(KH)}(1 \pm i\sqrt{\tanh(KH)}).$$

The perturbation amplitude grows by the law

$$a(t) = \exp\left(\frac{KU\sqrt{\tanh(KH)}}{1 + \tanh(2KH)}\right)t.$$

It is noteworthy that, as *H* tends to zero, so does the rate of growth of the perturbations.

(2) Elastoplastic medium. This approximation is closer to reality, but an analytical solution seems to be impossible to obtain. It is evident that the presence of the ultimate strength shifts the instability range towards lower Mach numbers compared with the case of perfect elasticity.

The stress intensity in a wave propagating in an elastic medium reaches a value

$$\sigma_i = G\varepsilon_i = G\frac{\xi}{\lambda},$$

where ξ is the perturbation amplitude at the boundary.

With $\sigma_i > Y$, where Y is the dynamic yield point, the material starts to plastically deform and the transition to the unstable regime takes place. If the initial perturbation at the initially unstrained ($\varepsilon_i = 0$, $\sigma_i = 0$) interface has the form $a(x) = a_0\cos(Kx)$, the perturbation first develops in the same manner as in a perfect fluid. The traveling wave amplitude first grows and reaches a maximum when the stress intensity becomes equal to the hydrodynamic pressure. From Eq. (3) in view of the condition for the transition to instability ($\mu > \mu_{cr}$), one can derive a qualitative expression for the maximal change in the perturbation amplitude at the interface:

$$(a - a_0)_{max} \approx \frac{a_0}{(\mu_{cr}/\mu)^2 - 1},$$

where μ_{cr} depends on KH (Fig. 4).

Accordingly, the maximal stress intensity is given by

$$\sigma_i \approx \frac{(a - a_0)_{max}}{\lambda} G \approx \frac{a_0}{\lambda}\frac{G}{(\mu_{cr}/\mu)^2 - 1}. \qquad (18)$$

Thus, the stability condition for an elastoplastic layer has the form

$$\frac{a_0}{\lambda} \le \left(\frac{a_0}{\lambda}\right)_{cr} \approx \frac{\sigma_y}{G}[(\mu_{cr}/\mu)^2 - 1], \qquad (19)$$

where μ_{cr} is the critical Mach number for a given wavelength.

For wavelengths much less than the thickness of the layer, $\mu_{cr} \approx 1.8$. Then,

$$\left(\frac{a_0}{\lambda}\right)_{cr} \approx \frac{\sigma_y}{G}[(1.8/\mu)^2 - 1] \approx \frac{\sigma_y}{\rho}\left[\left(\frac{1.8}{U}\right)^2 - \left(\frac{1}{C}\right)^2\right].$$

In a perfectly plastic medium, $C = \infty$, $G = \infty$, and this expression transforms into

$$\left(\frac{a_0}{\lambda}\right)_{cr} \approx 1.8^2\frac{\sigma_y}{\rho U^2}.$$

Qualitatively, critical amplitude vs. Mach number curves are depicted in Fig. 6.

Under conditions that are close to normal, $\sigma_y/G \sim 10^{-2}$ for many metals. The stability condition for short waves is thus written in the form

$$\left(\frac{a_0}{\lambda}\right)_{cr} \approx 10^{-2}[(1.8/\mu)^2 - 1].$$

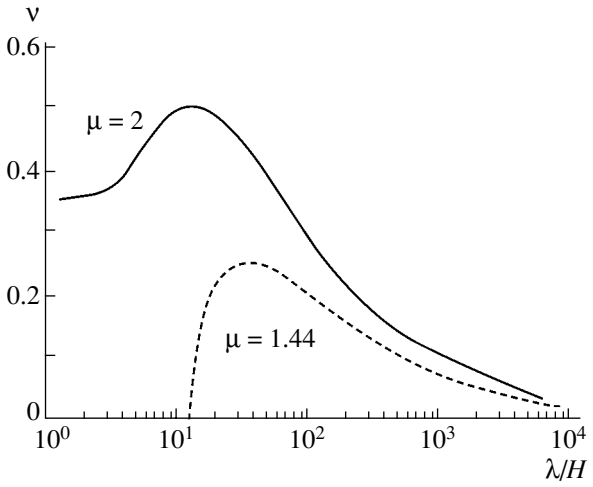

Fig. 5. Perturbation increment vs. relative wavelength λ/H.

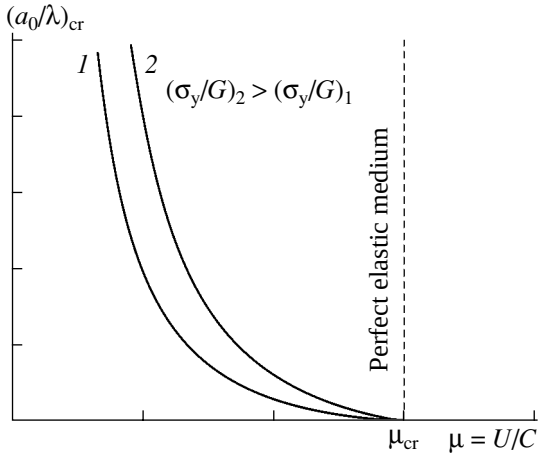

Fig. 6. Critical perturbation amplitude vs. Mach number.

For example, if $\mu = 1$ (i.e., $U \approx C$), perturbations with $a/\lambda < 0.02$ are unstable.

As follows from numerical calculations and experiments, oblique collision of the plates generates a high-temperature zone near the interface because of high strains even if the jet does not form. Moreover, a short-lived shear flow with the velocity gradient depending on the velocity and collision angle of the plates arises. In the high-temperature zone, the shear modulus and the yield point are appreciably lower than under normal conditions. Therefore, conditions (19) for instability development may be met. Perturbations with wavelengths somewhat longer than the critical one will build up most rapidly.

NUMERICAL SIMULATION

The scheme used in numerical simulation is shown in Fig. 7. The simulation was based on the two-dimensional Lagrangean technique [12].

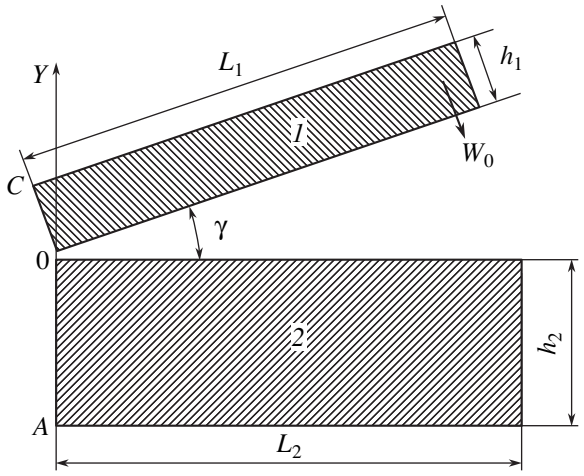

Fig. 7. Scheme used in the calculation: h_1 = 4 mm, h_2 = 15 mm, $L_1 = L_2$ = 40 mm, and γ = 14°. Material Al.

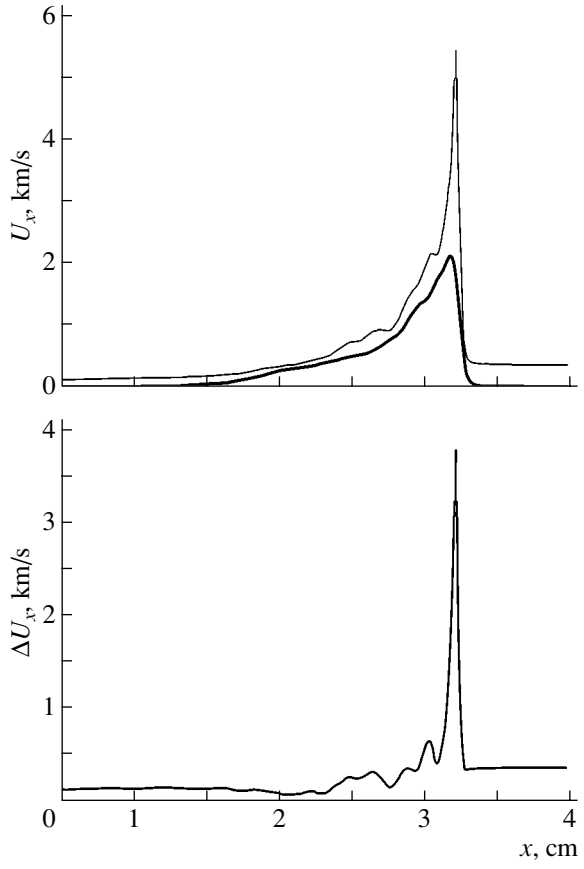

Fig. 8. Variation of the material velocity in the *OX* direction for the initial collision velocity W_0 = 1.5 km/s (M = 1.45).

Plate *1* with an initial velocity W_0 directed normally to its surface strikes plate *2*. It is assumed that displacements normal to the contour are absent on the sections *AO* and *OC*. The problem on interaction is solved for contacting surfaces. Two limit cases are considered: (i) perfect glide and (ii) perfect friction (the plates stick to each other when coming into contact).

The former case is akin to the situation when collision forms a local high-strain (and, accordingly, high-temperature) zone, in which the material softens.

The behavior of the plate material is described by the Mie–Grüneisen equation of state and equations of elastoplastic flow. The dynamic yield strength in the elastoplastic model is expressed in the conventional (for most metals) form

$$Y = (Y_0 + \alpha P)(1 - \beta E_y/E_m). \quad (20)$$

Here, E_m is the energy of material melting, which is a function of the parameters of the material state and is determined according to the Lindemann law.

Of special interest is the above-critical range, where the point of contact moves with a velocity v_c far exceeding the critical velocity v_{cr} and velocity of sound C_0 (shock waves are attached to the point of collision). In this regime (fast oblique collision), the jet does not form and, as argued in [1, 5], the interface must remain stable. In the zone adjacent to the contact surface, the material deforms in a very complicated manner, as follows from the simulation. Near the point of contact, a region with a high velocity gradient (hence, with a high strain rate) forms.

Figure 8 shows the boundary velocity distributions in the upper and lower plates at the instant the point of contact has traveled a distance of ≈3.3 cm. In spite of the above-critical collision conditions (W_0 = 1.5 km/s, $M = v_c/c_0$ = 1.45), boundary points of the upper plate move along the contact surface with a high velocity, v = 5.8 km/s, while those of the lower plate have a velocity of no higher than 2 km/s. As a result, a velocity gradient ($\Delta v_{max} \approx 3.8$ km/s) arises at the interface for a short time. As the collision velocity grows, the gradient declines.

Similar dependences are shown in Fig. 9 for the upper plate moving with a velocity W_0 = 2 km/s (M = 1.75). In this case, the gradient is $\Delta v_{max} \approx 0.7$ km/s.

The dependence of the maximal difference in the velocities of the upper and lower plates on the collision velocity W_0 is presented in Fig. 10.

This observation can be explained as follows. The collision velocity W_0 = 1.5 km/s (M = 1.45) corresponds to the near-critical range (see Fig. 2, where the perturbation amplitude a is plotted against Mach number). Oblique shock waves are attached to the point of contact (at M = 1.4), and a cumulative jet does not form. However, intense plastic strains near the contact (behind the shock front after the plate collision) cause the material to yield in the *OX* direction starting from the point of contact (it is as if the material tends to form a jet, and this incipient jet starts moving along the contact surface of the fixed plate). Such a yield is characterized by a great difference in the velocities of the boundaries of the plates. The high-velocity motion of

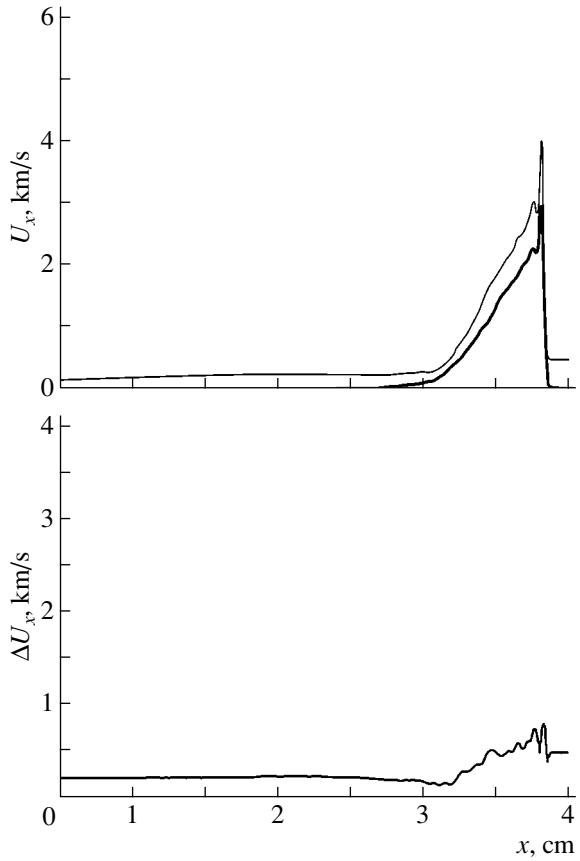

Fig. 9. The same as in Fig. 8 for W_0 = 2 km/s (M = 1.75).

the upper plate persists for a short time because of the slowing-down effect of the material located ahead. However, this velocity spike turns out to be sufficient for an initial perturbation to build up.

As the collision velocity W_0 increases, the process described above degenerates. The arising material yield is immediately "crushed" by the striking plate. The yield rate has no time to reach a significant value, and initial perturbations do not grow.

The short-lived yield at the point of contact arises virtually at once and is of self-similar character.

Above, we assumed perfect glide of the surface. The strain intensity distributions for Y_0 = 0.15 GPa and $\alpha = \beta = 0$ (see formula (20)) are shown in Fig. 11.

As follows from Figs. 10 and 11, the relative velocity of the contact surfaces diminishes and the high-strain zone shrinks with increasing collision velocity.

The calculations indicate that the strain distribution also depends on the material strength. The strain fields calculated under the assumption of perfect friction for two values of the shear strength are shown in Fig. 12. In Fig. 12a, the elastoplastic flow model with a constant yield strength Y_0 = 0.15 GPa is used. In Fig. 12b, the results were obtained with allowance for material hardening (due to compression) and thermal softening for Y_0 = 0.3 GPa, α = 0.1, and β = 1 (formula (20)). In both cases, W_0 = 3 km/s.

It is seen that the high-strain zone narrows as the strength grows, which agrees with the experimental data.

It should be noted that the high-strain zone with a significant velocity gradient is observed, in a certain range of collision velocities, under both perfect glide (Fig. 11) and perfect friction (Fig. 12) conditions.

High-strain-induced local heating substantially softens the material. Thus, at collision velocities W_0 < 2 km/s, the conditions for Kelvin–Helmholtz instability are realized. If the effect of strength is neglected, the

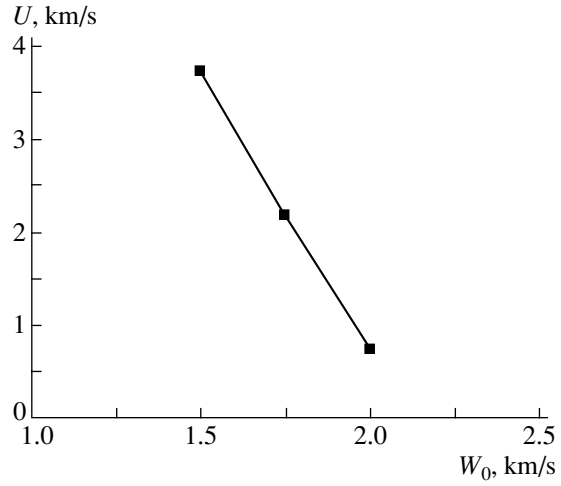

Fig. 10. Relative velocity at the interface vs. collision velocity.

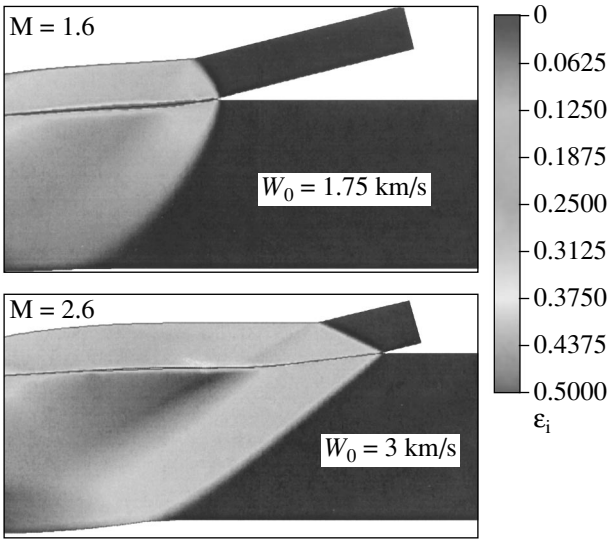

Fig. 11. Distribution of the strain intensity under perfect glide.

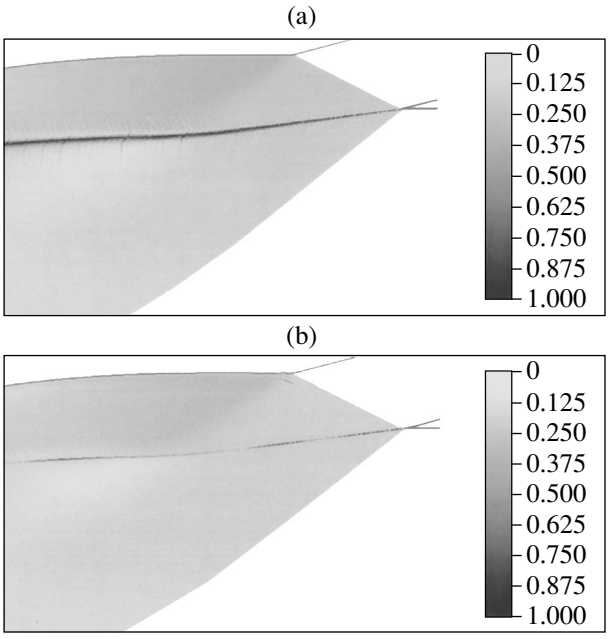

Fig. 12. Distribution of the strain intensity under perfect friction. Panels (a) and (b) are described in the text.

boundary perturbation amplitude will grow to

$$a \approx a_0 \cosh\left(\frac{UK}{2}\tau\right)$$

for the time of velocity gradient existence.

In the experiments with aluminum layers, the perturbation wavelength was largely $\lambda \approx 0.065$ cm with $W = 1.5$ km/s and $\gamma = 13.5°$. The initial roughness of the surfaces was about 10 μm; that is, initial perturbations had an amplitude $a_0 \approx 10^{-3}$ cm. As follows from the analytical calculations, for $W_0 = 1.5$ km/s, $\tau \approx 0.2$ μs and $\bar{U} \approx 2$ km/s. Then, $a/a_0 = \cosh(\pi\bar{U}\tau/\lambda) \approx 4.1$; in other words, within the velocity spike duration, the perturbation amplitude grows by a factor of 4.1 and reaches a value $a \approx 4.1 \times 10^{-3}$ cm. The value found experimentally is $a \approx 3.6 \times 10^{-3}$ cm, which is close to the analytical estimate.

Of interest are factors governing the perturbation wavelength. Assuming that $a_0/\lambda \approx 10^{-2}$ (where a_0 is the mean initial surface roughness and λ is the wavelength found in the experiments), we find from (19) that $\mu_{cr}/\mu \approx 1.4$. The numerical results obtained in terms of the elastoplastic model indicate that the thermal softening (by 70%) zone extends to 0.08–1.00 mm. The maximal velocity difference in this zone is $\Delta U \approx 3.8$ km/s (Fig. 8). Then, the average Mach number is $\mu \approx 1$. Hence, $\mu_{cr} \approx 1.4$ and $(\lambda/H)_{cr} \approx 10$ (Fig. 6). Thus, $\lambda \approx 0.8$ mm, which is in close agreement with the experimental value $\lambda \approx 0.65$ mm. Note that these estimates are only a rough approximation, since actually the transition from the cold to almost molten (softened) material occurs gradually.

Unfortunately, we have thus far failed to calculate the perturbation amplitude directly. The reason is the complex flow pattern near the contact.

CONCLUSIONS

(1) Upon oblique collision of metal plates, perturbations also arise under above-critical conditions, where the velocity of the contact point far exceeds the velocity of sound and a cumulative jet does not form.

(2) When the collision velocity is sufficiently high, perturbations stop growing.

(3) The reason why perturbations grow is the significant short-term velocity gradient near the point of contact and strain-induced heating of a narrow near-contact zone.

(4) Approximate analytical solutions show that Kelvin–Helmholtz instability arises at the interface between a fluid and an elastic or elastoplastic material if the velocity gradient is appreciable.

(5) The perturbation wavelength and amplitude estimated using numerical calculations and analytical solutions agree with experimental data.

ACKNOWLEDGMENTS

This work was supported by the Russian Foundation for Basic Research (project no. 02-01-00796).

REFERENCES

1. A. A. Deribas, *Physics of Hardening and Explosive Welding* (Nauka, Novosibirsk, 1980).
2. R. Courant and K. O. Friedrichs, *Supersonic Flow and Shock Waves* (Interscience, New York, 1948; Inostrannaya Literatura, Moscow, 1950).
3. G. R. Cowan and A. H. Holtzman, J. Appl. Phys. **34**, 928 (1963).
4. G. R. Cowan, O. R. Bergmann, and A. H. Holtzman, Metall. Trans. **2**, 3145 (1971).
5. A. V. Krupin, V. Ya. Solov'ev, N. I. Sheftel', *et al.*, *Deformation of Metals by Explosion* (Metallurgiya, Moscow, 1975).
6. G. E. Kuz'min, V. Ya. Simonov, and I. V. Yakovlev, Fiz. Goreniya Vzryva **13**, 458 (1976).
7. B. L. Glushak, S. A. Novikov, A. P. Pogorelov, *et al.*, Fiz. Goreniya Vzryva **17**, 90 (1981).
8. O. B. Drennov, Fiz. Goreniya Vzryva **27**, 118 (1991).
9. G. Birkhoff, *Hydrodynamics: A Study in Logic, Fact, and Similitude*, 2nd ed. (Princeton Univ., Princeton, 1960; Inostrannaya Literatura, Moscow, 1963).
10. L. D. Landau and E. M. Lifshitz, *Mechanics of Continuous Media* (GITTL, Moscow, 1954).
11. N. G. Kikina, Akust. Zh. **13**, 213 (1967).
12. A. I. Abakumov, A. I. Lebedev, I. A. Nizovtseva, *et al.*, Vopr. At. Nauki Tekh., Ser. Teor. Prikl. Fiz., No. 3, 14 (1990).

Translated by V. Isaakyan

Technical Physics, Vol. 48, No. 8, 2003, pp. 1009–1015. Translated from Zhurnal Tekhnicheskoĭ Fiziki, Vol. 73, No. 8, 2003, pp. 71–77.

SOLIDS

Study of Directionally Solidified Ceramics by Neutron Diffraction Methods

Yu. G. Abov*, N. O. Elyutin, D. V. L'vov*, and Yu. I. Smirnov****

** State Scientific Center of the Russian Federation, Institute of Theoretical and Experimental Physics, Bol'shaya Cheremushkinskaya ul. 25, Moscow, 117259 Russia*

e-mail: lvov@vitep1.itep.ru

*** Moscow State Engineering Physics Institute (Technical University), Kashirskoe sh. 31, Moscow, 115409 Russia*

Received January 9, 2003

Abstract—The effect of the growth rate of directionally solidified Al_2O_3–$Y_3Al_5O_{12}$ ceramics on the structural perfection of the two-phase material is studied by low-angle neutron scattering, as well as by constant-wavelength and time-of-flight neutron diffraction methods. When the growth rate is high, the orientation and size of $Y_3Al_5O_{12}$ needles remain unchanged, while the Al_2O_3 matrix phase decomposes into crystallites. Neutron diffraction methods are viewed as an effective tool for flexible crystal growth control. © *2003 MAIK "Nauka/Interperiodica".*

INTRODUCTION

Extensive studies of various ceramics (see, e.g. [1]), including those with anisotropic properties [2], are today aimed at clearing up the question of whether they may take the place of metals as structural materials offering a higher hardness, wear resistance, and temperature stability; a lower thermal conductivity, etc. Batog *et al*. [3] studied the effect of structure anisotropy on the mechanical performance of directionally solidified oxide-based eutectics, trying to discover causes of micro- and macroinhomogeneities and imperfections in cosolidifying phases by using optical spectroscopy methods and the low-angle scattering (LAS) of thermal neutrons [4].

In this work, we study the effect of the growth rate of directionally solidified two-phase Al_2O_3–$Y_3Al_5O_{12}$ eutectic on the microstructure of both phases by applying neutron diffraction methods. As in [3], changes in the material structure on the supraatomic scale (more than 1000 Å) are revealed by the LAS of neutrons on a double-crystal spectrometer [5, 6]. LAS data are verified and treated by using constant-wavelength and time-of-flight neutron diffraction methods [7]. Since the penetrability of thermal neutrons is much higher than the penetrability of X rays, the dimensions of test samples can be made comparable to those of directionally solidified boules.

It is hoped that the results obtained and the techniques used will be of interest for researchers engaged in novel material synthesis, nondestructive testing, and solid-state physics.

SAMPLE

The ceramic boule was grown by the Bridgman–Stockbarger method on a Granat installation with a rod submersion (pulling) rate of no higher than 10.9 mm/h. During the growth, the pulling rate was changed drastically from v_1 = 4.15 mm/h to v_2 = 10.9 mm/h. The resulting cylindrical boule with a base diameter of 15 mm consisted of two equal parts, which were grown with the various pulling rates in the direction coincident with the cylinder axis.

Theoretically, the as-grown boule would have to represent the single-crystal Al_2O_3 matrix (first phase) densely penetrated by single-crystal yttrium–aluminum garnet ($Y_3Al_5O_{12}$) threads (second phase). It was assumed that the preferred direction of the threads coincides with the pulling direction. $Y_3Al_5O_{12}$ threads were distinctly seen on the micrographs taken from the section near the end faces of the boule. The mean diameter of the threads is found to be $d \approx 1 \pm 0.1$ μm, and the typical center-to-center distance is no greater than 1.5–2.0 μm [3].

To perform experiments, a part of the as-prepared boule was cut off in such a way that the cut plane was parallel to the cylinder axis and the maximal distance from the cut plane to the surface (that is, the maximal thickness of the cut-off (semicylindrical) part was 3 mm). Thus, the thickness of the semicylindrical sample used in the experiments varied from zero (at the edges) to 3 mm (at the center) and its width and length were, respectively, 12 and 75 mm.

1063-7842/03/4808-1009$24.00 © 2003 MAIK "Nauka/Interperiodica"

LOW-ANGLE SCATTERING EXPERIMENTS

The experiments were carried out with the general-purpose neutron diffractometer [8] installed on the horizontal channel of the research reactor in the Moscow Engineering Physics Institute. We used the scheme of a double-crystal spectrometer [5, 6] with a parallel arrangement of the spectrometric pair (Fig. 1). A neutron beam from the active zone of the reactor passes through collimator *1* and is sequentially reflected by crystals *3* and *6* of dual monochromator *2*. The resulting monochromatic beam of intensity G_0 strikes crystal analyzer *9*, reflects from it, and is recorded by detector *10*. The monochromator and analyzer were perfect Ge crystals cut from the same ingot along the (111) crystallographic plane. Dual monochromator *2* was adjusted to the neutron wavelength $\lambda = 1.75$ Å. The dependence of the intensity I_0 recorded by the detector on the angle β between the reflecting planes of crystals *6* and *9* is usually called the instrumental line of a spectrometer. The half-width ω_0 of this curve was found to be $(2.9 \pm 0.1)''$. Some of the neutrons with the intensity $J_0(\beta) = G_0 T_c(\beta)$ pass through the crystal analyzer and are recorded by direct-beam detector *11* ($T_c(\beta)$ is the beam attenuation by crystal *9* at a misalignment angle β).

If sample *8* is placed between the crystals of the spectrometer, some of the monochromatic neutrons are lost because of absorption and Bragg scattering and others are scattered by low angles by inhomogeneities (microvoids, foreign inclusions, dislocations, etc.) [8, 9]. For the sample under study, single LAS prevails. A fraction of the neutrons scattered by angles γ larger than one angular minute is insignificant, while the divergence of the initial beam was $\alpha \approx 30'$. Therefore, the neutrons are left in the beam and strike the crystal analyzer. Then, the intensity recorded by detector *10* is given by

$$I(\beta) = T_0[T_{uns} I_0(\beta) + I_s(\beta)]. \quad (1)$$

Here, T_0 is the factor taking into account the attenuation of the beam passing through the sample, T_{uns} is the fraction of the neutrons that undergo not a single event of LAS when passing through the sample, and I_s is the intensity of the scattered neutrons that reflected from the crystal analyzer. The first term on the right of (1) stands for the intensity of doubly reflected neutrons, which did not interact with the sample.

When crystals *6* and *9*, making up the spectrometric pair, are aligned strictly (that is, $\beta = 0$) and the scattering by a sample is weak (T_{uns} is close to unity), the value of $I_s(0)$ can be ignored; then, expression (1) is recast as

$$I(0) \approx T_{uns} T_0 I_0(0). \quad (2)$$

For the parallel arrangement of the crystals, the temperature of the instrument was kept constant within 0.1°C [10]. For large angles of detuning, $\beta_m \gg \omega_0$, crystal *9* does not reflect. In this case, for the intensity J of the neutrons passed through the crystal analyzer, one can write the obvious relationship

$$J(\beta_m) = T_c(\beta_m) T_0 G_0 = T_0 J_0(\beta_m). \quad (3)$$

Thus, having measured two pairs of the intensities ($I_0(0)$, $I(0)$ and $J_0(\beta_m)$, $J(\beta_m)$), one easily finds T_{uns} from (2) and (3):

$$T_{uns} = \exp(-\Sigma_M L), \quad (4)$$

where L is the sample thickness and Σ_M is the total macroscopic cross section of LAS (linear attenuation factor) for the neutron beam.

In the simplest case of single inhomogeneities evenly distributed over the volume,

$$\Sigma_M = \sigma_t c, \quad (5)$$

where c is the concentration of the inhomogeneities and σ_t is the total cross section of LAS per scatterer, which depends on its characteristic size a and composition [9].

Thus, irradiating different areas of the sample by a narrow neutron beam and comparing the associated values of T_{uns} (or Σ_M), one can note changes in its microstructure on the supraatomic scale. Before scanning, the sample was mounted in a special fixture providing its translational movement with a desired step (Fig. 1). The sample was moved in the horizontal plane (the plane of Fig. 1) and vertical plane with a step of 1 mm. Slotted mask *7*, which is made of Cd and borated polyethylene, was placed in front of the sample. The width and height of the slot were 1.0 and 5.0 mm, respectively.

Four measurements differing in sample motion direction and angular position of the crystal analyzer were made: two measurements with the sample moving in the horizontal plane and the analyzer adjusted ($\beta = 0$ and the reflection is maximal) and misadjusted ($\beta > 2'$

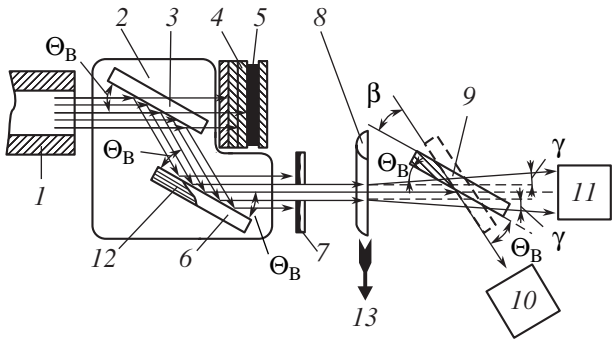

Fig. 1. Schematic of a double-crystal neutron diffractometer: (*1*) collimator, (*2*) dual monochromator, (*3*) Ge premonochromator, (*4*) protection of monitoring chamber against direct neutron and gamma-ray beams, (*5*) monitoring chamber, (*6*) basic Ge monochromator, (*7*) slotted mask, (*8*) test sample, (*9*) Ge crystal analyzer, (*10*) basic detector to record doubly reflected neutrons, (*11*) additional detector to record neutrons passing through crystal analyzer, (*12*) crystallographic planes, and (*13*) sample motion direction.

and the reflection is absent) and two similar measurements with the sample moving in the vertical direction. Prior to the motion, the sample was set off the beam.

The results obtained are illustrated in Fig. 2, where $J(x)$ is the intensity of the neutrons passed through the crystal analyzer that was measured with the spectrometer totally unadjusted and x is the coordinate of the translational motion of the sample scanned in the horizontal plane. The curve $J'(x)$ for the vertical scanning is naturally coincident with $J(x)$ and is omitted in Fig. 2 (hereafter, primed quantities will refer to those obtained for the vertical scanning). The upper and lower dashed lines indicate the mean values of the intensities J_0 and $J(x)$, respectively.

The parameters $I(x)$ and $I'(x)$ stand for the neutron intensities reflected at the horizontal and vertical scanning, respectively. The curves $N(x)$ and $N'(x)$ in Fig. 2 were obtained from the experimental dependences $I(x)$ and $I'(x)$ by the formula

$$N(x) = J_0(\beta_m)[I(x)/I_0] = J(\beta_m)T_{uns}. \qquad (6)$$

The curve $N'(x)$ was derived in the same way. Since $J(x)$ and $J'(x)$ are constant quantities, the middle and lower curves in Fig. 2 are the dependences $T_{uns}(x)$ and $T'_{uns}(x)$ multiplied by a constant (here, $T'_{uns}(x)$ is the fraction of unscattered ions at the vertical scanning. By definition, T_{uns} and T'_{uns} must identically equal unity and the curves $N(x)$ and $J(x)$ (as well as $N'(x)$ and $J'(x)$) must coincide if LAS in the sample is absent.

The step character of $N(x)$ and $N'(x)$ is apparently related to the change in the pulling rate during the growth, because the position of the step correlates with that part of the sample formed at the instant the pulling rate changed. Such a run of the curves $N(x)$ and $N'(x)$ indicates the presence of additional structural inhomogeneities in the left (Fig. 2) half of the sample that was grown at the higher rate. The ripples on the right of the curves are likely to be associated with the unstable operation of the pulling mechanism when the rod velocity was extremely low.

The anisotropy of the ceramic sample, which is induced by $Y_3Al_5O_{12}$ threads, has a substantial effect on its structural properties. To determine the preferred growth direction of the threads relative to the growth axis (pulling direction), the dependences of the intensities $I(0)$ and $J(\beta_m)$ on the angle φ between the crystal axis and vertical line were studied. The angular dependences of $I(0)$ and $J(\beta_m)$ were taken with detectors *10* and *11* for either half of the sample separately. To minimize the influence of the geometrical factor, the measurements were made with the use of a circular beam 1 mm in diameter. In this case, the variation of the sample thickness from the center to the edge of the hole was no more than ≈0.02 mm or 0.7% of its maximal thickness. Prior to the measurements, the sample was set vertically and rotated about the beam axis with a step of 15°.

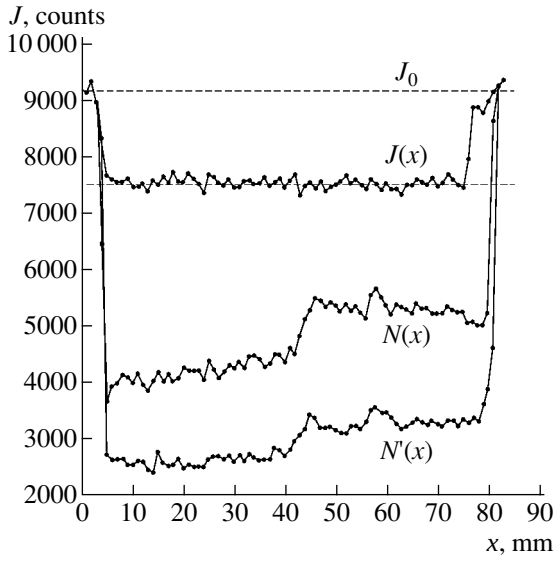

Fig. 2. Neutron intensities J recorded by detectors *10* and *11* vs. the coordinate x of the translational motion of the sample.

The results of the measurements (Fig. 3) show that the intensities $J(\beta_m)$ (Fig. 3a) are almost independent of φ for both parts of the sample, while $I(0)$, on the contrary, demonstrates orientational dependence. In Fig. 3b, the upper curve corresponds to that part of the sample grown with the lower rate v_1. The fact that the curve $I(0)_{v1}$ systematically (at all φ) runs over $I(0)_{v1} > I(0)_{v2}$ is explained by additional inhomogeneities arising in that part grown at the higher rate.

In relationship (2) for the intensity $I(0)$ recorded by the neutron detector, the orientational dependence in the plane normal to the neutron beam is absent. Indeed, under such a rotation, the neutron path in the sample does not change, nor do the attenuation coefficients T_0 and T_{uns}. However, the experiment exhibits orientational dependence. It is natural to assume that this dependence stems from different orientations of the $Y_3Al_5O_{12}$ threads relative to the scattering plane. Thus, relationship (2) fails in describing this effect, and the intensity $I_s(0)$ of the scattered neutrons must be taken into account.

Let us calculate the intensity $I_s(0)$ for single scattering, which occurs when the sample is sufficiently thin. Let a neutron beam striking the sample be directed along the y axis. When analyzing LAS, one takes into account that the wavevector changes in the plane orthogonal to y; i.e., the scattering vector $\mathbf{q} = \mathbf{k} - \mathbf{k}_0 \perp \mathbf{k}_0$ has the coordinates q_x and q_z. Note that a double-crystal spectrometer detects the deviation of neutrons only in one (horizontal) plane. Therefore, to obtain an expression for the observed scattering intensity, it is necessary to integrate the differential cross section $\sigma(\alpha)$ over the vertical divergence and convolve the result

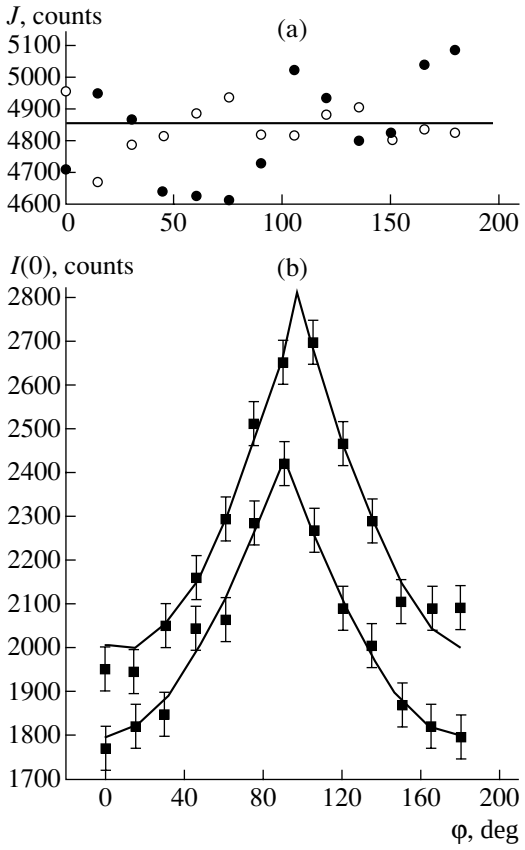

Fig. 3. Intensities of neutrons (a) passed through, *J*, and (b) reflected from, *I*(0), the crystal analyzer vs. the angle of rotation about the horizontal axis. The upper and lower curves in Fig. 3b correspond to the lower (4.15 mm/h) and higher (10.9 mm/h) pulling rates, respectively.

with the instrumental line of the device:

$$I_s(\beta) = \int I_0(\beta - \alpha_x) cLI(\alpha_x) d\alpha_x,$$

$$I(\alpha_x) = \int_{-\infty}^{\infty} \sigma(\alpha_x, \alpha_z) d\alpha_z.$$

In the case of a thin sample, the exponential in (4) can be expanded into the series: $T_{uns} = 1 - c\sigma_t L$. Then, with scattered neutrons taken into account, (2) takes the form

$$I(0) = T_0(1 - c\sigma_t L) I_0(0) + T_0 cL \int I_0(\alpha_x) I(\alpha_x) d\alpha_x. \quad (7)$$

It was shown [11] that the instrumental line $I_0(\alpha)$ can be approximated fairly accurately by the Lorentz function

$$I_0(\alpha_x) = \frac{I_0(0)\omega_0^2}{\alpha_x^2 + \omega_0^2}. \quad (8)$$

The LAS data for neutrons suggest that the differential scattering cross section of a thread is much smaller than the geometric value; hence, the Born approximation holds. Consider scattering by an infinitely long vertical thread of a transverse size *a*. Its neutron optical potential has the form $U = U_0\Theta(|x| < a)\Theta(|y| < a)$, where $\Theta(x) = 1$ if *x* is true; otherwise, $\Theta(x) = 0$. For the scattering amplitude, we have

$$f(\mathbf{q}) = -\frac{mU_0}{2\pi\hbar^2}\int dxdydz\Theta(|x| < a)\Theta(|y| < a) \times \exp(iq_x x + iq_y y + iq_z z) = -\frac{4mU_0}{\hbar^2 k_0}\delta\left(\frac{q_z}{k_0}\right)\frac{\sin(aq_x)}{q_x}\frac{\sin(aq_y)}{q_y}.$$

The differential cross section is given by

$$\sigma(\mathbf{q}) = \frac{16m^2U_0^2a^2}{\hbar^4 k_0^2}\frac{\sin^2(aq_x)}{q_x^2}\delta^2\left(\frac{q_z}{k_0}\right).$$

If the thread makes an angle φ with the vertical, the expression for the cross section takes the form

$$\sigma(\mathbf{q}) = A\frac{\sin^2(aq_x\cos\varphi - aq_z\sin\varphi)}{(q_x\cos\varphi - q_z\sin\varphi)^2}\delta^2(\alpha_x\sin\varphi + \alpha_z\cos\varphi),$$

where $A = 16m^2U_0^2a^2/\hbar^4k_0^2$, $\alpha_x = q_x/k_0$, and $\alpha_z = q_z/k_0$.

Then, integrating over the beam vertical divergence yields

$$I(\alpha_x) = \sigma_t\frac{|\cos\varphi|}{\pi ak_0}\frac{\sin^2(ak_0\alpha_x/\cos\varphi)}{\alpha_x^2}, \quad (9)$$

where $\sigma_t = Al\pi a/k_0$ is the total scattering cross section and *l* is the length of the thread.

Substituting (8) and (9) into (7) and integrating over α_x, one finds the neutron scattering intensity measured by the detector for the aligned monochromator and analyzer crystals:

$$I(0) = T_0I_0(0)\left\{1 - c\sigma_t L\frac{|\cos\varphi|}{2ak_0\omega_0} \times (1 - \exp(-2ak_0\omega_0/|\cos\varphi|))\right\}. \quad (10)$$

Based on expression (10) (with $\varphi - \varphi_0$ substituted for φ), we approximated the experimental data by the least-squares method with four adjusting parameters: $p_1 = T_0I_0(0)$, neutron flux intensity; $p_2 = c\sigma_t L$, effective thickness of the sample; $p_3 = \varphi_0$, angle between the thread direction and crystal growth direction; and $p_4 = 2ak_0\omega_0$, ratio of the instrumental line width to the characteristic angle of diffraction by the threads. The experimental φ dependence of *I*(0) and its approximation are given in Fig. 3b.

For the pulling rates v_1 and v_2, we have $\varphi_0 = 7° \pm 3°$ and $1° \pm 2°$, respectively. This leads us to conclude that the direction of the threads and that of crystal growth coincide within the experimental error.

The intensity vs. crystal orientation dependence is a consequence of the fact that a double-crystal spectrometer has a very high resolution along the horizontal projection q_x of the scattering vector and a poor resolution along q_z. As a result, under rotation, the instrumental line of a double crystal spectrometer cuts off domains of different intensities from the complete nonaxisymmetric distribution of neutrons scattered. Since the values of k_0 and ω_0 are known, the determination of the parameter p_4 gives the thread diameter. Eventually, we arrive at a new technique for finding the thread diameter: instead of the rotation of the crystal analyzer with the sample position fixed, one may rotate the sample with the monochromator and analyzer arranged parallel to each other. The latter approach provides the maximal neutron intensity at the detector. However, threads with a circular, rather than with a rectangular (as was considered above), cross section seem to be a more adequate model object, which helps to find the size of yttrium–aluminum garnet (YAG) threads with a higher accuracy. In this case, the neutron optical potential of a vertical thread has the form $U = U_0\Theta(\sqrt{x^2 + y^2} < a)$ and the scattered neutron intensity, instead of (10), appears as

$$I(0) = T_0 I_0(0)\left\{1 - \frac{3\pi}{8} c\sigma_t L \int_{-\infty}^{\infty} \frac{J_1^2(x)dx}{x^2 + c^2}\right\}, \qquad (11)$$

where $c = ak_0\omega_0/|\cos\varphi|$.

However, formula (10) approximates expression (11) with an accuracy of <5% throughout the interval of φ if the side of the square cross section of a rectangular rod is roughly 10% less than the diameter of the circular one. Hence, formulas (10) and (11) approximate experimental data with nearly the same accuracy for the given statistics.

Thus, we established the correlation between the pulling rate and the concentration of inhomogeneities in the material grown. Supposedly, these inhomogeneities are defects arising in the single-crystal Al_2O_3 matrix phase, since any noticeable changes in the size and orientation of the filamentary $Y_3Al_5O_{12}$ phase have not been discovered. One may however assume that an increase in the volumetric density of defects in the matrix phase will cause distortions in the crystal structure of the threads. To check this supposition, the LAS study was complemented by neutron diffraction investigation.

NEUTRON DIFFRACTION INVESTIGATION

The investigation was carried out for either half of the sample separately. Constant-wavelength neutron diffraction patterns were taken at $\lambda_n = 1.03$ Å with the powder diffractometer in the Moscow Engineering Physics Institute, and time-of-flight diffraction patterns were taken with the SFINKS instrument (Konstantinov Institute of Nuclear Physics, St. Petersburg) over a wide range of thermal neutron wavelengths. The diffraction patterns were not interpreted, since the mere fact of change in the crystal structure sufficed for us.

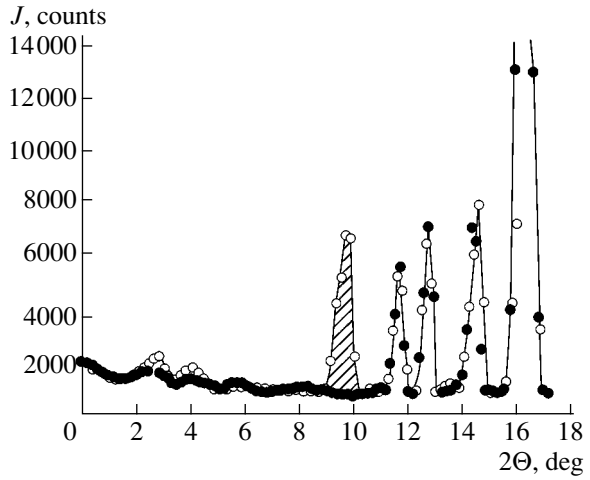

Fig. 4. Fragments of the neutron diffraction patterns taken at the constant wavelength $\lambda = 1.03$ Å from two halves of the sample, which were grown at pulling rates $v_1 = 4.15$ mm/h and $v_2 = 10.9$ mm/h.

In the former case, neutron diffractograms were taken by the well-known (see, e.g. [7]) method of taking diffractograms from polycrystalline samples, with the YAG threads playing the role of crystallites. The sample was placed in such a way that its axis (aligned with the pulling direction) was normal to the scattering plane and the neutrons reflected from those crystallographic YAG planes running parallel to the pulling direction. The sample was uniformly rotated about the vertical axis so that some of the reciprocal lattice sites of the single-crystal matrix could regularly fall on the Ewald sphere. Thus, the neutron diffraction pattern was expected to contain the maximum possible number of reflections. Accordingly, any modification in the crystal structure of one or both phases due to a change in the growth rate could be revealed by comparing the diffraction patterns taken from both halves of the sample. For example, if the matrix becomes polycrystalline after the pulling rate has been increased, the diffraction pattern must apparently contain all allowable reflections for the Al_2O_3 lattice.

The sample was also examined by the time-of-flight neutron diffraction method [7]. With the angular position of the detector fixed and the single crystal appropriately oriented, neutrons with wavelengths $\lambda_n = \lambda/n$ reflect from (*nh*, *nk*, *nl*) planes of the matrix, where *n* is an integer and *h*, *k*, *l* are the Miller indices. The thread reciprocal lattice sites lying between the Ewald spheres corresponding to the wavelengths λ_{max} and λ_{min} should

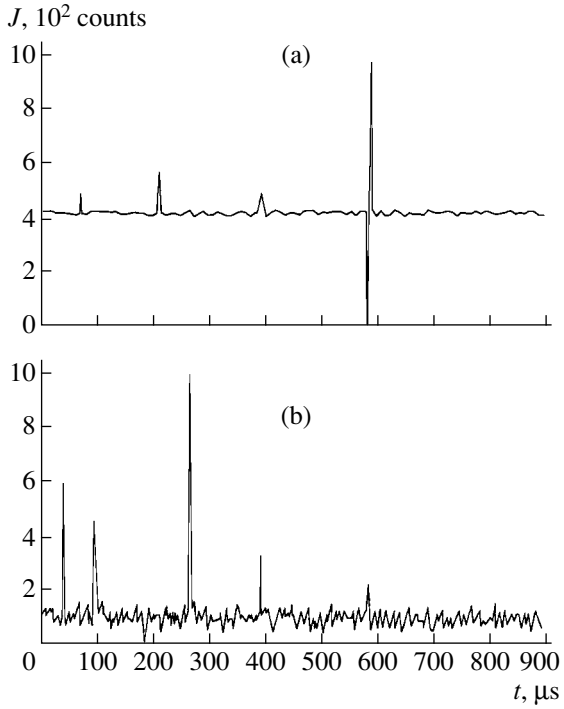

Fig. 5. Fragment of the time-of-flight neutron diffraction patterns taken from two halves of the sample. Pulling rate is (a) v_1 = 4.15 mm/h and (b) v_2 = 10.9 mm/h. *t* is the transit time.

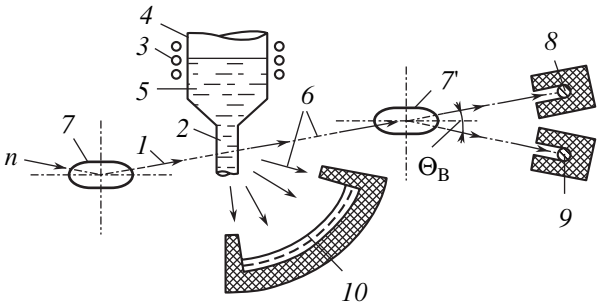

Fig. 6. Possible design of a setup for controlling the defect concentration in a material synthesized: (*1*) monochromatic neutron beam; (*2*) growing single crystal; (*3*) heater; (*4*) growth chamber; (*5*) starting melt; (*6*) neutrons passed through the sample; (*7*) crystal analyzer; (*8*, *9*) detectors to record direct and reflected neutron beams, respectively; and (*10*) position-dependent detector to record diffraction pattern.

also contribute to the diffraction pattern. However, the single crystal reflects neutrons by its entire volume, while a thread reflects them only by that part of it that is proportional to $\omega/2\pi < 0.01$, where ω is the reflection half-width. Since the volumes of the phases are comparable to each other, the above contribution is insignificant.

Experimental results are illustrated in Figs. 4 and 5. The former shows the superposition of the time-of-flight neutron diffraction patterns taken from both parts of the sample. All the diffraction reflections present on the pattern corresponding to the lower pulling rate are seen on the pattern corresponding to the higher pulling rate. However, the latter have a number of extra peaks (one of which is hatched). This suggests that the crystal structure of at least one of the phases undergoes transformations when the pulling rate is changed.

The time-of-flight neutron diffraction pattern shown in Fig. 5a was taken from that half of the sample grown at the lower pulling rate. It contains a series of equispaced peaks corresponding to multiples of λ_n ($\lambda/2$, $\lambda/4$, etc.), which is typical of single crystals. The curve in Fig. 5b demonstrates irregularly spaced peaks, indicating a substantial distortion of the single-crystal lattice. In this case, the Al_2O_3 matrix is likely to consist of several blocks. Thus, the neutron diffraction data are evidence that the single-crystallinity of the Al_2O_3 phase is lost when the pulling rate is high. The highest possible pulling rate at which the matrix remains perfect lies in the interval between 4.15 and 10.9 mm/h.

CONCLUSIONS

The structure of directionally solidified Al_2O_3–$Y_3Al_5O_{12}$ ceramics grown from the melt with different pulling rates is studied by neutron diffraction and LAS of neutrons. It is confirmed that the material grown with a pulling rate of 4 mm/h or below is single-crystal Al_2O_3 densely penetrated by YAG threads. For pulling rates ranging from 4.15 to 10.9 mm/h, the filamentary structure of the $Y_3Al_5O_{12}$ phase persists and the matrix phase decomposes into crystallites. It is found that the limiting pulling rate at which the matrix remains single-crystalline lies within the 4–10 mm/h interval.

A direct correlation between the defect concentration and pulling rate is demonstrated. It is established that an increase in the pulling rate raises the number of inhomogeneities (defects) at grain boundaries in the single-crystal phase. Even minor variations of the pulling rate due to the unstable operation of the pulling mechanism have a significant effect on the defect concentration in the material grown. A change in the pulling rate does not affect the preferred growth direction of the threads. This direction is the same as the pulling direction within the experimental error.

As is well known, the phases of directionally solidified eutectics are fairly perfect if conditions for their formation are equilibrium. The process dynamics has a decisive effect on the formation of individual phases and the material as a whole. Therefore, the technique used in this paper could be useful in searching for and maintaining optimal growth conditions (growth rate, melt temperature, growing ingot volume, etc.) to improve the product yield in commercial production of such materials.

The production of materials with desired properties implies the flexible control of growth processes with due regard for the state of a considerable part of the

crystal volume. Neutron diffraction methods are very suitable in this case: a growing ingot is irradiated by a beam of monoenergetic thermal neutrons that affects the material properties only slightly. The detection of Bragg-reflected radiation allows one to control the crystal structure, as was done in [12], where a pulsed source of neutrons was used. Macroinhomogeneities in the material structure can be visualized from the relative change in the flux of neutrons scattered from a perfect crystal by low angles (Fig. 6) or, if necessary, from the LAS curves. When combined, these two approaches will favor the monitoring and automatic control of the growth process with a view to increasing the yield of directionally solidified ceramics [13], e.g., by applying the optimal growth conditions on growth facilities outside the experimental reactor room.

ACKNOWLEDGMENTS

The authors thank researchers of the Konstantinov Institute of Nuclear Physics (St. Petersburg) for taking the time-transit neutron diffraction patterns, V.N. Batog for the preparation of the sample, as well as F.S. Dzheparov, A.O. Éĭdlin, and S.K. Matveev for valuable discussions.

This work was supported by the Russian Foundation for Basic Research (grant nos. 00-02-17837 and 00-15-96656) and by the Ministry of Education of the Russian Federation (grant no. TOO-7.5-2769).

REFERENCES

1. M. Hainbuchner, M. Villa, M. Baron, *et al.*, http://www.ati.ac.at/~neutropt/team/Publications/SAS SiC SiCf.pdf.
2. A. J. Allen and N. F. Berk, Neutron News **9**, 13 (1998).
3. V. N. Batog, V. G. Karabutov, N. N. Morozov, *et al.*, Neorg. Mater. **22**, 1864 (1986).
4. D. I. Svergun and L. A. Feĭgin, *Low-Angle Scattering of X rays and Neutrons* (Nauka, Moscow, 1986).
5. Z. G. Pinsker, *X-ray Crystal Optics* (Nauka, Moscow, 1982).
6. S. Sh. Shil'shteĭn, V. I. Marukhin, M. Kalanov, *et al.*, Prib. Tekh. Éksp., No. 13, 301 (1971).
7. Yu. A. Aleksandrov, É. I. Sharapov, and L. Cher, *Diffraction Methods in Neutron Physics* (Énergoizdat, Moscow, 1981).
8. Yu. G. Abov, N. O. Elyutin, D. S. Denisov, *et al.*, Prib. Tekh. Éksp., No. 6, 67 (1994).
9. R. J. Weiss, Phys. Rev. **83**, 380 (1951).
10. A. O. Éĭdlin, Yu. I. Smirnov, N. O. Elyutin, *et al.*, Prib. Tekh. Éksp., No. 3, 48 (1988).
11. Yu. G. Abov, D. S. Denisov, F. S. Dzheparov, *et al.*, Zh. Éksp. Teor. Fiz. **114**, 2194 (1998) [JETP **87**, 1195 (1998)].
12. A. M. Balagurov and G. M. Mironova, Kristallografiya **36**, 314 (1991) [Sov. Phys. Crystallogr. **36**, 162 (1991)].
13. Yu. P. Andreev, V. N. Batog, N. O. Elyutin, *et al.*, USSR Inventor's Certificate No. 141016 (1988).

Translated by V. Isaakyan

Technical Physics, Vol. 48, No. 8, 2003, pp. 1016–1019. Translated from Zhurnal Tekhnicheskoĭ Fiziki, Vol. 73, No. 8, 2003, pp. 78–81.

SOLID-STATE ELECTRONICS

Influence of a Circulating Current on the Thermal Conductivity of Heterogeneous Systems

V. V. Krjuk, D. A. Molodtzev, A. V. Pilugin, and A. A. Povzner

Ural State Technical University, ul. Mira 19, Yekaterinburg, 620002 Russia

e-mail: ppupi@k-uralsk.ru

Received October 7, 2002; in final form, December 24, 2002

Abstract—An approach describing the influence of thermoelectric effects and boundary conditions on the thermal conductivity of heterogeneous systems is developed. At a certain configuration of a heterogeneous system, circulating electric currents appearing in the system are shown to influence markedly the effective thermal conductivity. The maximum growth of the thermal conductivity is to be expected in heterogeneous semiconductors and semimetal systems with opposed thermoelectromotive forces. © *2003 MAIK "Nauka/Interperiodica".*

The study of transport processes in inhomogeneous media such as composites, alloys, and compounds, is a topical and challenging scientific and technical problem. Existing methods of solving this problem (described in [1–3]) are not adequate in some cases. Moreover, these methods do not allow one to find detailed field distributions in an inhomogeneous medium even for a single field. The case when several fields affect transport processes in inhomogeneous media simultaneously is still more complicated. Recent results [3], though encouraging, still involve fundamental drawbacks: the consideration was restricted to the plane case and periodic arrangement of impurities of a regular shape.

In this paper, a method for calculating effective kinetic coefficients in inhomogeneous systems subjected to the simultaneous action of stationary thermal and electric fields [4] is described. In addition, the thermal conductivity vs. the geometry of a heterogeneous structure, concentration and physical properties of its components, and boundary conditions is studied in the case of the self-consistent action of thermal and electric fields. Conditions in which the effective thermal conductivity reaches extremal values are found.

In order to calculate the effective thermal conductivity of a heterogeneous structure, we will use the equations of electromigration and heat transport [5]:

$$\mathbf{j} = -\frac{\sigma}{e}\mathrm{grad}(e\varphi - \mu) - S\sigma\mathrm{grad}T,$$
$$\mathbf{q} = \frac{\pi}{e}\mathbf{j} - \chi\mathrm{grad}T, \quad (1)$$

where **j** and **q** are, respectively, the electric and thermal flux densities; σ, χ, and S are the electric conductivity, thermal conductivity, and differential thermoelectromotive force, respectively; $\pi = ST$ is the Peltier coefficient; φ is the electric potential; μ is the chemical potential; $\tilde{\varphi} = e\varphi - \mu$ is the electrochemical potential; T is temperature; and e is the electron charge.

In calculating the effective thermal conductivity of a heterogeneous system, we will first determine the distributions of the potential $\tilde{\varphi}(x, y)$ and temperature $T(x, y)$ over the system. The heterogeneous region is divided into N finite (unit) homogeneous cells (Fig. 1a) in order to find the potential in the vicinity of an arbitrary point (x, y). A finite cell is an analogue of the infinitesimal neighborhood of the point (x, y). The equality of the averaged potentials and fluxes (first derivatives) on the cell surface (Fig. 1a, line *b*) is provided if the functions defined in this region are nonlinear. Let us write the potential $\tilde{\varphi}_i(x, y)$ and temperature $T(x, y)$ in an ith cell ($i = 1, \ldots, N$) in the form of quadratic functions:

$$\tilde{\varphi}_i(x, y) = a_{i,1}x^2 + a_{i,2}y^2 + a_{i,3}x + a_{i,4}y + a_{i,5},$$
$$T_i(x, y) = a_{i,6}x^2 + a_{i,7}y^2 + a_{i,8}x + a_{i,9}y + a_{i,10}, \quad (2)$$

where the coefficients $a_{i,j}$ have to be found.

The choice of the power dependence stems from the fact that physical effects related to the second derivatives are neglected in this paper. Besides, the coefficient

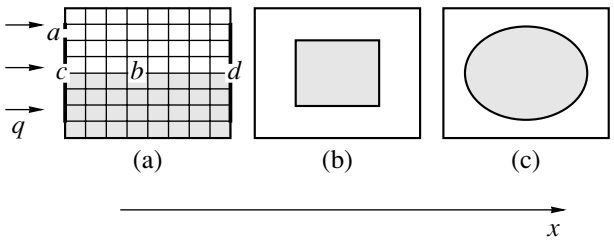

Fig. 1. Heterogeneous system. The filled regions show second-phase inclusions; (a) and (b), the boundary surfaces of unit cells; and (c), isothermal surfaces.

1063-7842/03/4808-1016$24.00 © 2003 MAIK "Nauka/Interperiodica"

multiplying xy is equal to zero because of the symmetry of the unit cells.

We will find the electrochemical potential and temperature based on the assumption that physical processes in the neighborhood of the point (x, y) depend on the physical properties of the neighborhood (the electric conductivity, thermal conductivity, and differential thermoelectromotive force in the vicinity of the point are assumed to be given) and on the conditions at the boundary of the neighborhood. At the boundary between two adjacent cells (Fig. 1a, line b), the averaged values of the electric current, thermal flux, electrochemical potential, and temperature on either side of the boundary are equal to each other:

$$\int_b \tilde{\varphi}_i ds = \int_b \tilde{\varphi}_j ds, \quad \int_b T_i ds = \int_b T_j ds,$$
$$\int_b \mathbf{j}_i d\mathbf{s} = \int_b \mathbf{j}_j d\mathbf{s}, \quad \int_b \mathbf{q}_i d\mathbf{s} = \int_b \mathbf{q}_j d\mathbf{s}, \tag{3}$$

where i and j are the numbers of the adjacent cells.

The absence of charge and heat sources in a cell is taken into account by the equations

$$\oiint_{S_i} \operatorname{grad}\tilde{\varphi}_i d\mathbf{s} = 0, \quad \oiint_{S_i} \operatorname{grad} T_i d\mathbf{s} = 0, \tag{4}$$

where S_i is the surface bounding the cell volume V_i.

On the surfaces of a unit cell that are the boundary surfaces for a sample (Fig. 1a, lines a), the averaged values of the potentials and fluxes are given:

$$\int_a \tilde{\varphi}_i ds = \tilde{\varphi}_{a,i}, \quad \int_a T_i ds = T_{a,i},$$
$$\int_a \mathbf{j}_i d\mathbf{s} = I_{a,i}, \quad \int_a \mathbf{q}_i d\mathbf{s} = Q_{a,i}, \tag{5}$$

where $\tilde{\varphi}_{a,i}$, $T_{a,i}$, $I_{a,i}$, and $Q_{a,i}$ are the averaged values of the potentials and fluxes on the boundary surface of an ith unit cell.

In view of (1) and (2), Eqs. (3)–(5) yield a set of nonlinear algebraic equations for the coefficients $a_{i,j}$. Nonlinearity arises because of the explicit temperature dependence of the Peltier coefficient and implicit temperature dependence of the partial kinetic coefficients.

We split a heterogeneous rectangular sample into (100×100) unit cells. Such a number of cells provides both the smooth variation of the potential and the possibility of approximating a circle by rectangles (Fig. 1c). On the left (Fig. 1a, line $c = \bigcup_i a_i$) and right (line $d = \bigcup_j a_j$) sample surfaces, the temperatures T_c and T_d were specified, the width of the region with a given temperature was varied ($0 < c$ and $d < 1$), and the thermal fluxes through this region were not preset. On the rest of the sample surface, adiabatic conditions were imposed. The electric flux through the sample surface was taken to equal to zero, and the electrochemical potential at the boundary was not specified. System (1) was linearized as follows: terms quadratic in the first derivatives were neglected if the temperature difference is small (in this paper, $\Delta T = T_c - T_d = 1$ K) and the number of unit cells along the sample is sufficiently large. Thus, the problem of determining the potentials was reduced to solving the set of linear algebraic equation.

The effective thermal conductivity and thermoelectromotive force of the heterogeneous system along the x axis (Figs. 1a–1c) were determined by the formulas

$$\chi_{\text{eff}} = \frac{Q}{\Delta T}, \quad S_{\text{eff}} = \frac{\Delta\varphi}{\Delta T},$$

where Q is the total thermal flux through the line c (Fig. 1a), $\Delta T = T_c - T_d$, and $\Delta\varphi = \varphi_c - \varphi_d$.

An increase in the thermal conductivity coefficient in two-phase semiconductors and semimetals with a high electrical conductivity (10^5–10^6 $(\Omega\ \text{m})^{-1}$) of the phases has been observed in [6]. It was noted that this increase may be caused by circulating currents. However, the contribution to the thermal conductivity due to circulating currents that was calculated in the approximation of the averaged thermal and electric fluxes turned out to be smaller than those observed experimentally. In these estimations, we ignored the fact that an increase in the thermal conductivity of two-component systems, especially at high temperatures (>600 K), is usually accompanied not only by a decrease in the thermoelectromotive force but also by the presence of a second phase with electrical properties that differ from those of the matrix. The homogeneous FeSi system, for example, has similar electron and hole densities [7–9]. In the presence of the second phase $FeSi_2$ with n-type conductivity (α lebeauite of high conductivity), the matrix has p-type conductivity due to an excess iron content. The same situation takes place in the PbTe system with Na (p-type) and Cl (n-type) impurities. In this system, the thermal conductivity increases and the thermoelectromotive force decreases at temperatures above 700 K [10–12].

We calculated the concentration dependencies of the effective thermal conductivity and effective thermoelectromotive force for heterogeneous systems schematically shown in Figs. 1a–1c. The increment of the thermal conductivity is maximum for the system shown in Fig. 1a. The real situation is simulated by the systems shown in Figs. 1b and 1c, where the second component is represented by rectangular and ellipsoidal impurities.

The addition to the effective thermal conductivity that was calculated by the technique described in [4] correlates with experimental data [6, 10]. However, if the difference between the thermal conductivities of the components is significant, the relative effect of the increment falls off, since the contribution from one of the components prevails. The numerical analysis shows

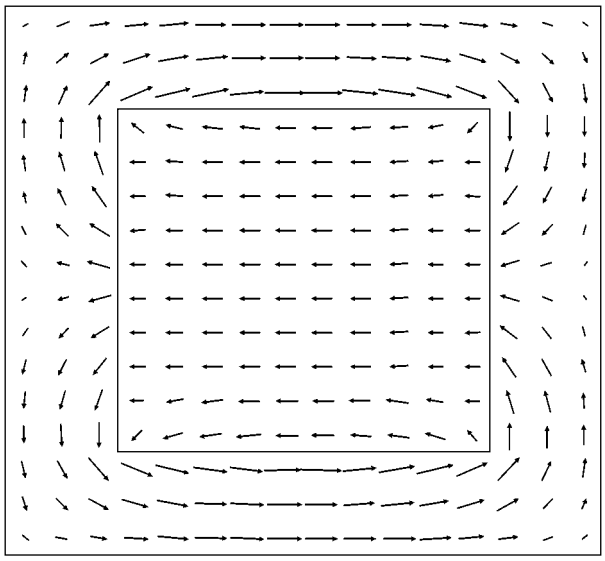

Fig. 2. Circulating electric current appearing in a heterogeneous system with opposing thermoelectromotive force (for the system shown in Fig. 1b).

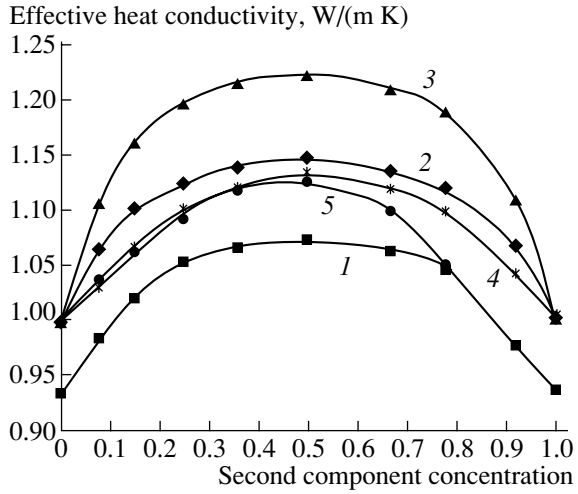

Fig. 3. Effective thermal conductivity as a function of the second component concentration. System shown in (*1*–*3*) Fig. 1a, (*4*) Fig. 1b, and (*5*) Fig. 1c. $\sigma_{1,2} = 10^5$ $(\Omega\ \mathrm{m})^{-1}$, $S_{1,2} = \pm 100$ μV/K, and $\Delta T = 1$ K. (*1*, ■) $c = 0.75$, $T_c = 300$ K; (*2*, ◆) $c = 1$, $T_c = 300$ K; (*3*, ▲) $c = 1$, $T_c = 500$ K; (*4*, ∗) $c = 1$, $T_c = 300$ K; and (*5*, ●) $c = 1$, $T_c = 300$ K.

that the maximum increase in the thermal conductivity due to circulating currents is to be expected in heterogeneous semiconductors and semimetals with opposing thermoelectromotive forces. In this case, a sufficiently high circulating current of unlike charge carriers arises (Fig. 2). The carriers move in the same direction and provide an additional contribution to the thermal conductivity. Electron–hole pairs are generated at the hot end of the sample and recombine at the cold end. The amount of the carriers is approximately proportional to the component concentrations, and the circulating current is maximal in the case of equal component concentrations.

The maximum growth of the thermal conductivity coefficient is observed at equal component concentrations and does not depend on the impurity's shape (Fig. 3). The effective thermoelectromotive force of the system varies monotonically from one partial thermoelectromotive force to the other with concentration of one of the components and vanishes when the component concentrations are equalized. The dependence of the thermal conductivity on the shape and concentration of impurities is displayed by curves *2*, *4*, and *5* (Fig. 3). It is seen that the more complex the shape of the impurities, the smaller the contribution of circulating currents to the thermal conductivity. In this case, the fraction of the charges moving directly along the *x* axis decreases.

The temperature dependence of the effective thermal conductivity is represented by curves *2* and *3* (Fig. 3). The thermal conductivity increases with temperature because of the linear temperature dependence of the Peltier coefficient.

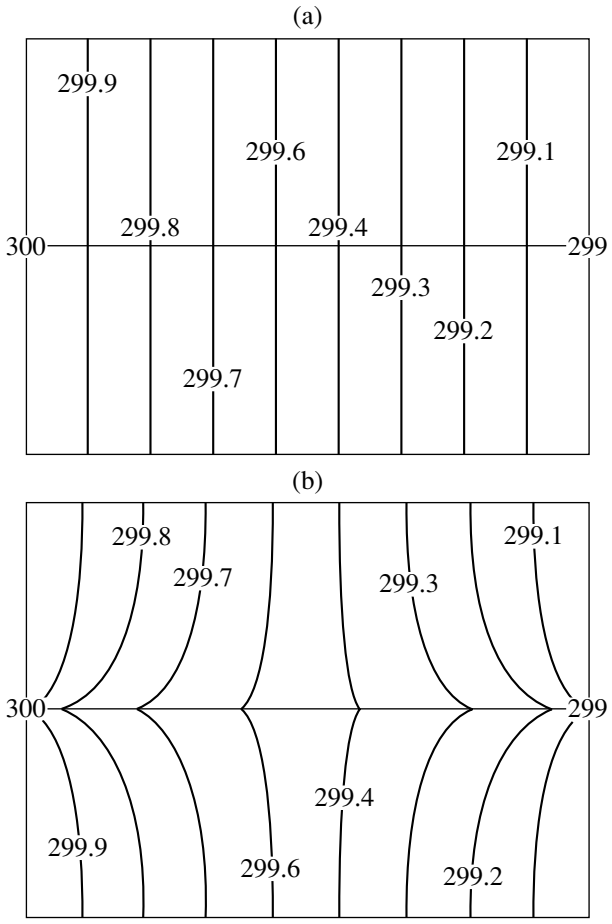

Fig. 4. Isothermal curves. (a) $c = 1$, $\sigma_{1,2} = 10^5$ $(\Omega\ \mathrm{m})^{-1}$, $S_{1,2} = \pm 100$ μV/K, $T_c = 300$ K, and $\Delta T = 1$ K. (b) $S_{1,2} = \pm 300$ μV/K; the other parameters are the same as for (a).

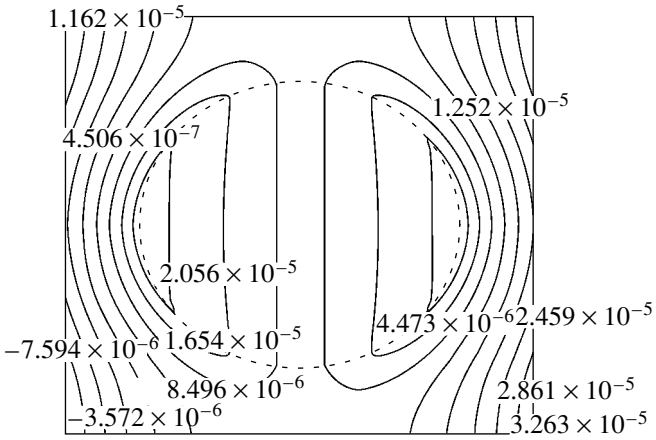

Fig. 5. Electric potential distribution in the heterogeneous system shown in Fig. 1c.

The influence of the boundary conditions on the thermal conductivity is shown by curves *1* and *2* (Fig. 3). As the widths of the input and output fluxes decrease, so does the integral thermal conductivity, including in the homogeneous sample.

Of practical interest are the distribution of the fields over a sample and their dependence on the partial kinetic coefficients and the shape of the inclusion. In Figs. 4a and 4b, the isotherms of the thermal field and their dependences on the thermoelectromotive force are shown. Although the partial thermal conductivities of the components are equal, circulating electric currents contribute significantly to the distribution of thermal fluxes (Fig. 4b). The electric field distribution in the case of elliptic inclusions is shown in Fig. 5. The isopotential curves make it possible to determine the regions of generation and recombination of electrons and holes, as well as the rates of these processes (from the value of the electric potential).

The effects considered have to be taken into account in developing new materials with desired thermoelectric characteristics as well as in analyzing experimental data for the thermoelectric properties of nonstoichiometric semiconductors and semimetals. The latter fact is of particular importance for compounds of transition metals, which cannot as yet be produced with a purity meeting the requirements of semiconductor materials science by means of today's technology.

REFERENCES

1. M. A. Aramyan and G. K. Karapetyan, Inzh.-Fiz. Zh. **74** (1), 92 (2001).
2. B. Ya. Balagurov and V. A. Kashin, Zh. Éksp. Teor. Fiz. **106**, 811 (1994) [JETP **79**, 445 (1994)].
3. B. Ya. Balagurov, Zh. Éksp. Teor. Fiz. **119**, 142 (2001) [JETP **92**, 123 (2001)].
4. V. V. Krjuk, A. V. Pilugin, A. A. Povzner, *et al.*, Inzh.-Fiz. Zh. **75** (3), 1 (2002).
5. I. I. Balmush, *Thermoelectric Effects in Multilayer Semiconductor Structures* (Chisinau, 1992).
6. G. N. Dul'nev and V. V. Novikov, *Transfer Processes in Inhomogeneous Media* (Leningrad, 1991).
7. R. Wolfe, J. H. Wernick, S. E. Hazsko, Phys. Lett. **19**, 449 (1965).
8. B. Buschinger, C. Geibel, F. Steglich, *et al.*, Physica B **230–232**, 784 (1997).
9. M. B. Hunt, M. A. Chernikov, E. Felder, *et al.*, Phys. Rev. B **50**, 14933 (1994).
10. T. G. Alekseeva, E. A. Gurieva, P. P. Konstantinov, *et al.*, Fiz. Tekh. Poluprovodn. (St. Petersburg) **30**, 2159 (1996) [Semiconductors **30**, 1125 (1996)].
11. T. G. Alekseeva, M. V. Vedernikov, E. A. Gurieva, *et al.*, Fiz. Tekh. Poluprovodn. (St. Petersburg) **34**, 935 (2000) [Semiconductors **34**, 897 (2000)].

Translated by M. Fofanov

Technical Physics, Vol. 48, No. 8, 2003, pp. 1020–1023. Translated from Zhurnal Tekhnicheskoĭ Fiziki, Vol. 73, No. 8, 2003, pp. 82–85.

OPTICS, QUANTUM ELECTRONICS

Study of the CdS Crystal Evaporation Kinetics by Laser Step Atomic Photoionization

R. R. Adzhimambetov, I. Sh. Muzhdabaev, A. T. Tursunov, and É. É. Khalilov

Navoi State University, Samarkand, 703004 Uzbekistan

e-mail: info@Samarkand.uz

Received May 29, 2002; in final form, October 31, 2002

Abstract—Laser resonant multistep atomic photoionization is employed to measure evaporation rates and saturated vapor pressures of cadmium sulfide and pure cadmium in temperature ranges of 585–950 and 350–535 K, respectively. It is shown that CdS thermally dissociates into Cd atoms and S_2 molecules. The photoionization of cadmium atoms follows the scheme

$$5s^1S_0 \xrightarrow{\lambda_1 = 326.1\ \text{nm}} 5p^3P_1 \xrightarrow{\lambda_2 = 479.9\ \text{nm}} 6s^3S_1 \xrightarrow{\lambda_3 = 488.1\ \text{nm}} 17p^3P_2 + (\varepsilon = 12\ \text{kV/cm}) \longrightarrow \text{Cd}^+ + e^-.$$

The minimal pressure of pure cadmium is found to be 10^{-11} mm Hg. © *2003 MAIK "Nauka/Interperiodica".*

Several methods of ultrasensitive and ultraselective high-resolution laser spectroscopy aimed at studying a wide class of phenomena have been developed in recent years [1, 2]. Molecular photodissociation by ultraviolet laser radiation was applied to determine the vapor pressure of RbI and KI [3, 4]. The photodissociation of the molecules produces alkaline atoms in the ground state, which are easily detected by two-step laser photoionization. It was shown that laser spectroscopy makes it possible to measure partial vapor pressures as low as ~10^{-15} mm Hg [5, 6]. Therefore, laser resonant spectroscopy seems to be promising for the monitoring of evaporation kinetics in a vacuum [7].

The vapor pressure of CdS is measured with different techniques [8]. One of the most widely used methods is built around high-sensitivity mass spectrometry; however, difficulties associated with an overlap of atomic and molecular mass spectra arise in measuring partial pressures in this case [9].

To study the evaporation kinetics of CdS, we use the thermal dissociation of CdS molecules with subsequent laser resonant step photoionization of resulting Cd atoms. In deciding on a subject of investigation, we took into account the thermal properties of crystalline CdS, which is sublimable solid. It intensely evaporates without melting at relatively low temperatures. In addition, CdS crystals are used in the production of photoelectric and solar cells and serve as lasing media of semiconductor lasers. Therefore, the study of CdS evaporation kinetics is of independent interest.

EXPERIMENTAL

The schematic of the evaporator is presented in Fig. 1. An atomic beam is generated by thermally heating CdS and Cd charges at a residual pressure of ~10^{-5} mm Hg. Laser beams λ_1, λ_2, and λ_3 cross the atomic beams in the space between two electrodes to which a pulsed electric field is applied. Cadmium ions formed by resonant selective photoionization are extracted through a slit in one of the electrodes and detected by a secondary emission electron multiplier. The temperature of the CdS and Cd atomizers is measured with a Ni–Ni/Cr thermocouple and an optical

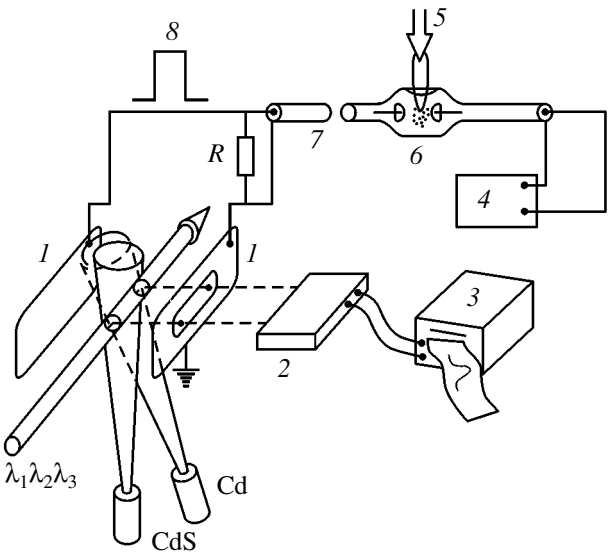

Fig. 1. Experimental setup for the laser photoionization detection of cadmium atoms through Rydberg states. λ_1, λ_2, and λ_3 are laser beams. (*1*) Electrodes; CdS and Cd, CdS and pure cadmium atomizers; (*2*) secondary emission electron multiplier; (*3*) recorder; (*4*) high-voltage power supply; (*5*) igniting pulse; (*6*) gap; (*7*) cable delay line; (*R*) shunt resistor; and (*8*) electric field pulse.

1063-7842/03/4808-1020$24.00

pyrometer. On heating, CdS dissociates into neutral Cd atoms and S_2 and S_3 molecules [10]. The beam of atoms and molecules formed is irradiated by three dye lasers pumped by a pulsed nitrogen laser (the peak power 900 kW, the pulse duration 8 ns, the repetition rate 10 Hz). The wavelengths of the dye lasers are tuned to the electronic transitions in a cadmium atom. To provide the precision and fast tuning of all the lasers, an additional atomizer with a cadmium sample is used at all excitation steps. Atomic beams from the two atomizers meet in the interelectrode space to form the mutual excitation zone. With the mutual excitation zone, one can quantitatively compared ionic signals from each of the atomic beams at the output of the detector, since the conditions for Cd atom excitation and ionization, as well as the conditions for ion detection, are virtually identical. We used the following scheme of the resonant photoionization of cadmium atoms [7]:

$$5s^1S_0 \xrightarrow{\lambda_1 = 326.1\ \text{nm}} 5p^3P_1 \xrightarrow{\lambda_2 = 479.9\ \text{nm}} 6s^3S_1$$
$$\xrightarrow{\lambda_3 = 488.1\ \text{nm}} 17p^3P_2 + (\varepsilon = 12\ \text{kV/cm}) \longrightarrow \text{Cd}^+ + e^-.$$

IONIZATION OF THE MAXIMAL NUMBER OF ATOMS

The optimal excitation of atoms into a high Rydberg state requires that the saturation of the transitions selected be provided. At the last step of excitation, its cross section σ decreases with n^* as $\sigma \sim n^{*-3}$. On the other hand, the critical field ε_c drops with n^* as $\varepsilon_c \sim n^{*-4}$ ($\varepsilon_c = \varepsilon_0/16n^{*4}$, $\varepsilon_0 = 5 \times 10^9$ V/cm, n^* is the effective principal quantum number of the excited state). The optimal case seems to correspond to field strengths achievable in laboratory conditions. The $17p^3P_2$ state of Cd meets this condition ($\varepsilon_c = 8.5$ kV/cm).

Figure 2 plots the cadmium ion yield vs. the energy density of laser pulses at the third step of excitation. Similar dependencies were also obtained at the first and second steps. These dependences were used to determine the laser pulse energy densities necessary to saturate the transitions selected. They were found to be $E_1 = 8.3 \times 10^{-6}$ J/cm^2, $E_2 = 2.4 \times 10^{-6}$ J/cm^2, and $E_3 = 3.5 \times 10^{-3}$ J/cm^2, respectively.

The calculated values of the saturation energy for the first and second steps of excitation were $E_1 = 2.2 \times 10^{-6}$ J/cm^2 and $E_2 = 5 \times 10^{-7}$ J/cm^2, respectively. The energies of laser pulses exceeded the saturation energy and corresponded to the plateau conditions (Fig. 2) for all the steps. In this case, atoms uniformly occupy states according to their statistical weights g_i. The occupancy of the last level for three-step excitation is given by the formula

$$n_3 = Ng_3/(g_0 + g_1 + g_2 + g_3) = \frac{5}{12}N,$$

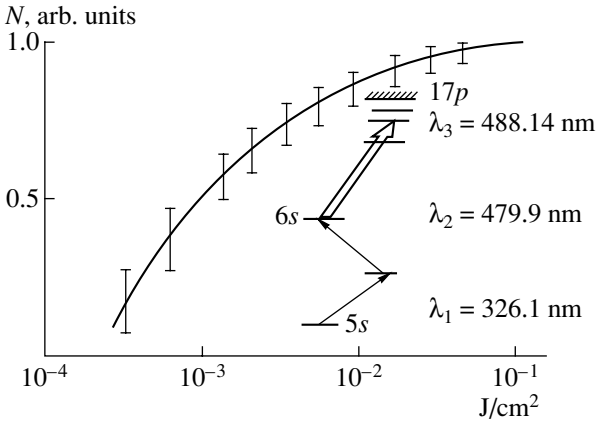

Fig. 2. Dependence of the number of cadmium ions on the laser power density at the third step of excitation.

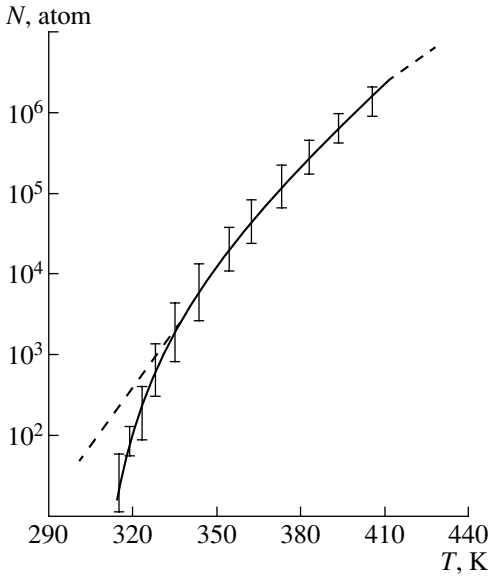

Fig. 3. Dependence of the number of cadmium atoms in the region of observation on the atomizer temperature. The dashed line shows calculated values.

where $N = n_0 + n_1 + n_2 + n_3$ is the atomic density in the excitation zone.

Thus, the fraction of cadmium atoms that are excited into the $17p^3P_2$ state is equal to 5/12 when the electric field $\varepsilon = 12$ kV/cm; i.e., approximately half the atoms exposed to the laser radiation ionize.

DEPENDENCE OF THE NUMBER OF ATOMS IN THE BEAM ON THE ATOMIZER TEMPERATURE

Figure 3 shows the dependence of the cadmium ion yield on the atomizer temperature. The experimental and analytical curves coincide at temperatures exceed-

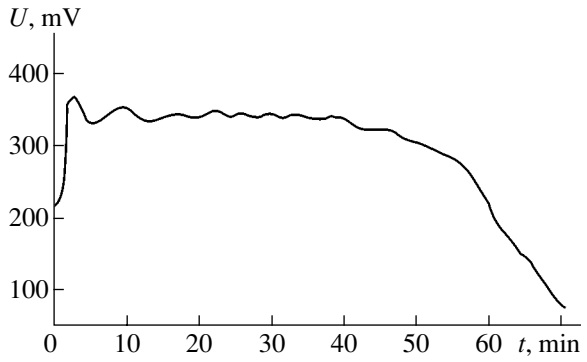

Fig. 4. Cadmium ion yield vs. time of evaporation at T = 943 K and m = 73 mg.

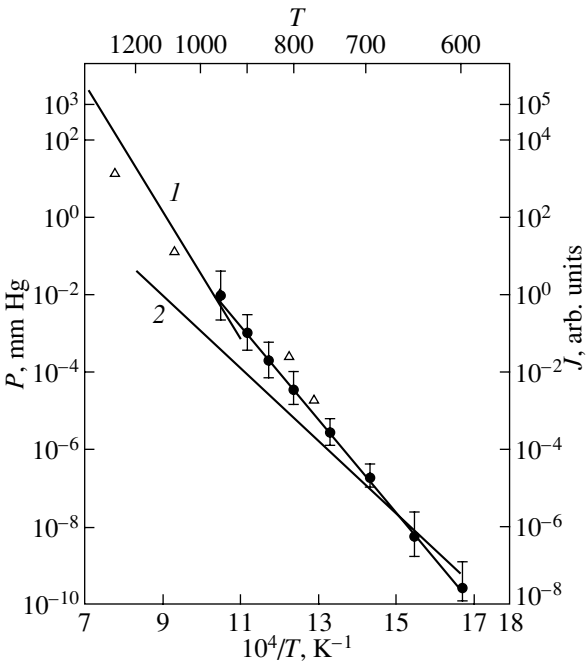

Fig. 5. Temperature dependence of the CdS vapor pressure determined by the thermal dissociation of CdS molecules with the subsequent resonant ionization detection of Cd atoms in vacuum (J). (*1*, *2*) Curves corresponding to the equations $\log p = -11460/T - 2.5 \log T + 16.06$ [12] and $\log p = -11760/T + 12.49$ [14], respectively; (△) data points from [10]; and (●) our data.

ing 350 K. Below 320 K, the photoionic signal becomes unstable. Background ionic pulses were absent. The instability of the photoionic signal is probably associated with fluctuations of the number of atoms in the region of interaction with the laser radiation. If the atomic beam density is low, the fluctuations may be of the same order of magnitude as the average number of atoms in this region ($N \approx 10$).

MEASUREMENT OF THE EVAPORATION RATE AND DETERMINATION OF THE VAPOR PRESSURE

The evaporation rate for Cd and CdS was measured by detecting Cd photoionic signals in the temperature ranges 350–535 K and 585–950 K for pure cadmium and CdS, respectively. As a measure of the CdS evaporation rate, we used the ionic signal at the output of the laser photoionization spectrometer that was amplified by the secondary electron multiplier. Figure 4 presents a continuous record of the photoionic signal upon the evaporation of a CdS sample of mass m = 73 mg at the atomizer temperature T = 943 K. The evaporation time was t = 4200 s. The application of the regulated voltage to the atomizer provided steadiness of the evaporation process.

Before the experiment, an empty crucible and the same crucible filled with CdS were weighed. After the evaporation, the crucible was weighed again. The results of the weighings confirmed that the time of recording the photoionic signal and the time of evaporation coincide. The evaporation rate was determined by the formula [11]

$$\theta = m/\chi A_s t = 5.834 \times 10^{-2} (M/T)^{1/2} p,$$

where $\chi = 3l/8r = 2.5$ is a correction; l and r are the length and radius of the atomizer, respectively; A_s is the cross-sectional area of the atomizer; t is the evaporation time; m is the mass of the material; p is the saturated vapor pressure in mm Hg; M is the molar weight of CdS; and T is the temperature of the atomizer.

From experimental data for the complete isothermal evaporation of CdS, we calculated the evaporation rate, $\theta = 2.46 \times 10^{-4}$ g/(cm^2 s), and the saturated vapor pressure, $p = 1.078 \times 10^{-2}$ mm Hg. The temperature dependence of the CdS saturated vapor pressure in the range from 585 to 950 K can be represented by the empirical formula

$$\log P = -(12\,360 \pm 100)/T + (14.110 \pm 0.036) - 0.99 \log T.$$

These temperature dependences of the pressure are usually extrapolated to higher temperatures, where the dependence is found from independent measurements. With such an approach, the vapor pressure curve can be constructed in a wide range from 10^3 to 10^{-10} mm Hg (Fig. 5).

By finding the evaporation rate for pure cadmium at different temperatures, we derived an equation for the vapor pressure at temperatures ranging from 350 to 535 K:

$$\log P = -(5472 \pm 100)/T + (8.384 \pm 0.1).$$

The dependences of the photoion yield and the number of atoms on the atomizer temperature under ultralow cadmium vapor pressure (Fig. 3) were used to

find the minimal vapor pressure of pure cadmium, 10^{-11} mm Hg at 300 K, by calibration.

CONCLUSIONS

It has been shown experimentally that CdS crystals evaporate in the form of Cd atoms and S_2 molecules. The detection of cadmium photoions with laser resonant ionization has been applied to determine the evaporation rate and vapor pressure of CdS molecules. In the same temperature range, our results for the CdS vapor pressure disagree with the published data insignificantly. This disagreement is probably related to the low sensitivity and selectivity of the conventional methods of investigation. Thus, we demonstrated the potential of atomic laser photoionization spectroscopy for measuring ultralow vapor pressures of metals and their compounds.

REFERENCES

1. V. S. Letokhov, *Photoionization Laser Spectroscopy* (Nauka, Moscow, 1987).
2. W. Demtroder, *Laser Spectroscopy* (Springer-Verlag, Berlin, 1996).
3. G. A. Capelle, D. A. Tessup, H. M. Borella, *et al.*, Appl. Phys. Lett. **44**, 177 (1984).
4. W. M. Fairbank, T. W. Hanch, and A. L. Schawlow, J. Opt. Soc. Am. **65**, 199 (1975).
5. S. V. Andreev, B. C. Letokhov, and V. I. Mishin, Opt. Commun. **57**, 317 (1986).
6. Zh. P. Temirov, A. T. Tursunov, and O. Tukhlibaev, Opt. Spektrosk. **85**, 709 (1998) [Opt. Spectrosc. **85**, 647 (1998)].
7. O. Tukhlibaev, A. T. Tursunov, and É. É. Khalilov, Opt. Spektrosk. **91**, 605 (2001) [Opt. Spectrosc. **91**, 571 (2001)].
8. *Physics and Chemistry of II–VI Compounds*, Ed. by M. Aven and J. S. Prener (North-Holland, Amsterdam, 1967; Mir, Moscow, 1970).
9. L. N. Sidorov and P. A. Akshin, Dokl. Akad. Nauk SSSR **151**, 136 (1963).
10. *Handbook of Thin-Film Technology*, Ed. by L. I. Maissel and R. Glang (McGraw-Hill, New York, 1970; Sov. Radio, Moscow, 1977).
11. S. Dushman, *Scientific Foundations of Vacuum Technology*, 2nd ed., Ed. by J. M. Lafferty (Wiley, New York, 1962; Mir, Moscow, 1964).
12. *Encyclopedia of Chemistry* (Sov. Éntsiklopediya, Moscow, 1990), Vol. 2.
13. *Handbook on Thermodynamic Properties of Inorganic Materials*, Ed. by A. P. Zefirov (Atomizdat, Moscow, 1965).

Translated by M. Lebedev

Technical Physics, Vol. 48, No. 8, 2003, pp. 1024–1027. Translated from Zhurnal Tekhnicheskoĭ Fiziki, Vol. 73, No. 8, 2003, pp. 86–89.

ACOUSTIC, ACOUSTOELECTRONICS

Features of Surface Acoustic Wave Propagation in Lithium Niobate Damaged by an Electron Beam

R. G. Kryshtal and A. V. Medved

Institute of Radio Engineering and Electronics (Fryazino Branch), Russian Academy of Sciences, pl. Vvedenskogo 1, Fryazino, Moscow oblast, 141190 Russia

e-mail: avm@ms.ire.rssi.ru

Received April 15, 2002; in final form, January 27, 2003

Abstract—The propagation of surface acoustic waves (SAWs) in a thin-film aluminum waveguide of $\Delta v/v$ type fabricated on a 128°*Y*–*X* $LiNbO_3$ plate by lift-off lithography and direct writing by a 20-keV electron beam is studied experimentally. The temperature dependence of the phase of the signal passed through an SAW delay line exhibits steps and hysteresis. The line consists of such a waveguide and two interdigital transducers with a center frequency of 486 MHz and is exposed to a nitrogen flow. The vapors of water-containing analytes introduced into the nitrogen flow cause anomalous phase changes. These changes are of opposite sign and more than one order of magnitude greater than the phase changes observed under similar conditions in specimens fabricated by optical lithography. It is concluded that these phenomena offer possibilities for designing SAW humidity sensors with a low threshold of sensitivity. © *2003 MAIK "Nauka/Interperiodica".*

INTRODUCTION

It is known that electron beams (e-beams) or electric fields applied in a special way cause radiation-induced damages in ferroelectric crystals. For example, submicron domains or domain structures of polarization opposite to the polarization of most of the crystal may appear in its surface layers, or even regular domain structures in the bulk of the ferroelectric plate may arise [1–3].

Not much is known about the properties of ferroelectrics damaged by e-beams and how these damages affect the parameters of SAW devices [4, 5]. However, investigation of these issues seems to be topical because of the ever increasing operating frequencies of SAW devices and the use of electron lithography for SAW device fabrication.

In this work, we study SAW propagation in a thin-film aluminum waveguide of $\Delta v/v$ type fabricated on a 128°*Y*–*X* $LiNbO_3$ plate by lift-off lithography and direct e-beam writing. It is this technology that causes the features of SAW propagation mentioned above and, above all else, interesting effects of the gaseous environment, which are apparently associated with e-beam-modified surface layers of $LiNbO_3$.

SPECIMENS AND MEASURING SETUP

The geometry of the specimens studied is shown in Fig. 1. An SAW was excited and received by interdigital transducers (IDTs), each consisting of 30 pairs of electrodes with a 110 μm-wide aperture and a period of 8 μm. A 500-μm-long acoustic waveguide with a total width of 40 μm was made of three parallel aluminum strips. The strip width and spacing equaled one wavelength, i.e., 8 μm. The IDT apertures were matched to the waveguide by horn-type SAW concentrators. In our opinion, SAWs propagating in such a waveguide have the regular plane front as in an ordinary single-strip continuous waveguide of type $\Delta v/v$. It has been experimentally shown that such a waveguide delay line

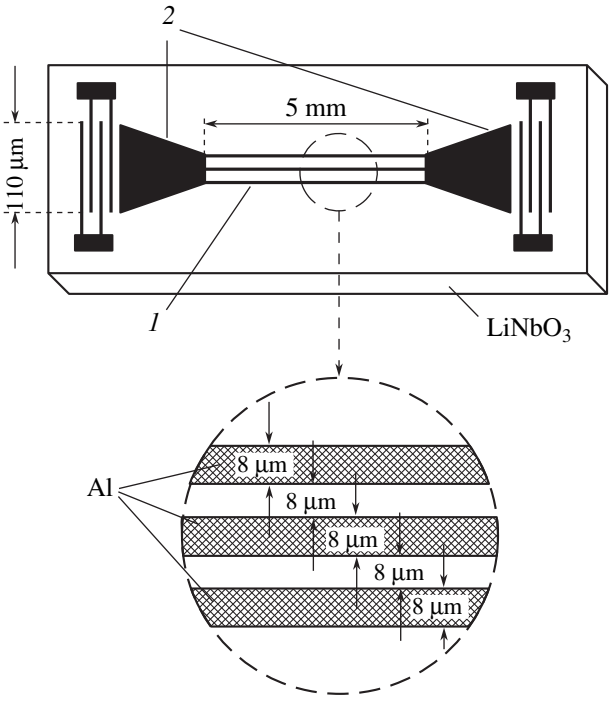

Fig. 1. Layout of test specimens. The substrate measures $9 \times 4 \times 0.5$ mm. (*1*) Waveguide and (*2*) concentrators.

1063-7842/03/4808-1024$24.00 © 2003 MAIK "Nauka/Interperiodica"

shows the linear frequency dependence of the phase velocity in the range from 474 to 498 MHz (in the 3-dB bandwidth).

The specimens were prepared on a 128°*Y*–*X* $LiNbO_3$ substrate by lift-off lithography. An electron resist was patterned by direct writing with a 20-keV electron beam. Thus, the substrate was irradiated by electrons. The irradiated surface area of the acoustic waveguide equaled two-fifths of the SAW aperture. The aluminum layer of the pattern features was 1500 Å thick. At a center frequency of 486 MHz, the insertion loss of this delay line as a part of an unmatched 50-Ω transmission line was 13–14 dB at room temperature.

The delay lines and a thermistor, which measured their temperature, were mounted on the working surface of a Peltier thermoelectric element (TEE) and placed into a measuring chamber. The chamber was provided with sockets to connect the delay lines to high-frequency measuring circuits and the TEE with the thermistor to the power supply and temperature control circuits. The chamber also had a gas inlet and outlet (Fig. 2). We used commercial single-stage TEEs, which were capable of keeping the SAW device temperature within ±0.003°C for 10 min and within ±0.01°C for 10 h for a temperature in the range from 4 to 60°C provided that the ambient the temperature is 20–30°C. A 486-MHz 1-mW signal was applied to the input IDT, and the phase shift of the signal transmitted was measured as a function of time. Knowing this dependence and the rate of change of the temperature at which the measurements were made, one can plot the phase shift versus the substrate temperature. During the measurements, dry chromatographically pure nitrogen (a dew point of no higher than –60°C) flowed through the measuring chamber with a controllable flow rate between 5 and 30 cm^3/min. The vapors of liquid analytes could be injected into the nitrogen flow using a standard chromatographic microsyringe and an evaporator with a rubber membrane. The evaporator temperature, 150°C, was higher than the boiling points of all the analytes used in our experiment. The measuring chamber with the specimen and connecting capillaries were placed in a thermostat.

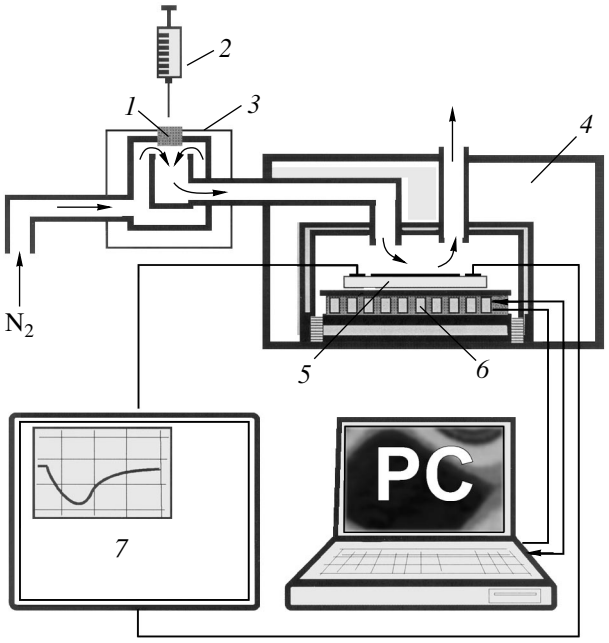

Fig. 2. Block diagram of the experimental setup: (*1*) rubber membrane, (*2*) microsyringe, (*3*) evaporator, (*4*) thermostat, (*5*) SAW specimen, (*6*) TEE, and (*7*) phase meter.

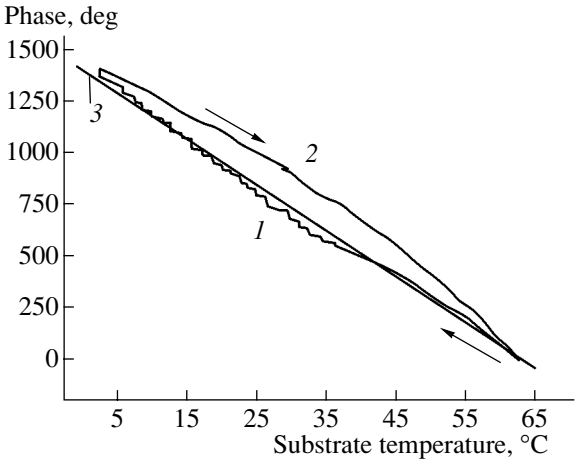

Fig. 3. SAW phase versus substrate temperature: (*1*) substrate temperature decreases, (*2*) substrate temperature increases, and (*3*) theoretical temperature dependence of the SAW phase for a specimen of the same topology with a temperature coefficient of delay of 75 ppm.

RESULTS AND DISCUSSION

We traced the phase of the signal passed through the SAW delay line as the substrate temperature dropped from 65 to 4°C (at a rate of 0.1°C/s) and increased from 4 to 65°C (Fig. 3). It was found that the experimental dependences exhibit appreciable steps and the descending and ascending phase curves do not coincide (hysteresis) and differ from the theoretical dependence. It should be noted that similar steps and hysteresic were also observed in the temperature dependence of the SAW amplitude.

Figure 4 shows the SAW phase measured as a function of time for five temperatures of the piezoelectric substrate with a test amount of 92% ethyl alcohol (8% of water) sample injected into the evaporator. The flow rate of the carrier gas was 18 cm^3/min. The measurements were conducted as follows. Prior to injecting ethyl alcohol into the evaporator, the temperature of the TEE working surface was raised to its maximum value (65°C) and the SAW device was kept at this temperature for several minutes until the phase completely relaxed. Then the temperature was decreased to a desired value at a rate of 0.1°C/s and the specimen was

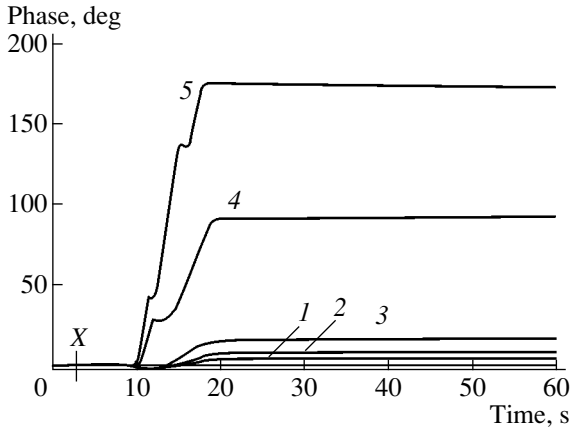

Fig. 4. Experimental time dependence of the SAW phase upon the sorption of the 92% aqueous ethanol solution at a substrate temperature of (*1*) 43.9, (*2*) 38.2, (*3*) 35.0, (*4*) 29.3, and (*5*) 21.9°C. The amount of the liquid analyte is 0.2 ml. *X* indicates the time instant of injection.

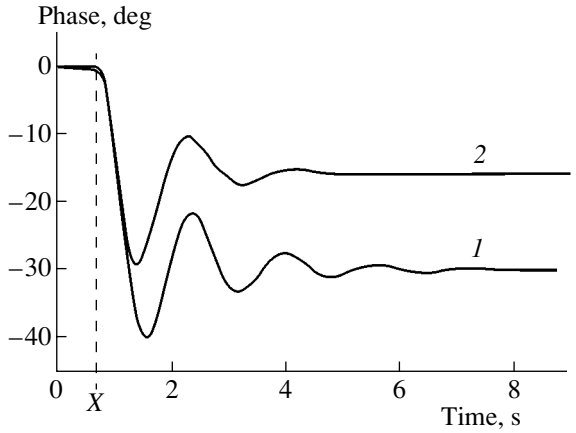

Fig. 5. Experimental time dependence of the SAW phase under the step change in the temperature of the TEE working surface (*1*) from 58.3 to 59.3°C (the substrate temperature transition time is ~5 s) and (*2*) from 9.8 to 10.3°C (the substrate temperature transition time is ~2 s). The instant the temperature is changed is indicated by *X*.

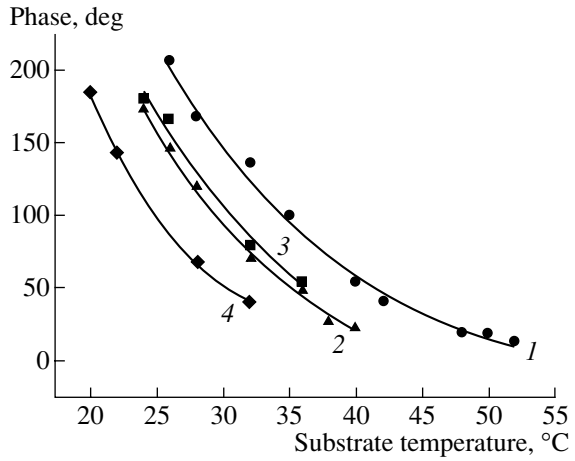

Fig. 6. SAW phase versus substrate temperature upon the injection of (*1*) 0.2 ml of water, (*2*) 0.1 ml of water, (*3*) 0.2 ml of 50% ethanol, and (*4*) 0.1 ml of 50% ethanol into the evaporator. Symbols, data points; solid lines, approximating exponentials.

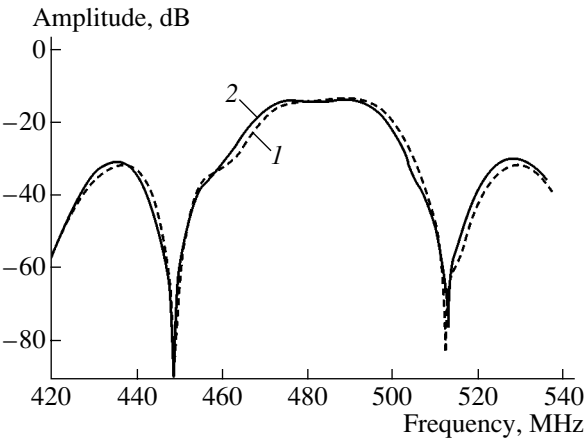

Fig. 7. Amplitude–frequency response of the waveguide delay line at a temperature of 20.5°C (*1*) before and (*2*) after injecting the analyte.

kept at this temperature again for several minutes until a new signal phase was established. This procedure was repeated for each of the substrate temperatures. If the first injection of the analyte is followed by the second one at the same substrate temperature, the phase of the SAW transmitted through the specimen changes again with the same sign (Fig. 4). Such changes will be accumulated after each subsequent injection of the analyte until the total phase shift reaches approximately 250°. Thereafter, the specimen responds to analyte injections in the same manner as a specimen prepared by optical lithography; i.e., the SAW phase change becomes smaller at least by one order of magnitude and has the opposite sign.

It should be noted that the extended time of SAW phase relaxation upon changing the piezoelectric substrate temperature (the time for which the specimen is kept at a specified temperature before an analyte is injected into the evaporator) is not the time taken for the substrate to come to the steady state. It is rather the duration of relaxation processes in the crystal damaged by the e-beam.

The phase response to a step change in the temperature of the TEE working surface from 58.3 to 59.3°C and from 9.8 to 10.3°C for specimens prepared by optical lithography is shown in Fig. 5. The rate of change of the temperature was 0.1°C/s. The substrate temperature was found to follow the variation of the TEE surface temperature without a significant delay. This fact indicates that the hysteresis (Fig. 3) observed in the temperature dependences is unrelated to the time the substrate takes to come to the steady state.

The phase anomalies occur when the SAW propagates between the input and output IDTs and not in the IDTs. We reached this conclusion when observing the smooth time variations of the phase of the reflected signal picked up from the output IDT of the waveguide delay line with the analyte injected into the evaporator and the substrate temperature varied. The input IDT was short-circuited. The experimental conditions were the same as in the previous experiments.

Figure 6 shows the SAW phase as a function of the substrate temperature for different samples of water or 50% ethanol injected into the evaporator. It is seen that nearly coincident curves are only those referring to the analytes containing the same amount (0.1 ml) of water (curves *2* and *3* and the exponents of the approximating exponentials). This means that the anomalous variation of the SAW phase at a given substrate temperature due to the adsorption of the analyte vapor on the substrate after the single injection is proportional to the water volume content in an analyte and is virtually independent of the nature of other analyte components. Similar results were obtained for water solutions of other (methyl, propyl, and isopropyl) alcohols.

Along with the anomalous phase variation, the injection of the analyte into the evaporator caused a step change in the amplitude of the signal picked up from the output IDT. Such behavior also persisted for a long time if the specimen temperature remained unchanged. Figure 7 shows the amplitude–frequency responses for one of the specimens that were taken at a specimen temperature of 20.5°C in the nitrogen flow before and after injecting 0.2 ml of 92% ethanol (8% of water). Note that, when the specimen temperature is higher than 40°C, the amplitude–frequency response is smooth. Kinks in the curve appear when the temperature decreases.

CONCLUSIONS

Thus, we experimentally studied the propagation of an SAW in a thin-film aluminum waveguide of $\Delta v/v$ type fabricated on a 128°*Y*–*X* $LiNbO_3$ plate by lift-off lithography and direct (maskless) e-beam writing. The most important results are (i) the discovery of steps and hysteresis in the phase vs. temperature dependence and (ii) the anomalous variations of the SAW phase and amplitude when water contained in the analyte is adsorbed on the substrate surface. In our opinion, these phenomena are associated with the electron-beam-induced damage to the $LiNbO_3$ crystal during fabrication. We are as yet unable to give a more accurate explanation of the results obtained. Direct observations will hopefully be carried out in the future.

In conclusion, our experimental results suggest that the SAW structures studied and the original fabrication technology may appear to be very promising for designing SAW-based gas sensors, in particular, humidity sensors with an extremely low threshold of sensitivity.

REFERENCES

1. L. A. Bursill and J. L. Peng, Ferroelectrics **77** (1), 81 (1988).
2. S. O. Fregatov and A. B. Sherman, Pis'ma Zh. Tekh. Fiz. **24** (6), 52 (1998) [Tech. Phys. Lett. **24**, 229 (1998)].
3. V. Ya. Shur, E. L. Rumyantsev, R. G. Bachko, *et al.*, Fiz. Tverd. Tela (St. Petersburg) **41**, 1831 (1999) [Phys. Solid State **41**, 1681 (1999)].
4. D. V. Roshchupkin, Th. Fournier, M. Brunel, *et al.*, Appl. Phys. Lett. **60**, 2330 (1992).
5. D. V. Roshchupkin, S. V. Tkachev, R. Tocoulou, *et al.*, Ferroelectrics Lett. **19**, 139 (1995).

Translated by A. Khzmalyan

Technical Physics, Vol. 48, No. 8, 2003, pp. 1028–1034. Translated from Zhurnal Tekhnicheskoĭ Fiziki, Vol. 73, No. 8, 2003, pp. 90–97.

ACOUSTIC, ACOUSTOELECTRONICS

Effect of an External Mechanical Load on Elastic Stresses near Radial Cracks in Al_2O_3–SiC–TiC Ceramics: Photoacoustic Study

K. L. Muratikov and A. L. Glazov

Ioffe Physicotechnical Institute, Russian Academy of Sciences, Politekhnicheskaya ul. 26, St. Petersburg, 194021 Russia

Received September 24, 2002; in final form, January 28, 2003

Abstract—The variation of the photoacoustic signal near the mouths of radial cracks in Vickers-indented externally loaded Al_2O_3–SiC–TiC ceramics is studied. A theoretical model of a photoacoustic signal that is recorded near the mouths of vertical cracks is suggested. Indentation zones in Al_2O_3–SiC–TiC ceramics are visualized by laser scanning photoacoustic microscopy. The sensitivity of the photoacoustic method with piezoelectric detection of signals to both normal and shear stresses acting on a crack is demonstrated. Experimental and theoretical data for the effect of external stresses on the photoacoustic signal near the mouths of radial cracks are compared. For the ceramics under study, agreement is fairly good. It is shown that the strain coefficients near the mouths of vertical cracks can be determined from photoacoustic experimental data. © *2003 MAIK "Nauka/Interperiodica"*.

The photoacoustic (PA) method as a tool for detecting internal mechanical stresses in various solid objects has recently attracted much attention. In this method, acoustic vibrations (or waves) are excited when the object absorbs time-varying optical radiation. The optical-to-acoustic energy conversion mechanism is typically based on the thermoelastic effect, where variable thermoelastic strains are generated near the irradiated region of the object when it expands on heating during irradiation and shrinks on cooling. The thermoelastic strains, in turn, generate thermoelastic stresses, which cause the vibration of the entire object or produce acoustic waves traveling in the object. The acoustic vibrations or waves are usually detected with a piezoelectric element connected to the object [1, 2].

The use of the PA method for internal stress detection has been discussed in [3–10]. However, those articles concern a number of specific applied problems and are purely illustrative. No theoretical models capable of explaining experimental data were suggested. The effects observed and the fundamental potentialities of the method thus remained unclear. Subsequently [11–13], we worked out a theoretical model of PA thermoelastic effect in deformable solids with internal stresses. Its major difference from the conventional linear theories of PA effect in condensed media [1, 2] is that thermoelastic and elastic processes in strained materials are treated in terms of an essentially nonlinear approach.

Without going into the model, we will briefly recall its basic features, which primarily concern the choice of expressions for the thermoelastic and elastic energies of a strained material. Chosen appropriately, these expressions allow one to determine the material's elastic and thermoelastic properties by solving relevant equations of motion.

An expression for the thermoelastic energy density derived in [11–13] includes the strain dependence of the thermoelastic coupling coefficient. In this case, the thermoelastic energy density accurate to first-order components of the strain tensor is given by

$$W_{\text{th}} = -\gamma_{ik}(u_{ik} - U_{ik})\Delta T. \qquad (1)$$

Here, $\gamma_{ik} = \gamma_0[(1 + \beta_0 U_{ll})\delta_{ik} + \beta_1 U_{ik}]$, γ_0 is the thermoelastic coupling coefficient for the unstrained body, β_0 and β_1 are the coefficients involved in the dependence of the thermoelastic coupling on the initial deformation,

$$u_{ik} = \frac{1}{2}\left(\frac{\partial u_i}{\partial x_k} + \frac{\partial u_k}{\partial x_i} + \frac{\partial u_l}{\partial x_i}\frac{\partial u_l}{\partial x_k}\right)$$

is the tensor of the total strain of the body, U_{ik} is the initial strain tensor, $\Delta T = T - T_0$, T is the temperature to which the body heats up absorbing the optical radiation energy, and T_0 is the environmental temperature.

Note that, at $\beta_0 = \beta_1 = 0$, expression (1) turns into the expression for the thermoelastic energy density for an isotropic solid free of internal stresses [14].

The elastic energy density for a solid with allowance for strain-related nonlinear effects was determined in terms of the Murnagan model [15]. In this model, the

elastic energy density is expressed in the form

$$W_{\text{el}} = (\lambda + 2\mu)\frac{I_1^2}{2} - 2\mu I_2 + (l + 2m)\frac{I_1^3}{3} - 2mI_1I_2 + nI_3, \quad (2)$$

where λ and μ are the Lamé coefficients; l, m, and n are the Murnagan constants; $I_1 = u_{kk}$; and

$$I_2 = \frac{1}{2}[(u_{kk})^2 - u_{lm}u_{lm}];$$

$$I_3 = \frac{1}{3}\left[u_{ik}u_{il}u_{kl} - \frac{3}{2}u_{ik}u_{ik}u_{ll} + \frac{1}{2}(u_{ll})^3\right].$$

Knowing the energy density of a solid, one can write an equation of motion for elements of the body. Omitting the solution procedure, we will give at once the final result for the signal detected by a piezoelectric element connected to the back side of the object. In terms of our model, the PA signal from solids with residual strains was shown to be expressed as [11–13]

$$V(\omega) = V_0(\omega)\frac{1}{(1 - U_{pp})^{3/2}} \times \frac{1 + \beta_0 U_{pp} + \beta_1 U_{zz}}{[1 + 2lU_{pp} + (4m + n)U_{zz}]^{3/2}}, \quad (3)$$

where $V_0(\omega)$ is the PA piezoelectric signal from the unstrained object, U_{ik} are the components of the initial strain tensor, $l' = l/(\rho_0 c_l^2)$, $m' = m/(\rho_0 c_l^2)$, $n' = n/(\rho_0 c_l^2)$, ρ_0 is the initial density of the object, and c_l is the longitudinal velocity of sound.

Expression (3) shows that the effect of the initial deformation on the PA signal is not associated with any specific properties of a material. It merely reflects the fact that an object has nonlinear thermoelastic and elastic properties. Thus, our approach is universal and, therefore, can be applied to detecting internal stresses in various materials.

In this work, we perform a detailed theoretical and experimental study of the PA thermoelastic signal near the mouths of cracks in ceramics, using the previously developed concept of PA effect in strained materials. It is known [16] that the crack mouths are concentrators of high internal stresses. Therefore, from the behavior of the PA signal near the mouths, one may gain a more penetrating insight into physical processes in strained regions, on the one hand, and judge the feasibility of using this effect in detecting internal stresses on the other.

It is essential that we applied a mechanical stress to the specimen. Our technique thus made it possible to compare the PA signals taken from specimens subjected to mechanical stresses of various types. This work elaborates upon preliminaries obtained in [17].

The object of study was an Al_2O_3–SiC–TiC composite ceramics Vickers-indented to generate internal stresses. Vickers indentation provides a well-reproducible pattern of cracking and internal stresses [18]. The specimens and the setup for recording the PA signal have been described elsewhere [19–21].

Indentation was carried out for various mutual orientations of the indenter and specimen. Therefore, the indentation zones to be examined had different orientations of radial cracks relative to the external stress vector. First, the PA image was taken from the Vickers-indented zone in the absence of an external load. Then, the same area was imaged when a given mechanical stress was applied to it. Thus, we could record PA signals from the regions adjacent to the mouths of radial cracks produced by Vickers indentation and variously oriented relative to the external stress.

Figures 1 and 2 show typical PA images of the externally stressed Al_2O_3–SiC–TiC ceramics for two mutual

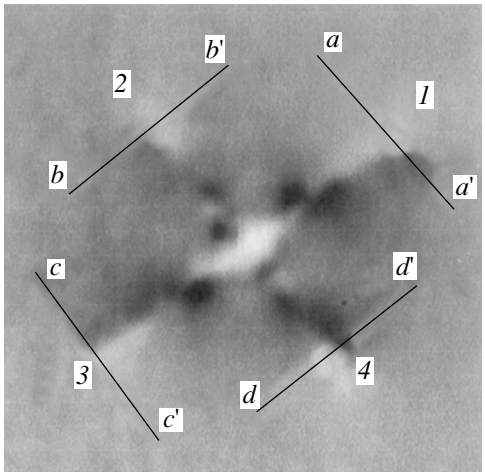

Fig. 1. PA image of the Vickers indentation on the ceramic surface. The image area is 450 × 500 μm. The modulation frequency is 142 kHz. The figures by the lines are crack numbers.

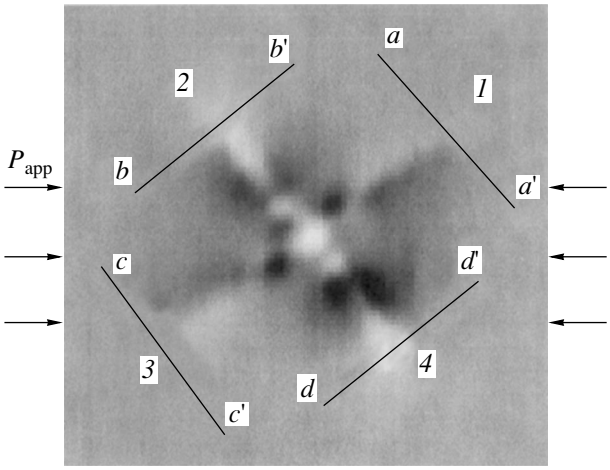

Fig. 2. The same image as in Fig. 1 under a compressive load of 170 MPa applied in the direction indicated by the arrows.

orientations of radial cracks and external load. Directions *aa*', *bb*', *cc*', and *dd*' in Fig. 2 run normally to the cracks near their mouths. Experimental and theoretical data concerning the PA signal behavior near the radial crack mouths were compared along these directions. From these images it follows that the signal varies in regions adjacent to the radial crack mouths, plastically strained zones, and subsurface lateral cracks. We will concentrate on the signal behavior near radial cracks, since the structure of plastically strained zones and other zones of cracking is much more complicated and needs additional identification. The images demonstrate that the external stress has an essentially different effect on the PA signal taken from radial cracks variously oriented relative to the external stress.

When using expression (3) to study the PA signal near the radial crack mouths in ceramic materials, one should take into account the following circumstances. First, residual strains in these materials are low even for a near-cracking load: no higher than 1.5% for most ceramic materials [22]. So, we can put U_{xx}, U_{yy}, $U_{zz} \ll 1$. Second, in ceramic materials, the PA image forms in a thin surface layer. For modulation frequencies of 100 kHz or higher, the penetration of thermal waves usually does not exceed 10 μm, i.e., is much smaller than the depth of radial cracks. Third, one should bear in mind that internal stresses near the radial crack mouths are directed largely along the object's surface. Because of this, we will thereafter assume that the conditions U_{xx}, $U_{yy} \ll U_{zz}$ hold near the radial crack mouths (the *z* axis runs normally to the surface). With all these factors taken into consideration, expression (3) for the PA signal taken from these areas can be represented in the form

$$\Delta V(\omega) = A(U_{xx} + U_{yy}), \tag{4}$$

where $A = V_0(\omega)(\beta_0 + 3/2 - 3l)$.

According to today's concepts of fracture mechanics, plastic strains in ceramic materials are of minor significance up to fracture. In these materials, they are localized within small regions near the crack mouths [16]. Regions with internal stresses are much more extended. Therefore, it may be assumed that here residual strains and internal stresses obey the Hooke law. For the tensor components we are interested in, the Hooke law has the form [16]

$$U_{xx} = \frac{\sigma_{xx} - \nu\sigma_{yy}}{E}, \quad U_{yy} = \frac{\sigma_{yy} - \nu\sigma_{xx}}{E}, \tag{5}$$

where ν is Poisson's ratio, *E* is the elastic modulus, and σ_{xx} and σ_{yy} are the stress tensor components.

Thus, according to (4) and (5), the PA signal as a function of internal stresses is expressed as

$$\Delta V(\omega) = A'(\sigma_{xx} + \sigma_{yy}), \tag{6}$$

where

$$A' = \frac{1-\nu}{E}A.$$

Relationships (4) and (6) have been derived from expression (3), which is valid within the one-dimensional model [9–11]. An essential restriction of this model is the assumption that thermal waves in the object are generated by a radiation uniformly illuminating its surface rather than by a focused laser beam. Therefore, relationships (4) and (6) are, strictly speaking, inapplicable when PA images of the radial crack mouths are analyzed. However, from symmetry considerations, one can infer that, when residual strains are oriented for the most part parallel to the object's surface, the strain dependence of the PA signal in the first order of the perturbation theory may be given only by expression (4). The specific form of the proportionality coefficient *A* remains unknown in this case. However, the specific form of this coefficient is of no significance for our investigation; therefore, we will adhere to expressions (4) and (6).

From (6), it follows first of all that the stress dependence of the PA signal is defined by the same quantities as in the SPATE (Stress Pattern Analysis by measurement of Thermal Emission) method. According to [23], the SPATE signal is also proportional to the sum $\sigma_{xx} + \sigma_{yy}$, although it depends on radically different physical processes. The difference in underlying processes results in different spatial resolutions of PA and SPATE methods. While the spatial resolution of the SPATE method lies in the millimeter range, the PA method provides a micrometer resolution.

As was noted, the PA signal associated with the vertical crack mouths is picked up from a thin surface layer in our case. In experiments like ours, the radial crack depth usually far exceeds the length of thermal waves excited in the specimen. Then, radial cracks may be roughly viewed as plane vertical cracks in thick plates. At the mouths of these cracks, the stress tensor components σ_{xx} and σ_{yy} (in view of the applied load, Fig. 3) are given by [24]

$$\sigma_{xx} = \frac{K_\mathrm{I}}{\sqrt{2\pi r}}\cos\frac{\Theta}{2}\left(1 - \sin\frac{\Theta}{2}\sin\frac{3\Theta}{2}\right) - \frac{K_\mathrm{II}}{\sqrt{2\pi r}}\sin\frac{\Theta}{2}\left(2 + \cos\frac{\Theta}{2}\cos\frac{3\Theta}{2}\right), \tag{7a}$$

$$\sigma_{yy} = \frac{K_\mathrm{I}}{\sqrt{2\pi r}}\cos\frac{\Theta}{2}\left(1 + \sin\frac{\theta}{2}\sin\frac{3\Theta}{2}\right) + \frac{K_\mathrm{II}}{\sqrt{2\pi r}}\sin\frac{\Theta}{2}\cos\frac{\Theta}{2}\cos\frac{3\Theta}{2}. \tag{7b}$$

Here, K_I and K_II are the stress intensity coefficients, which characterize the behavior of the crack under the action of normal and shear (relative to its edges) stress

components; r is the distance from the mouth to the point of observation; and Θ is the angle between the crack propagation direction and the direction to the point of observation.

In general, the crack stress intensity coefficients depend on both residual and applied stress fields. Therefore, in our case,

$$K_I = K_I^{(0)} + K_I^{(1)}, \quad K_{II} = K_{II}^{(0)} + K_{II}^{(1)}, \tag{8}$$

where $K_I^{(0)}$ and $K_{II}^{(0)}$ are the crack internal stress intensity coefficients and $K_I^{(1)}$ and $K_{II}^{(1)}$ are the applied stress intensity coefficients.

According to equalities (7) and (8), PA signal (6) taken from the radial crack mouths can be represented as

$$\Delta V(\omega) = A' \frac{2}{\sqrt{2\pi r}} \times \left[(K_I^{(0)} + K_I^{(1)}) \cos\frac{\Theta}{2} - (K_{II}^{(0)} + K_{II}^{(1)}) \sin\frac{\Theta}{2} \right]. \tag{9}$$

For residual stress fields near the mouths of radial cracks produced by Vickers indentation with a load P, the stress intensity factors are given by

$$K_I^{(0)} = \chi \frac{P}{L^{3/2}}, \quad K_{II}^0 = 0, \tag{10}$$

where χ is a dimensionless factor depending on the crack's shape and L is the length of the crack.

The stress intensity coefficients for a crack under load depend on this load and the angle between the crack and load vector. For plane vertical cracks, these dependences look like [24]

$$K_I^{(1)} = K_1' \sin^2\phi, \quad K_{II}^{(1)} = K_{II}' \sin\phi\cos\phi, \tag{11}$$

where ϕ is the angle between the crack and load and K_I' and K_{II}' are the ϕ-independent stress intensity coefficients characterizing the crack.

Thus, with regard to equalities (9)–(11), the PA piezoelectric signal near the crack mouth is given by the expression

$$\Delta V(\omega) = A' \frac{2}{\sqrt{2\pi r}} \left[(K_I^{(0)} + K_I' \sin^2\phi) \cos\frac{\Theta}{2} - K_{II}' \sin\phi\cos\phi \sin\frac{\Theta}{2} \right]. \tag{12}$$

Expression (12) describes the variation of the PA signal near the mouth of a radial crack under internal and external stresses. The model was checked by comparing expression (12) with experimental data obtained from PA images of Vickers indentations in Al_2O_3–SiC–TiC ceramics.

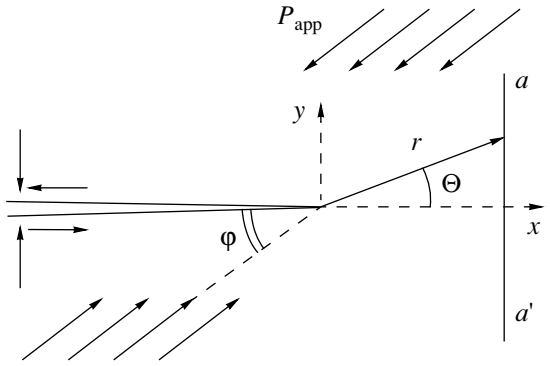

Fig. 3. Analytical scheme. Cracks, coordinate system, and applied load direction.

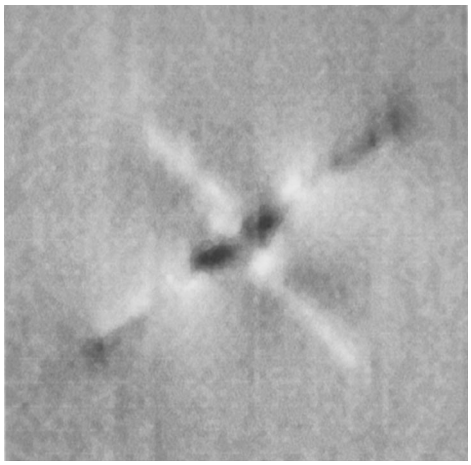

Fig. 4. Difference image (Fig. 2 minus Fig. 1).

In [25], we performed a detailed theoretical and experimental analysis of PA signals taken from radial cracks running normally or parallel to an applied load. For the former cracks, the variation of the PA signal corresponds to the case of normal stresses; for the latter, to the case of shear stresses. Both cases are well described by expression (12). Furthermore, the experimentally found stress intensity coefficients characterizing the effect of internal and external stresses on a crack in Al_2O_3–SiC–TiC ceramics [25] were found to be in good quantitative agreement with analytical results.

Therefore, in this work, we concentrated on a comparison between the theory and experiment for cracks making an angle with the applied load direction. To this end, we obtained PA images of Vickers indentations where the direction of radial cracks differs markedly from the direction of an applied load or from the direction normal to an applied load. The images from indentations were obtained with and without an applied load. For the better visualization of effects related to an applied load, the no-load images were subtracted from the "loaded" ones. By way of example, Fig. 4 shows the PA image of the Vickers indentation where radial

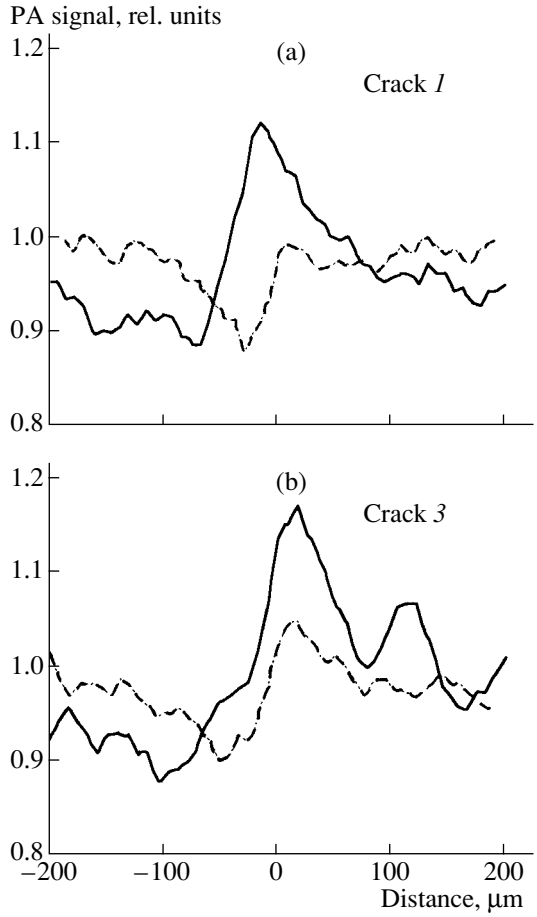

Fig. 5. PA signal distribution near the mouths of cracks (a) *1* and (b) *3* along the line normal to the crack direction. The signal is normalized to the specimen-averaged value. Continuous curves, unloaded specimen; dashed curves, loaded specimen.

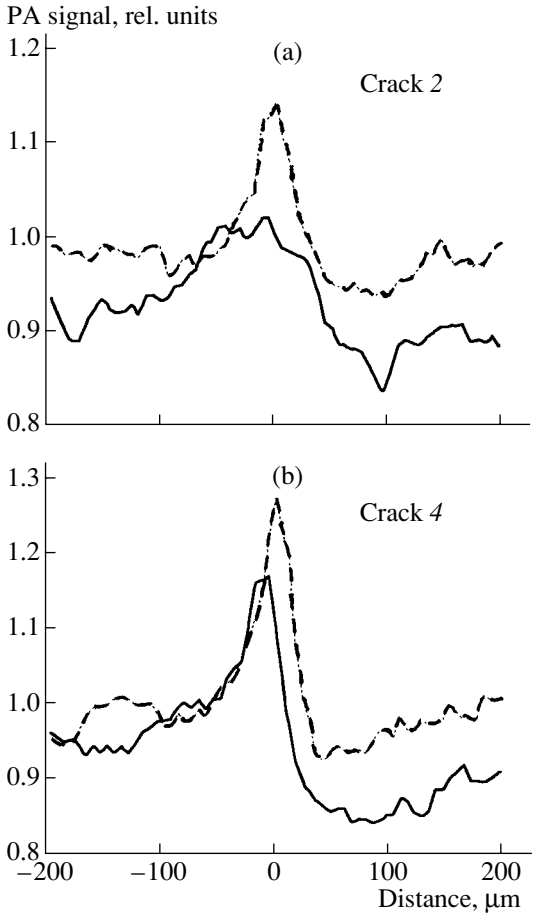

Fig. 6. The same as in Fig. 5 for cracks (a) *2* and (b) *4*.

cracks *1* and *3* run at an angle of 39° and cracks *2* and *4*, at an angle of 47° to the applied stress. The variation of the PA signal under normal and shear stresses was analyzed in terms of the approach suggested in [25]. In this approach, emphasis is on the behavior of the signal along directions normal to cracks. These directions for all radial cracks are shown in Fig. 2. Figure 5 demonstrates the variation of the PA signal along these directions for cracks *1* and *3* in the immediate vicinity of their mouths.

Available experimental data make it possible to establish quantitative relationships between various stress intensity coefficients for the cracks considered. For cracks *1* and *3*, the theoretical and experimental data are in good agreement when $K_I/K_{II} = 1.13$ and 1.25, respectively. These ratios suggest that, in terms of the model developed, normal and shear stresses near the mouths of these cracks have roughly the same effect on the PA signal.

Knowing this ratio for two cracks, one can also estimate the ratio K_I'/K_{II}', which is a ϕ-independent characteristic of a crack. With K_I/K_{II} and the angle ϕ known, we find $K_I'/K_{II}' = 1.36$ and 1.54 for cracks *1* and *3*, respectively. These values correlate with the theory of straight cracks in thick plates [24], which predicts the strict equality of these parameters.

Now let us consider the situation with cracks *2* and *4*. Since they run at roughly the same angles as cracks *1* and *3*, one might expect similar behavior of the PA signal near their mouths. However, Figs. 5 and 6 show that the signals behave in a radically different way. For cracks *1* and *3*, the external stress decreases the signal, while for cracks *2* and *4*, the signal grows, the normal component of the external stress being the dominant factor.

A thorough analysis of the PA image helps to clarify the situation. At the boundary of the Vickers indentation, there are two bright regions extending along the diagonal that coincides with the direction of cracks *2* and *4*. Along the other diagonal, which coincides with the direction of cracks *1* and *3*, such regions are absent. For more clarity, the variation of the PA signal along

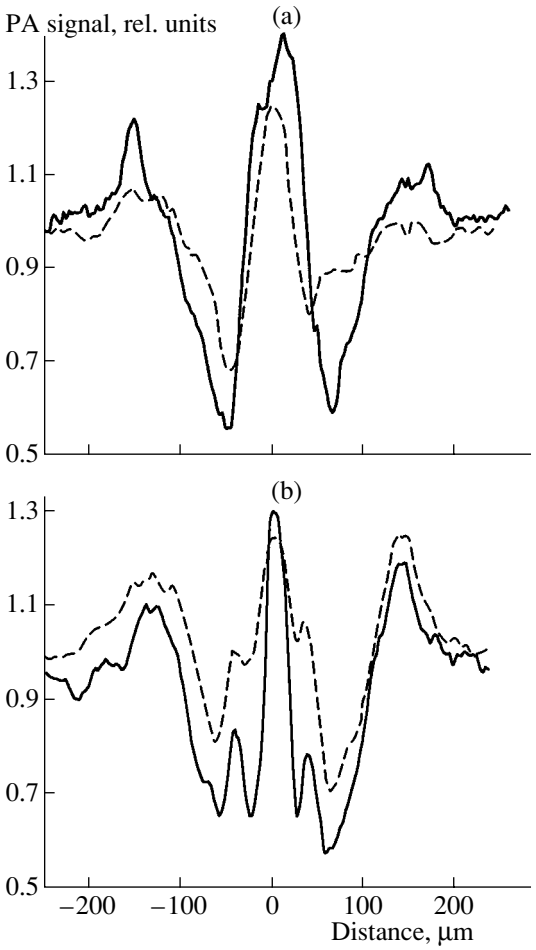

Fig. 7. PA signal distribution along cracks (a) *1* and *3* and (b) *2* and *4*. Continuous curves, unloaded specimen; dashed curves, loaded specimen.

cracks *1*, *3* and *2*, *4* is depicted in Fig. 7, where the brightness of these regions is seen to increase sharply when a load is applied. Such behavior of the PA signal indicates that the applied load partially closes the cracks (their edges merge together) in these regions. Eventually, specific bridges arise in areas where the edges of the cracks superpose on one another. Such phenomena in ceramics have been observed in a variety of studies [26–28]. The superposition effect greatly aggravates the situation and cannot be completely taken into account in terms of our model. In a first approximation, the effect of crack edge superposition at a particular site may be viewed as a decrease in the crack's effective length. According to expression (10), a decrease in the crack length must correlate with an increase in the normal stresses at the mouths. In our case, the cracks shorten roughly twice, which is consistent with the amount of the effect observed.

Thus, our analytical model of PA piezoelectric signal formation provides an adequate explanation of its behavior near the radial crack mouths. It gives a good fit to experimentally found internal stress field variations near the radial crack mouths under both normal and shear applied loads. The results obtained in this work demonstrate the feasibility of the PA piezoelectric method as a tool for studying the distribution of internal stresses near surface cracks in ceramics. Results obtained with the PA method when the specimen is under load may be helpful in studying cracking under load and determining stress intensity coefficients near the crack's mouths.

ACKNOWLEDGMENTS

This work was supported by the CRDF (grant no. RP1-2366-ST-02) and Russian Foundation for Basic Research.

REFERENCES

1. V. E. Gusev and A. A. Karabutov, *Laser Acoustooptics* (Nauka, Moscow, 1991).
2. L. M. Lyamshev, *Radiation Acoustics* (Nauka, Moscow, 1996).
3. M. Kasai and T. Sawada, in *Springer Series in Optical Sciences*, Vol. 62: *Theory of Photoacoustic and Photothermal Phenomena II* (Springer-Verlag, Berlin, 1990), pp. 33–36.
4. J. H. Cantrell, M. Qian, M. V. Ravichandran, *et al.*, Appl. Phys. Lett. **57**, 1870 (1990).
5. H. Zhang, S. Gissinger, G. Weides, *et al.*, J. Phys. (France), Colloq. C7 **4**, 603 (1994).
6. R. M. Burbelo, A. L. Gulyaev, L. I. Robur, *et al.*, J. Phys. (France), Colloq. C7 **4**, 311 (1994).
7. D. N. Rose, D. C. Bryk, G. Arutunian, *et al.*, J. Phys. IV, Colloq. C7 **4**, 599 (1994).
8. R. M. Burbelo and M. K. Zhabitenko, Prog. Nat. Sci. Suppl. **6**, 720 (1996).
9. F. Jiang, S. Kojima, B. Zhang, *et al.*, Jpn. J. Appl. Phys., part 1 **37**, 3128 (1998).
10. K. L. Muratikov, A. L. Glazov, D. N. Rose, *et al.*, Pis'ma Zh. Tekh. Fiz. **23** (5), 44 (1997) [Tech. Phys. Lett. **23**, 188 (1997)].
11. K. L. Muratikov, Pis'ma Zh. Tekh. Fiz. **24** (13), 82 (1998) [Tech. Phys. Lett. **24**, 536 (1998)].
12. K. L. Muratikov, in *Proceedings of the 10th International Conference on Photoacoustic and Photothermal Phenomena (ICPPP), Rome, 1998* (AIP Conf. Proc., No. 463), pp. 478–480.
13. K. L. Muratikov, Zh. Tekh. Fiz. **69** (7), 59 (1999) [Tech. Phys. **44**, 792 (1999)].
14. L. D. Landau and E. M. Lifshitz, *Course of Theoretical Physics*, Vol. 7: *Theory of Elasticity* (Pergamon, New York, 1986; Nauka, Moscow, 1987).
15. A. I. Lur'e, *Nonlinear Theory of Elasticity* (Nauka, Moscow, 1980).
16. B. R. Lawn and T. R. Wishaw, *Fracture of Brittle Solids* (Cambridge Univ. Press, Cambridge, 1975).
17. K. L. Muratikov, A. L. Glazov, D. N. Rose, *et al.*, Pis'ma Zh. Tekh. Fiz. **28** (9), 48 (2002) [Tech. Phys. Lett. **28**, 377 (2002)].

18. R. F. Cook and G. M. Pharr, J. Am. Ceram. Soc. **73**, 787 (1990).
19. K. L. Muratikov, A. L. Glazov, D. N. Rose, *et al.*, J. Appl. Phys. **88**, 2948 (2000).
20. K. L. Muratikov, A. L. Glazov, V. I. Nikolaev, *et al.*, Pis'ma Zh. Tekh. Fiz. **27** (12), 33 (2001) [Tech. Phys. Lett. **27**, 500 (2001)].
21. K. L. Muratikov, A. L. Glazov, D. N. Rose, *et al.*, in *Proceedings of the 4th International Congress on Thermal Stresses (Thermal Stresses'01), Osaka, 2001*, pp. 85–88.
22. T. J. Mackin and T. E. Purcell, Exp. Tech. **20** (2), 15 (1996).
23. P. Stanley and J. M. Dulieu-Smith, Exp. Tech. **20** (2), 21 (1996).
24. L. M. Sedov, *Mechanics of Continuous Media* (Nauka, Moscow, 1970).
25. K. L. Muratikov, A. L. Glazov, D. N. Rose, *et al.*, Pis'ma Zh. Tekh. Fiz. **28** (9), 48 (2002) [Tech. Phys. Lett. **28**, 377 (2002)].
26. S. J. Bennison and B. R. Lawn, Acta Metall. **37**, 2659 (1989).
27. P. L. Swanson, C. J. Fairbank, B. R. Lawn, *et al.*, J. Am. Ceram. Soc. **70**, 279 (1987).
28. C. W. Li, D. J. Lee, and S. C. Lui, J. Am. Ceram. Soc. **75**, 1777 (1992).

Translated by V. Isaakyan

Technical Physics, Vol. 48, No. 8, 2003, pp. 1035–1041. Translated from Zhurnal Tekhnicheskoĭ Fiziki, Vol. 73, No. 8, 2003, pp. 98–104.

ELECTRON AND ION BEAMS, ACCELERATORS

Effect of Electron and Optical Factors on the Beam Extraction Coefficient of Large-Area Electron Accelerators

M. A. Abroyan, Yu. V. Zuev, S. L. Kosogorov, and V. Ya. Shvedyuk

State Unitary Enterprise Efremov Research Institute of Electrophysical Equipment, St. Petersburg, 196641 Russia

e-mail: glukhikh@niiefa.spb.su

Received November 6, 2002

Abstract—A combined numerical–analytical model for the electron–optical system of a large-area accelerator is suggested. The model is used to analyze various electron and optical factors that affect the beam extraction coefficient. To find ways of improving the beam extraction coefficient, the spatial and angular characteristics of the beam are calculated in various cross sections. The effect of the magnetic field produced by the cathode filament current is studied in detail for the first time. © *2003 MAIK "Nauka/Interperiodica"*.

INTRODUCTION

Large-area electron accelerators in which the exit beam cross-sectional area varies from 10^2 to 10^4 cm^2 are finding wide application in radiation technology and also as ionization devices in gas lasers [1] and plasma-chemical reactors. The efficiency of these accelerators depends on the ratio between the extracted and accelerated currents, i.e., on the beam extraction coefficient. To improve the characteristics of the accelerated beam and increase the extraction coefficient, a planar electron–optical system (EOS) with discrete extended cathodes and grids in the form of rods parallel to the cathodes has been proposed [2]. In particular, such a system has been applied in the ionization device of an industrial CO_2 laser with non-self-sustained discharge [3]. This paper gives recommendations on how to increase the EOS efficiency in large-area electron accelerators.

Electron–optical systems like those reported in [2, 3] form a large-area beam with the uniform current density distribution. The resulting beam is the superposition of elementary beams emitted by individual cathode filaments. The elementary beams mix up to form the integral electron flow with a typical spread of transverse velocities. Figure 1 schematically shows such an EOS with analytical trajectories of electrons generated by one emitter in the coordinate system chosen. The cathode consists of coplanar filamentary emitters connected so that the filament currents in adjacent emitters flow in opposite directions. The cathode operates in the space-charge-limited current mode. The reflecting screen (spreader) is at the cathode potential. The current is controlled by the potential of the first (control) grid. The second grid screens the cathode region from the strong accelerating field of the anode, which accelerates the main beam. The grids have the form of rods parallel to the cathode filaments. The rod diameter and spacing are chosen with regard for the dielectric strength. The anode of the accelerator also serves as a beam extraction device. It consists of a foil support window, through which the electrons are extracted out of the vacuum space of the accelerator into a medium under atmospheric of other pressure.

The current loss in holes of the foil support window depends on its design and the beam angular divergence. For the electrons to be extracted effectively, their trajectories must be orthogonal to the foil support window. This requirement to some extent comes into conflict with the discrete nature of the system, the necessity to superimpose the elementary beams, and the trend to maximize the cathode's emitting surface [3]; in other words, the problem of loss minimization is a multicriterion problem and requires a comprehensive analysis of a great number of factors using models of different levels.

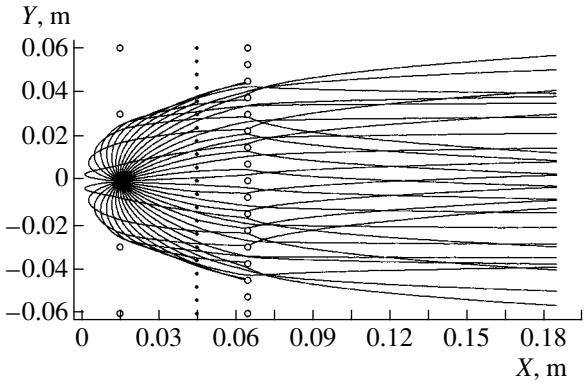

Fig. 1. Diagram of the EOS and theoretical trajectories produced by one cathode filament (the *z* axis is perpendicular to the plane of the figure).

1063-7842/03/4808-1035$24.00 © 2003 MAIK "Nauka/Interperiodica"

ANALYTICAL MODEL RELATING THE BEAM DIVERGENCE TO THE EOS PARAMETERS

To derive basic relationships between the angular electron divergence and the electrical and geometrical parameters of the system, we characterize each grid by the focal length of the equivalent thin lens [4, 5]:

$$f = 2U_{\text{eff}}/(E_2 - E_1),$$

where U_{eff} is the effective potential in the plane of the grid and E_2 and E_1 are the electric field intensities on both its sides.

The gap between the grid's rods deflects the trajectories by an angle α whose maximum value is given by

$$(\tan\alpha)_{\max} = (p - d)/2f,$$

where p is the rod spacing and d is the rod diameter.

Clearly, the effect of the grid on the angular divergence decreases as E_2 approaches E_1 and the rod spacing p decreases.

For the operating modes and EOS geometries under study, the screening grid contributes most significantly (more than 75%) to the angular divergence because of a high step in the field intensity. The cathode (with allowance for acceleration) gives about 20%. The remaining 5% is due to the control grid.

The above analytical relationships give general information about the effect of individual factors on the angular divergence of the electron flow but do not provide the distribution of the current over the cross section, which is necessary for designing large-area accelerators. Reliable quantitative estimates that include the current loss on the grids, the real geometry of the foil support window, and the shape and properties of the emitting surfaces need detailed trajectory analysis of the system as a whole.

ELECTRIC AND MAGNETIC FIELDS

If translation symmetry at the ends is broken, the electric and magnetic fields in the EOS may be treated in the two-dimensional approximation.

To obtain accurate estimates of highly irregular fields near fine filaments, the electric field in the region occupied by the beam was represented as the superposition of fields produced by grids composed of infinitely thin parallel equispaced filaments placed in a uniform field between the spreader and anode [4, 5]:

$$U(x, y) = A + Bx + \sum_{i=1}^{N_g} q_i \ln\left(2\cosh\left(\frac{2\pi(x - x_i)}{p_i}\right) - 2\cos\left(\frac{2\pi y}{p_i}\right)\right), \quad (1)$$

$$\mathbf{E} = -\nabla U.$$

Here, p_i, x_i, and q_i are the grid spacing and the coordinate and charge of an ith grid, respectively. The number of grids, N_g, and the parameters A, B, x_i, and q_i were taken such that the corresponding equipotential lines fit real metal surfaces most closely.

The magnetic field induced by the cathode's filament current was calculated in the quasi-static approximation through the vector magnetic potential **A**:

$$\mathbf{B} = \nabla \times \mathbf{A}, \quad \nabla \cdot \mathbf{A} = 0.$$

In plane-parallel fields, the vector **A** has a single component $A_z(x, y)$, which satisfies the Poisson equation [6]

$$\frac{\partial^2 A_z}{\partial x^2} + \frac{\partial^2 A_z}{\partial y^2} = -\mu_0 j_z(x, y), \quad (2)$$

where j_z is the filament current density.

A solution to Eq. (2) with allowance for translation symmetry (equispaced cathode filaments and oppositely directed currents in adjacent filaments) can be obtained in the same manner as a solution to the problem of an infinitely charged rod placed between parallel metal plates [5, 7]:

$$A_z(x, y) = A_0 \ln\left[\frac{\cosh\left(\frac{\pi(x - x_0)}{p}\right) + \cos\left(\frac{\pi y}{p}\right)}{\cosh\left(\frac{\pi(x - x_0)}{p}\right) - \cos\left(\frac{\pi y}{p}\right)}\right], \quad (3)$$

$$B_x = \frac{\partial A_z}{\partial y}, \quad B_y = -\frac{\partial A_z}{\partial x}.$$

Here, p is the spacing between the cathode filaments and x_0 is the coordinate of the central filament. The constant of integration A_0 is calculated from the condition

$$\oint_l \mathbf{B} dl = \mu_0 I,$$

where l is an arbitrary contour that encloses the filament with a current I.

SPATIAL AND ANGULAR ELECTRON BEAM DISTRIBUTIONS

The particle trajectories were found by integrating Newton–Lorentz field equations (1) and (3). Since the relativistic mass factor $\gamma = (1 - (\dot{x}^2 + \dot{y}^2 + \dot{z}^2)/c^2)^{-1/2}$ becomes as high as 1.4 as the particles are accelerated, we used these equations in the form

$$\begin{cases} \ddot{x} = \dfrac{1}{m_0\gamma}\left(F_x - \dfrac{\dot{x}}{c}\Omega\right), \quad F_x = e(E_x - \dot{z}B_y), \\ \ddot{y} = \dfrac{1}{m_0\gamma}\left(F_y - \dfrac{\dot{y}}{c}\Omega\right), \quad F_y = e(E_y + \dot{z}B_x), \\ \ddot{z} = \dfrac{1}{m_0\gamma}\left(F_z - \dfrac{\dot{z}}{c}\Omega\right), \quad F_z = e(\dot{x}B_y - \dot{y}B_x), \end{cases} \quad (4)$$

$$\Omega = F_x\frac{\dot{x}}{c} + F_y\frac{\dot{y}}{c} + F_z\frac{\dot{z}}{c}.$$

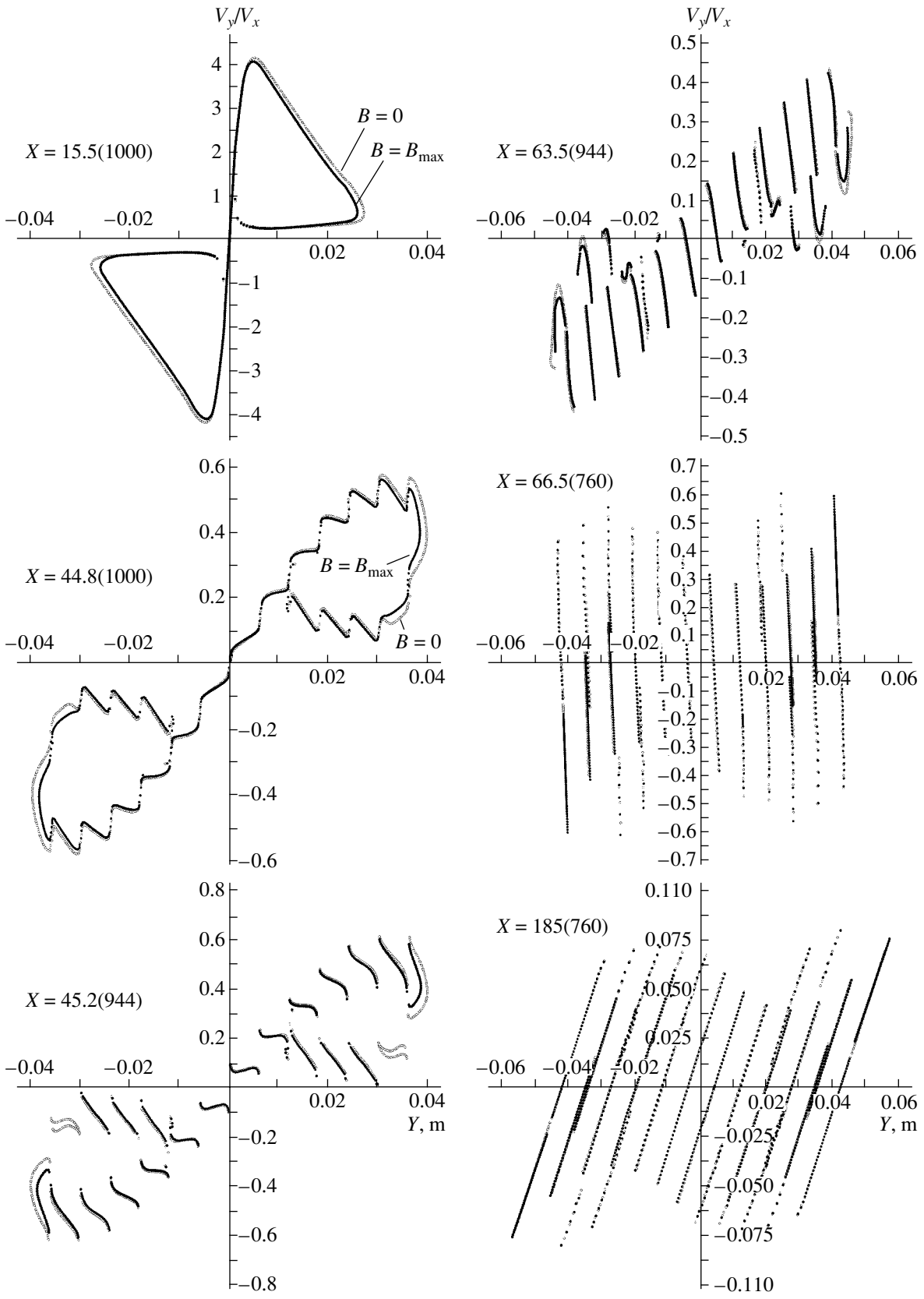

Fig. 2. Phase portrait of the particles on the *yy*' plane at the zero and maximal magnetic field intensities at X = 15.5, 44.8, 45.2, 63.5, 66.5, and 185 mm. The particles are emitted by one cathode filament.

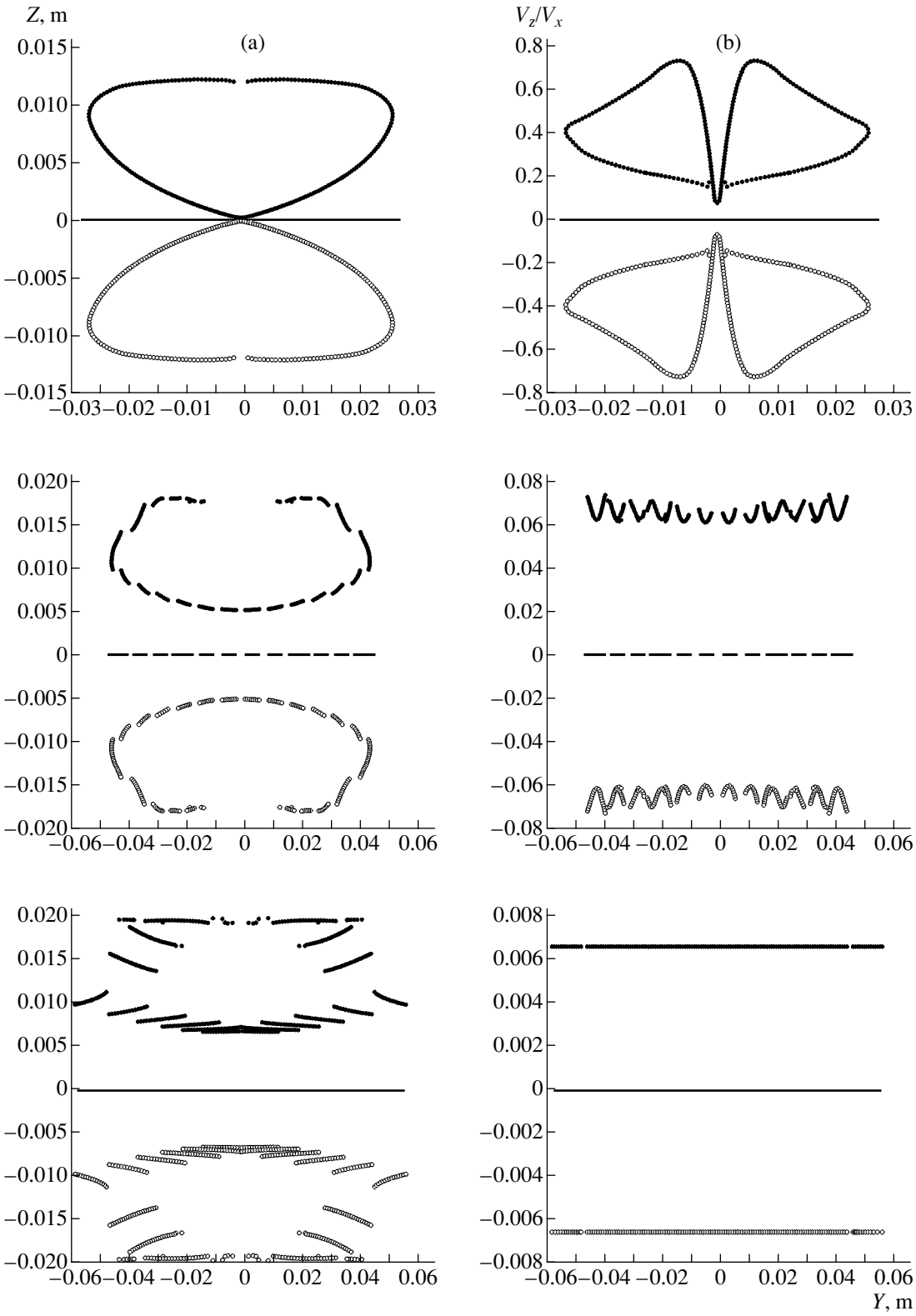

Fig. 3. Space and phase portraits of particles emitted by one filament of the cathode at the zero (the central group of circles) and maximum (the upper and lower groups depending on the current direction in the filament) magnetic field intensity at X = 15.5, 63.5, and 185 mm. (a) yz plane and (b) yz' plane.

It was assumed that, at the initial moment, all particles are uniformly distributed over the surface of the cathode filament at $z = 0$. We also assumed that each of the particles carries away a fraction I_j/I of the current:

$$\frac{I_j}{I} = \frac{\exp(4.39\sqrt{E_j}/T)}{\sum_{j=1}^{N}\exp(4.39\sqrt{E_j}/T)},$$

where $T = 1950$ K is the cathode temperature, E_j (V/cm) is the initial electric field for a jth particle [4], and I is the current transferred by all N particles per unit filament length dx.

System of dynamic equations (4) was integrated numerically by the fourth-order Runge–Kutta technique with automatic step selection. The solution accuracy was checked with the integrals of motion

$$\begin{aligned} m_0\gamma c^2 &= m_0c^2 - e(U(x, y) - U(x_0, y_0)), \\ m_0\gamma\dot{z} &= -e(A_z(x, y) - A_z(x_0, y_0)), \end{aligned} \quad (5)$$

the relative deviation from which was no greater than 0.1%. Here, $U(x_0, y_0)$ and $A_z(x_0, y_0)$ are the electrostatic and vector potentials at the starting point that are the same for all particles from the same emitter, because $x_0^2 + y_0^2 = r_c^2$, where r_c is the radius of the cathode filament [6]. Since the time of particle travel from the cathode to the anode is much shorter than the period of filament current variation, effects associated with the magnetic field variation in time were neglected.

Figure 2 shows the evolution of the phase portrait for particles generated by one emitter (i.e., of an elementary beam) on the *yy*' plane as the particles travel through the EOS. The beam-cutting and beam-focusing effects due to the grid's rods placed in the planes $x = 45$ and 65 mm are clearly seen. The effect of the magnetic field on the phase characteristics in the *yy*' plane is insignificant. Similar characteristics in the *yz* and *yz*' planes are shown in Fig. 3. With the zero magnetic field, the directed motion of the particles along the cathode filaments is absent. Otherwise, the particles drift along the *z* axis. This drift correlates with the intensity and direction of the filament current. The drift is maximum for particles that are emitted from the rear side of the cathode filament (Fig. 6) and arrive at the cathode later. The magnitude of the *z* component of the velocity near the foil support window is almost the same for all the particles. Its asymptotic value,

$$|\dot{z}| \cong \frac{|A_z(x_0, y_0)|c^2}{U_a + m_0c^2/e}$$

(U_a is the accelerating voltage), can be found from integral of motion (5).

The beam loss on the grids versus accelerating voltage U_a and potentials U_{g1} and U_{g2} across the control and screening grids is summarized in the table. The current transmission coefficients K_{g1} and K_{g2} of the grids were

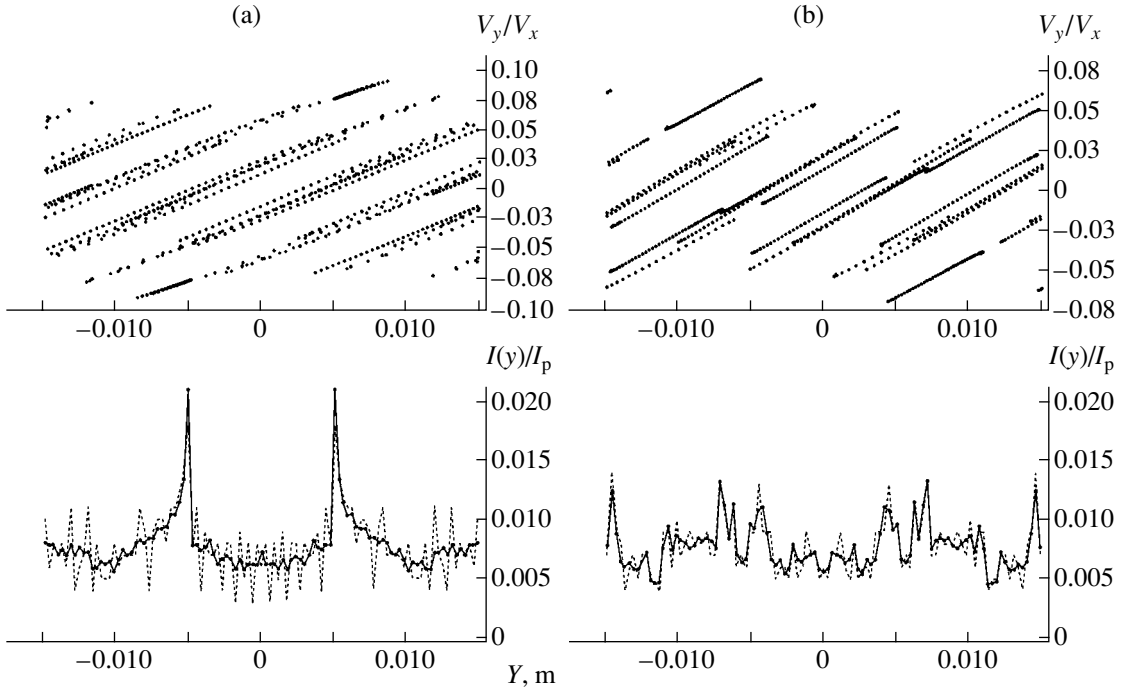

Fig. 4. Phase and space particle distributions over an elementary cell near the foil support window (the cathode location is $Y = 0$) at zero magnetic field intensity and various screening grid potentials: U_{g2} = (a) 1500 and (b) 3000 V, $U_{g1} = 800$ V, $U_a = 200\,000$ V, $L =$ 185 mm, and $I_c = 0$.

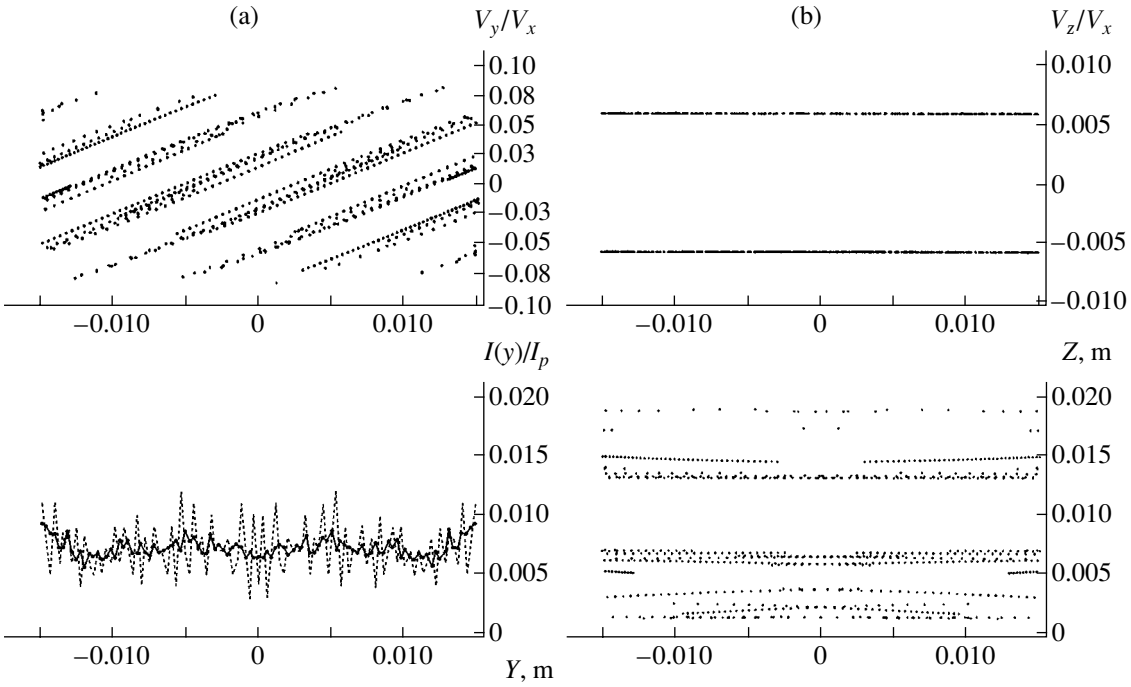

Fig. 5. The same as in Fig. 4 for the maximum magnetic field intensity (I_c = 11 A).

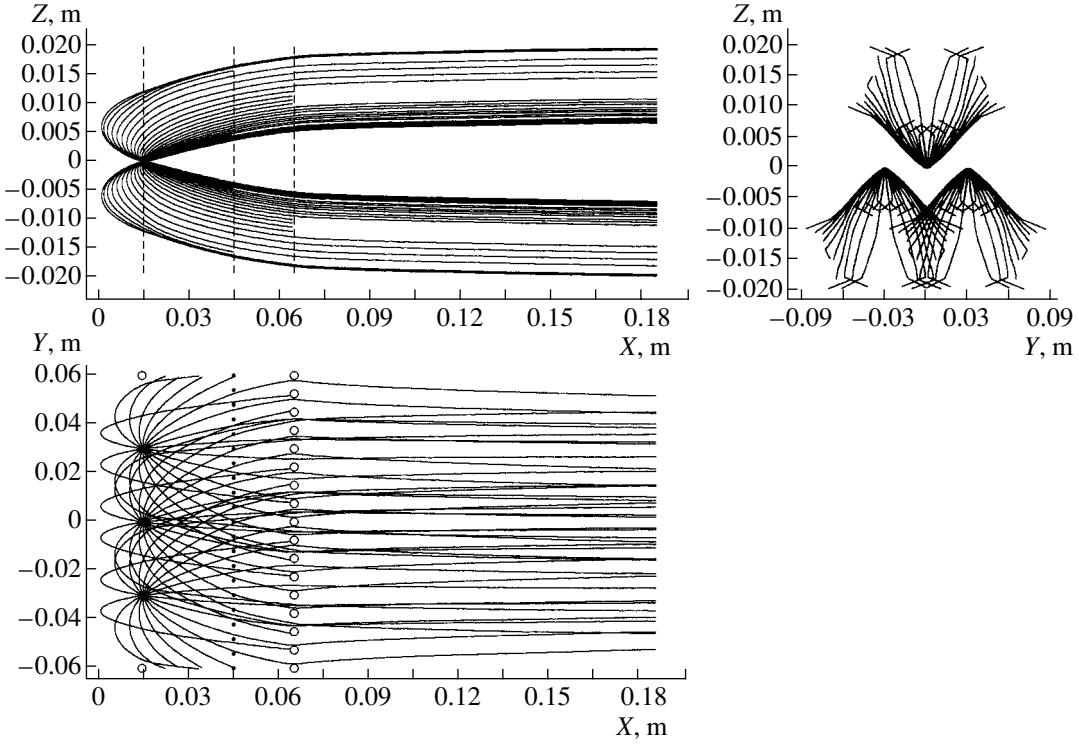

Fig. 6. Projections of particle trajectories at the maximum magnetic field intensity.

calculated as the ratio of the current of particles that passed through the grid to the current of particles emitted by the cathode.

The phase portraits with allowance for emission from all filaments and the respective current distributions $I(y)$ over an elementary cell (the emitter spacing)

Operating modes of the accelerator and current transmission coefficient of the grids

Electrode potentials				Instantaneous filament current			
				0 A		11 A	
U_c, V	U_{g1}, V	U_{g2}, V	U_a, V	K_{g1}, %	K_{g2}, %	K_{g1}, %	K_{g2}, %
0	600	1500	160	94.88	74.68	94.44	78.20
0	600	1500	200	94.88	75.52	94.56	79.40
0	800	1500	200	94.52	78.80	94.24	72.68
0	800	3000	200	95.08	77.36	94.88	80.24

of the EOS are shown in Figs. 4 and 5. The trajectory projections for particles emitted by three adjacent filaments at the maximum of the filament current are shown in Fig. 6.

DISCUSSION

As follows from the trajectory analysis, the width of the elementary beam in the *y* direction near the foil support window (x = 185 mm) is 120 mm, which is four times the emitter spacing (Fig. 2). The angle at which the particles approach the foil support window in the *xy* plane reaches 4.5°–5°. As the potential U_{g2} increases, this angle decreases, because the step in the field intensity at the screening grid becomes smaller (cf. Figs. 4a, 4b). The kink in the trajectories in Fig. 6 corresponds to the location of the screening grid.

Under the action of the magnetic field, the electrons generated by adjacent emitters are deflected in opposite directions when passing along the filaments (Fig. 6). The maximum drift along the *z* axis may be as large as 20 mm for an angle of arrival of about 0.5° (Fig. 3). Since elementary beams overlap, the transverse size of the beam extracted varies periodically with the doubled filament current frequency.

The current distribution over the cross section was found to be dependent on the instantaneous magnetic field intensity. The geometry of the EOS under study inevitably causes a caustic overlap of the trajectories, which increases the particle density at the periphery of the elementary beam (Fig. 1). The resultant density distribution is the most uniform when the edges of elementary beams are intercepted by the second grid (Fig. 5). Otherwise, the efficiency of the accelerator is higher (see table) but the particle distribution contains anomalous higher density regions (Fig. 4a), which consist of peripheral particles that have passed in the immediate neighborhood of the grid rods and, therefore, have the highest divergence.

CONCLUSIONS

The combined numerical–analytical method for studying beams in large-area electron accelerators allows one to obtain the spatial and angular particle distributions in any cross section of the EOS and evaluate the effect of electron and optical factors on the accelerator's output parameters.

The beam losses upon extraction depend mostly on the geometrical transparency of the foil support window and on the losses due to particle divergence. Since the *y* component of the electron transverse velocity is one order of magnitude higher than its *z* component, the foil support window must have slits oriented in the *y* direction. In this case, the total beam loss on the walls of the support window may be reduced to 1.5–3.0%. The support window must allow for not only the elementary beam widening in the *y* direction but also the particle drift along the *z* axis. Here, of importance is the proper choice of the proportion between the transverse size of the support window and grid apertures.

To optimize the effect of the magnetic field induced by the filament current, a pulse of the accelerating voltage must be phase-synchronized with the sinusoidal filament current.

The angular divergence in the *y* direction may to a certain extent be decreased by shortening the rod spacing in the control grid or in the cathode. The effect of the screening grid is more difficult to minimize. Its geometry governs the dielectric strength of the accelerating gap, and the grid's potential cannot be increased significantly in order to decrease a step in the field intensity because of the growth of the thermal loss due to beam overlapping.

REFERENCES

1. S. P. Bugaev, Yu. E. Kreĭndel', and P. M. Shchanin, *Wide Electron Beams* (Énergoatomizdat, Moscow, 1984).
2. M. A. Abroyan and G. I. Trubnikov, Zh. Tekh. Fiz. **59**, 129 (1989) [Sov. Phys. Tech. Phys. **34**, 207 (1989)].
3. M. A. Abroyan, V. V. Bogdanov, L. V. Bodakin, *et al.*, in *Proceedings of the 9th Meeting on Application of Charged Particle Accelerators in Industry and Medicine, St. Petersburg, 1998*.
4. É. Yu. Kleĭner, *Theory of Electron Tubes* (Moscow, 1974), Vol. III.
5. A. M. Strashkevich, *Electron Optics of Electrostatic System* (Énergiya, Moscow, 1966).
6. S. I. Molokovskiĭ and A. D. Sushkov, *Intense Electron and Ion Beams* (Énergoatomizdat, Moscow, 1991).
7. G. A. Grinberg, *Selected Topics of Mathematical Theory of Electrical and Magnetic Phenomena* (Akad. Nauk SSSR, Moscow, 1948).

Translated by A. Khzmalyan

Technical Physics, Vol. 48, No. 8, 2003, pp. 1042–1046. Translated from Zhurnal Tekhnicheskoĭ Fiziki, Vol. 73, No. 8, 2003, pp. 105–110.

ELECTRON AND ION BEAMS, ACCELERATORS

Interaction between an Intense Proton Bunch and Electron Beam in a Tevatron

V. V. Parkhomchuk*, V. B. Reva*, and V. D. Shil'tsev**

** Budker Institute of Nuclear Physics, Siberian Division, Russian Academy of Sciences, pr. Akademika Lavrent'eva 11, Novosibirsk, 630090 Russia*

e-mail: reva@inp.nsk.su

*** Fermi National Accelerator Laboratory, P.O. Box 500, Batavia, IL 60510-0500*

Received October 2, 2002

Abstract—An electron lens is capable of producing focusing fields of controllable profile separately for proton and antiproton bunches. This makes it possible to neutralize collision effects. The pioneering experiments with this lens demonstrated that the antiproton lifetime can be reduced from several hundreds to several tens of hours. In this work, we experimentally study processes arising when a high-intensity proton bunch meets an electron beam. Two physical mechanisms that may diminish the lifetime of the antiproton bunch are suggested.

INTRODUCTION: AN ELECTRON LENS AS A TOOL FOR SUPPRESSING COLLISION EFFECTS

An electron beam on the orbit of a proton bunch makes it possible to generate focusing fields of controllable profiles in the transverse direction. In essence, this means that we are dealing with a lens that has nonlinear components. An electron lens may focus proton and antiproton bunches separately, thus providing the possibility of suppressing (to an extent) collision effects at the site where the bunch and beam meet [1]. The lens of such a type was first mounted on a Tevatron in 2001 (Fig. 1).

The first year of operation of the Tevatron electron lens (TEL) proved its efficiency. In particular, the calculated shift of betatron frequencies (about 0.01) for 980-GeV protons and antiprotons at an electron current of 2.5 A and energy of 7 kV was confirmed. It was also found that the interaction with electrons reduces the antiproton lifetime τ from several hundreds to several tens of hours, this time varying with the electron current as $\tau \propto J_e^{-2}$.

The maximum lifetime, which was reached at a current of 2 A and a frequency shift of 0.008, is about 20 h. Three explanations of this fact have been suggested:

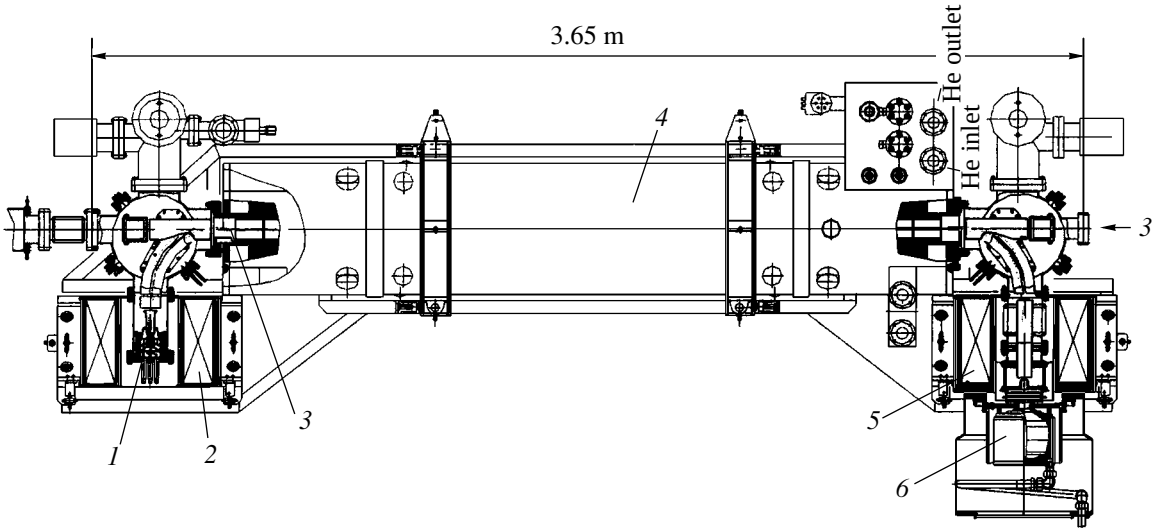

Fig. 1. General view of the TEL: (*1*) electron gun, (*2*) gun's solenoid, (*3*) electron beam, (*4*) superconducting solenoid, (*5*) collector's solenoid, and (*6*) collector.

1063-7842/03/4808-1042$24.00 © 2003 MAIK "Nauka/Interperiodica"

(1) nonlinear collision effects upon meeting, which are the most pronounced at the edges of the electron beam; (2) noise, as well as fluctuations of the current and electron position; and (3) weak instability due to the electron motion upon interaction. In this work, we theoretically and experimentally examine the last factor.

High fields of primary beams may substantially affect *e–p* interaction because of a high electron mobility. To decrease the mobility, an electron lens uses a high longitudinal magnetic field of up to 4 T, which magnetizes the transverse degrees of freedom of electrons [2]. The longitudinal mobility, however, remains high, and the number of longitudinal plasma oscillations for the transit time of a proton or antiproton bunch may be large. While the phase shift of plasma oscillations in interacting proton and antiproton bunches is always much less than unity, electrons, whose mass (with regard of energy) is two million times smaller, oscillate at a much higher frequency, which may pose a problem. The situation closely resembles a highly asymmetric collider where the transverse motion of light particles is suppressed while their longitudinal mobility remains high. The study of oscillations in such a system may be helpful in designing high-luminosity electron–ion colliders.

INTERACTION OF A HIGH-INTENSITY PROTON BUNCH WITH AN ELECTRON BEAM: EXPERIMENTAL STUDY

Experiments were performed with a 980-GeV proton bunch with an initial number of particles of 1.63×10^{11} and an initial rms length of 52.5 cm (the bunch peak current equaled 5.9 A). Its radius over the length of the electron lens was 0.6 mm, i.e., three times less than the radius of the electron beam.

The peak current of the electron beam was 0.5 A, as determined from the voltage amplitude at the anode modulator. During the experiments, the energy of the electron beam was varied from 3 to 10 keV in order to vary its density in the intersection region. The electrons travel in the same direction as the proton bunch. As a result of the combined action of the electric and magnetic fields, the influence on the proton bunch was depressed as the electron velocity increased. The phase shift of proton bunch oscillations is

$$\Delta\nu = \frac{n_e r_p \beta_x}{2\gamma}(1-\beta_e) l_e. \qquad (1)$$

Here, n_e is the electron density, l_e is the electron beam length, $r_p = 1.53 \times 10^{-18}$ m is the classical radius of a proton, $\beta_e = v_e/c$ is the electron velocity, and $\gamma = 1044$ is the relativistic Lorentz factor for 980 GeV protons. With an energy of 4 keV, (1) yields 0.0015.

The signal from a pickup electrode, which was applied to an oscilloscope with a 50-Ω matched load, was proportional to the rate of change of the space charge near the pickup. The space charge dynamics was determined by numerically integrating measured data. The pickup electrode was placed at a distance of 2.3 m from the site where the proton bunch meets the electron beam.

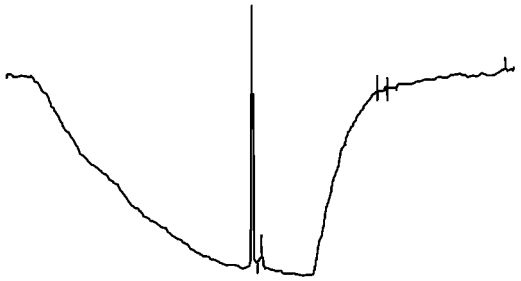

Fig. 2. Time variation of the space charge in the pickup. The signal is normalized to the maximal linear density of the proton bunch charge.

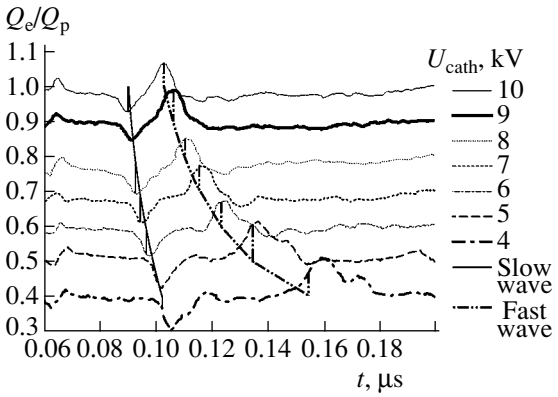

Fig. 3. Charge disturbances in the pickup for various electron beam (cathode) energies. For clarity, the curves are pulled apart by 0.1 in the vertical direction.

Figure 2 shows the integrated signal from the pickup electrode, which was recorded at the time instant the electron beam and proton bunch coincide in space and time. In the interval from 0.1 to 1.6 μs, we see the electron beam pulse. At the instant 0.95 μs, the proton bunch appears. The higher peak is the signal from the basic bunch. The nearby lower peak is presumably the signal from particles captured into the adjacent separatrix (the rf period is 19 ns). It is noteworthy that secondary peaks were of much lesser intensity (or absent at all) at the very beginning of the proton bunch appearance. Below we consider in detail what happens with electrons within the first 200 ns after the proton transit.

Figure 3 shows the difference between the space charges with and without the proton bunch passing through the lens for various cathode voltages (electron beam energies). At the time instant 0.065 μs, a polarization field moving together with the proton field is observed. In the interval between 0.095 and 0.115 μs, the fast space-charge wave arrives (it is excited when the proton bunch enters into the electron beam). In the interval between 0.11 and 0.17 μs, the slow space-charge wave appears. As the electron energy decreases

(the electron density grows) at a fixed current of 0.5 A, the time delay between these two waves increases. Two continuous lines marked by vertical segments indicate the times of arrival of the disturbances. The time of arrival was calculated by the formula

$$\tau = \frac{L_{\text{pickup}}}{\omega_{\text{pl, e}} a_{\text{e}} \sqrt{1 + 2\ln(b/a_{\text{e}})}}, \qquad (2)$$

where L_{pickup} is the distance to the pickup electrode, a_{e} is the radius of the electron beam, b is the radius of the vacuum chamber (7 cm), and $\omega_{\text{pl, e}}$ is the plasma oscillation frequency (here it is taken into account that the actual electron velocity in a TEL is lower than that calculated by the simple formula for the energy because of the presence of the space charge).

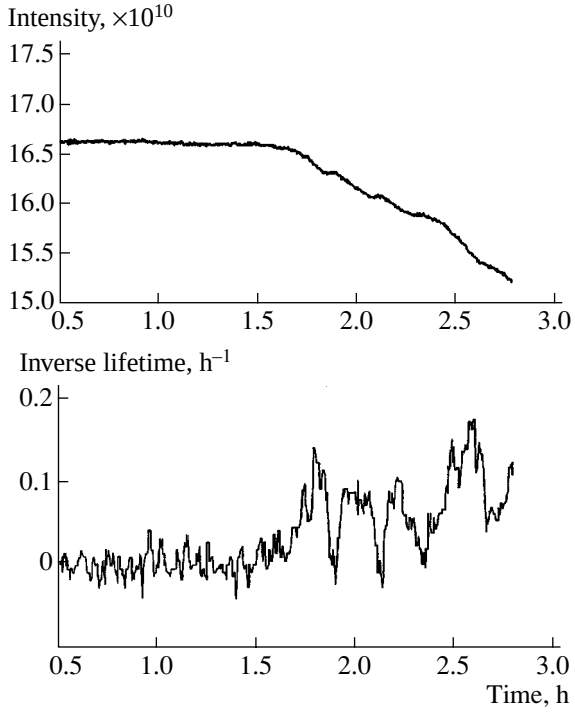

Fig. 4. (a) Proton bunch intensity and (b) inverse proton lifetime vs. time of experiment.

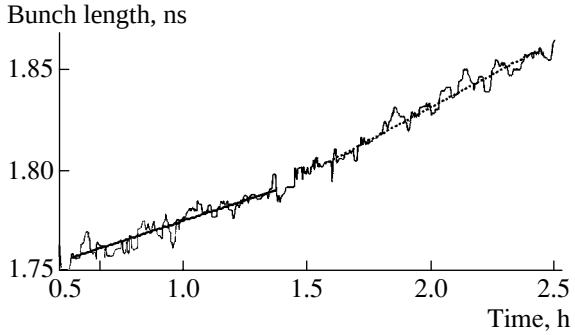

Fig. 5. Root-mean-square length of the proton bunch vs. time of experiment.

From Fig. 3, it follows that the entry of the proton bunch causes a strong disturbance of the bunch that is much greater than the disturbance propagating with the bunch.

Figure 4 plots (a) the intensity and (b) the inverse mean lifetime of the proton bunch vs. time of experiment. Within the initial 1.5 h, the proton bunch and electron beam were separated. During this time interval, the proton bunch intensity did not change and equaled 16.6×10^{10}. After the protons and electrons had met, the proton bunch intensity began to decrease steadily. The descending portion of the curve between 1.5 and 2.5 h exhibits distinct small steps. They are observed at the time instants the electron beam was switched off. At these time instants, the intensity of the proton bunch stopped decreasing. From Fig. 4b, it is seen that the interaction of the proton bunch with the electron beam leads to a considerable decrease in the proton bunch lifetime. In Fig. 5, the proton bunch length is plotted against the time of experiment. At the early stage (no interaction), the time of rise of the length $\sigma/(d\sigma/dt)$ is 44 h; when the bunch interacts with the electron beam, this time is 27 h.

MODEL OF LONGITUDINAL WAVES IN AN ELECTRON BEAM

The formation of space charge disturbances in an electron beam may be considered as a two-stage process: the generation of a polarization field moving with the beam and the occurrence of two waves arising when the proton bunch comes in and goes out of the electron beam.

Polarization field. The hydrodynamic equations that describe the evolution of long-wave longitudinal disturbances (the length of a disturbance far exceeds the dimension of the chamber and the size of the bunch) have the form

$$\frac{\partial n_{\text{e}}}{\partial t} + n_{0\text{e}} \frac{\partial v_{\text{ez}}}{\partial z} = 0 \text{ (continuity equation)}, \qquad (3)$$

$$\frac{\partial v_{ez}}{\partial t} = \frac{e}{m_{\text{e}}} E_z \text{ (equation of motion)}, \qquad (4)$$

$$E_z = -2\pi a_{\text{e}}^2 e \ln\frac{b}{a_{\text{e}}} \frac{\partial n_{\text{e}}}{\partial z} + 2\pi a_{\text{p}}^2 e \ln\frac{b}{a_{\text{p}}} \frac{\partial n_{\text{p}}}{\partial z}$$
(relationship between the space charge and longtudinal electric field). (5)

Introducing the longitudinal displacement of electrons from the equilibrium position in the form

$$v_{\text{ez}} = \partial\xi_{\text{e}}/\partial t, \qquad (6)$$

we obtain

$$\frac{\partial^2 \xi_{\text{e}}}{\partial t^2} - c_{\text{e}}^2 \frac{\partial^2 \xi_{\text{e}}}{\partial z^2} = c_{\text{p}}^2 \frac{\partial f_{\text{p}}}{\partial z}. \qquad (7)$$

Here, c_e and c_p are the velocities of space charge waves that are calculated from the electron and proton densities, respectively, and $f_p = n_p(z)/n_{p0}$ is the dimensionless longitudinal distribution of the proton bunch density.

Assuming that ξ_e and f_p depend only on $x = z - ct$ and taking into consideration that $c \gg c_e$, we get

$$\frac{\partial^2 \xi_e}{\partial x^2} = -\frac{c_p^2}{c^2}\frac{\partial f_p(x)}{\partial x}. \quad (8)$$

The final expression for the polarization-field-induced disturbance of the electron density takes the form

$$n_e = \frac{c_e^2}{c^2} n_p(x). \quad (9)$$

For $a_e = 1.75$ mm, $J_e = 0.5$ A, $E_e = 7$ kV, $N_p = 1.63 \times 10^{11}$, $a_p = 0.6$ mm, and $\sigma_p = 52$ cm, the maximum disturbance of the electron density is

$$\frac{n_e}{n_{e0}} \approx 0.024, \quad (10)$$

which is in reasonable agreement with the experimental results (Fig. 3).

Disturbances arising upon the entry and egress of the proton bunch. To estimate these disturbances, we will use the following model. Assume that electrons coming to the point of meeting simultaneously with protons will be displaced by a finite distance (at zero residual velocity) by the time instant the proton bunch leaves the point of meeting. Those arriving at the point of meeting somewhat later will acquire a smaller displacement at a nonzero residual velocity. Electrons that come to this point much later will remain undisturbed. Thus, the problem splits into two subproblems: the determination of the initial velocities and displacements of electrons under the action of the proton-generated electric field and finding the temporal and spatial evolution of the initial disturbance.

The displacement of an electron disk located at a point z relative to the point of meeting (at the time of passage of the proton bunch, the self-field of the electron beam can be neglected, as follows from (7)) obeys the equation

$$\frac{\partial^2 \xi_e}{\partial t^2} = \frac{c_p^2}{c}\frac{\partial f_p}{\partial t}, \quad (11)$$

where $t = z/c$.

The values of ξ_e and $d\xi_e/dt$ at the instant $t = z/v_e$ will correspond to initial conditions at the point z for an equation describing the propagation of longitudinal waves along the electron beam. Thus, at $t = 0$ (actually, the point $z = 0$ in initial conditions (12) corresponds to the point $z = v_e l_p/c$; this fact may be ignored or, otherwise, the spacing between pickup electrodes must be appropriately decreased), we have

$$\xi'_{e0}(z) = \left.\frac{\partial \xi_e}{\partial t}(z)\right|_{t=0} = -\frac{c_p^2}{c} f_p\left(\frac{c}{v_e} z\right),$$
$$\xi_{e0}(z) = -\frac{c_i^2}{c^2}\int_{-\infty}^{zc/v_e} f_p(z')dz'. \quad (12)$$

A solution to wave equation (7) with the zero right-hand side (the proton bunch has left the point of meeting) is well known:

$$\xi_e(z, t) = \frac{1}{2}(\xi_{e0}(z - c_e t) + \xi_{e0}(z + c_e t)) + \frac{1}{2c_e}\int_{z-c_e t}^{z+c_e t} \xi'_{e0}(z')dz'. \quad (13)$$

From (13), one can immediately find a disturbance of the electron beam density at any time instant. This expression takes into account that the electron beam has a relative velocity v:

$$n_e(z, t) = n_{e0}\frac{1}{2}\frac{c_p^2}{c^2}\left[f_p\left(\frac{c}{v_e}(z - c_e t - v_e t)\right)\left(\frac{c}{v_e} + \frac{c}{c_e}\right) + f_p\left(\frac{c}{v_e}(z + c_e t - v_e t)\right)\left(\frac{c}{v_e} - \frac{c}{c_e}\right)\right]. \quad (14)$$

For the parameters listed above, the maximal disturbance of the electron beam is

$$\frac{n_e}{n_{e0}} \approx 0.32.$$

It is seen that the disturbance calculated in terms of the linear model is not small. Therefore, finding adequate estimates requires a numerical calculation. Figure 6 shows results obtained by the flat disk model. The electron beam and proton bunch are partitioned into plane rigid disks spaced at $d \le a_e, a_p$. Each of the disks produces an electrostatic field influencing the other disks. At the area of meeting, proton disks are instantly immersed in the electron disk flux.

MODEL OF SCATTERING BY PLASMA FLUCTUATIONS ARISING AFTER THE PASSAGE OF THE PROTON BUNCH

Estimates suggest that a sharp decrease in the lifetime in the presence of an electron beam cannot be related to single-particle scattering by electrons. A possible mechanism enhancing scattering by an electron beam is scattering by plasma oscillations arising in response to the proton bunch passage. Each proton in its passage through the electrons excites plasma oscillations (leaves wakes) along its path. The energy of these oscillations is the ionization loss of the proton. The wakes oscillate with the plasma oscillation frequency. Since the proton spacing during the passage remains unchanged, so does the phase of oscillations of

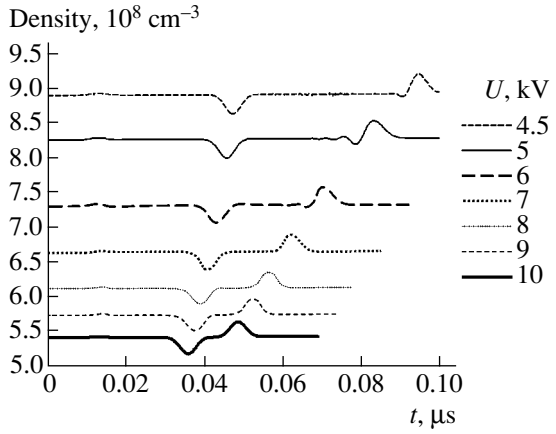

Fig. 6. Waves in the electron beam after the passage of the proton bunch with 1.57×10^{11} protons. The distance between the pickup and the point of entry is 200 cm.

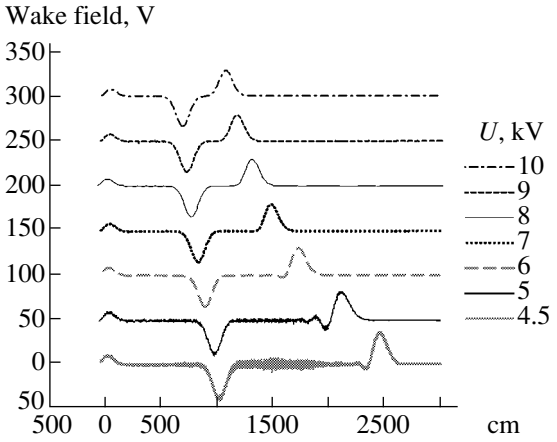

Fig. 7. Potentials of the longitudinal waves in the electron beam after the passage of the proton bunch.

the electric field acting on a particular proton. The total energy evolution per proton passage through the electron beam is

$$\Delta E = \frac{2\pi n_e e^4 l_e}{m_e c^2} \ln(\rho_{max}/\rho_{min}), \quad (15)$$

where ρ_{max} and ρ_{min} are the maximal and minimal impact parameters in electron–proton collision.

The electric field in the plasma oscillations may be estimated as

$$\delta E = \sqrt{\frac{16\pi r_e n_e e^2 N_p}{a_e^2} \ln(\rho_{max}/\rho_{min})}. \quad (16)$$

In the tail of the bunch, protons will experience transverse impacts $\Delta p = e\delta E l_e/c$. Accordingly, the lifetime of tail protons drops to

$$\frac{1}{\tau} = \frac{16\pi r_e r_p^2 l_e^2 N_p n_e}{a_e^2 \gamma_p^2 \Theta_p^2} \ln\left(\frac{\rho_{max}}{\rho_{min}}\right) f_0. \quad (17)$$

For an electron energy of 4 keV, an electron current of 0.5 A, and an electron density of 1.4×10^{10} cm^{-3}, (17) yields 5 h, which agrees well with the measurements. It should be emphasized that the impacts are due to randomly distributed fields excited by individual protons. Therefore, the field amplitudes squared (energies), rather than the fields amplitudes, add up.

LONGITUDINAL WAKE FIELDS IN THE ELECTRON BEAM

To evaluate the effect of coherent waves on the proton bunch, we calculated a set of the proton bunch energies per pass through the electron lens. Figure 7 shows the so-called wake potentials for different electron beam energies. The potential curves are seen to have three characteristic features: a near zone, which exhibits the rapid electron beam polarization and local plasma oscillations, and two extrema, which are associated with the effect of the fast and slow waves at the place where the electron beam and proton bunch move apart. Protons traveling across the longitudinal wave in the rectilinear portion undergo the action of both the positive and negative fields of the wave. Therefore, the effect of the wave in this region is insignificant. At the place where the beam and bunch move apart, protons cross only part of the wave and the effect grows considerably. The change in the energy is small (about 50 eV); hence, for the effect on 1-TeV protons to be appreciable, it is necessary to gain an energy of about 100 MeV (approximate energy spread). This requires 2×10^6 turns (40 s). In the presence of coherent oscillations in proton or antiproton bunches, these wake fields may basically heat up particles strongly deflected from the equilibrium position. In this case, the particles will be lost without any noticeable increase in the beam emittance.

CONCLUSIONS

We considered space charge waves excited by a short Tevatron-accelerated proton bunch meeting a low-energy beam of magnetized electrons. The velocities and amplitudes of the waves found experimentally are in good agreement with the theoretical model. Two mechanisms responsible for the proton bunch lifetime degradation due to the charge waves are suggested. Further investigations involving an electron lens will aim to check the prediction (see (17)) that the proton lifetime varies with the electron and proton currents as $1/\tau \propto N_p J_e$. Also, it would be of interest to observe the extension of the proton bunch and, possibly, the formation of satellites with increasing electron current.

REFERENCES

1. V. Shiltsev *et al.*, Phys. Rev. ST Accel. Beams **2**, 071001 (1999).
2. A. Burov, V. Danilov, and V. Shiltsev, Phys. Rev. E **59**, 3605 (1999).

Translated by V. Isaakyan

Technical Physics, Vol. 48, No. 8, 2003, pp. 1047–1052. Translated from Zhurnal Tekhnicheskoĭ Fiziki, Vol. 73, No. 8, 2003, pp. 111–117.

EXPERIMENTAL INSTRUMENTS AND TECHNIQUES

Magnetic Cumulative Effect upon the Explosion of a Shaped Charge with an Axial Magnetic Field in Its Sheath

S. V. Fedorov, A. V. Babkin, and S. V. Ladov

Bauman Moscow State Technical University, Vtoraya Baumanskaya ul. 5, Moscow, 105005 Russia

e-mail: sm4@sm.bmstu.ru

Received January 14, 2003

Abstract—Experiments on creating an axial magnetic field in the metallic sheath of a shaped charge immediately before explosion are reported. Under such conditions, the penetrability of the charge is shown to decrease substantially. For instance, the penetration into a steel target is reduced more than twice when the initial field in the sheath is several tenths of a tesla. The most plausible reason for this effect is a drastic rise in the magnetic field (to a level as high as several hundreds of teslas) in the jet formation area, which disturbs the cumulative jet formation process. This pumping effect is presumably related to the magnetic field "freezing" into the deforming conductive material. Such a mechanism shows up when the tensile strain of the sheath's fragments along the magnetic flux lines is significant. The ability of the deformation mechanism of field generation to disturb greatly the jet formation process upon collapsing the shaped charge sheath is substantiated by calculations. © *2003 MAIK "Nauka/Interperiodica".*

INTRODUCTION

A cumulative effect that is observed upon the explosion of an axisymmetric explosive charge with a conic cavity covered by a thin metallic sheath generates fast jets with a high penetrability [1]. When the metallic sheath is subjected to an axial magnetic field, the explosion of the shaped charge (SC) and the compression of the sheath cause the effect of magnetic cumulation, which shows up as a rise in the intensity of the sheath-compressed field [2]. Essentially, the SC behaves as a magnetic cumulative generator (MCG)—a device generating ultrahigh magnetic fields. Magnetic cumulation is capable of giving rise to intense thermal and mechanical phenomena, which may have far-reaching consequences.

EXPERIMENTAL RESULTS AND DISCUSSION

In previous experiments [3] on studying the effect of a magnetic field produced in the SC sheath on the piercing (penetrating) power of the charge (Fig. 1), the charge had a diameter of 50 mm and the vertex angle of its copper sheath was 50°. The field in the cavity and sheath was generated by a single-wound multiturn coil 50 mm long with an inner diameter slightly exceeding that of the SC. The coil enclosed the lower part of the charge (cavity). Electrical energy was applied from a capacitor bank, which was discharged through the coil upon closing an explosive switch.

The explosion was initiated same time after closing the switch, during which the current in the discharge circuit reached a necessary (threshold) value and its magnetic field diffused into the sheath. The delay was typically about 300 μs, as determined from tentative runs on magnetic field generation in the sheath of an inactive SC simulator. In these runs, an inductive sensor placed in the cavity recorded the variation of the magnetic field, and the current strength in the discharge circuit was simultaneously measured with a Rogowski loop. In the explosion experiments, only the current strength in the sheath at the instant of explosion was measured, while the magnetic induction in the sheath was estimated from the preestablished relationship between the discharge current and magnetic field intensity. Figure 2 shows typical experimental curves of the discharge current and magnetic induction in the sheath.

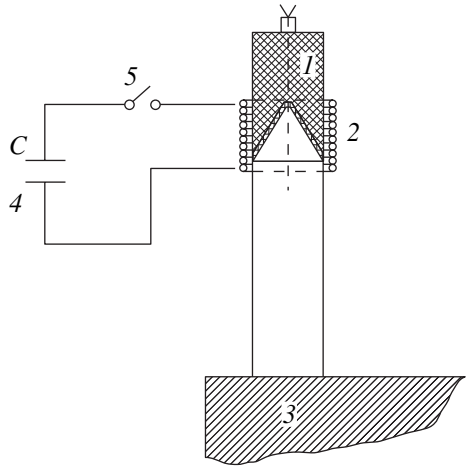

Fig. 1. Experimental scheme. (*1*) Shaped charge, (*2*) coil inducing magnetic field in shaped charge sheath, (*3*) steel obstacle, (*4*) capacitor bank, and (*5*) explosive switch.

1063-7842/03/4808-1047$24.00 © 2003 MAIK "Nauka/Interperiodica"

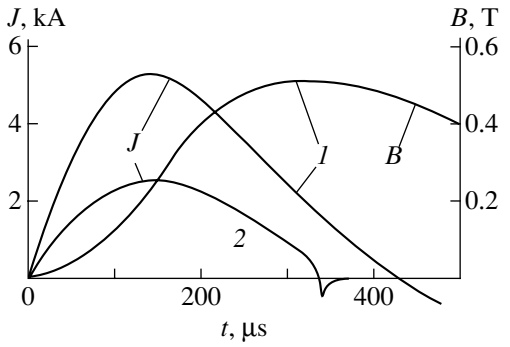

Fig. 2. Experimental curves of the discharge current and magnetic induction in the cavity of the SC sheath: (*1*) runs performed with the inactive simulator and (*2*) explosion experiment 4 (see table).

It is seen that the magnetic field in the cavity reaches a maximum much later than the current in the discharge circuit.

In the explosion experiments, the spacing between the SC and steel target was 200 mm. For such a spacing, the freely acting SC used has a mean penetration L_0 = 250 mm. As follows from the experimental results listed in the table (B_0 is the magnetic induction in the sheath at the instant of explosion, L is the depth of penetration), the magnetic field in the sheath reduces sharply the SC penetrability even at an intensity of as low as several tenths of a tesla. When the intensity exceeds 2 T, the target remains almost intact, except for many small surface craters no more than 5 mm across and copper traces immediately below the SC location. Such an appearance suggests either the dispersion of the SC jet or the collapse of the sheath. The craters formed at a field induction of about 0.6 T were similar in shape to those formed by fast compact "crushing balls" [4].

Reasons for this effect were discussed in [3]. The most plausible one is a sharp growth of the magnetic field in the jet formation area. However, here a mechanism behind field enhancement due to the sheath collapse seems to be different from the mechanism taking place in MCGs. While the MCG liner has a cylindrical shape and shrinks over the entire length simultaneously, the SC sheath collapses gradually from top to bottom. The enhancement of the compressed magnetic field at the top, where the cross-sectional area of the sheath is small, is insignificant and cannot prevent the collapse of this part with the formation of SC jet fragments. Straightforward estimates show that, when the initial field induction in the cavity is on the order of several tenths of a tesla (in the experiments, the SC penetrability was noticeably reduced under these conditions), the shrinkage of the sheath to the radius of a forming SC jet could enhance the field to a level of no more than several tens of teslas (even if the diffusion of the magnetic flux is ignored). The creation of such a weak field could hardly influence the process of sheath collapse and SC jet formation.

Results of experiments on producing an axial magnetic field in the SC sheath before explosion

No.	B_0, T	L/L_0
1	2.5	0
2	0.65	0.12
3	0.35	0.4
4	0.25	0.4
5	0.25	0.64

The "disbalance" of cumulative action when a magnetic field is generated in the SC sheath may be associated with a field enhancement mechanism taking place immediately in the conducting medium when it executes a specific motion. According to the concept of magnetic field freezing [5], the field grows when particles of the medium, while moving, elongate in the direction of the magnetic flux lines. If the compressibility of the medium, as well as the field diffusion due to the finiteness of the material conductivity, is disregarded, the magnetic induction B must vary in proportion to the elongation of material fibers initially aligned with the flux lines. Diffusion processes, which smooth out field nonuniformities and speed up as the conductivity of the medium decreases, will prevent the generation of the field. Therefore, for the enhancement of the magnetic field to be significant, the rate of build-up must exceed the rate of diffusion.

When the jet forms, the material of the sheath ceases to move in the radial direction upon colliding on the charge axis and thereby experiences giant axial tensile strains. In this case, the freezing-in effect would have to generate and enhance the field directly in the forming jet (Fig. 3).

MAGNETIC FIELD GENERATION MODEL

A simplified one-dimensional magnetohydrodynamic model of magnetic field generation in a conducting medium when it deforms into a jet with the attendant "alignment" of the magnetic flux lines, as well as prerequisites for the disbalance of the SC piercing action, has been discussed in [6]. Consider the collision of two plane flows of an incompressible material that move with the same velocity u_0 along the same line (Fig. 4). The material of the flows contains a magnetic field that makes a right angle with the flow direction and has an induction B_0 at an infinitely large distance from the plane of collision. We choose a coordinate system such that the x axis is aligned with the flow direction and the origin is in the plane of collision. It is assumed that the slowing-down of either flow, causing the material to spread in the transverse direction, occurs in the area of length l_0 in the x direction and that the lon-

gitudinal velocity u of the flows in this area drops linearly from u_0 to zero in the plane of collision.

It is clear that material particles will elongate in the transverse direction and, accordingly, the field frozen in them will grow. In the horizontal plane of flow symmetry, this field will retain its single transverse component $B(x, t)$ upon evolution. Taking into account the symmetry of the problem about the plane of collision, we will trace the evolution of this component in the material of the right-hand flow (Fig. 4). With the field diffusion in the transverse direction ignored, the equation describing the variation of $B(x, t)$ in the domain $x > 0$ is given by [6]

$$\frac{\partial B}{\partial t} = u\frac{\partial B}{\partial x} + B\frac{\partial u}{\partial x} + \frac{\eta}{\mu_0}\frac{\partial^2 B}{\partial x^2}, \tag{1}$$

where $\mu_0 = 4\pi 10^{-7}$ H/m is the magnetic constant and η is the resistivity of the flowing material.

In view of the dependence $u(x)$ adopted above,

$$u = \begin{cases} -u_0 x/l_0, & 0 \le x \le l_0 \\ -u_0, & x > l_0 \end{cases}$$

and writing Eq. (1) in dimensionless form, we obtain the differential equations for the magnetic field induction in the moving material

$$\frac{\partial \bar{B}}{\partial \bar{t}} = \begin{cases} x\dfrac{\partial \bar{B}}{\partial \bar{x}} + \bar{B} + \dfrac{1}{\mathrm{Re_m}}\dfrac{\partial^2 \bar{B}}{\partial \bar{x}^2}, & 0 \le \bar{x} \le 1 \\ \dfrac{\partial \bar{B}}{\partial \bar{x}} + \dfrac{1}{\mathrm{Re_m}}\dfrac{\partial^2 \bar{B}}{\partial \bar{x}^2}, & \bar{x} > 1, \end{cases} \tag{2}$$

where

$$\bar{x} = x/l_0, \quad \bar{t} = tu_0/l_0, \quad \bar{B} = B/B_0$$

are the dimensionless coordinate, time, and magnetic induction, respectively, and the magnetic Reynolds number

$$\mathrm{Re_m} = \frac{\mu_0 u_0 l_0}{\eta} \tag{3}$$

is the ratio between the field generation and diffusion rates.

It is easy to check that here the Reynolds number specifies the ratio of the characteristic field diffusion time $\mu_0 l_0^2/\eta$ for a conducting layer of thickness l_0 to the characteristic time l_0/u_0 of material deformation in the stagnation area (the latter governs the field generation rate).

First let us consider the collision of two perfectly conducting flows ($\mathrm{Re_m} \longrightarrow \infty$). According to the first equation in (2), the time variation of the magnetic field induction $\bar{B}_{\mathrm{col}}(\bar{t}) = \bar{B}(0, \bar{t})$ in the plane of collision

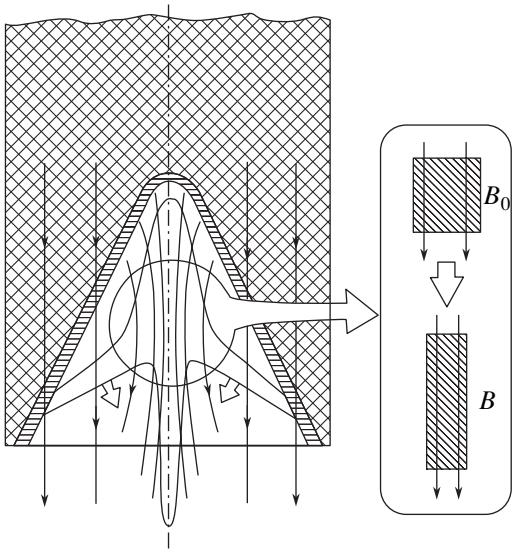

Fig. 3. Possible mechanism of magnetic field enhancement in the jet formation area upon collapsing the SC sheath.

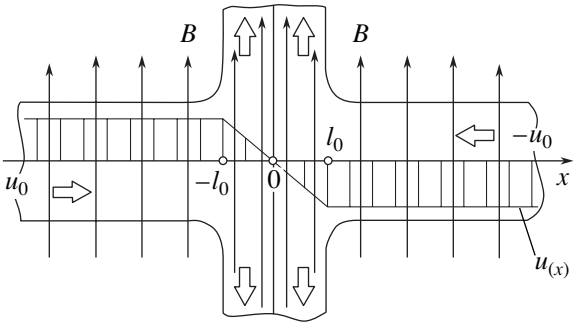

Fig. 4. Scheme for magnetic field generation analysis at the fast spread of the conducting material along the magnetic flux lines.

($\bar{x} = 0$, Fig. 4) is described by the equation $d\bar{B}_{\mathrm{col}}/d\bar{t} = \bar{B}_{\mathrm{col}}$. For the initial condition $\bar{B}_{\mathrm{col}}(0) = 1$, its solution gives the exponential increase in the field intensity

$$B_{\mathrm{col}} = B_0 \exp(\bar{t}) = B_0 \exp(u_0 t/l_0). \tag{4}$$

For real-conductivity media ($\mathrm{Re_m}$ is finite), the generation of the magnetic field with allowance for diffusion was described by numerically integrating Eqs. (2). It was assumed that the condition $\partial \bar{B}/\partial \bar{x} = 0$, which includes the symmetry of the flow about the plane of flow collision, is fulfilled at the contact boundary $\bar{x} = 0$.

Computed results for various $\mathrm{Re_m}$ are demonstrated in Figs. 5–7. Figure 5 shows the distribution of the magnetic field induction in time for the right-hand flow (Fig. 4); Fig. 6, the variation of $\bar{B}_{\mathrm{col}}$ in the plane of collision. From the plots in Fig. 7, one can see how the value of $\mathrm{Re_m}$ affects the thickness h of the layer adja-

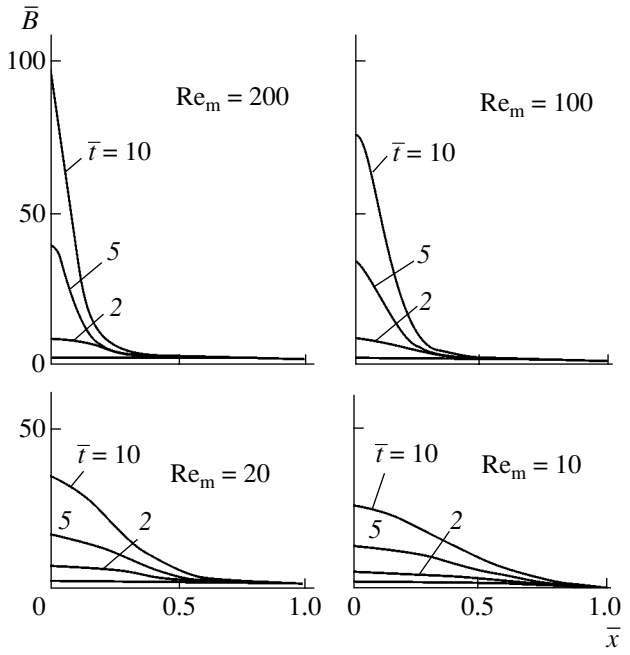

Fig. 5. Magnetic induction distribution in the flowing material at different time instants.

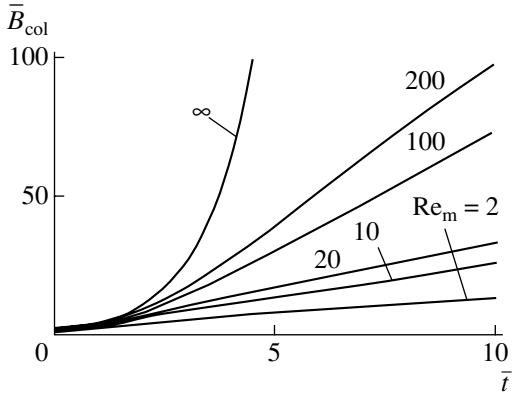

Fig. 6. Time variation of the magnetic field induction in the plane of collision.

cent to the plane of collision. In this layer, which will be referred to as the magnetic layer, the magnetic induction sharply increases. As the thickness of the magnetic layer, we take the extension of the area over which the magnetic induction increment $\Delta B = B - B_0$ decreases no more than twice compared with the increment $\Delta B_{\mathrm{col}} = B_{\mathrm{col}} - B_0$ in the plane of collision.

The results suggest that the diffusion of the magnetic field has a significant effect on the rate of its enhancement in the deforming material. The rate of field enhancement in the narrow boundary layer at the plane of collision drops as the diffusion rate increases ($\mathrm{Re_m}$ decreases). Simultaneously, the magnetic layer thickens. After $\dot{t} = 4$–5 (which corresponds to a length of interpenetrating flow parts $(4–5)l_0$), the field intensity in the plane of collision grows almost linearly (Fig. 6) and the magnetic layer thickness remains unchanged (Fig. 7).

As follows from Fig. 7, when $\mathrm{Re_m}$ is sufficiently high, one can talk of a skin layer forming near the plane of collision. For example, at $\mathrm{Re_m} = 100$, the field builds up intensely (roughly 70 times at $\dot{t} = 10$) within an area whose extension is about 10% of the thickness l_0 of the flow spreading layer. With small $\mathrm{Re_m}$ ($\mathrm{Re_m} < 1$), the diffusion of the field causes the magnetic layer to expand beyond the flow spreading area ($h > l_0$); however, the field intensity grows insignificantly in this case.

As follows from (3), the scale factor is of great significance for magnetic field enhancement in the deforming conductor: as the deformed area expands ($\mathrm{Re_m}$ grows), the field must rise faster.

ESTIMATION OF THE MAGNETIC FIELD ENHANCEMENT IN THE FORMING SHAPED CHARGE JET

The results obtained within the framework of the one-dimensional model where the sheath material is assumed to be perfectly conducting (specifically Eq. (4)) indicate that the magnetic field intensity grows exponentially at the point where collapsing elements of the sheath are in contact:

$$B = B_0 \exp(\dot{\varepsilon}_{zs} t). \qquad (5)$$

Here, B_0 is the initial induction of the magnetic field in the sheath and $\dot{\varepsilon}_{zs}$ is the axial strain rate of sheath particles in the jet formation area.

The effect of diffusion on the rate of field enhancement in a finite-conductivity sheath material can be estimated from the parameter $\mathrm{Re_m}$ (which is the ratio of the generation and diffusion rates, as was noted above). In our case, expression (3) for the Reynolds number can be recast as $\mathrm{Re_m} = \mu_0 r_0 u_c/\eta$, where u_c is the rate of sheath collapse and r_0 is the radius of the forming SC jet. Under jet formation conditions typical of a copper sheath collapse (u_c is on the order of several kilometers per second, and r_0 equals several millimeters), $\mathrm{Re_m}$ may reach 10^3. This indicates that the magnetic field growth rate in the material of the forming SC jet far exceeds the rate of field diffusion.

Considering the fact that the effect of diffusion is weak and assuming that u_c/r_0 is the typical value of $\dot{\varepsilon}_{zs}$, we can state based on (5) that the magnetic field in the jet formation area may be enhanced from several hundreds to several thousands of times for the characteristic time of sheath collapse. Thus, if the initial field in the SC sheath has an induction of 0.1 T [3], it may rise to 100 T within a time after the sheath starts collapsing. Such high fields may cause considerable mechanical and thermal effects. Simple estimates show [2, 6] that

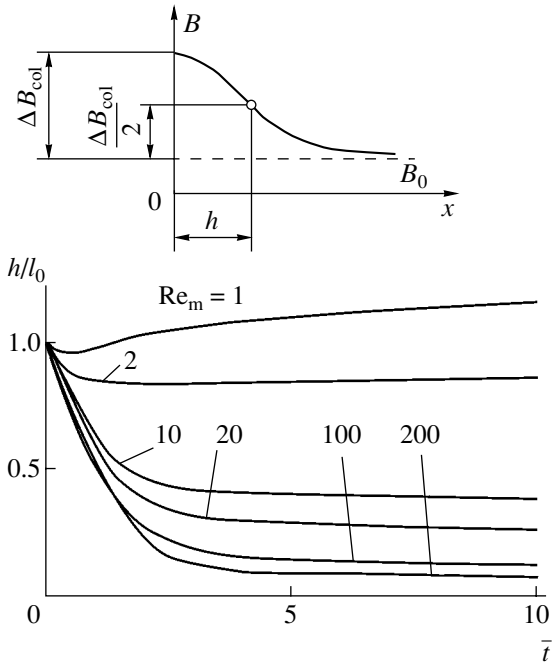

Fig. 7. Variation of the thickness of the material with the enhanced magnetic field.

the rate of material heating in the jet formation area may be as high as 1000 K/μs when the field increases to 100 T. The force effect of such a field (magnetic pressure) is estimated as 10 GPa. This value is close to pressures arising at the detonation of explosives [4].

A strong heating of the jet formation area may turn the material into the liquid state and even the vapor phase via thermal explosion. The simultaneous action of intense tensile electromagnetic forces may cause the dispersion of the jet formation area in the sheath, which prevents the further formation of the SC jet. Such a scenario of collapsing the sheath with a magnetic field inside correlates well with experimental data [3]. The residual penetration of the charge observed in [3] is associated with the part of the jet that formed before the magnetic field reached its critical value. The higher the initial field strength in the sheath, the smaller this part of the jet.

NUMERICAL SIMULATION OF PERFECTLY CONDUCTING MATERIAL JETS WITH A FROZEN-IN MAGNETIC FILED

The effect of the magnetic field on the jet formation was studied by numerically solving the 2D problem of oblique collision of plane jets of a compressible perfectly conducting fluid that is subjected to a magnetic field directed normally to the plane of collision. For this problem, the continuity equation and the equation of motion for the medium in the x and y directions of the plane Cartesian system (Fig. 8, $t = 0$) with allowance for bulk electromagnetic forces are written as

$$\frac{d\rho}{dt} + \rho\left(\frac{\partial v_x}{\partial x} + \frac{\partial v_y}{\partial y}\right) = 0,$$

$$\rho\frac{dv_x}{dt} = -\frac{\partial p}{\partial x} - j_z B_y,$$

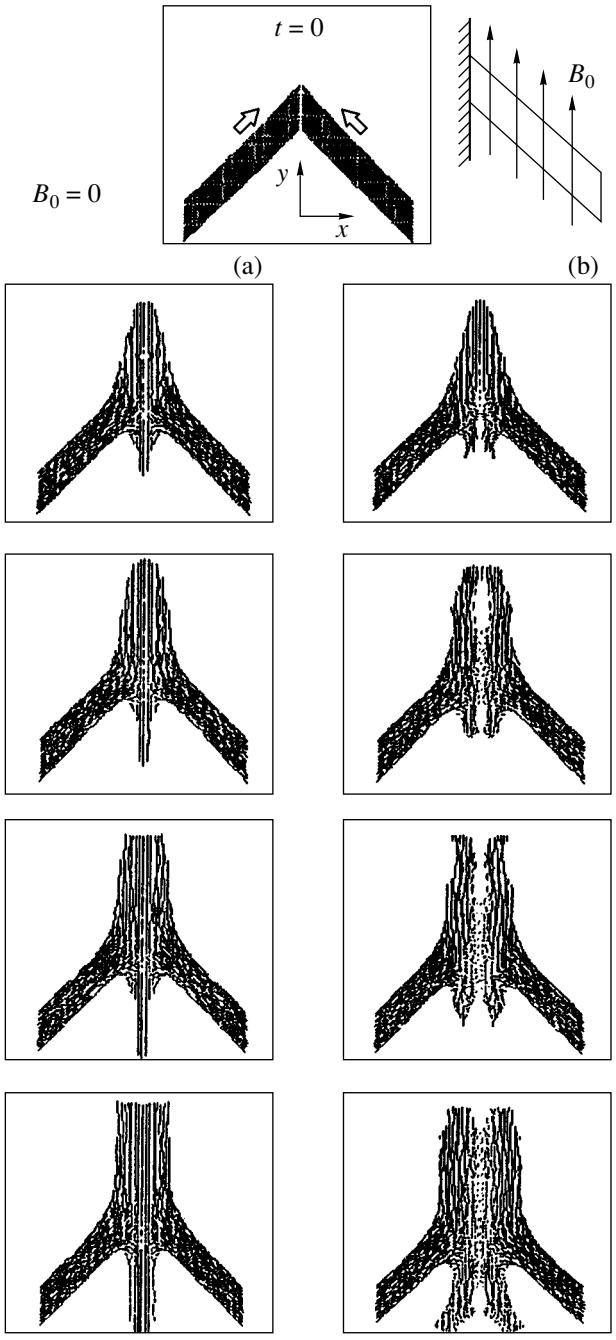

Fig. 8. Effect of the magnetic field on jet flows upon the collision of plane jets of a compressible perfectly conducting fluid. B_0 = (a) 0 and (b) 5 T.

$$\rho\frac{dv_y}{dt} = -\frac{\partial p}{\partial y} + j_z B_x.$$

Here, ρ is the fluid density; v_x and v_y are the velocity vector components; p is the hydrodynamic pressure in the fluid; B_x and B_y are the magnetic induction vector components; and j_z is the bulk density of induction currents:

$$j_z = \frac{1}{\mu_0}\left(\frac{\partial B_y}{\partial x} - \frac{\partial B_x}{\partial y}\right).$$

The evolution of the magnetic field in the case of a plane magnetohydrodynamic flow of a perfectly conducting medium is described by the equations

$$\frac{d}{dt}\left(\frac{B_x}{\rho}\right) = \frac{B_x}{\rho}\frac{\partial v_x}{\partial x} + \frac{B_y}{\rho}\frac{\partial v_x}{\partial y},$$

$$\frac{d}{dt}\left(\frac{B_y}{\rho}\right) = \frac{B_x}{\rho}\frac{\partial v_y}{\partial x} + \frac{B_y}{\rho}\frac{\partial v_y}{\partial y}.$$

The fluid flow was assumed to be barotropic with the density dependence of the hydrodynamic pressure in the form of the Tate adiabat [4]

$$p = A((\rho/\rho_0)^n - 1),$$

where ρ_0 is the fluid density under normal conditions and A and n are empirical material constants.

This set of equations was numerically integrated with the computational algorithm based on the Lagrangean free point representation [7].

Figure 8 illustrates jets appearing (a) in the absence of the magnetic field and (b) in the presence of the field with an initial induction $B_0 = 5$ T that is oriented along the y axis. The velocity of the jets toward the plane of collision is 2 km/s. The material constants for copper were used. From Fig. 8b, it follows that the magnetic field makes the formation of a continuous jet moving along the plane of collision impossible. This is because the field is greatly enhanced in the contact area, where the material of the colliding jets, spreading in the transverse direction, undergoes high tensile strains along the magnetic flux lines, which causes the field generation. Eventually, strong electromagnetic forces arising when the field grows make the further deformation of the particles in the jet spreading area impossible, "freezing" this area and, thereby, blocking the outgoing jet. Simultaneously, these strong electromagnetic forces disperse the jet material entering into the collision area.

CONCLUSIONS

Thus, our analysis supports the hypothesis that the deformation mechanism of magnetic field generation (enhancement) may substantially weaken the cumulative effect observed upon the SC explosion. However, a comprehensive idea of this issue will be given after X-ray investigation into the collapse of the SC sheath with a magnetic field inside.

REFERENCES

1. M. A. Lavrent'ev, Usp. Mat. Nauk **12** (4), 41 (1957).
2. H. Knoepfel, *Pulsed High Magnetic Fields* (North-Holland, Amsterdam, 1970; Mir, Moscow, 1971).
3. S. V. Fedorov, A. V. Babkin, and S. V. Ladov, Fiz. Goreniya Vzryva **35**, 145 (1999).
4. F. A. Baum, L. P. Orlenko, K. P. Stanyukovich, *et al.*, *Physics of Explosion* (Nauka, Moscow, 1975).
5. L. D. Landau and E. M. Lifshitz, *Course of Theoretical Physics*, Vol. 8: *Electrodynamics of Continuous Media* (Nauka, Moscow, 1982; Pergamon, New York, 1984).
6. S. V. Fedorov, A. V. Babkin, and V. I. Kolpakov, Prikl. Mekh. Tekh. Fiz. **41** (3), 13 (2000).
7. E. S. Oran and J. P. Boris, *Numerical Simulation of Reactive Flow* (Elsevier, New York, 1987; Mir, Moscow, 1990).

Translated by V. Isaakyan

Technical Physics, Vol. 48, No. 8, 2003, pp. 1053–1057. Translated from Zhurnal Tekhnicheskoĭ Fiziki, Vol. 73, No. 8, 2003, pp. 118–122.

EXPERIMENTAL INSTRUMENTS AND TECHNIQUES

Silicon Photodiodes as Thomson Scattering Detectors in Experiments on the Tuman-3M Tokamak and in Bench Experiments

V. V. Zabrodsky, D. V. Kalinina, E. E. Mukhin, G. T. Razdobarin, V. L. Sukhanov, S. Yu. Tolstyakov, and A. S. Tukachinsky

Ioffe Physicotechnical Institute, Russian Academy of Sciences, Politekhnicheskaya ul. 26, St. Petersburg, 194021 Russia

e-mail: e.mukhin@mail.ioffe.ru

Received February 3, 2003

Abstract—Experiments on Thomson scattering in the Tuman-3M tokamak plasma with silicon photodiodes applied as radiation detectors are performed. Bench tests and numerical simulation are used to compare the efficiency of detector modules based on conventional and avalanche photodiodes in recording weak pulses of various durations against uniform background light. When the pulse duration increases to several hundreds of nanoseconds, the increase in sensitivity due to avalanche gain disappears. This is of importance for diagnosing the tokamak plasma, where the background radiation is relatively intense. © *2003 MAIK "Nauka/Interperiodica".*

PLASMA DIAGNOSTICS BY THOMSON SCATTERING WITH SILICON PHOTODIODES USED AS DETECTORS

Experiments on plasma diagnostics by the method of Thomson scattering employ various detectors, such as photoelectric multipliers (PEMs) in the visible range and avalanche photodiodes (APD) for the near-IR range. The diagnostics system based on the Tuman-3M tokamak is equipped with PEMs to record the short-wave part of the scattered ruby laser radiation. The diagnostic feature of the Tuman-3M tokamak, as applied to Thomson scattering, is the long duration (≈500 ns) of pulses recorded, which is typical of intracavity plasma probing [1]. Such an approach allows researchers to increase the probe energy by using simple and cost-effective lasers. In the experiments reported, we made an attempt to apply an alternative detector based on a silicon photodiode (PD) without internal amplification (avalanche gain). Such detectors offer a much higher quantum efficiency compared with avalanche photodetectors. The experiments were performed under standard discharge conditions: a discharge current of 120 kA; a toroidal magnetic field of 0.8 T; and an electron density and temperature $\bar{n}_e = 3 \times 10^{13}$ cm^{-3} and $T_e \sim 500$ eV, respectively.

The experimental setup based on the Tuman-3M is depicted in Fig. 1. It consists of the discharge chamber of the tokamak, a laser and optics forming a probing beam, a spectrometer analyzing the scattering spectrum, and a multichannel detecting system. In the experiments using a PD-based detector module, the fiber light guide of one of the measuring channel transmitted the radiation to the 3-mm-diam. sensitive area of the detector. The circuit diagram of the photodetector is shown in Fig. 2. As follows from bench tests, the basic parameters responsible for the equivalent noise charge [2] are as follows: the total input capacitance $C_{in} = 1.8 \times 10^{-11}$ F, the noise voltage at the input of the preamplifier $U_n = 1.7 \times 10^{-9}$ V/$\sqrt{\text{Hz}}$, and the equivalent input noise current (with allowance for Nyquist noise and leakage currents) $i_n = 2.5 \times 10^{-14}$ A/$\sqrt{\text{Hz}}$ (which corresponds to an equivalent dark input current $I_d = i_n^2/2e = 2 \times 10^{-9}$ A). To tune the frequency band, output signals of the amplifier were applied to an RC shaper to select the optimal S/N ratio upon detecting the plasma-scattered radia-

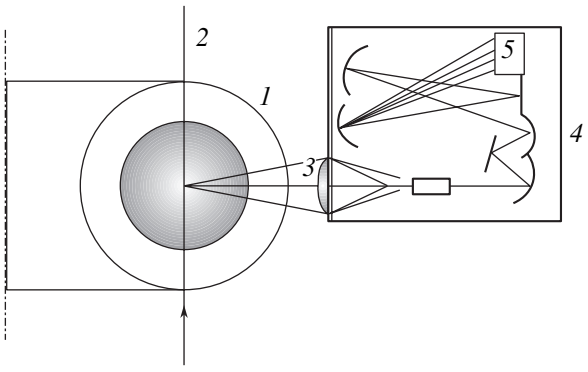

Fig. 1. Experimental setup for plasma diagnostics by Thomson scattering on the Tuman-3M tokamak: (*1*) tokamak chamber, (*2*) probing laser beam, (*3*) input optics, (*4*) spectrometer, and (*5*) array of photodetectors.

1063-7842/03/4808-1053$24.00 © 2003 MAIK "Nauka/Interperiodica"

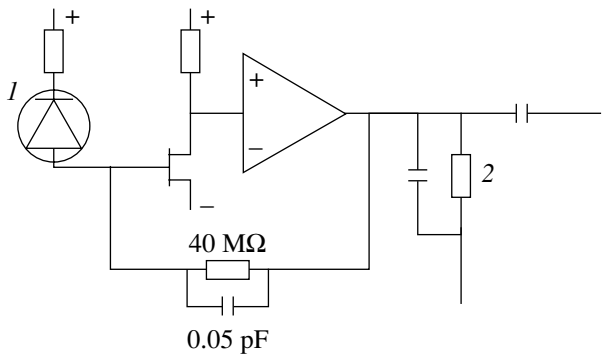

Fig. 2. Circuit diagram of the detector module: (*1*) photodiode and (*2*) *RC* shaper.

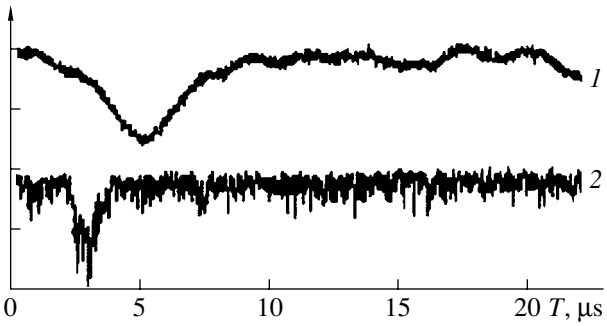

Fig. 3. Waveforms of scattered signal recorded by (*1*) PD and (*2*) PEM in adjacent spectral channels.

tion. Figure 3 shows the scattered pulse waveform (curve *1*) in the PD-equipped spectral channel. According to absolute calibration data for the diagnostic system, the number of photons per pulse incident on the detector's faceplate was about 10^3. A typical scattered signal waveform recorded by the adjacent PEM-equipped channel is shown by curve *2* for comparison. The noise in the upper and lower waveforms is of various origin. In the case of the PEM, we are dealing largely with the shot noise of the photocurrent due to the background radiation of the plasma. As can be judged from the photocurrent measured, ≈1 nA, its intensity was comparable to the intensity of the scattered signal averaged over a time interval of ≈500 ns. As to the PD, the basic source of fluctuations is the noise of the amplifier's input circuit. With the frequency spectrum of the noise signal optimized by means of the RC shaper, the relative rms error of charge measurement was ≈15%. This value is quite acceptable for plasma diagnostics by the Thomson scattering method.

RESULTS OF BENCH TESTS

The aim of bench tests was to optimize the performance of the PDs as optical detectors in a wide range of input parameters. An objective lens projected the radiation from an AL106 light-emitting diode, which simulated Thomson scattering signals, onto a diaphragm 1 mm in diameter. Behind the diaphragm, we placed an absolutely calibrated detector, as well as PD- and APD-based detector modules. Signals from the amplifier were applied to the Nuclear Enterprises NE5259 RC shaper and digitized. The primary function of the shaper was to improve the S/N ratio by tuning the noise bandwidth. The parameters of the PD-based detector module to be tested were the same as in the Tuman-3M tokamak plasma experiments. Without additional tuning, the rise and fall times of the pulsed response were 0.5 and 2.0 μs, respectively.

In the alternative experiment with the photodetector based on a Perkin Elmer C30955E APD, we used a low-noise amplifier with a KP341A FET at the input. Therein lies the basic difference between our design and conventional ones [3, 4] with CLC-425 and MAX-4107 op amps. The high input noise current, $\sim 10^{-12}$ A/$\sqrt{\text{Hz}}$, which is characteristic of such circuits, makes us use APDs of high avalanche gain at the penalty of an increase in the excess noise factor [4].

The responsivity of the system was determined by measuring the output amplitudes with calibrated-flux optical signals of various durations (500 and ≈50 ns) applied to the input. Noise signals were generated by the quasi-uniform illumination of the detectors from a calibrated light source with a photocurrent ranging up to 50 nA. To find the equivalent noise charge, we calculated the rms error fluctuation of the noise signal. To this end, the noise waveform was digitized at 2500 time instants over a period of several milliseconds. The results of computer processing were contrasted with records of an rms voltmeter. The equivalent noise charge was found as the number of photoelectrons that generates a pulsed signal at the shaper output with an amplitude equal to the measured rms fluctuation of the noise signal. Curve *1* in Fig. 4 shows the time variation of the equivalent noise charge $\sqrt{N_{\text{PD}}^2}$ for the PD without the uniform background light. Along the abscissa axis, experimentally found rise times of the pulsed response formed at the output of the shaper and displayed on an oscilloscope are plotted. The measurements are nearly independent of the duration of input light pulses, which was varied between several tens to 500 ns. Curve *1*, which fits experimental data, is approximated by a simple dependence $\sqrt{a\tau + b/\tau}$, which is typical of the equivalent CR–RC shaper with the same time constants of differentiation and integration τ [5].

Good agreement between the data points and fitting curve *1* makes it possible to consider experimental data in terms of a simplified model of the equivalent CR–RC shaper. This model assumes that the shaping time equals the rise time of the pulsed response. With this assumption, curves *2* and *3* in Fig. 4 show the contribu-

tions of the current, $\sqrt{a\tau}$, and voltage, $\sqrt{b/\tau}$, noises versus the shaping time τ. In the absence of uniform background light, the value of τ should be selected within the smooth minimum of curve *1*. In the presence of the background photocurrent exceeding the dark current, $I_b > I_d$, the contribution from the current noise increases in proportion to $\sqrt{I_b/I_d}$ (the dashed curves in Fig. 4). To minimize the noise under these conditions, one should decrease τ so that the noise components of the voltage and current equal each other in the presence of background light.

The family of curves in Fig. 5 demonstrates the dependence of the measured equivalent noise charge $\sqrt{N_{PD}^2}$ on the square root of the steady-state background photocurrent. Each of the curves corresponds to a certain shaping time, which is varied between 1.0 and 2.2 μs. Analytical curve *5* shows the minimal value of the noise charge, which is obtained when the shaping time τ meets the equality condition for the noise components of the current and voltage. With signals generated in such a way, the equivalent noise charge decreases appreciably, especially if the background photocurrent is high, as follows from Fig. 5.

Figure 6 shows the results of the experiments with the APD-based photodetector. The avalanche gain, $M \approx 30$, was established for a bias voltage of 250 V. When the avalanche gain increases by a factor of 3, the noise signal grows by roughly 25% in accordance with the well-known effect of increase in the excess noise factor [6].

The dependences of the equivalent noise charge on the square root of the steady-state background photocurrent (Fig. 6) were taken at two durations (500 and 50 ns) of the input pulsed signal. It is seen that the contribution of the voltage noise in the APD-based detector is small especially if a low-noise input amplifier stage is used. In this case, large shaping times are unneeded. For the longer signal (Fig. 6a), the shaping time was $\tau \approx$ 500 ns according to the signal duration. In the case of the shorter signal (Fig. 6b), the shaping time was ≈100 ns. This value takes into account the rise time of the pulsed response of the preamplifier without additional (external) shaping. To suppress low-frequency noise, the fall time of the pulsed response was limited by differentiating output signals. Without external illumination, the equivalent noise charge equaled 30 electron charges. In the presence of the background photocurrent exceeding the dark current, the equivalent noise charge varied as the square root of the photocurrent. The dashed lines in Fig. 6 show the increase in sensitivity due to the avalanche gain of the APD compared with the sensitivity of the PD-based detector. The signal shaping time is the same as that corresponding to the dashed curve in Fig. 5.

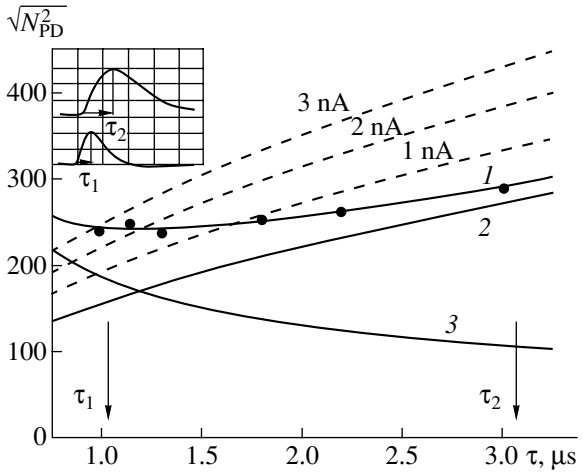

Fig. 4. Equivalent noise charge (in units of the electron charge) vs. shaping time. The arrows indicate shaping times τ_1 = 1 μs and τ_2 = 3 μs for the output waveforms shown at the top of the figure. (*1*) Data points and (*2*, *3*) relative contributions of the current and voltage components to the noise. The dashed lines show the variation of the current component in the presence of the background photocurrent. The figures by the dashed curves are photocurrent values.

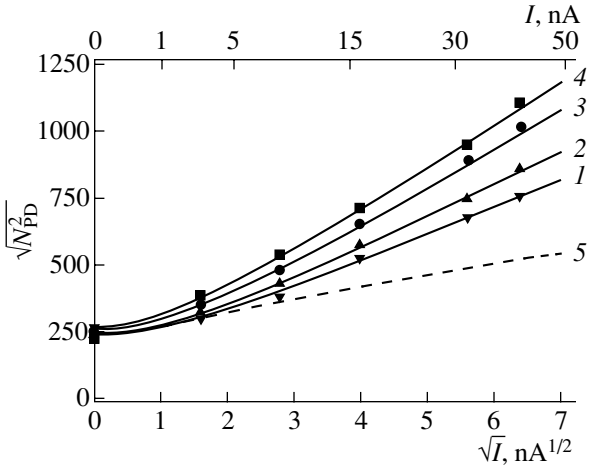

Fig. 5. Equivalent noise charge (in units of the electron charge) in the PD vs. square root of the steady-state background photocurrent. τ = (*1*) 1, (*2*) 1.3, (*3*) 1.8, and (*4*) 2.2 μs. Dashed line *5* shows the equivalent noise charge calculated for the case when the shaping time meets the equality condition for the current and voltage noise components.

EXPERIMENTAL RESULTS AND DISCUSSION

The detectivities of PD- and APD-based photodetectors can be conveniently compared by using the well-known relationships for equivalent noise charge [5] when a gated integrator is used as a pulse shaper. For such shapers with low-frequency noise filtering by means of double correlated sampling, the equivalent noise charge (for an avalanche gain $M \geq 1$) is well

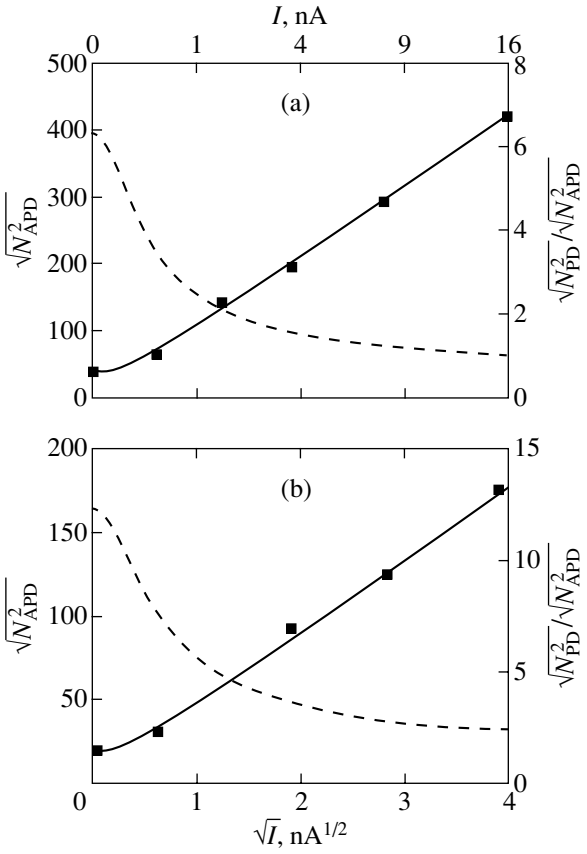

Fig. 6. Equivalent noise charge (in units of the electron charge) in the APD vs. square root of the steady-state background photocurrent for signals of duration (a) 500 and (b) 50 ns (solid lines). The dashed lines (the vertical axis on the right) show the increase in sensitivity due to the avalanche gain of the APD compared with the conventional PD for the case when the shaping time corresponds to the dashed line in Fig. 5.

approximated by the formula

$$\sqrt{N^2} = \sqrt{F\frac{I}{e}\left(t+\frac{2}{3}\tau\right)+\frac{1}{M^2}\left(\frac{\sigma}{e}\right)^2}. \qquad (1)$$

Here, $\sigma = C_{in}U_n/\sqrt{\tau}$ is the equivalent noise charge, which depends on the input noise voltage U_n, total input capacitance C_{in}, and gating time τ; t is the input (measured) pulse duration; F is the excess noise factor in avalanche-gain detectors; I is the total input background current, which includes the photocurrent and dark current. Small terms associated with the shot noise of the input signal and with the FET leakage current at the output of the avalanche-gain detector are neglected.

For conventional photodiodes, the gating time τ in (1) should be selected according to the rated parameters of the detector module so as to minimize the noise signal at the output of the shaper. Usually, the gating time is taken such that the current and voltage noise components in (1) are the same [2]. Under the obvious conditions $M = 1$ and $F = 1$, formula (1) transforms into

$$\sqrt{N^2_{PD}} = \sqrt{2\frac{I_{PD}}{e}\left(t+\frac{2}{3}\tau_{PD}\right)}, \qquad (2)$$

where the gating time, which normally exceeds the input signal duration, is

$$\tau_{PD} = \frac{C_{in}U_n}{\sqrt{\frac{2}{3}eI_{PD}}}.$$

For avalanche photodiodes with $M \gg 1$, the gating time τ, unlike PDs, may be short. In any case, it must not exceed appreciably the signal duration. Otherwise, the current component of the charge noise would increase. For an APD with typical $M \approx 50$, $\tau \geq 100$ ns, and $I \geq 0.1$ nA, the current component

$$\sqrt{F_{APD}\frac{I_{APD}}{e}\left(t+\frac{2}{3}\tau_{APD}\right)}$$

of the noise in (1) exceeds the voltage component

$$\frac{1}{M}\left(\frac{\sigma_{APD}}{e}\right),$$

calculated for $U_n = 1.7 \times 10^{-9}$ V/$\sqrt{\text{Hz}}$ and $C_{in} = 1.8 \times 10^{-11}$ F. In these conditions, the equivalent noise charge of a PD (formula (2)) and the same parameter of an APD are related as

$$\frac{\sqrt{N^2_{PD}}}{\sqrt{N^2_{APD}}} = \frac{\sqrt{2\frac{I_{PD}}{e}\left(t+\frac{2}{3}\tau_{PD}\right)}}{\sqrt{F_{APD}\frac{I_{APD}}{e}\left(t+\frac{2}{3}\tau_{APD}\right)}}. \qquad (3)$$

To compare analytical results with the bench measurements, we estimated the equivalent noise charges in the PD and APD-based detectors for the following parameters: the equivalent input noise currents $\sqrt{2eI_{PD}} = 2.5 \times 10^{-14}$ A/$\sqrt{\text{Hz}}$ and $\sqrt{2eI_{APD}F} \approx 10^{-14}$ A/$\sqrt{\text{Hz}}$ and the respective gating times $\tau_{PD} = 2$ μs and $\tau_{APD} = 0.1$ μs. According to (3), the ratio $\frac{\sqrt{N^2_{PD}}}{\sqrt{N^2_{APD}}}$ is 6.5 and 12.5 for signal durations of 500 and 50 ns, respectively. This estimate is in good agreement with the data in Fig. 6 without the steady-state background photocurrent. When comparing the performances of the detectors, one should take into account the background photocurrent due to the self-radiation of the plasma. The associated value of the photocurrent in this case ranges from ≈1 nA (according to the measurements on the Tuman-3M tokamak) to several tens of nanoamperes for large tokamaks. As follows from Fig. 5, the

equivalent noise charge of the APD-based photodetector varies insignificantly until the steady-state background photocurrent exceeds the dark current (≈2 nA). However, such background photocurrents far exceed the small dark current of APDs. As a result, the difference in sensitivity becomes much smaller especially in the case of long input pulses (with durations of several hundreds of nanoseconds). Expression (3) implies that, for an APD, the increase in sensitivity due to avalanche gain virtually vanishes when the light pulse duration reaches 500 ns with background currents no higher than several nanoamperes.

CONCLUSIONS

In experiments on plasma diagnostics by the method of Thomson scattering, silicon photodiodes were tested as detectors of weak signals against the background of the plasma self-radiation. It was shown that the performance of such detector modules is suitable for measuring scattered signal intensities on the order of $\sim 10^3$ photons per pulse. In bench tests, we compared the sensitivities of detectors based on conventional PDs and APDs. For short (≈50 ns) pulses and moderate photocurrents due to the plasma self-radiation, the sensitivity of APDs is three or four times that of PDs (because of the avalanche gain reaching 50). As the duration of light signals at the input grows and reaches ≈500 ns, as well as when the photocurrent due to the plasma radiation is as high as several tens of nanoamperes, the sensitivities of both devices become nearly the same. The obvious advantages of photodiodes over other detectors are simple design and reliability, which is of special importance for multichannel detecting systems.

REFERENCES

1. Yu. V. Petrov, G. T. Razdobarin, S. Yu. Tolstyakov, and A. S. Tukachinsky, in *Proceedings of the 8th International Symposium on Laser Aided Plasma Diagnostics, Doorwerth, 1997*, p. 211.
2. M. A. Trishenkov, *Photodetectors and Charge-Coupled Devices: Detection of Weak Optical Signals* (Radio i Svyaz', Moscow, 1992).
3. C. L. Hsieh, J. Haskovec, T. N. Carlstrom, *et al.*, Rev. Sci. Instrum. **61**, 2855 (1990).
4. F. Orsitto, A. Brusadin, and E. Giovannozzi, Rev. Sci. Instrum. **68**, 1201 (1997).
5. F. S. Goulding, Nucl. Instrum. Methods **100**, 493 (1972).
6. R. J. McIntyre, IEEE Trans. Electron Devices **13**, 164 (1966).

Translated by V. Isaakyan

Technical Physics, Vol. 48, No. 8, 2003, pp. 1058–1060. Translated from Zhurnal Tekhnicheskoĭ Fiziki, Vol. 73, No. 8, 2003, pp. 123–125.

BRIEF COMMUNICATIONS

Effect of the Shape and Size of Conducting Particles on the Percolation Cluster Formation in a Ceramic Composition

A. Yu. Dovzhenko and V. A. Bunin

Institute of Structural Macrokinetics and Materials Sciences Problems, Russian Academy of Sciences, Chernogolovka, Moscow oblast, 142432 Russia

e-mail: alex@itp.ac.ru

Received December 3, 2002

Abstract—The electrical properties of a ceramic composition are considered. A profound influence of the conducting phase structure on the electrical conductivity of the material is shown. Computational experiments indicate the considerable dependence of the percolation cluster properties on the anisotropy of its components. © *2003 MAIK "Nauka/Interperiodica".*

INTRODUCTION

Much effort has recently been made to prepare multicomponent refractory ceramics intended for operation in the corrosive and high-temperature environment [1–3].

The electrical conductivity of ceramic materials is of great importance in many applications. For example, semiconducting materials are used in electrical heaters and in a variety of electron devices, such as rectifiers, photosensitive devices, thermistors, detectors, and modulators, which are finding increasing use in electrical engineering.

In the recent study [4] of the formation of a conducting ceramic system by filtration combustion under high nitrogen pressure, the threshold volume fraction of the conducting phase (titanium diboride) was found to be 19%. At this concentration, a step change in the material conductivity is observed. It is known, however, that the threshold fraction of the conducting phase in similar systems is usually no less than 50%, as follows from analytical calculations [5, 6]. A possible explanation of such a discrepancy is the formation of fractal structures.

Conducting particles in the system considered have an unusual shape. In the final product, titanium diboride particles are rod-shaped (see micrograph in Fig. 1, where the bright and dark phases correspond to TiB and AlN, respectively). Particles of a similar shape were also observed in [7].

An abrupt change in the conductivity of the final material is related to the classical percolation problem [6]. The key quantity to be determined in such problems is the so-called percolation limit, i.e., the conducting phase fraction such that individual particles coalesce to form a single infinite cluster extending over the whole volume. The percolation limits for different media are presented in [8]. The effect of the size distribution of particles making up a cluster on the percolation limit has been studied in [9]. Among other things, it has been found that the two-mode distribution (which includes particles of size 1 and 20 arbitrary units) may appreciably decrease the percolation limit because of the mutual influence of two spatial scales.

In this study, we numerically investigate the percolation cluster formation in a ceramic composition in relation to the size and shape of conducting particles.

Theoretical studies of fractal geometry allow one to describe the percolation cluster formation with regard to the size and shape of constituent particles and explain the decrease in the threshold concentration in terms of the following model. The conducting particles

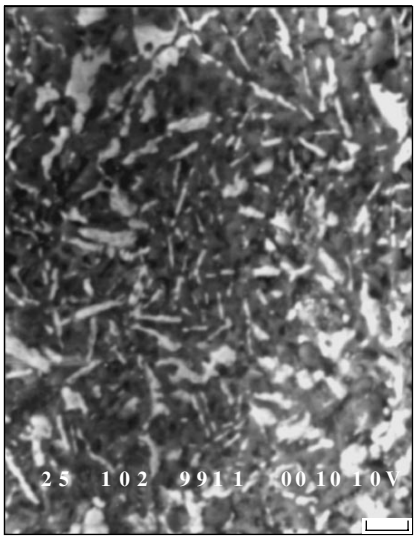

Fig. 1. Microstructure of the TiB (36 vol.%)–AlN composition, ×1000.

1063-7842/03/4808-1058$24.00

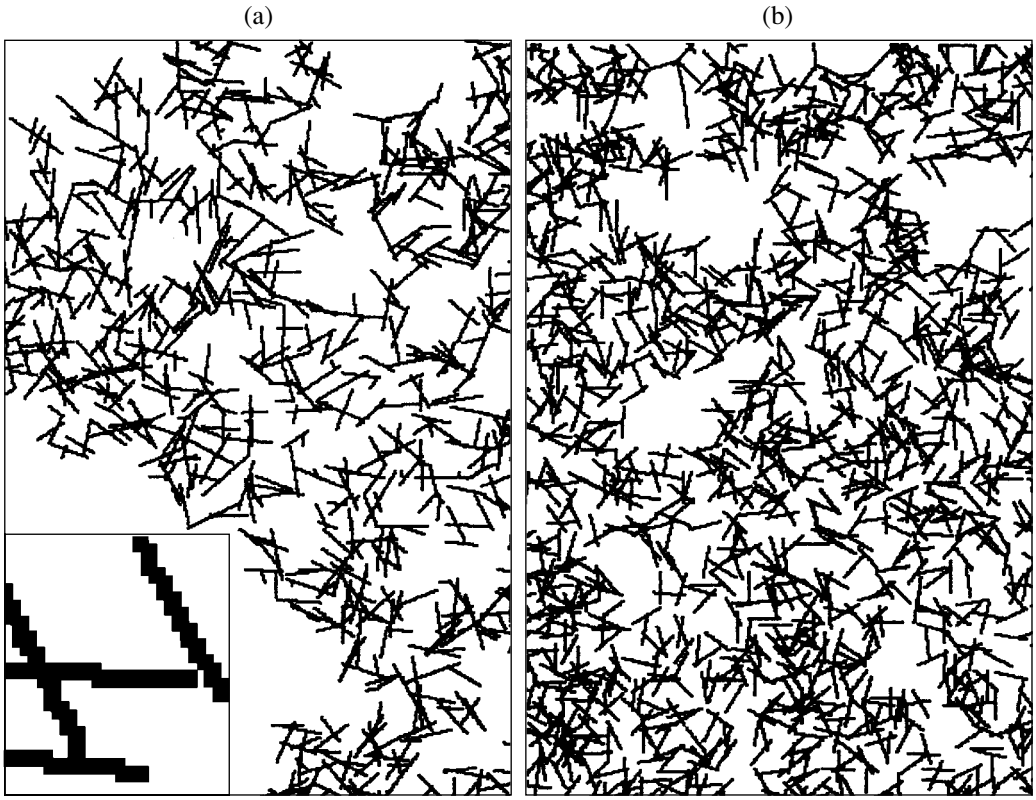

Fig. 2. Percolation clusters comprising needles with a size (a) ranging from 4 to 40 and (b) of 20 arbitrary units. The inset shows the enlarged view of intersecting and nonintersecting needles.

are represented as needle-shaped objects with their characteristic length exceeding the thickness by one order of magnitude. Both the spatial position and the orientation of the needles are assumed to be random. We restrict the discussion to the 2D case, since (i) the results obtained for the 2D case can, with some reservations, be extended to the 3D case and (ii) the solution of the 3D problem requires significant computational resources.

SIMULATION ALGORITHM

We consider a 2048×2048 array of integer numbers as a model field. This dimension is typical of most problems and allows for the variation of the needle length over wide limits (0–200). Initially, all elements of the array are zero.

The parameters given are the volume fraction of the conducting phase, the volume of the needles, and the needle size distribution.

The problem of sites [6] with the Neumann neighborhood was analyzed. Sites that were nearest neighbors at the top, at the bottom, to the left, and to the right were assumed to be connected. Since the needles may be variously oriented, they may appear to be disconnected when represented on a rectangular mesh. Therefore, the size of needles filling the space was deliberately increased to 2 units. Conditions at the array boundaries were assumed to be periodic. A fragment of the array is graphically shown in the inset to Fig. 2.

Given the size distribution of the needles, the array was filled up to a prescribed volume fraction V. A random number generator specified the coordinates, orientation, and length of the needles within the limit of the distribution function. Next, the positions of the needles in the array were calculated. They were assigned the value 1. The needles were free to overlap each other. Then, clusters of connected needles were revealed. Each of them was tested and recognized as infinite (percolation) if it crossed the upper and lower boundaries of the array simultaneously.

The desired fill of the space and the needle size distribution were input parameters; the number of the clusters formed, the size of the greatest cluster, and its "percolation status" were the output parameters. In each of the experiments, the random number generator was restarted. Ten thousand independent experiments were conducted, which ensured an accuracy of ~1%.

NUMERICAL EXPERIMENTS

The validity of the algorithm used was checked by finding the critical (percolation) volume fraction for needles of length 2, i.e., for grains without a preferen-

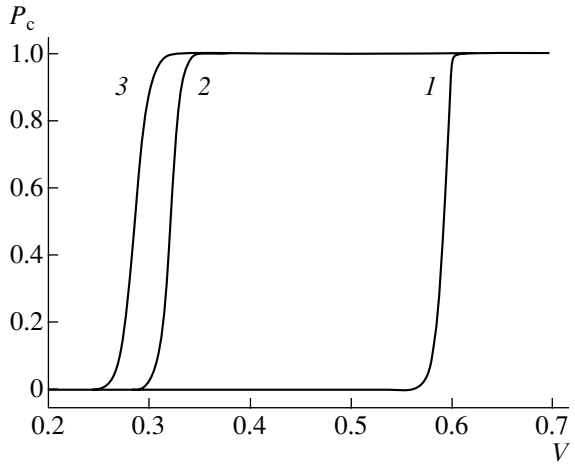

Fig. 3. Probability of the percolation cluster formation, P_c, vs. the fill V for grain lengths of (*1*) 2 and (*2*) 20 units. (*3*) Needles with the normal distribution of sizes from 4 to 40 units.

tial direction. The critical fraction V_c corresponding to the percolation threshold was estimated as 0.59, which agrees with the published data [8].

In the next experiment, the needles had a length of 20 units. No size distribution was specified in this case. The percolation fraction V_c turned out to be 0.35, which is appreciably lower than that for grains of length 2.

The effect of the needle size distribution was estimated by the example of the normal distribution with a peak at 20 and with the shortest and longest lengths of the needles equaling 4 and 40 units, respectively. In this case, the critical fill was equal to 0.32. The decrease in the critical value as compared with the single-mode case is consistent with data in [9].

Figure 2 shows the simulated 2D patterns for needles of (a) variable and (b) equal lengths. In both cases, the percolation cluster alone is depicted. The cluster made up of needles with different lengths is noticeably less dense than the cluster of equally long needles. Even visually, the pattern in Fig. 2a resembles Fig. 1 more closely than that in Fig. 2.

The formation probability of the percolation cluster, P_c, versus the fill V is shown in Fig. 3.

Thus, we argue that the rarefication of the cluster causes the reduction of V_c. On scales on the order of the needle length, the filling is no longer probabilistic, as in the classical site problem, and the spatial orientation of objects is of more significance in clustering.

In the 3D case, the value of V_c in the cubic lattice with grains without the preferential size was predicted to be 0.31 [6]. In a real experiment, the threshold value V_c equaled 0.19, which also indicates the significant effect of local anisotropy on the properties of the whole cluster.

CONCLUSIONS

Numerical simulations confirmed a considerable reduction of the fill required for the percolation cluster with anisotropic components to form. The spread of the size of the components (needles, in our case) also affects the percolation threshold.

It is also worth noting that even a more pronounced difference might be expected in the 3D case, since one more spatial coordinate is available for connecting the components in this case.

ACKNOWLEDGMENTS

This work was supported by the Russian Foundation for Basic Research (project no. 00-03-32481a).

REFERENCES

1. R. Kiffer and F. Benezovskiĭ, *Hard Materials* (Metallurgiya, Moscow, 1968).
2. W. Weimer, *Carbide, Nitride, and Boride Materials Synthesis and Processing* (Chapman and Hall, London, 1997), pp. 228–271.
3. Y. G. Gogotsi and R. A. Andrievski, *Materials Science of Carbides, Nitrides, and Borides* (Kluwer, Dordrecht, 1999), pp. 267–284.
4. V. A. Bunin, A. V. Karpov, and M. Yu. Senkovenko, Neorg. Mater. **38** (6), 1 (2002).
5. V. I. Odelevskiĭ, Zh. Tekh. Fiz. **21**, 678 (1951).
6. J. Feder, *Fractals* (Plenum, New York, 1988; Mir, Moscow, 1991).
7. B. Y. Taneoka, Y. Kaieda, and O. Odawara, in *Proceedings of the 32nd Japanese Congress on Material Research, 1989*, Vol. 32, pp. 164–167.
8. R. M. Ziff, Phys. Rev. Lett. **56**, 545 (1986).
9. A. Yu. Dovzhenko and P. V. Zhirkov, Zh. Tekh. Fiz. **65** (10), 201 (1995) [Tech. Phys. **40**, 1087 (1995)].

Translated by A. Sidorova

Technical Physics, Vol. 48, No. 8, 2003, pp. 1061–1066. Translated from Zhurnal Tekhnicheskoĭ Fiziki, Vol. 73, No. 8, 2003, pp. 126–131.

BRIEF COMMUNICATIONS

Feasibility of RF Plasma Heating in the Globus-M Spherical Tokamak at Frequencies above the Ion Cyclotron Frequency

V. V. D'yachenko, M. A. Irzak, E. N. Tregubova, and O. N. Shcherbinin

Ioffe Physicotechnical Institute, Russian Academy of Sciences, Politekhnicheskaya ul. 26, St. Petersburg, 194021 Russia

e-mail: o.shcherbinin@ioffe.ru

Received December 27, 2002

Abstract—Feasibility of rf plasma heating in the Globus-M spherical tokamak at frequencies several times higher than the ion cyclotron frequency is considered. Results from a numerical analysis of this problem by using one- and two-dimensional codes are presented. It is shown that, for the plasma parameters attainable in this device, the single-pass absorption of fast magnetosonic waves reaches 60%. The energy is released near the plasma axis. The radiation resistance of a one-loop antenna should be close to 1 Ω. The design of an antenna that allows one to match the rf oscillator to the load is described. The parameters of the antenna resonator required for optimum operation of the antenna are given. © *2003 MAIK "Nauka/Interperiodica".*

It is well known that the heating of the tokamak plasma requires applying auxiliary heating methods. Among those, the rf heating by fast magnetosonic (FMS) waves at the ion cyclotron frequencies seems to be most promising. However, the use of this method in spherical tokamaks encounters difficulties. The point is that the characteristic feature of spherical tokamaks (in view of their small aspect ratio) is that the magnetic field varies strongly along the magnetic field line as it passes from the outer to inner side of the plasma column (for the Globus-M tokamak [1] with R_0 = 36 cm and a_0 = 24 cm, the field varies more than fourfold). As a result, in the scenario of plasma heating at the cyclotron resonance of light ion minority (a classical experimental scenario), conditions for the cyclotron absorption of the wave at the fundamental and nearest harmonics for different ions in different regions of the vacuum chamber can simultaneously be satisfied. Figure 1a shows the positions of the resonances at the fundamental, second, and third harmonics for hydrogen and deuterium ions in the Globus-M cross section at a frequency of 11 MHz: (*1*) the fundamental resonance for deuterium, (*2*) the second-harmonic resonance for deuterium and the fundamental resonance for hydrogen, (*3*) the third-harmonic resonance for deuterium, (*4*) the second-harmonic resonance for hydrogen, and (*5*) the third-harmonic resonance for hydrogen. In calculations, it was assumed that the vacuum magnetic field at the axis was 0.5 T, the paramagnetic field at the axis was 0.23 T, and the poloidal field on the plasma surface was 0.21 T. The closed curves show the positions of the magnetic surfaces, which reflect the topology of the magnetic field in the tokamak. It can be seen that, in this heating scenario, some of the energy deposition regions are located near the chamber wall, which may reduce the heating efficiency.

A few years ago, in the paper by Ono (Princeton University, NJ) [2], it was proposed that plasma be heated at frequencies several times higher than the ion

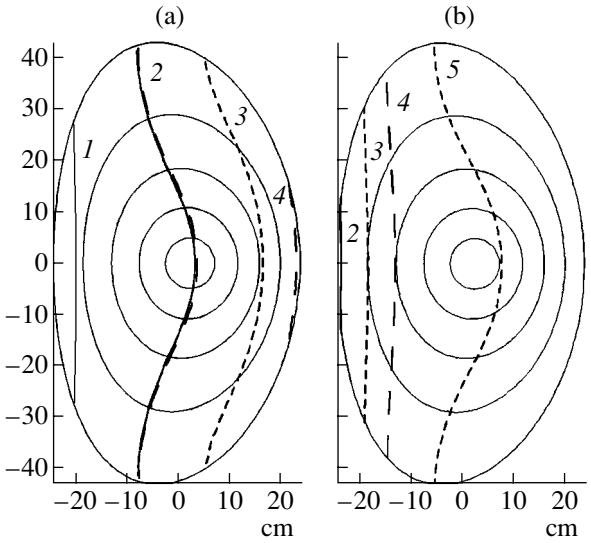

Fig. 1. Positions of the resonance surfaces in the cross section of the chamber of the Globus-M tokamak for f = (a) 11 and (b) 30 MHz: (*1*) fundamental resonance for deuterium, (*2*) second-harmonic resonance for deuterium and fundamental resonance for hydrogen, (*3*) third-harmonic resonance for deuterium, (*4*) second-harmonic resonance for hydrogen, and (*5*) third-harmonic resonance for hydrogen.

1063-7842/03/4808-1061$24.00 © 2003 MAIK "Nauka/Interperiodica"

cyclotron frequency. In this case, the resonances at low cyclotron harmonics shift toward the higher magnetic field and can even fall outside the chamber. Figure 1b shows the positions of the lower harmonics in the Globus-M cross section at a frequency of 30 MHz, which is chosen in subsequent calculations as a fundamental frequency. In this case, the absorption of FMS waves is provided by magnetic pumping and Landau damping. These mechanisms are not resonant in terms of the magnetic field, and their efficiency increases with increasing plasma density and temperature. Of course, the resonances at the higher (than third) harmonics of the ion cyclotron frequencies will be present in the plasma in this case too; however, estimates made in the geometric-optics approximation show that the wave absorption at these harmonics will be of minor importance. The subsequent calculations are performed for a purely deuterium plasma; in this case, there are no resonances at lower harmonics inside the plasma.

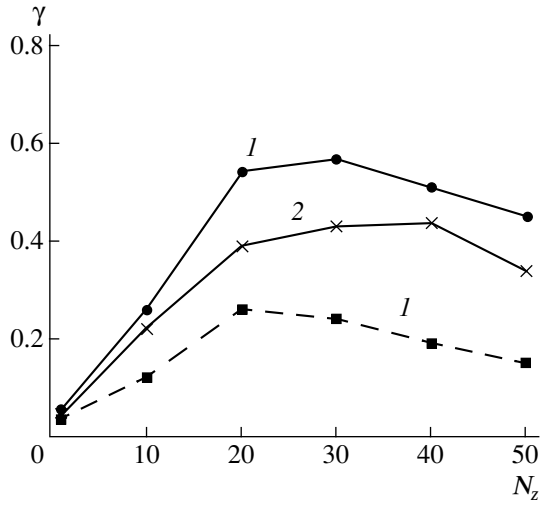

Fig. 2. Efficiency γ of single-pass absorption of FMS waves in the plasma of the Globus-M tokamak for B_0 = 0.56 T, T_{e0} = 500 eV, T_{i0} = 200 eV, and f = (*1*) 30 and (*2*) 20 MHz. The plasma density at the axis is 10^{20} (solid curves) and 5×10^{19} m^{-3} (dashed curve).

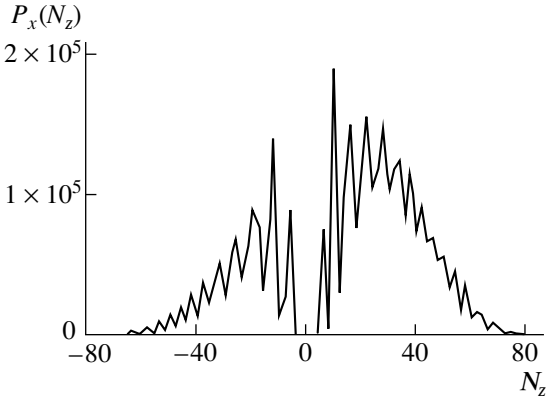

Fig. 3. Spectrum of waves excited by a one-loop antenna for $n_0 = 10^{20}$ m^{-3} at a frequency of 30 MHz.

The wave absorption efficiency was examined by using a one-dimensional code that was elaborated in the Ioffe Physicotechnical Institute of the Russian Academy of Sciences. This code describes the propagation of FMS waves with allowance for cyclotron absorption, Landau damping, and magnetic pumping [3]. Calculations were performed in cylindrical geometry, which corresponded to a tokamak with an infinite elongation, but the radial dependences of all the parameters were similar to their real dependences in the equatorial plane of the Globus-M tokamak. The rf fields are represented as a sum of the toroidal and poloidal modes. All modes in this model are decoupled and are calculated independently. This model adequately describes wave absorption in the plasma core and at the outer and inner plasma edges; however, it does not take into account the effects related to the poloidal inhomogeneity and the processes occurring at the upper and lower sides of the plasma column. Another disadvantage of this model is that the role of the axial region is overestimated, because, unlike the actual device, all the waves pass through the plasma layer with the parameters characteristic of the axial region.

Figure 2 shows the single-pass absorption efficiency γ of FMS waves at frequencies of (*1*) 30 and (*2*) 20 MHz as a function of the longitudinal (along the toroid axis) refractive index N_z. The central plasma density was taken to be 10^{20} m^{-3} (solid curves) and 5×10^{19} m^{-3} (dashed curves). The other plasma parameters were the following: B_0 = 0.56 T, T_{e0} = 500 eV, T_{i0} = 200 V, and I_p = 300 kA. These parameters are close to the limiting experimental parameters. The value of N_z was taken at the outer plasma boundary, where the antenna was located. It can be seen that the absorption efficiency reaches its maximum value of nearly 60% for $N_z \approx 30$. As the longitudinal refractive index increases further, the efficiency decreases because the cutoff plane for FMS waves appears near the far wall and then approaches the near wall, thereby restricting the wave propagation region. It should be remembered that these results refer only to a plasma with definite dimensions and parameters attainable in the Globus-M device.

Figure 3 shows the calculated spectrum of the waves excited by a one-loop antenna of reasonable dimensions, which can be inserted into the chamber through one of the available ports (the antenna design is shown schematically in Fig. 7). The spectrum contains several peaks that arise due to wave reflection from both the far wall of the chamber and the cutoff zones. The absence of the radiation symmetry in the toroidal direction is explained by the fact that the magnetic field lines are inclined at a rather large angle (up to 40°) at the periphery of the plasma column. This effect is of interest because it offers an opportunity to excite plasma currents by rf waves. The antenna radiation resistance calculated in the one-dimensional model is about 1 Ω.

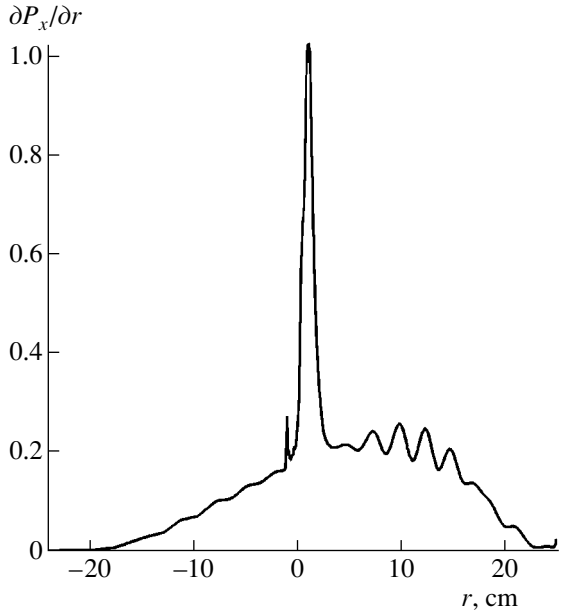

Fig. 4. Energy deposition profile at B_0 = 0.68 T, T_{e0} = 500 eV, and T_{i0} = 200 eV (calculations by the one-dimensional code).

Figure 4 shows the profile of energy deposited by FMS waves. The smooth part of this curve is explained by nonresonant mechanisms such as magnetic pumping and Landau damping. The sharp peak near the discharge axis corresponds to the resonant absorption at the second harmonic of hydrogen. This peak appeared because, in this case, we took into account the presence of residual hydrogen in the chamber (up to 2%). The fraction of the absorbed energy associated with the resonance mechanism depends on the amount of the residual hydrogen and, in the case at hand, is small (nearly 15%). For the given curve, the magnetic field on the axis was increased by 30% for the energy deposition maximum to be located at the chamber axis. For the standard magnetic field, this peak can also be present, but it lies in the inner half of the diameter.

In order to more accurately calculate the wave propagation and absorption in plasma, we developed a two-dimensional code that describes the behavior of waves in the real toroidal geometry (similar to calculations performed in [4]). In this case, because of the poloidal inhomogeneity of the plasma, all the poloidal modes (m) are coupled and the electric fields of the toroidal modes (n) are represented in the form

$$\mathbf{E}_n(\rho, \vartheta, \varphi) = e^{in\varphi}\sum_m e^{im\vartheta}\mathbf{E}(\rho).$$

Here, ρ is the flux coordinate and ϑ and φ are the poloidal and toroidal angles, respectively. After the toroidal modes are found, the total field can be reconstructed at every point in the plasma. At present, the program includes all of the main absorption mechanisms (in

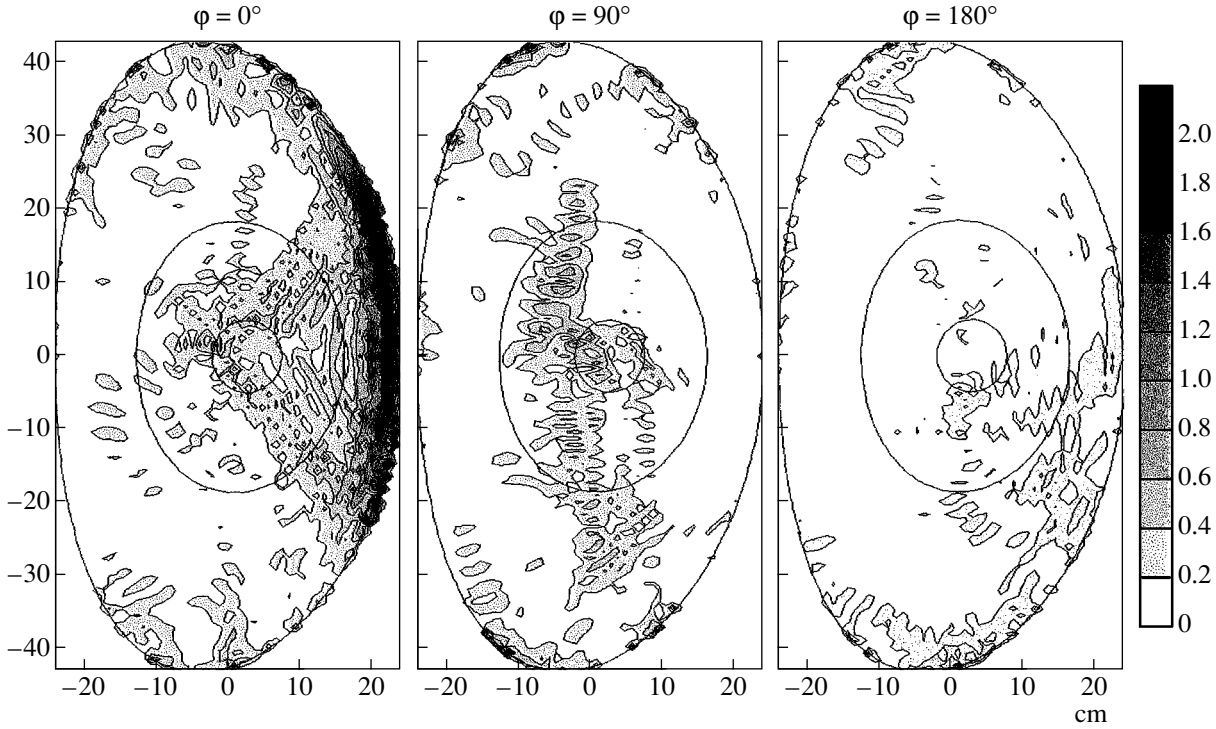

Fig. 5. Two-dimensional distribution of the total rf field in three sections of the Globus-M tokamak at different toroidal angles φ = 0°, 90°, and 180°. The darker regions correspond to the higher field amplitude.

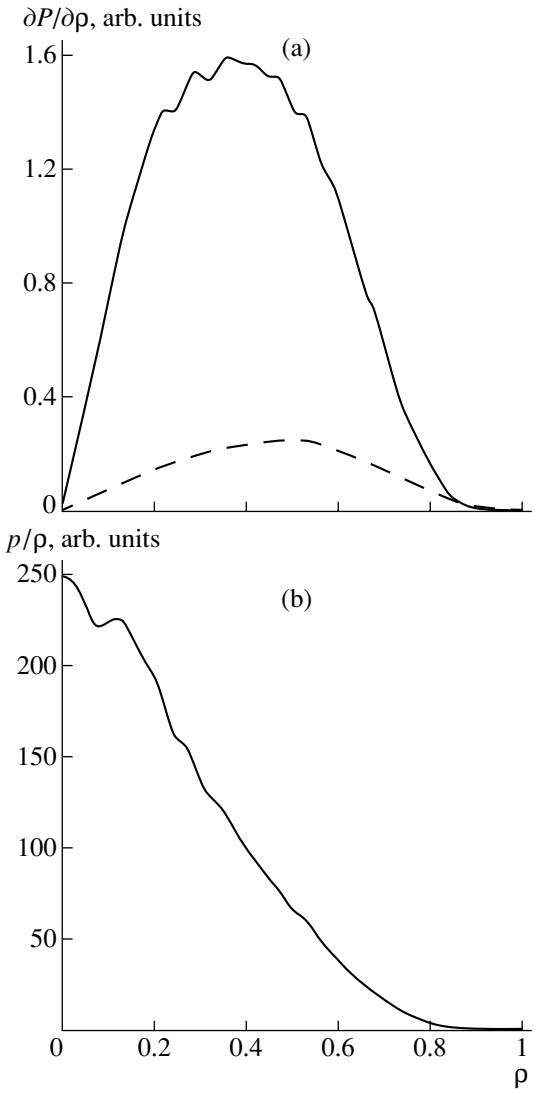

Fig. 6. (a) Energy deposition profile and (b) specific energy absorption calculated by the two-dimensional code.

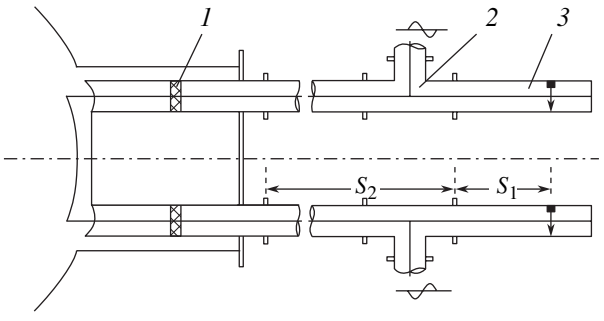

Fig. 7. Schematic of the one-loop antenna: (*1*) vacuum transition, (*2*) T-branch, and (*3*) stub.

addition to the cyclotron mechanism) such as collisions, magnetic pumping, and Landau damping.

Two-dimensional simulations of the FMS wave propagation were performed for B_0 = 0.56 T, T_{e0} = 500 eV, T_{i0} = 200 eV, I_p = 300 kA, and $n_{e0} = 10^{20}$ m^{-3}. The data on the Shafranov shift (Δ_0 = 2.8 cm), elongation (λ_0 = 1.8), and triangularity (γ_0 = 0.16) were taken from calculations by the equilibrium code. It was assumed that the tangential components of the rf electric field on the inner surface of the chamber (except for the antenna port) were zero. At the outlet from the antenna port, we assumed a certain distribution of the poloidal electric field, which simulated the antenna operation.

Figure 5 shows the distribution of the total rf electric field averaged over the oscillation period and integrated over the entire emitted spectrum in three cross sections of the Globus-M tokamak: in the cross section φ = 0, in which the antenna is situated; in the cross section displaced by a quarter of a turn in the toroidal direction from the antenna (φ = 90°); and in the cross section opposite to the antenna port (φ = 180°). The shades of gray reflect the field amplitude in these cross sections (the darker regions correspond to the higher field amplitude). It can be seen that the rf field is concentrated in the antenna cross section and are markedly weaker on the opposite side of the torus. Figure 6a shows the energy deposition profile ($\partial P/\partial\rho$) integrated over the magnetic surface as a function of the flux coordinate ρ. The solid and dashed curves show the energy deposited due to magnetic pumping and Landau damping, respectively. It can be seen that energy is primarily deposited at the middle of the radius. Figure 6b shows the profile of energy deposited in unit volume, i.e., the specific absorption averaged over the magnetic surface. It can be seen that, for the given plasma parameters, the maximum absorption efficiency is reached at the center of the plasma.

A schematic of the one-loop antenna that was used to excite FMS waves in plasma is shown in Fig. 7. The vacuum part of the antenna is separated from its other components by a vacuum transition (*1*). A Faraday screen that protects the antenna emitter from the plasma is not shown in the figure. To match the rf oscillator to the plasma at such a low radiation resistance ($R_c \approx 1\ \Omega$), we used a coaxial resonator consisting of the antenna itself and external coaxial elements: T-branches (*2*) and coaxial stubs (*3*). RF power from the oscillator is fed to the antenna through two lines connected to the resonator via T-branches. When the resonator is optimally tuned (by properly choosing the field frequency and the length of shorting stubs), its length is equal to the wavelength of the rf field. In this case, the voltage node and the current antinode are located at the middle of the antenna emitter, the output resistance at the terminal of the transmission lines is 50 Ω, and the rf oscillator is matched to the load.

At a constant input power, different values of R_c correspond to different maximum voltages in the resonator. Table 1 presents the results of calculations for an input power of 50 kW in each channel. It can be seen that, at small R_c values, the resonator voltage becomes

Table 1

f, P_c per one channel	R_c per one channel, Ω	U_{max}, kV
23 MHz	0.1	50
50 kW	0.2	35
	0.3	29
	0.5	22.5
	1.0	16

Table 2

f, P_c, R_c	C, nF	S_2, cm	Q	U_{max}, kV
23 MHz	0.2	530	100	17.5
50 kW	0.4	500	56	12.7
0.5 Ω	0.5	480	40	10.3
	0.7	390	19	5.9
	1.0	20	17	3.5

unacceptably high, especially when the input power increases to 200 kW in each channel (the value planned for the experiment).

To decrease the maximum voltage in the resonator, it was decided to install a special duct capacitor at the vacuum transition (Fig. 7, item *1*). Simultaneously, both the resonator size (S_2) and its Q-factor (Q) increase, which is favorable from the experimental standpoint. The influence of such a capacitor on the listed parameters can be clearly seen from the data presented in Table 2 for a constant input power and a radiation resistance of 0.5 Ω per one channel.

Figure 8 shows the voltage distribution in the antenna resonator for three values of the duct capacitance and $R_c = 0.5$ Ω. The dashed line shows the voltage distribution inside the stub. The resonator length is counted from the emitting conductor. It is seen that, for $C = 1$ nF, the maximum voltage inside the resonator is reduced to a reasonable level and the length of the external part of the resonator together with the stub does not exceed 2 m.

Then, the tuning curves of the antenna resonator were calculated as functions of the antenna radiation resistance (per one channel) at a constant duct capacitance ($C = 0.95$ nF) for the case of the optimum matching of the transmission lines to the antenna load (Fig. 9). The upper curve in Fig. 9 shows the position of the shorting stub (S_1), the next curve shows the resonance frequency, and the lower curve shows the Q-factor of the resonator. It follows from these curves that, when there is a strong coupling between the antenna and the plasma (i.e., at high values of R_c), small detunings of the stub position or the rf oscillator frequency

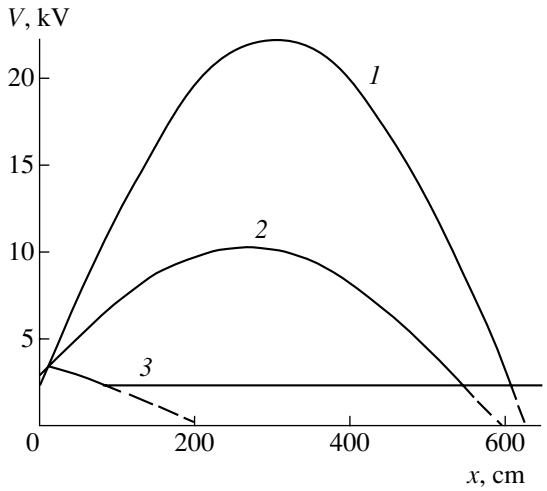

Fig. 8. Distribution of the voltage in the antenna resonator for $R_c = 0.5$ Ω, $P_1 = 50$ kW, and three values of the duct capacitance C = (*1*) 0.01, (*2*) 0.5, and (*3*) 1.0 nF.

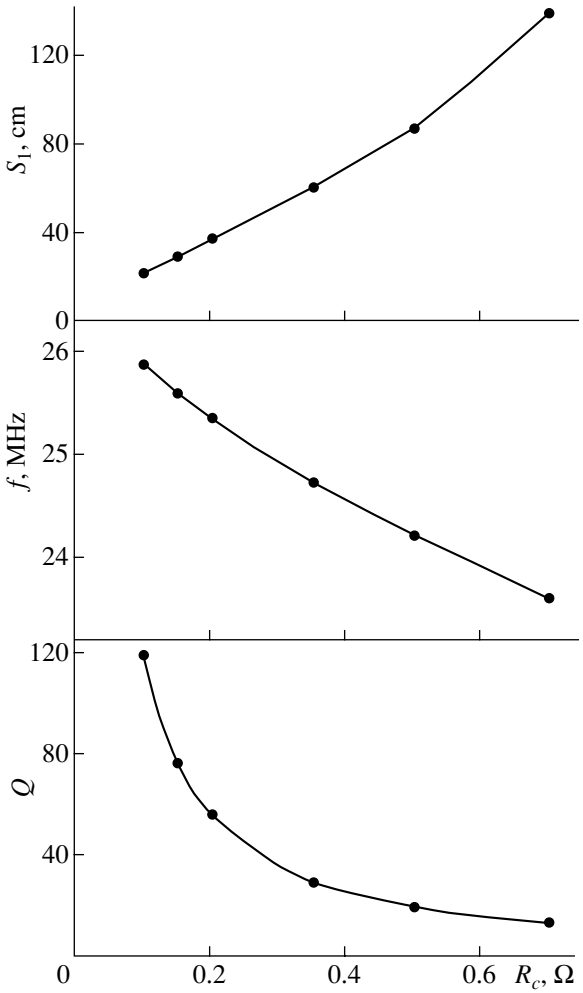

Fig. 9. Tuning curves of the antenna resonator as functions of the antenna radiation resistance.

from their optimum values should not cause overvoltages in the components of the antenna transmission line.

Therefore, we have shown that experiments on plasma heating in the Globus-M tokamak at frequencies far above the cyclotron frequency are quite feasible.

ACKNOWLEDGMENTS

We thank V.K. Gusev for supporting this work. This study was supported in part by the Russian Foundation for Basic Research, project no. 01-02-17924.

REFERENCES

1. V. K. Gusev, V. E. Golant, E. Z. Gusakov, *et al.*, Zh. Tekh. Fiz. **69** (9), 58 (1999) [Tech. Phys. **44**, 1054 (1999)].
2. M. Ono, Phys. Plasmas **2**, 4075 (1995).
3. M. A. Irzak, E. N. Tregubova, and O. N. Shcherbinin, Fiz. Plazmy **25**, 659 (1999) [Plasma Phys. Rep. **25**, 601 (1999)].
4. M. Brambilla, Preprint No. IPP5/66 (Max-Planck Institut für Plasmaphysik, Garching, 1996).

Translated by N. Larionova

Technical Physics, Vol. 48, No. 8, 2003, pp. 1067–1070. Translated from Zhurnal Tekhnicheskoĭ Fiziki, Vol. 73, No. 8, 2003, pp. 132–135.

BRIEF COMMUNICATIONS

Targets for Studying the Dynamic and Radiative Properties of Material with Laser Facilities

V. A. Pronin, V. N. Gornov, A. V. Lipin, and I. L. Svyatov

Zababakhin All-Russia Research Institute of Technical Physics, Russian Federal Nuclear Center, Snezhinsk, Chelyabinsk oblast, 456670 Russia

e-mail: c 5@five.ch70.chel.su

Received January 14, 2003

Abstract—The technology of target preparation for direct and indirect laser irradiation is developed to study the shock compressibility of materials on the Sokol-2 and Iskra-5 laser facilities. Copper and aluminum films with a density close to that of the bulk materials are prepared by ion-beam deposition. The difference in the densities of the film and bulk materials is 0.8–1.7%, and the accuracy of density measurement is 0.4–1.5%. Processes for the preparation of porous materials (aluminum, copper, nickel, gold, etc.) are also devised. Porous copper samples of thickness 10–50 μm, pore size 0.1–5.0 μm, mean density 0.065–0.4 g/cm^3, and porosity 20–140 are obtained. The preparation of freely suspended film targets 0.1–0.2 μm thick that are irradiated by picosecond laser shots on the Progress-P and Élas-PS facilities is described. © *2003 MAIK "Nauka/Interperiodica".*

INTRODUCTION

High-power laser equipment for investigating material properties under high pressure and temperatures is being used to an increasing extent [1, 2].

Difficulties in preparing targets for measuring shock compressibility arise when the experiment requires the accuracy to be better than 1%. Today, the targets are usually made accurate to 2% [2].

Of great interest are experiments on studying the compressibility of ultraporous materials of initial density 0.05–0.10 g/cm^3 or porosity p = 10–100. However, the production of ultraporous metals with $p \le 100$ is a great technological and experimental challenge; therefore, the experiments were carried out with metals with $p \le 20$ [3].

The application of femtosecond laser pulses to the target material opens up fresh opportunities for the study of material–radiation interaction. It has been found that the most promising targets are those made of nanostructured porous materials in the form of freely suspended thin films that have a mean density 2–100 times lower than the density of the bulk material [4].

Our goal was to prepare ultraporous metallic targets for the investigation of the dynamic and radiation properties of materials under high pressures and temperatures on laser facilities.

TARGETS FOR STUDYING SHOCK COMPRESSIBILITY

Experiments on studying the shock compressibility of materials on laser facilities are carried out by directly irradiating the samples or by using hohlraums of different design. In the former case, targets have the form of steps 50 to 150 μm distant from each other that are made from 10- to 30-μm-thick films of reference and test materials [2].

Since such targets are usually prepared by vacuum evaporation, it is difficult to obtain metal films of density close to that of the bulk material. When a metal condenses on a substrate, the resulting film takes on a columnar structure, which persists throughout the deposition process. As a result, the film has voids and its density differs from the density of the bulk material (sometimes by 5–10%) [5]. Furthermore, films 5–30 μm thick possess strains, which cause the films to shrink and peel off.

To produce denser films with a more regular structure and higher adhesion to the substrate, we suggested the use of ion-beam deposition methods, such as electron-beam evaporation and magnetron sputtering [6], to obtain aluminum, copper, tungsten, nickel, titanium, and zirconium films of thickness ranging from 5 to 30 μm.

The condensation of the metals on the substrate was accomplished at temperatures of 150–200°C and bias potentials of 40–200 V. Such conditions proved to be optimal [7–9]. The table lists the process parameters and the parameters of the copper and aluminum films grown by vacuum evaporation and magnetron sputtering. These process conditions were used to prepare targets in shock compressibility experiments performed on the Sokol-2 (All-Russia Research Institute of Technical Physics, Snezhinsk, Russia) and Iskra-5 (All-Russia Research Institute of Experimental Physics, Sarov, Russia) facilities. The design of the target for indirect irradiation is shown in Fig. 1.

1063-7842/03/4808-1067$24.00

Measured and calculated parameters of the films deposited

Material	m, mg	$\pm\Delta m$, mg	δm, %	l, μm	$\pm\Delta l$, μm	δl, %	δv, %	ρ, g/cm^3	ρ_0, g/cm^3	$\pm\delta\rho$, %	$1-\frac{\rho}{\rho_0}$, %	V, μm/h	T, °C	U, V
Aluminum; vacuum evaporation	13.6	0.08	0.59	16.11	0.07	0.43	0.94	2.68	2.69	1.1	0.4	20	150	100
Aluminum; magnetron sputtering	2.72	0.03	0.4	8.8	0.08	0.9	1.0	2.65		1.7	0.5	2.5	20	60
Copper; vacuum evaporation	17.3	0.04	0.23	6.2	0.1	1.6	1.62	8.82	8.96	1.64	1.5	6	200	150
Copper; magnetron sputtering	14.5	0.1	0.69	26.3	0.08	0.3	0.43	8.84		0.8	0.9	3.8	20	40

Note: m and l are the weight and thickness of the film, respectively; ρ is the density of the porous material; ρ_0 is the density of the continuous (bulk) material [10]; Δm and Δl are the absolute errors in measuring the weight and thickness of the films; δm, δl, δv, and $\delta\rho$ are the relative errors in measuring the weight, thickness, volume, and density of the films ($\delta v = \sqrt{2\delta r^2 + \delta l^2}$, $\delta\rho = \sqrt{\delta m^2 + \delta v^2}$, where δr is the relative error in measuring the radius of the films); $1 - \rho/\rho_0$ is the difference between the densities of the film and bulk materials; U is the bias potential applied to the sample; T is the sample temperature; and V is the rate of condensation.

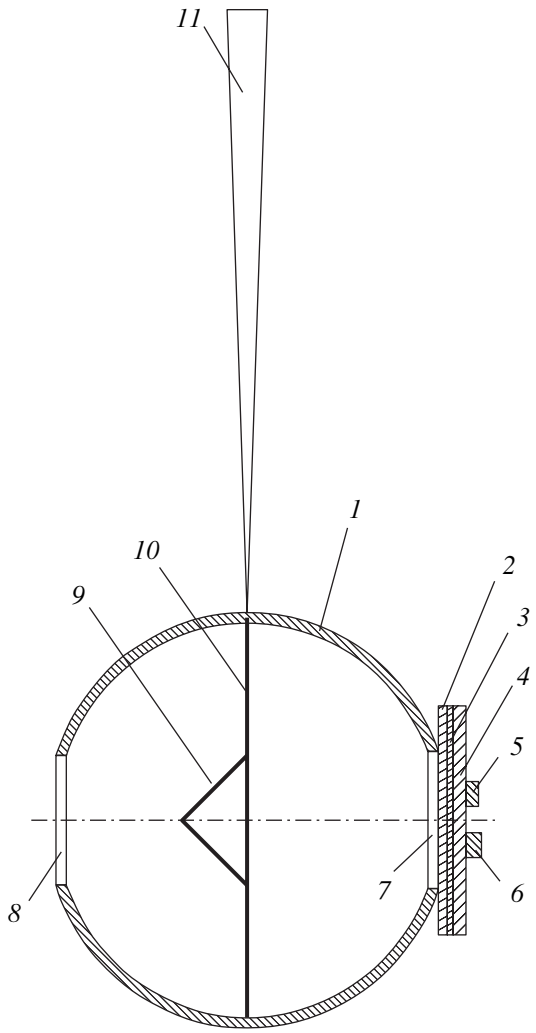

Fig. 1. Target used in shock compressibility experiments on the Sokol-2 and Iskra-5 facilities: (*1*) 40-μm-thick converter (gold film of diameter 1000 μm), (*2*) aluminum film 3 μm thick, (*3*) tungsten, (*4*) aluminum film 10 μm thick, (*5*) test sample made of copper film 6.8 μm thick, (*6*) reference sample (aluminum film 10.7 μm thick), (*7*) diagnostic opening of diameter 360 μm, (*8*) laser beam opening of diameter 350 μm, (*9*) cone with a base diameter of 500 μm made of 30-μm-thick gold film, (*10*) polymer film, and (*11*) suspension.

POROUS METAL TARGETS AND FREELY SUSPENDED THIN-FILM TARGETS

The process of porous metal production was accommodated to making laser targets with the following parameters: the step thickness is 10–30 μm; the pore (cell) size, 0.1–5.0 μm; and the porosity (the ratio of the bulk and film material densities), 5–100. The step size and spacing were the same as in shock compressibility experiments with normal (nonporous) materials.

The production of porous metals was considered in [10–12]. We designed and created a setup that is similar to that described in [12].

Porous metal films were prepared by the thermal evaporation of metals in an inert gas at pressures between 0.3 and 3.0 mm Hg. Under appropriate conditions, particles (mostly spherical) appearing in the evaporation zone condense as clusters, forming a porous structure.

The process of porous metal film production was carried out at different temperatures with rates of evaporation in the interval 1–5 mg/s and inert gas pressures in the chamber varying from 0.3 and 3.0 mm Hg. The inert gases were argon and nitrogen; the metals evapo-

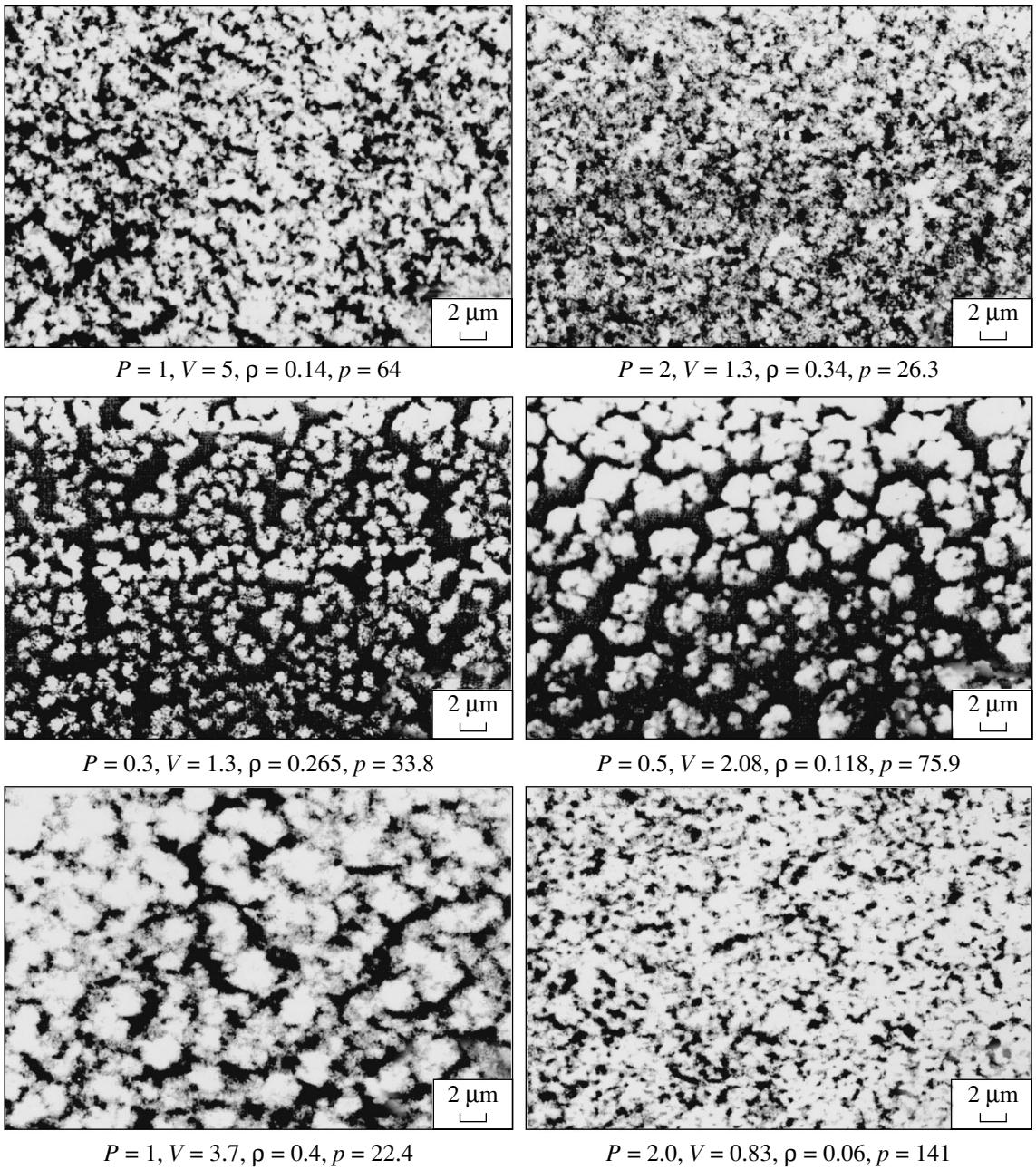

Fig. 2. Surface structure of the porous copper films. ρ, mean density of the porous copper (g/cm^3); *p*, porosity; *P*, argon pressure in the chamber (mm Hg); and *V*, rate of copper evaporation (mg/s).

rated were copper, nickel, and aluminum. The mean density of the films was determined by measuring the weight and thickness of the sample deposited. The weight was found with an analytical balance to the nearest 0.1 mg. The thickness was measured in an optical microscope equipped with a specially designed sensor that has a scale division of 0.3–0.5 μm. The thickness and weight of the films deposited on the sensor was selected in such a way that the mean density was measured accurate to 2%. The porosity was determined as the ratio of the bulk copper density 8.96 g/cm^3 to the mean density of the porous (film) copper. The structure and pore size of the metal film deposited were examined in an RÉM-200 scanning electron microscope. The micrographs taken from the surface of the porous metal films are presented in Fig. 2.

We prepared freely suspended thin-film targets to study the spectral coefficients of X-ray absorption under high pressures and temperatures. Specifically, 0.2- to 0.3-μm-thick freely suspended aluminum films were used as targets irradiated by picosecond laser

shots in experiments performed on the Progress-P and Élas-PS facilities.

CONCLUSIONS

The technology of target preparation for direct and indirect laser irradiation is developed to study the shock compressibility of materials on the Sokol-2 and Iskra-5 laser facilities.

It is suggested that copper and aluminum films with a density close to that of the bulk materials be prepared by ion-beam deposition. The difference in the densities of the film and bulk materials turned out to be 0.8–1.7%, and the accuracy of density measurement is 0.4–1.5%. Porous copper samples of thickness 10–50 μm, pore size 0.1–5.0 μm, mean density 0.065–0.4 g/cm^3, and porosity 20–140 are obtained.

Freely suspended aluminum films 0.1–0.2 μm thick that were used as targets irradiated by picosecond laser shots on the Progress-P and Élas-PS facilities are prepared.

REFERENCES

1. G. W. Collins, K. S. Budil, *et al.*, Phys. Rev. Lett. **78**, 483 (1997).
2. S. D. Rothman, E. M. Evans, R. T. Eagleton, *et al.*, Int. J. Impact Eng. **23**, 803 (1999).
3. V. K. Gryaznov, R. F. Trunin, *et al.*, Zh. Éksp. Teor. Fiz. **114**, 1242 (1998) [JETP **87**, 678 (1998)].
4. V. M. Gordienko and A. B. Savel'ev, Usp. Fiz. Nauk **169**, 78 (1999) [Phys. Usp. **42**, 72 (1999)].
5. L. S. Palatnik and P. G. Chernetskiĭ, *Voids in Films* (Énergoizdat, Moscow, 1982).
6. G. F. Ivanovskiĭ and V. I. Petrov, *Ion–Plasma Processing of Materials* (Radio i Svyaz', Moscow, 1986).
7. *Sputtering by Particle Bombardment*, Ed. by R. Behrisch (Springer-Verlag, New York, 1991; Mir, Moscow, 1998), Vol. 3.
8. L. S. Palatnik, M. Ya. Fuks, and V. M. Kosevich, *Formation Mechanisms and Substructure of Condensed Films* (Nauka, Moscow, 1972).
9. *Physical Quantities: A Handbook*, Ed. by I. S. Grigor'ev and E. Z. Meĭlikhov (Énergoatomizdat, Moscow, 1991).
10. L. Harris, D. Jeffris, *et al.*, J. Appl. Phys. **10**, 791 (1948).
11. M. Ya. Gen, M. S. Ziskin, and Yu. N. Petrov, Dokl. Akad. Nauk SSSR **127**, 366 (1959).
12. C. G. Gragvist and R. A. Buhrman, J. Appl. Phys. **47**, 2200 (1976).

Translated by V. Isaakyan

Technical Physics, Vol. 48, No. 8, 2003, pp. 1071–1073. Translated from Zhurnal Tekhnicheskoĭ Fiziki, Vol. 73, No. 8, 2003, pp. 136–138.

BRIEF COMMUNICATIONS

Superconducting Films with T_c = 39 K Prepared from Stoichiometric MgB_2 Targets

S. I. Krasnosvobodtsev, A. V. Varlashkin, N. P. Shabanova, and A. I. Golovashkin

Lebedev Physics Institute, Russian Academy of Sciences, Leninskiĭ pr. 53, Moscow, 119991 Russia

e-mail: varlash@sci.lebedev.ru

Received January 28, 2003

Abstract—Oriented films of MgB_2 high-T_c superconductor are synthesized by pulsed laser sputtering of stoichiometric MgB_2 targets with subsequent annealing of the amorphous Mg–B material deposited onto MgO(111) substrates. The critical temperature of the films depends on the purity of the targets sputtered. The purification of boron powder in a vacuum makes it possible to minimize the content of impurities in the targets and to prepare MgB_2 films exhibiting a critical temperature above 39 K and a sharp inductive transition. A high room-temperature to residual resistivity ratio (more than 3) indicates the good quality of the films.

INTRODUCTION

Since the discovery of superconductivity in MgB_2 [1], which has the highest critical temperature (about 40 K) among oxygen-free superconductors, the preparation of high-quality films of this compound for basic research and applications has been a most topical problem. The synthesys of MgB_2 films encounters serious difficulties, such as the high oxidizability of Mg and its high volatility as compared to boron at high temperatures. To avoid the contamination of the films by oxygen, it is necessary to use high-vacuum equipment and high-purity materials for film evaporation. A desired Mg content is provided by annealing as-deposited amorphous B or Mg–B films in a closed space [2–9]. The loss of Mg is also minimized if superconducting MgB_2 films are grown immediately during deposition at a significantly lower temperature as compared to the synthesis of bulk materials [9–12]. However, a significant decrease in the temperature hinders crystallization, which adversely affects the superconducting properties of the films. In [13], high-quality MgB_2 films were prepared by the decomposition of boron hydrides [13]. A high temperature of the substrate and a high pressure of the Mg vapor over its surface were provided by maintaining a high (almost atmospheric) pressure of the buffer gas during deposition. Obviously, such a high pressure cannot be used for growing films by pulsed laser evaporation, cathode sputtering, electron-beam (or thermal) evaporation, and other methods in common use.

Thus, the general trend in searching for optimum conditions for synthesizing MgB_2 films by the methods noted above is obvious (a high pressure and temperature of deposition). However, this trend gives rise to a large number of challenges to be overcome. As was mentioned above, one is related to the necessity of using high-purity targets for pulsed laser sputtering.

In this work, we discuss the conditions for synthesizing MgB_2 films by the pulsed laser sputtering of MgB_2 targets followed by heat treatment in the Mg vapor.

EXPERIMENTAL RESULTS

For evaporation, we applied a solid-state laser with a wavelength of 1.06 μm, a pulse duration of 10 ns, and a repetition rate of 30 Hz. The energy density of the laser radiation on the target was 30 J/cm^2. We used both direct evaporation and a two-beam scheme [14]. The process was carried out in a vacuum chamber at a residual pressure of 10^{-8} torr. The critical temperature of the films was measured by the conventional dc four-probe method, and the uniformity of their superconducting properties was judged by measuring the ac magnetic susceptibility. An X-ray diffractometer was used for structural analysis.

It was already noted that the two-stage method of preparing MgB_2 films consists in the deposition of B or Mg–B amorphous films followed by heat treatment in the Mg vapor. As follows from published data, MgB_2 films synthesized by annealing amorphous B films have a higher quality than those prepared from Mg–B amorphous films. In particular, the critical temperature of the latter films is about two degrees lower. However, for the production of MgB_2 films of fairly high quality in one cycle (without additional heat treatment), the use of stoichiometric targets seems to be more promising.

Our experiments showed that the main cause of reducing the critical temperature of the final films synthesized from Mg–B amorphous films is the contamination of the latter by impurities from the target.

1063-7842/03/4808-1071$24.00 © 2003 MAIK "Nauka/Interperiodica"

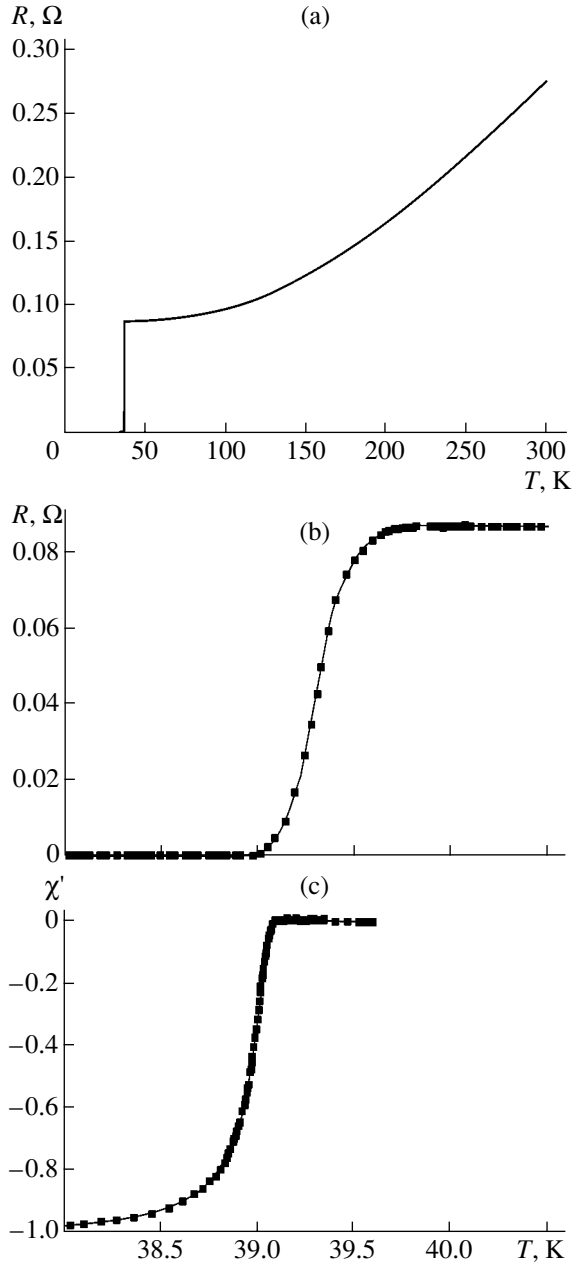

Fig. 1. (a) Superconducting and transport properties of the MgB_2 film grown on the Mg(111) substrate, (b) the temperature dependence of the resistance, and (c) the superconducting transition (the temperature dependence of the ac magnetic susceptibility).

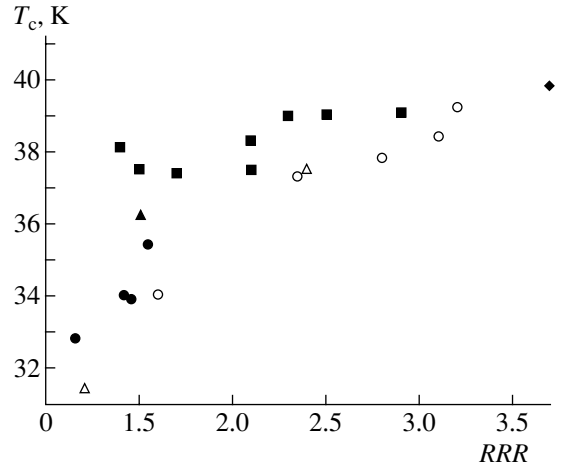

Fig. 2. Correlation between the critical temperature T_c and the residual resistivity ratio (*RRR*) for MgB_2 films grown on the Al_2O_3 (filled symbols) and MgO (open symbols) substrates. (○) and (●) our results, (■) data from [2, 8], (△) and (▲) data from [9], and (◆) data from [13].

The films were deposited onto MgO(100) and MgO (111) single-crystalline substrates at room temperature in a vacuum. For heat treatment, the films with Mg (99.9%) fragments were placed in niobium capsules. Annealing was performed in sealed quartz ampoules in the Ar atmosphere at 900°C for 15–60 min. When the targets were prepared from Alfa Aesar MgB_2 powder with boron (99.9%) powder as a binder, the pressure during the deposition rose to 10^{-5} torr. The critical temperature of such films after heat treatment was 33–34 K, and the residual resistivity ratio (*RRR*) varied from 1 to 1.5 although the widths of the inductive and resistive transitions (ΔT_c) did not exceed 1 K. Targets fabricated by the standard procedure from boron (99.9%) allowed us to perform sputtering at a pressure of 5×10^{-6} torr. The critical temperature of the films increased to 37 K; *RRR*, to 2.5. To further improve the target purity, the boron powder was purified in a vacuum and the targets were heated in a high vacuum before the last heat treatment in the Mg vapor. When sputtering these targets, we managed to deposit an Mg–B amorphous film at a pressure of 4×10^{-7} torr and then reproducibly fabricate MgB_2 films with $T_c > 30$ K by annealing. Figures 1a and 1b show the temperature dependence of the resistivity and the curve of the superconducting transition for a 1000-Å-thick film on the MgO(111) substrate. The transition is complete at $T =$ 39 K. Its width is $\Delta T_c = 0.4$ K. The *RRR* value for this film was 3.2. For films of such a thickness, the transition determined from the magnetic susceptibility curve was rather sharp (Fig. 1c).

X-ray diffraction data showed that the film grown on MgO(111) had a clear-cut texture with the *c* axis normal to the substrate surface: only (000*l*) reflections were present in the θ–2θ X-ray diffraction pattern.

Our results and analysis of published data let us conclude that the fabrication of high-T_c MgB_2 films imposed severe constraints on the process purity. The purity of the target is also very important. However, the purity alone is insufficient. The temperature conditions of synthesis (in the one-stage process, the relation between the temperature and buffer gas pressure), as well as the material and orientation of the substrate, are also of significance. The substrate parameters often have a decisive effect on the concentration of defects in

the films. Figure 2 shows the correlation between the critical temperature and the *RRR* value for MgB_2 films grown on Al_2O_3 $(1\bar{1}02)$ and Al_2O_3 (0001) substrates and on MgO (100) and MgO (111) substrates. Note that, at the same critical temperature, the *RRR* values for the films on sapphire are significantly lower than those films on magnesium oxide. We believe that this fact cannot be explained by the measurement error or the differences in the film synthesis conditions. The lower *RRR* value for the MgB_2 films grown on sapphire is likely to be due to the effect of the substrate, namely, the chemical interaction between Mg and Al_2O_3 [13, 15] and the quality of grain boundaries.

Thus, we succeeded in solving the problem of contamination of MgB_2 films synthesized in two stages from bulk MgB_2 targets. Oriented films with a critical temperature above 39 K and a high residual resistivity ratio (*RRR*) were grown on MgO (111) substrates. This result offers possibilities for growing MgB_2 films by pulsed laser sputtering in one cycle without additional heat treatment.

ACKNOWLEDGMENTS

This work was supported by the Russian Foundation for Basic Research (grant no. 02-02-17353) and the state contract "Controllable Superconductivity" (contract no. 40.0121.1.11.46).

REFERENCES

1. J. Nagamatsu, N. Nakagava, T. Muranaka, *et al.*, Nature **410**, 63 (2001).
2. W. N. Kang, H.-J. Kim, E.-M. Choi, *et al.*, Science **292**, 1521 (2001).
3. C. B. Eom, M. K. Lee, J. H. Choi, *et al.*, Nature **411**, 558 (2001).
4. M. Paranthaman, C. Cantoni, H. Y. Zhai, *et al.*, Appl. Phys. Lett. **78**, 3669 (2001).
5. S. H. Moon, J. H. Yun, H. N. Lee, *et al.*, Appl. Phys. Lett. **79**, 2429 (2001).
6. H. Y. Zhai, H. M. Christen, L. Zhang, *et al.*, J. Mater. Res. **16**, 2759 (2001).
7. A. Plecenik, L. Satrapinsky, P. Kus, *et al.*, cond-mat/0105612.
8. W. N. Kang, E.-M. Choi, H.-J. Kim, *et al.*, cond-mat/0209226.
9. V. Ferrando, S. Amoruso, E. Bellingeri, *et al.*, cond-mat/0210048.
10. K. Ueda, M. Naito, *et al.*, Appl. Phys. Lett. **79**, 2046 (2001).
11. G. Grassano, W. Ramadan, V. Ferrando, *et al.*, Supercond. Sci. Technol. **14**, 762 (2001).
12. K. Ueda and M. Naito, cond-mat/0203181.
13. X. Zeng, A. Pogrebnyakov, A. Kotcharov, *et al.*, Nat. Mater. **1**, 35 (2002).
14. A. I. Golovashkin, E. V. Ekimov, S. I. Krasnosvobodtsev, *et al.*, Physica C **162–164**, 715 (1989).
15. W. Tian, Q. Pan, S. S. Bu, *et al.*, Appl. Phys. Lett. **81**, 685 (2002).

Translated by K. Shakhlevich

Technical Physics, Vol. 48, No. 8, 2003, pp. 1074–1077. Translated from Zhurnal Tekhnicheskoĭ Fiziki, Vol. 73, No. 8, 2003, pp. 139–142.

BRIEF COMMUNICATIONS

Chaos-Controlling Technique for Suppressing Self-Modulation in Backward-Wave Tubes

A. M. Dolov and S. P. Kuznetsov

Institute of Radio Engineering and Electronics (Saratov Branch), Russian Academy of Sciences, Saratov, 410019 Russia

e-mail: kuznetsov@sgu.ru

Received January 29, 2003

Abstract—A method for suppressing self-modulation in backward-wave tubes is proposed. Additional delay is introduced into the feedback circuit, owing to which the output signal amplitude affects the electron beam current that enters into the interaction space. Numerical simulations demonstrate that the operating current in the single-frequency oscillation mode may be increased roughly twofold. *© 2003 MAIK "Nauka/Interperiodica".*

The treatment of microwave electron devices with long-term interaction as nonlinear distributed dynamic systems relies on the nonstationary nonlinear theory. Such an approach has been developed for backward-wave tubes (BWTs) of various modifications [1–3], traveling-wave tubes [4], and gyrotrons [5]. In particular, nontrivial bifurcations (loss of stability in single-frequency oscillations that is accompanied by self-modulation and dynamic chaos) have been discovered in conventional O-type BWTs [1, 6–12].

Nonstationary processes and complex dynamic modes in BWTs may be of practical interest. Specifically, a BWT operating in the chaotic dynamic mode may be used as a noise generator whose spectrum concentrates within a certain frequency range, the center frequency being tuned by the accelerating voltage [7–10]. In relativistic BWTs, a feature of transient oscillations (an initial spike of the field amplitude) can be used to increase the pulse generation efficiency [11, 12]. However, in many cases, self-modulation is a parasitic effect that makes difficult single-frequency generation of high power and efficiency, which would otherwise be achieved by increasing the operating current. To eliminate self-modulation, it was recommended, in particular, that high-space-charge operating modes be used [8]. Another way discussed in [13] is to apply a BWT with coupled guiding structures. In this paper, considering a BWT as a dynamic system, we make use of the idea of state stabilization that is referred to as chaos control in nonlinear dynamics.

This concept was first put forward in 1990 by Ott *et al*. from the University of Maryland [14]. They demonstrated the possibility of periodic dynamics, instead of random oscillations, being realized in a nonlinear system by applying weak controllable actions to an adjustable parameter of the system. Later, other chaos-controlling techniques intended for system stabilization and/or directing a phase trajectory into a desired region have been proposed. One simple and often efficient method is to use delayed feedback [15]. To date, many examples of efficient chaos control have been demonstrated: in nonlinear oscillators [16], lasers [17], systems with spin-wave instability [18], biology and medicine [19], and space navigation [20].

As is well known, in a BWT (Fig. 1a), an electron beam moves at a speed that is close to the phase velocity of the wave, which provides efficient interaction. The group velocity of the wave is opposite to the beam, which produces internal feedback and absolute instability and also gives rise to self-sustained oscillations when the beam current exceeds a certain starting value. With a further increase in the current, self-modulation appears. Its mechanism is illustrated by the space–time diagram shown in Fig. 1b. Let the amplitude of the HF field at the left end of the system, where the electron beam is injected, be relatively high at a certain time instant I. This leads the beam's electrons to rebunch along the line (characteristic) $x - v_0 t = \text{const}$: the HF current varies along the length as shown in the bottom panel. As a result, at the instant II, the amplitude of the current at the right end appears to be small. Then, on the line along which the wave packet propagates with the group velocity by the law $x + v_g t = \text{const}$, the field amplitude will be lower. Therefore, at the instant $t \cong L/v_0 + L/v_g$, the signal amplitude at the left end is minimal (instant III). The weaker field bunches the beam more effectively (top panel), and the current attains a maximum value on the corresponding characteristic at the right end (instant IV). As a result, the field reaches a maximum (instant V) at the left end within the time $T \cong 2(L/v_0 + L/v_g)$. This gives an estimate of the self-modulation period. Numerical calculations refine the factor in this expression: it appears to be close to 1.5 instead of 2.

1063-7842/03/4808-1074$24.00

Apparently, self-modulation may be suppressed by varying the beam current at the entrance into the interaction space so that it will increase when the field amplitude is near the maximum and decrease when the field amplitude approaches the minimum. Figure 1a schematically shows that this can be implemented by introducing an additional control circuit that uses the chaos-controlling technique with delay [15]. The HF signal picked up from the BWT output is detected and filtered. As a result, the signal envelope is extracted in the BWT operating mode for which self-modulation exists or may exist. Further, the signal is separated and fed to the input of a differential amplifier with a delay of about half the self-modulation period in one of the branches. The output signal of the amplifier is applied to the control electrode (grid) of the electron gun as an additional bias voltage, thereby controlling the beam current at the entrance into the interaction space.

Let us confirm the possibility of suppressing self-modulation by a numerical experiment. To this end, we will invoke the equations of the nonstationary nonlinear theory of BWT [1, 8]. It is convenient to use the standard normalization of dimensionless variables and parameters, in terms of which the beam current is represented by the mean direct current I_0. The variation of the current due to the control circuit is allowed for by a factor on the right of the excitation equation. This factor is constant on the characteristic line that refers to the beam but varies in time, i.e., from characteristic to characteristic. The equations have the form

$$\partial^2\theta/\partial\zeta^2 = -\mathrm{Re}F\exp(i\theta), \quad \partial F/\partial\tau - \partial F/\partial\zeta = A(\tau)I,$$
$$I = -\frac{1}{\pi}\int_0^{2\pi}\exp(-i\theta)d\theta_0, \tag{1}$$

$$\theta|_{\varsigma=0} = \theta_0, \quad \partial\theta/\partial\zeta|_{\varsigma=0} = 0, \quad F|_{\varsigma=l} = 0. \tag{2}$$

Here, the dimensionless independent variables $\varsigma = \beta_0 Cx$ and $\tau = \omega_0 C(1 + v_0/v_g)^{-1}(t - x/v_0)$ are defined so that the ς coordinate is directed along the characteristic (Fig. 1b); β_0 and ω_0 are the wavenumber and circular frequency of the wave in the slow-wave structure when it is in synchronism with the electron beam; $C = \sqrt[3]{I_0K/4U}$ is the Pierce parameter, which is expressed in terms of the beam current, coupling impedance K of the slow-wave structure, and accelerating voltage U; $F(\varsigma, \tau) = \mathscr{E}/2\beta_0 UC^2$ is the dimensionless complex amplitude of the HF field $E(x, t) = \mathrm{Re}[\mathscr{E}(x, t)\exp(i\omega_0 t - i\beta_0 x)]$; and $\theta(\varsigma, \tau, \theta_0)$ characterizes the electron's phase relative to the wave and refers to a particle that enters into the interaction space with a phase θ_0 and has a coordinate ζ at the time instant τ. In the absence of the control circuit, stationary oscillations occur when the dimensionless length is $l > l_{st} \cong 1.974$ and self-modulation appears when $l > l_{sm} \cong 2.9$ [1]. Note that the condition under which the field amplitude varies slowly in time and space, which is fundamental for the applicability of the theory, is the smallness of the Pierce parameter.

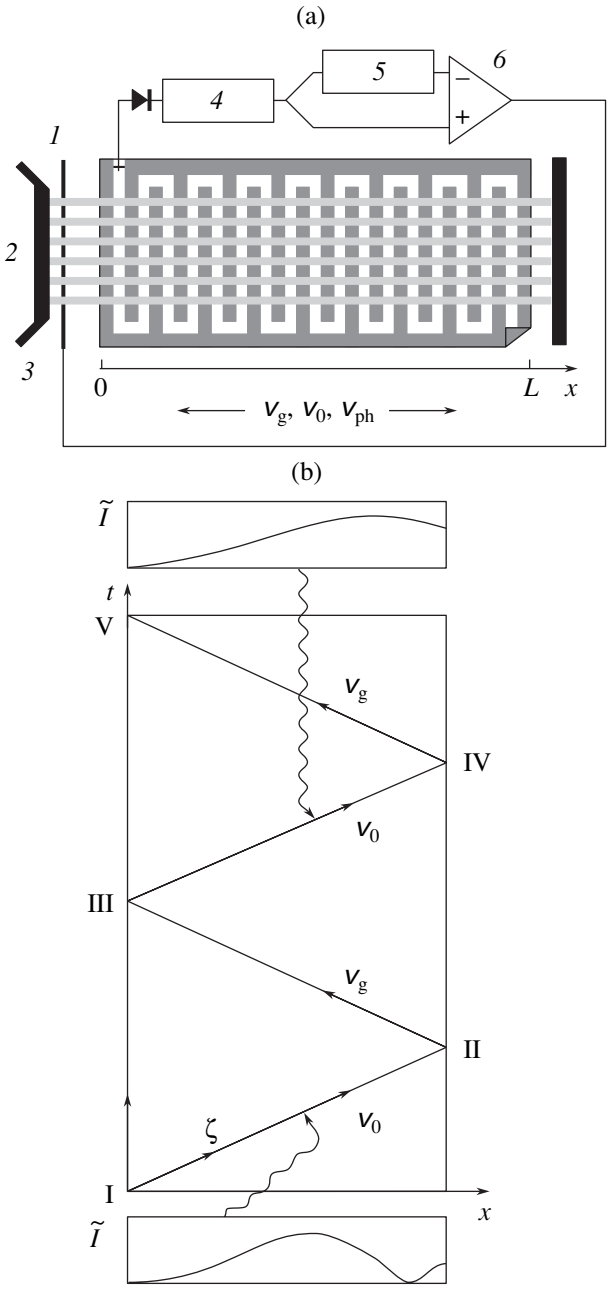

Fig. 1. (a) Diagram of a backward-wave tube (with the circuit that suppresses self-modulation by the chaos-controlling technique with delayed feedback) and (b) space–time diagram that illustrates the self-modulation mechanism: (*1*) microwave output, (*2*) cathode, (*3*) control electrode, (*4*) filter, (*5*) delay, and (*6*) amplifier.

Let us assume that, with the control circuit enabled, the electron beam current is given by the expression

$$J(t) = I_0 + g\Delta V, \tag{3}$$

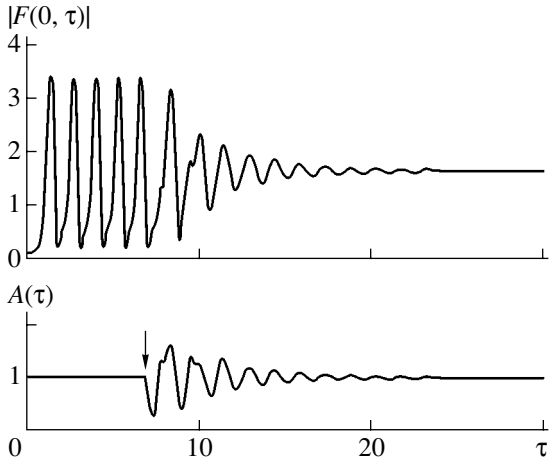

Fig. 2. Dimensionless HF field at the BWT output and the normalized beam current versus time at $l = 3.5$. The switching time of the control circuit is indicated by the arrow. The parameters of the control circuit are $c = 0.95$ and $T = 0.8$.

where

$$\Delta V = V(t) - V(t - \Delta t) \cong \beta_0^{-1}(|\mathscr{E}(0, t)| - |\mathscr{E}(0, t - \Delta t)|)$$

is the voltage at the output of the control circuit; $V(t)$ is the amplitude of the HF potential at the BWT output; Δt is the delay; and g is a constant coefficient, which has the dimension of admittance.

Putting $A = J/J_0$ and passing to the dimensionless variables, we can write

$$\begin{aligned} A(\tau) &= 1 + 2gUI_0^{-1}C^2(|F(0, \tau)| - |F(0, \tau - T)|) \\ &= 1 + cl^{-1}(|F(0, \tau)| - |F(0, \tau - T)|), \end{aligned} \quad (4)$$

where $c = 2gUC^2l/I_0 = \pi gKN$ and $T = \omega_0 C(1 + v_0/v_g)^{-1}\Delta t$ are dimensionless constants, which characterize the control circuit.

Equation (1) in view of (2) and (4) was solved numerically by the finite-difference method [1, 8]. Figure 2 shows the output signal amplitude versus time at $l \cong 3.5$. The control circuit, initially disabled, was enabled at the time indicated by the arrow. It is clearly seen that the intense self-modulation decays and stationary single-frequency oscillations are established; i.e., the signal amplitude becomes constant. The additional terms in relationship (4) cancel out and $A \equiv 1$. Such an operating mode is also predicted by the stationary theory. However, the presence of the control circuit makes it stable. The empirical parameters of the control circuit, $c = 0.95$ and $T = 0.8$, were selected such that the stationary oscillations occurred in a wide range of the dimensionless length l. For the above values of the parameters c and T, this situation takes place when $l_{st} < l \leq 3.7$. Thus, compared with an ordinary BWT, we managed to increase the self-modulation threshold in l by a factor of about 1.27 and by a factor of about 2 (1.27^3) in the operating current with a minor change in the dimensionless amplitude $|F|$ of the output signal. Therefore, the maximum attainable single-frequency efficiency $\eta = 2^{-5/3} I_0^{1/3} U^{-1/3} K^{1/3} |F|^2$ and power $P = 2^{-5/3} I_0^{4/3} U^{2/3} K^{1/3} |F|^2$ grow, respectively, 1.3 and 2.5 times. Apparently, these parameters may be improved by applying more sophisticated control techniques.

To conclude, we note several points that should be taken into account when suppressing self-modulation in practice. First, the filter must reject the HF component of the signal and pass the fundamental self-modulation frequency (in the experiments reported in [6–9], these frequencies were 1 GHz and 50 MHz, respectively). Second, the delay must be about half the self-modulation period, i.e., about the time $L/v_0 + L/v_g$ of signal travel through the feedback loop. Third, the transfer coefficient of the control circuit must be such that the input signal of amplitude on the order of the HF field amplitude causes the output current to vary by about the beam mean current. The magnitude of the HF voltage is estimated as C^2U, where C is a small parameter (in the experiments reported in [6–9], $C = 0.005$–0.1), whereas the voltage on the control electrode may apparently be lower than the accelerating voltage U by no more than one order of magnitude. Therefore, the presence of an amplifier in the control circuit seems to be necessary.

ACKNOWLEDGMENTS

This work was supported by the Russian Foundation for Basic Research, project no. 03-02-16192.

REFERENCES

1. N. S. Ginzburg, S. P. Kuznetsov, and T. N. Fedoseeva, Izv. Vyssh. Uchebn. Zaved. Radiofiz. **21**, 1037 (1978).
2. S. P. Kuznetsov and D. I. Trubetskov, Izv. Vyssh. Uchebn. Zaved. Radiofiz. **20**, 300 (1977).
3. S. P. Kuznetsov and A. P. Chetverikov, Izv. Vyssh. Uchebn. Zaved. Radiofiz. **24**, 109 (1981).
4. L. V. Bulgakova and S. P. Kuznetsov, Izv. Vyssh. Uchebn. Zaved. Radiofiz. **31**, 207 (1988); Izv. Vyssh. Uchebn. Zaved. Radiofiz. **31**, 612 (1988).
5. N. S. Ginzburg, N. A. Zavol'skiĭ, G. S. Nusinovich, *et al.*, Izv. Vyssh. Uchebn. Zaved. Radiofiz. **29**, 106 (1986).
6. B. P. Bezruchko and S. P. Kuznetsov, Izv. Vyssh. Uchebn. Zaved. Radiofiz. **21**, 1053 (1978).
7. B. P. Bezruchko, S. P. Kuznetsov, and D. I. Trubetskov, Pis'ma Zh. Éksp. Teor. Fiz. **29**, 180 (1979) [JETP Lett. **29**, 162 (1979)].
8. B. P. Bezruchko, L. V. Bulgakova, S. P. Kuznetsov, *et al.*, in *Lectures on Microwave Electronics and Radiophysics* (Saratov. Gos. Univ., Saratov, 1981), Vol. 5, pp. 25–77.
9. B. P. Bezruchko, L. V. Bulgakova, S. P. Kuznetsov, *et al.*, Radiotekh. Élektron. (Moscow) **28**, 1136 (1983).
10. N. M. Ryskin, V. N. Titov, and D. I. Trubetskov, Dokl. Akad. Nauk **358**, 620 (1998).

11. N. S. Ginzburg, N. I. Zaĭtsev, E. V. Ilyakov, *et al.*, Pis'ma Zh. Tekh. Fiz. **24** (20), 66 (1998) [Tech. Phys. Lett. **24**, 816 (1998)].
12. N. S. Ginzburg, N. I. Zaĭtsev, E. V. Ilyakov, *et al.*, Izv. Vyssh. Uchebn. Zaved. Prikl. Nelineinaya Din. **7** (5), 60 (1999).
13. R. Sh. Amirov, B. P. Bezruchko, V. A. Isaev, *et al.*, in *Lectures on Microwave Electronics and Radiophysics* (Saratov. Gos. Univ., Saratov, 1983), Vol. 2, pp. 90–105.
14. E. Ott, C. Grebogi, and J. A. Yorke, Phys. Rev. Lett. **64**, 1196 (1990).
15. K. Pyragas, Phys. Lett. A **170**, 421 (1992).
16. E. R. Hunt, Phys. Rev. Lett. **67**, 1953 (1991).
17. R. Meucci, W. Gadomski, M. Ciofini, *et al.*, Phys. Rev. E **49**, R2528 (1994).
18. A. Azevedo and S. M. Rezende, Phys. Rev. Lett. **66**, 1342 (1991).
19. D. J. Christini and J. J. Collins, Phys. Rev. E **53**, R49 (1996).
20. E. M. Bollt and J. D. Meiss, Phys. Lett. A **204**, 373 (1995).

Translated by A. Khzmalyan

Technical Physics, Vol. 48, No. 8, 2003, pp. 939–944. Translated from Zhurnal Tekhnicheskoĭ Fiziki, Vol. 73, No. 8, 2003, pp. 1–6.

THEORETICAL AND MATHEMATICAL PHYSICS

Effective Potential of Planar Channeling in LiH Crystals

N. A. Korkhmazyan, N. N. Korkhmazyan, and N. É. Babadzhanyan

Abovyan State Pedagogical University of Armenia, Yerevan, 375010 Armenia

e-mail: norayrk@web.am

Received July 15, 2002

Abstract—The problem of calculating the effective potential of planar channeling along the charged (111) and $(1\bar{1}1)$ planes in a finite LiH crystal is considered. The criteria of applicability of expressions obtained for an infinite crystal are derived. The surface layer thickness below which these formulas become invalid is estimated.

INTRODUCTION

As is well known, a relativistic charged particle channeled along crystallographic surfaces (axes) of a crystal executes oscillations across the channel, and this motion is accompanied by radiation [1–3]. In special conditions, it becomes feasible to generate a laser-like gamma radiation with characteristics vastly superior to other types of radiation in the same spectral range [4]. These hard gamma rays are finding a variety of applications, which calls for the investigation of a wider class of crystal radiators. Of particular interest are the effective potentials of channeling along charged planes with the (111) and $(1\bar{1}1)$ Miller indices in LiH-type light-ion crystals, since the dechanneling length in this case is more than one order of magnitude larger than upon channeling along other planes [5]. A significant step forward in the investigation of channeling potentials in ion crystals is the development of a general approach to calculating the potentials that includes the partial contributions of all ions in the crystal [6–9]. However, the expressions are awkward and difficult to treat analytically. According to recent experiments [10] concerned with radiation emitted by electrons and positrons channeled along the main crystallographic planes in LiH and LiD crystals, the concept of a free-ion potential yields results that contradict the experiment and, hence, should be revised. Thus, it seems to be topical to derive a correct formula for the channeling potential in light crystals of finite size. The solution for an infinite crystal has been obtained in [5].

In this study, the same problem is solved for finite-size crystals.

EFFECTIVE POTENTIAL OF AN INFINITE CRYSTAL

The calculation will be performed in terms of the method of equivalent cells, which was first presented in [9]. The essence of this method is that ions (the centers of ions in a "frozen" crystal) lying on the planes parallel to the planes of channeling are redistributed so as to simplify the geometry of the problem. In this case, the averaging cell may be configured into a desired shape with its surface area remaining unchanged.

LiH and LiD are fcc crystals with the structure shown in Fig. 1a. We choose the coordinate system as shown in Fig. 1b. The spacing between the nearest like ions along the x' and y' axes (the lattice constant of the crystal) is $d = 4.084$ Å. The (HHH) plane is obtained by rotating the (x', y') plane about the z' axis by an angle $\varphi = \pi/4$ and then about the new axis x by an angle α, where $\tan\alpha = \sqrt{2}$. The spacing between like and unlike planes are

$$d_z = d/\sqrt{3} = 2.358 \text{ Å}, \quad d_z/2 = 1.179 \text{ Å}, \qquad (1)$$

respectively.

Figure 2 shows the distribution of ions on the charged $(1\bar{1}1)$ plane. Averaging will be accomplished over a rhombic cell with a surface area of $\sqrt{3}\,d^2/4$ (hatched). For an equiareal square cell ($d_0 \times d_0$), we find

$$d_0 = 3^{\frac{1}{4}} d/2 = 2.6874 \text{ Å}. \qquad (2)$$

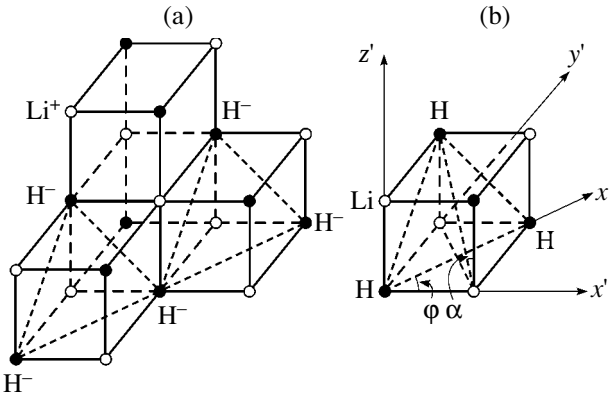

Fig. 1. (a) LiH crystal structure ((HHH) is the charged plane) and (b) the system of coordinates.

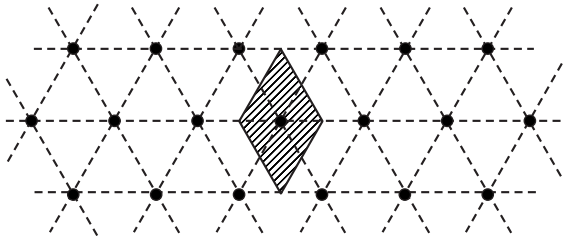

Fig. 2. Distribution of like ions on the $(1\bar{1}1)$ plane. The area of averaging is hatched.

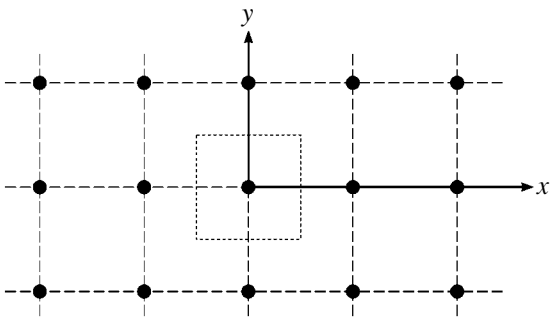

Fig. 3. Equiareal square cells.

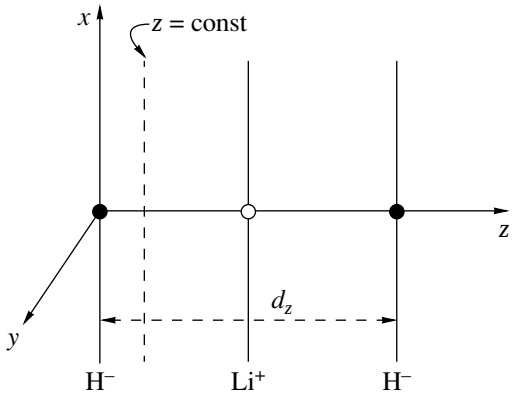

Fig. 4. Channel selected and the plane z = const on which the averaged potential is determined.

Thus, the distribution of ions on the (x, y) plane is eventually reduced to the form presented in Fig. 3 (the z axis is normal to the plane of the figure). The square averaging cell lies in the plane z = const (Fig. 4) and is centered on the z axis. Hydrogen ion (H^-) and lithium ion (Li^+) are located at the origin of coordinates, (0, 0, 0), and at the point (0, 0, $d_z/2$), respectively. We will call these two ions basis ions. Their effective radii are known [9] to be

$$R(H^-) = 1.50\ \text{Å}, \quad R(Li^+) = 0.68\ \text{Å}. \tag{3}$$

It is sufficient to calculate the effective potential of planar channeling in a half-channel

$$0 \le z \le d_z/2, \tag{4}$$

since the channel is symmetric about the plane $z = d_z/2$. Physically, the effective radii given by (3) represent the distance from the ion nucleus at which the electron cloud density may be set equal to zero. As follows from (3) and (4), all positive ions, except for the basis positive ion, may be treated as point charges. The same assertion is true for negative ions even though $R(H^-) > d_z/2$. Indeed, the electron cloud density in a two-electron ion (atom) depends on the distance r from the nucleus as [11]

$$\rho(r) = -\frac{e\lambda^3}{4\pi}e^{-\lambda r}, \quad \lambda = \frac{2z^*}{a_0}, \quad z^* = z - 5/16, \tag{5}$$

where $a_0 = 0.528$ Å is the Bohr radius, z is the number of protons in the nucleus, and e is the electron charge.

Using the value given by (3) for the H^- ion, we may assume that $\rho(1.5\ \text{Å}) = 0$. Let us estimate ρ at a distance $r = d_z/2 = 1.179$ Å.

According to (5), we have

$$[\rho(1.179\ \text{Å}) - \rho(1.5\ \text{Å})]/\rho(1.5\ \text{Å})$$

$$= \exp(2z^*(1.5 - 1.179)/0.53) - 1 \cong 1.3, \quad z^- = 1.$$

Hence, $\rho(1.179\ \text{Å}) \cong 2.3\rho(1.5\ \text{Å})$, which may be considered as zero to a high accuracy.

In the crystal thus constructed, negative ions occupy sites $\mathbf{L} = (ld_0, md_0, nd_z)$, where $l, m, n = 0, \pm1, \pm2, \ldots$. The positive sublattice is shifted with respect to the negative one by the vector $\boldsymbol{\alpha} = (0, 0, d_z/2)$. The potential produced by the negative sublattice at the point $\mathbf{r} = (x, y, z)$ is given by

$$\varphi^-_{\text{tot}} = \frac{ez^-}{|\mathbf{r}|} + \varphi^-_{\text{el}} - e\sum_{\mathbf{L}\neq 0}\frac{1}{|\mathbf{r}-\mathbf{L}|}, \tag{6}$$

where the first and second terms account for the fields of the nucleus and electron cloud of the basis ion, respectively, and the third term integrates the field of all other negative point ions.

We calculate the function φ^-_{el} with the use of the Gauss theorem and the function defined by formula (5). The projection of the electric field strength on the radius $\mathbf{r}$ can be written in the form

$$E_r = \frac{q(r)}{r^2},$$

$$q(r) = -\frac{2e}{\pi}\left(\frac{z^-*}{a_0}\right)^3 4\pi\int_0^r \exp(-2z^-*\xi/a_0)\xi^2 d\xi, \tag{7}$$

$$r = |\mathbf{r}|.$$

Using the formula

$$\varphi_\infty - \varphi(r) = -\int_r^\infty E_r dr, \quad \varphi_\infty = 0,$$

we find

$$\varphi_{\text{el}}^-(r) = e\lambda^- e^{-\lambda^- r} + \frac{2e}{r}e^{-\lambda^- r} - \frac{2e}{r}. \tag{8}$$

Substituting of this expression into Eq. (6) yields

$$\varphi_{\text{tot}}^- = e\bar{\lambda}e^{-\bar{\lambda}r} + \frac{2e}{r}e^{-\bar{\lambda}r} - e\sum_{l,m,n}\frac{1}{|\mathbf{r}-\mathbf{L}|}, \tag{9}$$

where the sum also includes the contribution of the site $\mathbf{L} = 0$.

The potential derived should be averaged over a unit cell:

$$\langle\varphi_{\text{tot}}^-\rangle = \frac{1}{d_0^2}\int_{-d_0/2}^{d_0/2} dx \int_{-d_0/2}^{d_0/2} \varphi_{\text{tot}}^- dy. \tag{10}$$

The first two terms in Eq. (9) can be conveniently averaged in the cylindrical coordinates by integrating over a circle of radius $R_0 = d_0/\sqrt{\pi}$:

$$\langle\varphi_{1,2}^-\rangle = \frac{2\pi}{d_0^2}\int_0^{R_0}\varphi_{1,2}^-\rho d\rho, \quad r = \sqrt{\rho^2+z^2}. \tag{11}$$

Then, instead of Eq. (10), we have

$$\langle\varphi_{\text{tot}}^-\rangle = \frac{2\pi e}{d_0}(f_1^- + f_2^-) - e\left\langle\sum_{l,m,n}^- \ldots\right\rangle,$$

$$f_1^- = \frac{1}{\lambda^- d_0}\left[(\lambda^-|z|+1)e^{-\lambda^-|z|}\right.$$
$$\left. -(\lambda^-\sqrt{R_0^2+z^2}+1)e^{-\lambda^-\sqrt{R_0^2+z^2}}\right]; \tag{12}$$

$$f_2^- = \frac{2}{\lambda^- d_0}\left[e^{-\lambda^-|z|} - e^{-\lambda^-\sqrt{R_0^2+z^2}}\right],$$

where all the lengths in f_1^- and f_2^- are expressed in terms of d_z.

Now z varies in the range $0 \le z \le 1/2$. The potential of the positive sublattice is found from Eq. (12) via the replacements $\bar{\lambda} \longrightarrow \lambda^+$ and $z \longrightarrow -(1/2 - z)$. Before calculating the average sum in Eq. (12), it should be noted that this sum of the contributions from the infinite number of negatively charged crystal planes tends to infinity. A finite result is provided only by simultaneously taking into account the contributions of both negatively and positively charged planes. Denoting the last term in Eq. (12) by I^-, we have

$$I^- = -\frac{e}{d_0^2}\sum_{l,m,n}\int_{-d_0/2}^{d_0/2} dx$$

$$\times\int_{-d_0/2}^{d_0/2}\frac{dy}{\sqrt{(x-ld_0)^2+(y-md_0)^2+(z-nd_z)^2}} \tag{13}$$

$$= -\frac{e}{d_0}\sum_{l,m,n}\int_{-1/2}^{1/2} dx\int_{-1/2}^{1/2}\frac{dy}{\sqrt{(x-l)^2+(y-m)^2+p^2(z-n)^2}},$$

where x and y are expressed in terms of d_0, z is expressed in terms of d_z, and $p = d_z/d_0 = 0.8774$.

With the notation $p^2(n-z)^2 = a^2$, the summation over m in Eq. (13) yields

$$\sum_{l,m,n}\ldots = 2\sum_{l,n}\int_{-1/2}^{1/2} dx\left[\int_0^{1/2}\frac{dy}{\sqrt{(x-l)^2+y^2+a^2}}\right.$$
$$\left. +\int_{1/2}^{3/2}\frac{dy}{\sqrt{(x-l)^2+y^2+a^2}}+\ldots\right] \tag{14}$$
$$= 2\sum_{l,n}\int_{-1/2}^{1/2} dx\int_0^\infty\frac{dy}{\sqrt{(x-l)^2+y^2+a^2}}$$

$$= 2\sum_{l,n}\int_{-1/2}^{1/2} dx\ln\left|\frac{y}{\sqrt{(l-x)^2+a^2}} + \sqrt{1+\frac{y^2}{(l-x)^2+a^2}}\right|_0^\infty.$$

Combining this expression with the sum for the positive sublattice and putting $p^2(n+1/2-z)^2 = b^2$, we find

$$I = I^- + I^+$$
$$= \frac{e}{d_0}\sum_n\left[\sum_l\int_{-1/2}^{1/2}\ln\frac{(l-x)^2+a^2}{(l-x)^2+b^2}dx\right]. \tag{15}$$

Summation over l yields

$$I = \frac{2\pi e}{d_0}p\left[\sum_{n^-}|n^- - z| - \sum_{n^+}|n^+ + 1/2 - z|\right], \tag{16}$$

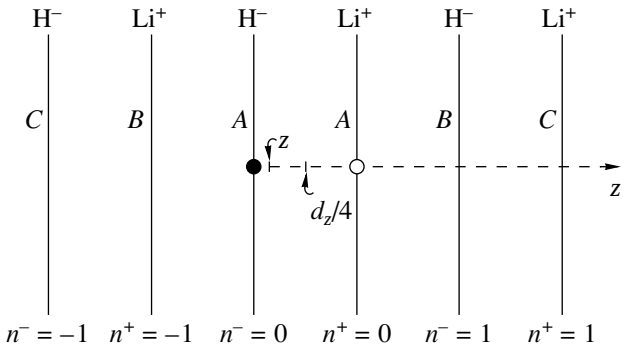

Fig. 5. Charged planes in an infinite crystal.

where n^- and n^+ refer to the negative and positive sublattices, respectively (Fig. 5).

Adding up the contributions from the corresponding pairs of planes (*AA*), (*BB*), …, we finally obtain

$$I = \frac{2\pi e}{d_0} p[(2z - 1/2) - (2z - 1/2) + (2z - 1/2) - \ldots]. \quad (17)$$

It is easily seen that this potential has an uncertain value. Below, we will show that this result reflects the fact that the crystal size in the direction of particle travel is many times greater than the transverse size.

EFFECTIVE POTENTIAL OF A FINITE CRYSTAL

The series in Eq. (17) is convergent if one assumes a finite crystal length L in the direction of planar channeling in the (x, y) plane. Let a channeled particle move along the x axis. Also let the distance from the unit cell to one crystal face be l_1 and to the other face, l_2 (in terms of d_0). To be definite, we put $l_1 \le l_2$. The crystal thickness L is usually on the order of $\approx 10^7$ Å, and the dechanneling length varies in the range from 10^4 to 10^5 Å. Therefore, a 100-Å-thick surface layer may be safely excluded from consideration. In other words, we may believe that $l_1 \gg 1$. This assumption is quite reasonable, since the thickness of the layer omitted is two orders of magnitude less than the length of dechanneling. The summation over l in the range $-l_2 \le l \le l_1$ in Eq. (15) yields

$$I = I(l_1) + I(l_2) = \frac{e}{d_0}\sum_n \left[\int_0^{l_1 + 1/2} \ln\frac{x^2 + a^2}{x^2 + b^2} dx + \int_0^{l_2 + 1/2} \ln\frac{x^2 + a^2}{x^2 + b^2} dx \right]. \quad (18)$$

From this expression, we obtain

$$I(l_{1,2}) = \frac{e}{d_0}\sum_{n^- = -N}^{N} \left[(l_{1,2} + 1/2)\ln[(l_{1,2} + 1/2)^2 + a^2] + 2a\arctan\frac{l_{1,2} + 1/2}{a} \right] - \frac{e}{d_0}\sum_{n^+ = -N}^{N} \left[(l_{1,2} + 1/2) \times \ln[(l_{1,2} + 1/2)^2 + b^2] + 2b\arctan\frac{l_{1,2} + 1/2}{b} \right]. \quad (19)$$

Denoting $(l_{1,2} + 1/2)/p \equiv A_{1,2}$, we find

$$I(l_1) = \frac{e}{d_0}P\sum_{n^- = -N}^{N} \left[A_1 \ln[A_1^2 + (n^- - z)^2] + 2(n^- - z)\arctan\frac{A_1}{n^- - z} \right] - \frac{e}{d_0}P \times \sum_{n^+ = -N}^{N} \left[A_1 \ln[A_1^2 + (n^+ - z + 1/2)^2] + 2(n^+ - z + 1/2)\arctan\frac{A_1}{n^+ - z + 1/2} \right]. \quad (20)$$

In view of the fact that $A_1 \gg 1$, the logarithms are slowly varying functions of the arguments $n^\pm$. Therefore, the sums in (20) may be replaced by integrals:

$$\sum_{n^- = -N}^{N} A_1 \ln[A_1^2 + (n^- - z)^2] \longrightarrow A_1 \int_{-N}^{N} \ln[A_1^2 + (n^- - z)^2] dn^-. \quad (21)$$

It is easy to check that, in the limiting cases $N \gg A_1$ and $N \ll A_1$, the respective integrals of the logarithmic functions satisfy the inequalities

$$\frac{5}{2}\frac{A_1}{N} \ll 1, \quad 3\frac{N}{A_1} \ll 1. \quad (22)$$

With this in mind, Eq. (20) may be recast as

$$I(l_1) = \frac{2e}{d_0}P\left[\sum_{n^- = -N}^{N} (n^- - z)\arctan\frac{A_1}{n^- - z} - \sum_{n^+ = -N}^{N} (n^+ - z + 1/2)\arctan\frac{A_1}{n^+ - z + 1/2} \right]. \quad (23)$$

If $A_1 \gg N$, this expression can be reduced to

$$I(l_1) = \frac{\pi e}{d_0} P\left(\sum_{n^- = -N}^{N} |n^- - z| - \sum_{n^+ = -N}^{N} |n^+ - z + 1/2| \right) \quad (24)$$

and, since $I(l_2) = I(l_1)$, we finally arrive at formula (17). Therefore, if the crystal size in the z direction is appreciably smaller than in the channeling direction ($N \ll A_1$), the potential inside a finite crystal behaves in the same manner as the potential of an infinite crystal.

In the opposite case ($N \gg A_1$), the functions under the summation sign in Eq. (23) are not slowly varying functions of their arguments; therefore, prior to the calculation of the potential, one should find the field strength

$$E_z = -\frac{1}{d_z}\frac{dI}{dz}. \quad (25)$$

Differentiating Eq. (23) with respect to z, we have

$$\begin{aligned} \frac{dI(l_1)}{dz} &= -\frac{2e}{d_0} P\left[\sum_{n=-N}^{N} \arctan\frac{A_1}{n-z} \right. \\ &\left. - \sum_{n=-N}^{N} \arctan\frac{A_1}{n-z+1/2} \right] \\ &+ \frac{2e}{d_0} P\left[\sum_{n=-N}^{N} (n-z)\frac{d}{dz}\left(\arctan\frac{A_1}{n-z} \right) \right. \\ &\left. - \sum_{n=-N}^{N} (n-z+1/2)\frac{d}{dx}\arctan\frac{A_1}{n-z+1/2} \right]. \end{aligned} \quad (26)$$

Since the second term is small,

$$P\frac{2e}{d_0}\frac{A_1}{N}. \quad (27)$$

Eq. (26) appears in the form

$$\begin{aligned} \frac{dI(l_1)}{dz} &= -\frac{2e}{d_0} P\left[\sum_{n=-N}^{N} \arctan\frac{A_1}{n-z} \right. \\ &\left. - \sum_{n=-N}^{N} \arctan\frac{A_1}{n-z+1/2} \right]. \end{aligned} \quad (28)$$

Except for the terms with $n = 0$, the other functions under the summation sign are slowly varying functions; therefore instead of Eq. (28), we come to

$$\begin{aligned} \frac{dL(l_1)}{dz} &= \frac{2\pi e}{d_0} P + \frac{2e}{d_0} P\left[\int_1^N \arctan\frac{A_1}{n+z} dn \right. \\ &- \int_1^N \arctan\frac{A_1}{n-z} dn + \int_1^N \arctan\frac{A_1}{n+(1/2-z)} dn \\ &\left. - \int_1^N \arctan\frac{A_1}{n-(1/2-z)} dn \right]. \end{aligned} \quad (29)$$

Using the formulas

$$\begin{aligned} &\arctan x = \operatorname{arccot}\frac{1}{x}; \quad x > 0, \\ &\int \operatorname{arccot}\frac{x}{A} = x\operatorname{arccot}\frac{x}{A} + \frac{A}{2}\ln(A^2 + x^2), \end{aligned} \quad (30)$$

one obtains

$$\frac{dL(l_1)}{dz} = \frac{2\pi e}{d_0} P - \frac{\pi e}{d_0} P = \frac{\pi e}{d_0} P. \quad (31)$$

Eventually, taking into account the contribution of the term $dI(l_2)/dz$, we find for the field strength

$$E_z = -\frac{1}{d_z}\frac{2\pi e}{d_0} P. \quad (32)$$

Since $I(1/4) = 0$, we obtain the potential of a point lattice in the same form as in [5]:

$$I(z) = \frac{2\pi e}{d_0} P(z - 1/4). \quad (33)$$

According to Eq. (12), the planar channeling potential is finally given by

$$\begin{aligned} \langle \varphi_{\text{tot}} \rangle &= \langle \varphi_{\text{tot}}^+ \rangle + \langle \varphi_{\text{tot}}^- \rangle \\ &= \frac{2\pi e}{d_0}[f_1^+ + f_2^+ + f_1^- + f_2^- + P(z - 1/4)] \end{aligned} \quad (34)$$

or, in terms of Eq. (12),

$$\langle \varphi_{\text{tot}} \rangle = \frac{2\pi e}{d_0} f, \quad f = f^+ + f^- + P(z - 1/4).$$

Here,

$$\begin{aligned} f^- &= \frac{1}{\lambda d_0}\left[(3 + \lambda^- z) e^{-\lambda^- z} \right. \\ &\left. - (3 + \lambda^- \sqrt{R_0^2 + z^2}) e^{-\lambda^- \sqrt{R_0^2 + z^2}} \right], \end{aligned} \quad (35)$$

and f^+ is found by substituting λ^+ for λ^- and $1/2 - z$ for z.

In conclusion, we note that the potential in the surface layer of a crystal calls for special consideration.

REFERENCES

1. M. A. Kumakhov, *Radiation by Channeled Particles in Crystals* (Énergoatomizdat, Moscow, 1986).
2. V. G. Baryshevskiĭ, *Channeling, Radiation, and Reactions at High Energies* (Belarus. Gos. Univ., Minsk, 1982).
3. V. A. Bazylev and N. K. Zhevago, *Radiation from Fast Particles in Matter and External Fields* (Nauka, Moscow, 1987).
4. L. A. Gevorkyan and N. A. Korkhmazyan, Dokl. Akad. Nauk SSSR **273**, 849 (1983) [Sov. Phys. Dokl. **28**, 1026 (1983)].
5. V. I. Vysotskiĭ, R. N. Kuz'min, and N. V. Moksyuta, Zh. Éksp. Teor. Fiz. **93** (12), 2015 (1987) [Sov. Phys. JETP **66**, 1150 (1987)].
6. A. S. Gevorkyan, N. N. Korkhmazyan, and G. G. Melikyan, Zh. Tekh. Fiz. **59** (3), 54 (1989) [Sov. Phys. Tech. Phys. **34**, 285 (1989)]; Preprint No. EFI-1051 (Yerevan Physical Institute, Yerevan, 1988).
7. A. S. Gevorkyan, N. N. Korkhmazyan, and G. G. Melikyan, in *Proceedings of the 15th All-Union Workshop on Physics of the Interaction of Charged Particles with Crystals, Moscow, 1988*, p. 32.
8. N. N. Korkhmazyan and G. G. Melikyan, Izv. Nats. Akad. Nauk Arm., Ser. Fiz. **28** (2), 56 (1993).
9. N. A. Korkhmazyan and N. N. Korkhmazyan, Izv. Akad. Nauk Arm. SSR, Ser. Fiz. **32** (5), 198 (1955).
10. B. L. Berman *et al.*, Phys. Res. B **119**, 71 (1996).
11. G. Bete and É. Solpiter, *Quantum Mechanics of One- and Two-Electron Atoms* (Academic, New York, 1957; Fizmatgiz, Moscow, 1960).

Translated by A. Sidorova

Technical Physics, Vol. 48, No. 8, 2003, pp. 945–951. Translated from Zhurnal Tekhnicheskoĭ Fiziki, Vol. 73, No. 8, 2003, pp. 7–12.

THEORETICAL AND MATHEMATICAL PHYSICS

On the Polarizability of a Pair of Cylinders in a Transverse Electric Field

B. Ya. Balagurov

Emanuel Institute of Biochemical Physics, Russian Academy of Sciences, ul. Kosygina 4, Moscow, 119991 Russia
e-mail: balagurov@deom.chph.ras.ru

Received December 6, 2002

Abstract—A sequential scheme for calculating the polarizability of a pair of parallel cylinders with an arbitrary (but fairly symmetric) form is suggested. An infinite set of algebraic equations is derived for coefficients involved in an expression for the potential. The numerical solution of this set makes it possible to find the polarizability with any degree of accuracy. This method is unrelated to the cylinder shape. The electrostatic properties of the cylinders are described in terms of the multipolar polarizability matrix. © *2003 MAIK "Nauka/Interperiodica".*

INTRODUCTION

The two-body problem is a fundamental problem in macroscopic electrostatics [1]. It has been considered in a number of works (see, e.g., [2–5]), where it was stated for the most part as the problem of two spheres. However, a closed solution is absent even in this simple case. Considering the bodies of different shape complicates the problem still further. The situation is more favorable in the 2D case, where the problem of two circles (parallel circular cylinders in the 3D case) admits an exact solution. Yet, here again, the general approach to the two-body problem is lacking when cylinders are of an arbitrary shape.

In this work, we suggest a sequential approach to calculating the polarizability tensor $\hat{\Lambda}$ for a pair of cylinders of arbitrary (but fairly symmetric) shape. The complex potential of the problem outside the cylinders is found in general form. An infinite set of algebraic equations is derived for coefficients involved in an expression for the potential. The numerical solution of this set makes it possible to find the polarizability $\hat{\Lambda}$ with any degree of accuracy. For a large spacing ρ between the cylinders, an analytical expression for the polarizability that follows from general formulas has the form of a series in powers of $1/\rho$.

The electrical properties of either of the cylinders enter into the solution to the problem through their multipolar polarizabilities, i.e., factors multiplying "responses" to various external fields. The determination of a related polarizability matrix is an independent problem, which must be solved separately (numerically or analytically) for each specific case. For an elliptical inclusion, expressions for the multipolar polarizabilities can be found in explicit form [6].

MULTIPOLAR POLARIZABILITIES

Consider a cylinder with the dipolar polarizability tensor $\hat{\Lambda}$ that is placed in a uniform transverse electric field $\mathbf{E}_0$. We assume that the principal axes of the tensor $\hat{\Lambda}$ coincide with the x and y axes and $\mathbf{E}_0$ is directed along the x axis. Then, at a large distance r from the body, the electrical potential φ in the dipole approximation has the form

$$r \longrightarrow \infty: \varphi(\mathbf{r}) = -E_0\left\{x - 2\frac{x\Lambda^{(x)}}{r^2} + \ldots\right\}. \qquad (1)$$

Here, $\Lambda^{(x)}$ is the principal value of the tensor $\hat{\Lambda}$. The value $\Lambda^{(x)}$ per unit cylinder length is proportional to the cross-sectional area of the body and depends on the argument $h = \varepsilon^{(c)}/\varepsilon^{(e)}$, where $\varepsilon^{(c)}$ and $\varepsilon^{(e)}$ are, respectively, the permittivities of the cylinder and environment.

Later on, it is more convenient to use the complex potential $\Phi(z)$ ($z = x + iy$). Its real part yields the electrical potential, $\varphi(\mathbf{r}) = \mathrm{Re}\,\Phi(z)$, and its derivative is the component of the field $\mathbf{E}$:

$$\Phi'(z) = -E_x + iE_y. \qquad (2)$$

The complex potential satisfying expression (1) has the form

$$|z| \longrightarrow \infty: \Phi(z) = -E_0\left\{z - \frac{2\Lambda^{(x)}}{z} + \ldots\right\}, \qquad (3)$$

where $\Lambda^{(x)}$ is a real constant.

1063-7842/03/4808-0945$24.00

With higher (multipole) moments included, the expression for $\Phi(z)$ outside the body takes the form

$$\Phi(z) = z + \sum_{m=0}^{\infty} \frac{\Lambda_{1,2m+1}^{(x)}}{z^{2m+1}}, \quad (4)$$

where $\Lambda_{1,2m+1}^{(x)}$ are real constants. In (4), the common multiplier is omitted and it is assumed that the body is fairly symmetric (see Appendix). So, the complex potential $\Phi(z)$ is odd in z. Comparing (4) with (3) yields

$$\Lambda_{11}^{(x)} = -2\Lambda^{(x)}. \quad (5)$$

Below, we will need the response of the body to a nonuniform external field of type $\mathrm{Re}z^{2n+1} = r^{2n+1}\cos(2n+1)\Theta$, where Θ is the polar angle. In this case, instead of (4), we have

$$\Phi(z) = z^{2n+1} + \sum_{m=0}^{\infty} \frac{\Lambda_{2n+1,2m+1}}{z^{2m+1}} \quad (n \geq 0), \quad (6)$$

where $\Lambda_{2n+1,2m+1}$ are real constants, which will be referred to as multipolar polarizabilities. Even–even multipolar polarizabilities $\Lambda_{2n,2m}$ are introduced in a similar way:

$$\Phi(z) = z^{2n} + \sum_{m=1}^{\infty} \frac{\Lambda_{2n,2m}}{z^{2m}} \quad (n \geq 1). \quad (7)$$

In (6) and (7) and below, the superscript x by $\Lambda_{nm}^{(x)}$ is dropped.

If the field $\mathbf{E}_0$ is aligned with the y axis (quantities corresponding to this case are marked by a bar), we have, instead of (3),

$$|z| \longrightarrow \infty: \bar{\Phi}(z) = iE_0\left\{z + \frac{2\bar{\Lambda}}{z} + \ldots\right\}, \quad (8)$$

where $\bar{\Lambda} \equiv \Lambda^{(y)}$ is the dipolar polarizability (the principal value of the tensor $\hat{\Lambda}$) along the y axis.

With higher moments included, instead of (8), we have (similarly to (4))

$$\bar{\Phi}(z) = -i\left\{z - \sum_{m=0}^{\infty} \frac{\bar{\Lambda}_{1,2m+1}}{z^{2m+1}}\right\}, \quad (9)$$

where $\bar{\Lambda}_{1,2m+1}$ are real constants. Comparing (9) with (8) yields

$$\bar{\Lambda}_{11} = -2\Lambda^{(y)}. \quad (10)$$

If an external field has the form $\mathrm{Im}z^{2h+1} = r^{2n+1}\sin(2n+1)\Theta$, instead of (9), we have (similarly to (6))

$$\bar{\Phi}(z) = -i\left\{z^{2n+1} - \sum_{m=0}^{\infty} \frac{\bar{\Lambda}_{2n+1,2m+1}}{z^{2m+1}}\right\} \quad (n \geq 0), \quad (11)$$

where $\bar{\Lambda}_{2n+1,2m+1} = \Lambda_{2n+1,2m+1}^{(y)}$ are related odd–odd multipolar polarizabilities.

Even–even polarizabilities have a form similar to (7):

$$\bar{\Phi}(z) = -i\left\{z^{2n} - \sum_{m=1}^{\infty} \frac{\bar{\Lambda}_{2n,2m}}{z^{2m}}\right\} \quad (n \geq 1). \quad (12)$$

It should be noted that the Dykhne symmetry transformation [7] allows one to relate the complex potentials of the initial, $\Phi(z)$, and so-called reciprocal, $\tilde{\Phi}(z)$, systems (the latter differs from the initial one by the substitution $\varepsilon^{(c)} \rightleftarrows \varepsilon^{(e)}$ (cf. [8]):

$$\tilde{\Phi}^{(x)}(z) = i\Phi^{(y)}(z)$$

or

$$\tilde{\Phi}(z) = i\bar{\Phi}(z). \quad (13)$$

The substitution of (6) into (11) and (13) yields [6]

$$\bar{\Lambda}_{2n+1,2m+1} = -\tilde{\Lambda}_{2n+1,2m+1}. \quad (14)$$

The same relationship holds for the even–even polarizabilities $\bar{\Lambda}_{2n,2m}$ and $\tilde{\Lambda}_{2n,2m}$. From dimension considerations, (6) and (7) yield $\Lambda_{nm} = R^{n+m}\alpha_{nm}$, where R is the characteristic transverse size of the cylinder and α_{nm} are dimensionless quantities depending on the body's shape and argument $h = \varepsilon^{(c)}/\varepsilon^{(e)}$. Note that the equality [9]

$$m\Lambda_{nm} = n\Lambda_{mn}, \quad (15)$$

which is the symmetry relationship for the matrix Λ_{nm}, also holds.

METHOD OF SUCCESSIVE APPROXIMATIONS

Let us find the potential induced by two parallel cylinders (with their directrices directed along the z axis) placed in a uniform transverse electric field. To simplify the mathematics, we assume that the principal axes of the polarizability tensors of both (fairly symmetric) solids coincide with the x and y coordinate axes. Then, if the electric field $\mathbf{E}_0$ is directed along the x (or y) axis, all Λ_{nm} in formulas (4)–(7) and (9)–(12) are real. It is also assumed that the centers of the cylinders are located on the y axis at points $y = \pm\rho/2$. The potential will be sought by the method of successive approximations. The reciprocal influence of the cylinders is exactly taken into account in each order of approximation.

In the zeroth approximation, the complex potential corresponding to a uniform external field applied along the x axis has the form

$$\Phi^{(0)}(z) = \beta z, \tag{16}$$

where $\beta = -E_0$.

According to (4), the response of the first cylinder (centered at the point $y = \rho/2$) to field (16) is given by

$$\Phi_{\rm I}^{(1)}(z) = \beta\sum_{n=0}^{\infty}\frac{b_{2n+1}^{(1)}}{(z-z_{\rm I})^{2n+1}};$$
$$b_{2n+1}^{(1)} = \Lambda_{1,2n+1}^{({\rm I})}, \quad z_{\rm I} = \frac{i}{2}\rho. \tag{17}$$

Similarly, the response of the second cylinder is

$$\Phi_{\rm II}^{(1)}(z) = \beta\sum_{n=0}^{\infty}\frac{d_{2n+1}^{(1)}}{(z-z_{\rm II})^{2n+1}};$$
$$d_{2n+1}^{(1)} = \Lambda_{1,2n+1}^{({\rm II})}, \quad z_{\rm II} = -\frac{i}{2}\rho. \tag{18}$$

In (17) and (18), $\Lambda_{1,2n+1}^{(a)}$ (where a = I or II) are the related principal values of the multipolar moment tensors for the bodies. The sum of $\Phi_{\rm I}^{(1)}(z)$ and $\Phi_{\rm II}^{(1)}(z)$ gives a first-order correction to the complex potential outside the cylinders.

In the second-order approximation, expression (18) is the external field potential relative to the first cylinder. With $z \longrightarrow z_{\rm I}$, we have the following expansions in powers of $(z - z_{\rm I})$:

$$\frac{1}{(z-z_{\rm II})^{2n+1}} = \sum_{k=0}^{\infty}\frac{(-1)^{n+k}}{\rho^{2n+2k+2}}\frac{(2n+2k+1)!}{(2n)!(2k+1)!}(z-z_{\rm I})^{2k+1}$$
$$-i\sum_{k=1}^{\infty}\frac{(-1)^{n+k}}{\rho^{2n+2k+1}}\frac{(2n+2k)!}{(2n)!(2k)!}(z-z_{\rm I})^{2k} - \left(\frac{i}{\rho}\right)^{2n+1} \tag{19}$$
$$(n \geq 0);$$

$$\frac{1}{(z-z_{\rm II})^{2n}} = i\sum_{k=0}^{\infty}\frac{(-1)^{n+k}}{\rho^{2n+2k+1}}\frac{(2n+2k)!}{(2n-1)!(2k+1)!}(z-z_{\rm I})^{2k+1}$$
$$+\sum_{k=1}^{\infty}\frac{(-1)^{n+k}}{\rho^{2n+2k}}\frac{(2n+2k-1)!}{(2n-1)!(2k)!}(z-z_{\rm I})^{2k} + \left(\frac{i}{\rho}\right)^{2n} \tag{20}$$
$$(n \geq 1).$$

The response of the first cylinder to the external nonuniform potential is determined through correspondences following from (6) and (12):

$$(z-z_{\rm I})^{2k+1} \longrightarrow \sum_{n=0}^{\infty}\frac{\Lambda_{2k+1,2n+1}^{({\rm I})}}{(z-z_{\rm I})^{2n+1}}, \tag{21}$$

$$-i(z-z_{\rm I})^{2k} \longrightarrow i\sum_{n=1}^{\infty}\frac{\bar{\Lambda}_{2k,2n}^{({\rm I})}}{(z-z_{\rm I})^{2n}}. \tag{22}$$

In view of (19), (21), and (22), we find the response of the first body to potential (18):

$$\Phi_{\rm I}^{(2)}(z) = \beta\left\{\sum_{n=0}^{\infty}\frac{b_{2n+1}^{(2)}}{(z-z_{\rm I})^{2n+1}} + i\sum_{n=1}^{\infty}\frac{b_{2n}^{(2)}}{(z-z_{\rm I})^{2n}}\right\}, \tag{23}$$

where

$$b_{2n+1}^{(2)} = \sum_{m=0}^{\infty}M_{nm}^{({\rm I})}d_{2m+1}^{(1)}, \quad b_{2n}^{(2)} = \sum_{m=0}^{\infty}P_{nm}^{({\rm I})}d_{2m+1}^{(1)}; \tag{24}$$

$$M_{nm}^{({\rm I})} = \sum_{k=0}^{\infty}\frac{(-1)^{m+k}}{\rho^{2m+2k+2}}\frac{(2m+2k+1)!}{(2m)!(2k+1)!}\Lambda_{2k+1,2n+1}^{({\rm I})} \tag{25}$$
$$(n \geq 0,\ m \geq 0);$$

$$P_{nm}^{({\rm I})} = \sum_{k=1}^{\infty}\frac{(-1)^{m+k}}{\rho^{2m+2k+1}}\frac{(2m+2k)!}{(2m)!(2k)!}\bar{\Lambda}_{2k,2n}^{({\rm I})} \tag{26}$$
$$(n \geq 1,\ m \geq 0).$$

The quantities $d_{2n+1}^{(1)}$ are given in (18). Expression (23) is a second-order correction to the potential induced by the first cylinder. Pure imaginary constants appearing in expansion (19) are omitted in (23).

The response of the second body to external field (17) is found in a similar way. Expansions of $(z - z_{\rm I})^{-n}$ in powers of $(z - z_{\rm II})$ follow from (19) and (20) with the substitution $\rho \longrightarrow -\rho$. The response is determined through correspondences (21) and (22) with superscript I changed to II. Eventually, we obtain

$$\Phi_{\rm II}^{(2)}(z) = \beta\left\{\sum_{n=0}^{\infty}\frac{d_{2n+1}^{(2)}}{(z-z_{\rm II})^{2n+1}} - i\sum_{n=1}^{\infty}\frac{d_{2n}^{(2)}}{(z-z_{\rm II})^{2n}}\right\}, \tag{27}$$

where

$$d_{2n+1}^{(2)} = \sum_{m=0}^{\infty}M_{nm}^{({\rm II})}b_{2m+1}^{(1)}, \quad d_{2n}^{(2)} = \sum_{m=0}^{\infty}P_{nm}^{({\rm II})}b_{2m+1}^{(1)}. \tag{28}$$

Here, $b_{2n+1}^{(1)}$ is given in (17) and expressions for $M_{nm}^{({\rm II})}$ and $P_{nm}^{({\rm II})}$ follow from (25) and (26) with superscript II substituted for I.

In the third approximation, expression (27) is the external field potential relative to the first cylinder. Using expansions (19) and (20) and correspondences (21) and (22), we find the response of the first body:

$$\Phi_{\rm I}^{(3)}(z) = \beta\left\{\sum_{n=0}^{\infty}\frac{b_{2n+1}^{(3)}}{(z-z_{\rm I})^{2n+1}} + i\sum_{n=1}^{\infty}\frac{b_{2n}^{(3)}}{(z-z_{\rm I})^{2n}}\right\}, \tag{29}$$

where

$$b_{2n+1}^{(3)} = \sum_{m=0}^{\infty} M_{nm}^{(\mathrm{I})} d_{2m+1}^{(2)} + \sum_{m=1}^{\infty} N_{nm}^{(\mathrm{I})} d_{2m}^{(2)} \quad (n \geq 0), \quad (30)$$

$$b_{2n}^{(3)} = \sum_{m=0}^{\infty} P_{nm}^{(\mathrm{I})} d_{2m+1}^{(2)} + \sum_{m=1}^{\infty} Q_{nm}^{(\mathrm{I})} d_{2m}^{(2)} \quad (n \geq 1). \quad (31)$$

Here, the matrices $M_{nm}^{(\mathrm{I})}$ and $P_{nm}^{(\mathrm{I})}$ are also defined by (25) and (26), while

$$N_{nm}^{(\mathrm{I})} = \sum_{k=0}^{\infty} \frac{(-1)^{m+k}}{\rho^{2m+2k+1}} \frac{(2m+2k)!}{(2m-1)!(2k+1)!} \Lambda_{2k+1,\,2n+1}^{(\mathrm{I})} \quad (32)$$

$$(n \geq 0, m \geq 1),$$

$$Q_{nm}^{(\mathrm{I})} = \sum_{k=1}^{\infty} \frac{(-1)^{m+k}}{\rho^{2m+2k}} \frac{(2m+2k-1)!}{(2m-1)!(2k)!} \bar{\Lambda}_{2k,\,2n}^{(\mathrm{I})} \quad (33)$$

$$(n \geq 1, m \geq 1).$$

The correction $\Phi_{\mathrm{II}}^{(3)}(z)$ is found in a similar way.

In subsequent approximations, the potential $\Phi_{\mathrm{I}}^{(N)}(z)$ repeats the form of (29) and the coefficients $b_n^{(N)}$ and $d_n^{(N-1)}$ are related by expressions like (30) and (31) with the same matrices $M_{nm}^{(\mathrm{I})}$, $N_{nm}^{(\mathrm{I})}$, $P_{nm}^{(\mathrm{I})}$, and $Q_{nm}^{(\mathrm{I})}$. The same holds for $\Phi_{\mathrm{II}}^{(N)}(z)$.

COMPLEX POTENTIAL OF THE PROBLEM

With the corrections of all orders taken into account, the complex potential outside the cylinders takes the form

$$\Phi(z) = \beta\{z + \Phi_{\mathrm{I}}(z) + \Phi_{\mathrm{II}}(z)\}, \quad (34)$$

where

$$\Phi_{\mathrm{I}}(z) = \sum_{n=0}^{\infty} \frac{b_{2n+1}}{(z-z_{\mathrm{I}})^{2n+1}} + i\sum_{n=1}^{\infty} \frac{b_{2n}}{(z-z_{\mathrm{I}})^{2n}}, \quad (35)$$

$$\Phi_{\mathrm{II}}(z) = \sum_{n=0}^{\infty} \frac{d_{2n+1}}{(z-z_{\mathrm{II}})^{2n+1}} - i\sum_{n=1}^{\infty} \frac{d_{2n}}{(z-z_{\mathrm{II}})^{2n}}. \quad (36)$$

The coefficients b_{2n+1}, b_{2n}, d_{2n+1}, and d_{2n} obey a set of equations that is written in vector form as

$$\mathbf{x}_n - \sum_{m=0}^{\infty} \hat{S}_{nm}^{(\mathrm{I})} \mathbf{y}_m = \mathbf{x}_n^{(1)}, \quad (37)$$

$$\mathbf{y}_n - \sum_{m=0}^{\infty} \hat{S}_{nm}^{(\mathrm{II})} \mathbf{x}_m = \mathbf{y}_n^{(1)}; \quad (38)$$

$$\mathbf{x}_n = \begin{pmatrix} b_{2n+1} \\ b_{2n} \end{pmatrix}, \quad \mathbf{y}_n = \begin{pmatrix} d_{2n+1} \\ d_{2n} \end{pmatrix}; \quad (39)$$

$$\hat{S}_{nm}^{(a)} = \begin{pmatrix} M_{nm}^{(a)} & N_{nm}^{(a)} \\ P_{nm}^{(a)} & Q_{nm}^{(a)} \end{pmatrix}, \quad (40)$$

where the superscript a is I or II.

The matrices M_{nm}, P_{nm}, N_{nm}, and Q_{nm} are given by expressions (25), (26), (32), and (33). Their definitions are extended as

$$N_{n0} = 0, \quad P_{0n} = 0, \quad Q_{0n} = Q_{n0} = 0, \quad (41)$$

since $b_0 = d_0 = 0$. It should also be noted that, by virtue of the equalities $b_{2n}^{(1)} = d_{2n}^{(1)} = 0$, we have

$$\mathbf{x}_n^{(1)} = \begin{pmatrix} b_{2n+1}^{(1)} \\ 0 \end{pmatrix}, \quad \mathbf{y}_n^{(1)} = \begin{pmatrix} d_{2n+1}^{(1)} \\ 0 \end{pmatrix} \quad (42)$$

with $b_{2n+1}^{(1)}$ from (17) and $d_{2n+1}^{(1)}$ from (18).

Solving Eqs. (37) and (38) by iterations, we arrive at an expansion of $\mathbf{x}_n$ in powers of the matrices $\hat{S}_{nm}^{(\mathrm{I})}$ and $\hat{S}_{nm}^{(\mathrm{II})}$:

$$\mathbf{x}_n = \sum_m \Bigg\{ \delta_{nm} + \sum_l \hat{S}_{nl}^{(\mathrm{I})} \hat{S}_{lm}^{(\mathrm{II})} + \sum_j \sum_k \sum_l \hat{S}_{nj}^{(\mathrm{I})} \hat{S}_{jk}^{(\mathrm{II})} \hat{S}_{kl}^{(\mathrm{I})} \hat{S}_{lm}^{(\mathrm{II})} + \ldots \Bigg\} \mathbf{x}_m^{(1)} \quad (43)$$

$$+ \sum_m \Bigg\{ \hat{S}_{nm}^{(\mathrm{I})} + \sum_k \sum_l \hat{S}_{nk}^{(\mathrm{I})} \hat{S}_{kl}^{(\mathrm{II})} \hat{S}_{lm}^{(\mathrm{I})} + \ldots \Bigg\} \mathbf{y}_m^{(1)}.$$

For $\mathbf{y}_n$, we have an expansion like (43) with the substitutions $\mathrm{I} \rightleftharpoons \mathrm{II}$ and $\mathbf{x}_m^{(1)} \rightleftharpoons \mathbf{y}_m^{(1)}$.

The case where an external uniform field is applied along the y axis, so that

$$\bar{\Phi}^{(0)}(z) = -i\beta z \quad (44)$$

is considered in a similar way. The related quantities are marked by a bar:

$$\bar{\Phi}(z) = \beta\{-iz + \bar{\Phi}_{\mathrm{I}}(z) + \bar{\Phi}_{\mathrm{II}}(z)\}, \quad (45)$$

$$\bar{\Phi}_{\mathrm{I}}(z) = i\sum_{n=0}^{\infty} \frac{\bar{b}_{2n+1}}{(z-z_{\mathrm{I}})^{2n+1}} - \sum_{n=1}^{\infty} \frac{\bar{b}_{2n}}{(z-z_{\mathrm{I}})^{2n}}, \quad (46)$$

$$\bar{\Phi}_{\mathrm{II}}(z) = i\sum_{n=0}^{\infty} \frac{\bar{d}_{2n+1}}{(z-z_{\mathrm{II}})^{2n+1}} + \sum_{n=1}^{\infty} \frac{\bar{d}_{2n}}{(z-z_{\mathrm{II}})^{2n}}. \quad (47)$$

The coefficients $\bar{b}_{2n+1}$, $\bar{b}_{2n}$, $\bar{d}_{2n+1}$, and $\bar{d}_{2n}$ obey a set of equations that is written in vector form as

$$\bar{\mathbf{x}}_n + \sum_{m=0}^{\infty} \hat{\bar{S}}^{(\mathrm{I})}_{nm} \bar{\mathbf{y}}_m = \bar{\mathbf{x}}^{(1)}_n, \tag{48}$$

$$\bar{\mathbf{y}}_n + \sum_{m=0}^{\infty} \hat{\bar{S}}^{(\mathrm{II})}_{nm} \bar{\mathbf{x}}_m = \bar{\mathbf{y}}^{(1)}_n. \tag{49}$$

The quantities $\bar{\mathbf{x}}_n$, $\bar{\mathbf{y}}_n$, and $\hat{\bar{S}}^{(a)}_{nm}$ are determined from formulas like (39) and (40). The expressions for the matrices $\bar{M}^{(\mathrm{I})}_{nm}$ and $\bar{N}^{(\mathrm{I})}_{nm}$ follow from (25) and (32), where $\Lambda^{(\mathrm{I})}_{2k+1,\,2n+1}$ is replaced by $\bar{\Lambda}^{(\mathrm{I})}_{2k+1,\,2n+1}$, and those for the matrices $\bar{P}^{(\mathrm{I})}_{nm}$ and $\bar{Q}^{(\mathrm{I})}_{nm}$ follow from (26) and (33), where $\bar{\Lambda}^{(\mathrm{I})}_{2k,\,2n}$ is replaced by $\Lambda^{(\mathrm{I})}_{2k,\,2n}$. The matrices $\bar{M}^{(\mathrm{II})}_{nm}$, $\bar{N}^{(\mathrm{II})}_{nm}$, $\bar{P}^{(\mathrm{II})}_{nm}$, and $\bar{Q}^{(\mathrm{II})}_{nm}$ are found in a like manner. By virtue of equality (14), comparing (48) and (49) with (37) and (38) yields

$$\tilde{\mathbf{x}}_n = -\bar{\mathbf{x}}_n, \quad \tilde{\mathbf{y}}_n = -\bar{\mathbf{y}}_n, \tag{50}$$

hence, the potentials given by (34)–(36) and (45)–(47) satisfy relationship (13).

From the asymptotics of complex potentials (34)–(36) and (45)–(47), one finds the principal values Λ_{xx} and Λ_{yy} of the dipolar polarizability tensor $\hat{\Lambda}$ for a pair of cylinders:

$$\Lambda_{xx} = -\frac{1}{2}(b_1 + d_1), \quad \Lambda_{yy} = -\frac{1}{2}(\bar{b}_1 + \bar{d}_1). \tag{51}$$

From (50), it follows, in particular, that $\bar{b}_1 = -\tilde{b}_1$ and $\bar{d}_1 = -\tilde{d}_1$; hence, from (51), we find that $\Lambda_{yy} = -\tilde{\Lambda}_{xx}$, which coincides with general relationship (14) at $n = m = 0$.

Formula (43) and a similar relationship for $\mathbf{y}_n$ define the expansions of the coefficients b_{2n+1}, b_{2n}, d_{2n+1}, and d_{2n} in powers of the matrices $\hat{S}^{(\mathrm{I})}_{nm}$ and $\hat{S}^{(\mathrm{II})}_{nm}$. From (43), one can also find the expansion in powers of $1/\rho$. Specifically, putting $n = 0$ in (43), we find

$$b_1 = \Lambda^{(\mathrm{I})}_{11} + \frac{1}{\rho^2}\Lambda^{(\mathrm{I})}_{11}\Lambda^{(\mathrm{II})}_{11} + \frac{1}{\rho^4}[(\Lambda^{(\mathrm{I})}_{11})^2\Lambda^{(\mathrm{II})}_{11} - 3\Lambda^{(\mathrm{I})}_{11}\Lambda^{(\mathrm{II})}_{13} - \Lambda^{(\mathrm{II})}_{11}\Lambda^{(\mathrm{I})}_{31}] + \ldots. \tag{52}$$

An expression for d_1 is obtained from (52) with the substitution $\mathrm{I} \rightleftharpoons \mathrm{II}$.

For similar (and equally oriented in the plane x, y) cylinders, Eqs. (37) and (38) are somewhat simplified. Since $\hat{S}^{(\mathrm{I})}_{nm} = \hat{S}^{(\mathrm{II})}_{nm} = \hat{S}_{nm}$ in this case, comparing (43) with a similar expansion for $\mathbf{y}_n$ yields $\mathbf{y}_n = \mathbf{x}_n$; that is, $d_{2n+1} = b_{2n+1}$ and $d_{2n} = b_{2n}$. As a result, the set of Eqs. (37) and (38) is reduced to one vector equation

$$\mathbf{x}_n - \sum_{m=0}^{\infty} \hat{S}_{nm}\mathbf{x}_m = \mathbf{x}^{(1)}_n. \tag{53}$$

THE CASE OF CIRCULAR CYLINDERS

For a circular cylinder of radius R, the multipolar polarizability matrix has diagonal form:

$$\Lambda_{nm} = R^{n+m}\frac{1-h}{1+h}\delta_{nm}, \quad h = \frac{\varepsilon^{(\mathrm{c})}}{\varepsilon^{(e)}}. \tag{54}$$

If the radii of the cylinders are the same, we put

$$b_{2n+1} = \xi_n R^2\delta, \quad b_{2n} = \zeta_m R^2\delta; \quad \delta = \frac{1-h}{1+h}, \tag{55}$$

and reduce Eq. (53) to the form

$$\boldsymbol{\zeta}_n - \sum_{m=0}^{\infty} \hat{S}_{nm}\boldsymbol{\zeta}_m = \mathbf{1}\cdot\delta_{n0}, \tag{56}$$

where

$$\boldsymbol{\zeta}_n = \begin{pmatrix}\xi_n\\ \zeta_n\end{pmatrix}, \quad \mathbf{1} = \begin{pmatrix}1\\ 0\end{pmatrix}. \tag{57}$$

Substituting Λ_{nm} from (54) into (40) yields an expression for the matrix $\hat{S}_{nm}$ ($\zeta_0 = 0$). Solving Eq. (56) by iterations, we obtain

$$\boldsymbol{\zeta}_n = \left\{\delta_{n0} + \hat{S}_{n0} + \sum_{l=0}^{\infty}\hat{S}_{nl}\hat{S}_{l0} + \sum_{k=0}^{\infty}\sum_{l=0}^{\infty}\hat{S}_{nk}\hat{S}_{kl}\hat{S}_{l0} + \sum_{j=0}^{\infty}\sum_{k=0}^{\infty}\sum_{l=0}^{\infty}\hat{S}_{nj}\hat{S}_{jk}\hat{S}_{kl}\hat{S}_{l0} + \ldots\right\}\mathbf{1}. \tag{58}$$

At $n = 0$, (58) yields an expansion of the coefficient ξ_0 in powers of $1/\rho$ and, thereby, an expansion of the polarizability Λ_{xx}:

$$\Lambda_{xx} = -\xi_0 R^2\delta = -R^2\delta\left\{1 + \left(\frac{R}{\rho}\right)^2\delta + \left(\frac{R}{\delta}\right)^4\delta^2 + \left(\frac{R}{\rho}\right)^6(2+\delta)\delta^2 + \left(\frac{R}{\delta}\right)^8(1+\delta)(3+\delta)\delta^2 + \ldots\right\}. \tag{59}$$

Note that expansion (59) could be obtained in a simpler way (other than by using formula (58)). We will

take advantage of the following expedient. At $n = 0$, (56) gives

$$\zeta_0 - \hat{S}_{00}\zeta_0 - \sum_{m=1}^{\infty} \hat{S}_{0m}\zeta_m = \mathbf{1}. \quad (60)$$

Accordingly, at $n \neq 0$,

$$\zeta_0 = \hat{S}_{n0}\zeta_0 + \sum_{m=1}^{\infty} \hat{S}_{nm}\zeta_m. \quad (61)$$

Solving Eq. (61) by iterations, we come to

$$n \neq 0: \zeta_n = \left\{ \hat{S}_{n0} + \sum_{m=1}^{\infty} \hat{S}_{nm}\hat{S}_{m0} + \sum_{l=1}^{\infty}\sum_{m=1}^{\infty} \hat{S}_{nl}\hat{S}_{lm}\hat{S}_{m0} + \ldots \right\}\zeta_0. \quad (62)$$

The substitution of (62) into (60) yields

$$\left\{1 - \hat{S}_{00} - \sum_{m=1}^{\infty} \hat{S}_{0m}\hat{S}_{m0} - \sum_{l=1}^{\infty}\sum_{m=1}^{\infty} \hat{S}_{0l}\hat{S}_{lm}\hat{S}_{m0} - \ldots\right\}\zeta_0 = \mathbf{1}. \quad (63)$$

Hence, we find an expansion of ξ_0^{-1} in powers of R/ρ:

$$\xi_0^{-1} = 1 - \left[\left(\frac{R}{\rho}\right)^2\delta + 2\left(\frac{R}{\rho}\right)^6\delta^2 + 3\left(\frac{R}{\rho}\right)^8\delta^2 + \ldots\right]. \quad (64)$$

Expression (64) gives expansion (59) if $\Lambda_{xx} = -\xi_0 R^2\delta$.

The polarizability of a pair of cylinders can be exactly found in the bipolar coordinates (see, e.g., the associated expression in [7], where the substitution $x \rightleftarrows y$ should be made):

$$\Lambda_{xx} = -\frac{1}{2}(1-h)(\rho^2 - 4R^2)\sum_{n=1}^{\infty} n\frac{1 - \tanh n\mu_0}{h + \tanh n\mu_0}, \quad (65)$$

$$\mu_0 = \ln\frac{\rho + \sqrt{\rho^2 + 4R^2}}{2R}. \quad (66)$$

The expansion of Λ_{xx} from (65) in powers of R/ρ to $(R/\rho)^8$ inclusive gives expression (59).

APPENDIX

In the general form, expansions (6) and (7) have the form

$$\Phi_n(z) = z^n + \sum_{m=1}^{\infty} \frac{\Lambda_{nm} + i\Gamma_{nm}}{z^m}, \quad (A.1)$$

where Λ_{nm} and Γ_{nm} are real constants. For a nonuniform external field with the complex potential in the form

$$\Phi_{2n+1}(z) = z^{2n+1} \quad (A.2)$$

the field strength has the symmetry

$$E_x^0(-x, y) = E_x^0(x, y), \quad E_y^0(-x, y) = -E_y^0(x, y),$$
$$E_x^0(x, -y) = E_x^0(x, y), \quad E_y^0(x, -y) = -E_y^0(x, y). \quad (A.3)$$

If the body is symmetric about the y axis, the total field strength is $E_x(-x, y) = E_x(x, y)$. This is valid only if $\Lambda_{2n+1, 2m} = 0$ and $\Gamma_{2n+1, 2m+1} = 0$; then, the complex potential is given by

$$\Phi_{2n+1}(z) = z^{2n+1} + \sum_{m=0}^{\infty} \frac{\Lambda_{2n+1, 2m+1}}{z^{2m+1}} + i\sum_{m=1}^{\infty} \frac{\Gamma_{2n+1, 2m}}{z^{2m}}. \quad (A.4)$$

In this case, the relationship $E_y(-x, y) = -E_y(x, y)$ is fulfilled identically. If the body is symmetric about the x axis, $E_x(x, -y) = E_x(x, y)$; then,

$$\Phi_{2n+1}(z) = z^{2n+1} + \sum_{m=1}^{\infty} \frac{\Lambda_{2n+1, m}}{z^m}. \quad (A.5)$$

In this case, $E_y(x, -y) = -E_y(x, y)$. Finally, if the body is symmetric about both axes, the complex potential has the form of (6).

For the external field strength with the complex potential in the form

$$\Phi_{2n}^0(z) = z^{2n} \quad (A.6)$$

we have

$$E_x^0(-x, y) = -E_x^0(x, y), \quad E_y^0(-x, y) = E_y^0(x, y),$$
$$E_x^0(x, -y) = E_x^0(x, y), \quad E_y^0(x, -y) = -E_y^0(x, y). \quad (A.7)$$

If the body is symmetric about the y axis, it follows from (A.1) that

$$\Phi_{2n}(z) = z^{2n} + \sum_{m=1}^{\infty} \frac{\Lambda_{2n, 2m}}{z^{2m}} + i\sum_{m=0}^{\infty} \frac{\Gamma_{2n, 2m+1}}{z^{2m+1}}. \quad (A.8)$$

For the body symmetric about the x axis, we have

$$\Phi_{2n}(z) = z^{2n} + \sum_{m=1}^{\infty} \frac{\Lambda_{2n, m}}{z^m}. \quad (A.9)$$

For the body symmetric about both axes, the complex potential has the form of (7).

The potential

$$\bar{\Phi}_n(z) = -i\left\{z^n - \sum_{m=1}^{\infty} \frac{\bar{\Lambda}_{nm} - i\Gamma_{nm}}{z^m}\right\} \quad (A.10)$$

with real $\bar{\Lambda}_{nm}$ and $\bar{\Gamma}_{nm}$ is treated in a similar way. For the body symmetric about the *y* axis,

$$\bar{\Phi}_{2n+1}(z) = -i\left\{z^{2n+1} - \sum_{m=0}^{\infty} \frac{\bar{\Lambda}_{2n+1,2m+1}}{z^{2m+1}} + i\sum_{m=1}^{\infty} \frac{\bar{\Gamma}_{2n+1,2m}}{z^{2m}}\right\}, \quad \text{(A.11)}$$

$$\bar{\Phi}_{2n}(z) = -i\left\{z^{2n} - \sum_{m=1}^{\infty} \frac{\bar{\Lambda}_{2n,2m}}{z^{2m}} + i\sum_{m=0}^{\infty} \frac{\bar{\Gamma}_{2n,2m+1}}{z^{2m+1}}\right\}. \quad \text{(A.12)}$$

Accordingly, for the body symmetric about the *x* axis,

$$\bar{\Phi}_{2n+1}(z) = -i\left\{z^{2n+1} - \sum_{m=1}^{\infty} \frac{\bar{\Lambda}_{2n+1,m}}{z^{m}}\right\}, \quad \text{(A.13)}$$

$$\bar{\Phi}_{2n}(z) = -i\left\{z^{2n} - \sum_{m=1}^{\infty} \frac{\bar{\Lambda}_{2n,m}}{z^{m}}\right\}. \quad \text{(A.14)}$$

Finally, for the body symmetric about both axes, the complex potential has the form of (11) or (12),

REFERENCES

1. W. R. Smythe, *Static and Dynamic Electricity* (Hemisphere, New York, 1989; Inostrannaya Literatura, Moscow, 1954).
2. H. B. Levine and D. A. McQuarrie, J. Chem. Phys. **49**, 4181 (1968).
3. A. A. Lucas, A. Ronveaux, M. Schmeits, *et al.*, Phys. Rev. B **12**, 5372 (1975).
4. A. Goyette and A. Navon, Phys. Rev. B **13**, 4320 (1976).
5. R. Ruppin, Phys. Rev. B **26**, 3440 (1982).
6. B. Ya. Balagurov, Zh. Éksp. Teor. Fiz. **120**, 668 (2001) [JETP **93**, 586 (2001)].
7. A. M. Dykhne, Zh. Éksp. Teor. Fiz. **59**, 110 (1970) [Sov. Phys. JETP **32**, 63 (1970)].
8. B. Ya. Balagurov, Zh. Tekh. Fiz. **53**, 428 (1983) [Sov. Phys. Tech. Phys. **28**, 269 (1983)].
9. B. Ya. Balagurov, Zh. Éksp. Teor. Fiz. **122**, 419 (2002) [JETP **95**, 361 (2002)].

Translated by V. Isaakyan

Technical Physics, Vol. 48, No. 8, 2003, pp. 952–957. Translated from Zhurnal Tekhnicheskoĭ Fiziki, Vol. 73, No. 8, 2003, pp. 13–18.

THEORETICAL AND MATHEMATICAL PHYSICS

Screening of Low-Frequency Electric Fields by a Set of Screens: A Thin Unclosed Ellipsoidal Sheath Plus a Thin-Walled Penetrable Cylinder

S. M. Apollonskiĭ*, V. T. Erofeenko, and G. Ch. Shushkevich*****

** International Academy of Sciences in the Field of Environmental Protection and Life Safety, St. Petersburg, 194021 Russia*

e-mail: appolo@promt.spb.su

*** Belarussian State University, Leningradskaya ul. 14, Minsk, 220050 Belarus*

**** Kupala State University, Grodno, 230023 Belarus*

Received December 17, 2002

Abstract—The problem of penetration of a low-frequency electric field into a thin-walled infinitely long conducting cylinder with an ideally thin unclosed ellipsoidal perfectly conducting sheath on its axis is solved by the method of paired equations, which is combined with addition theorems and relevant averaged boundary conditions. The effect of the vertex angle of the unclosed ellipsoidal sheath on the coefficient of field attenuation inside the sheath is numerically evaluated for different screen geometries. © *2003 MAIK "Nauka/Interperiodica".*

The screening of electromagnetic fields is an important electrodynamic problem from both scientific and applied points of view. In the case of thin-walled screens, electromagnetic processes inside the screen are not studied; instead, electromagnetic fields on both sides of the screen are related to each other through equivalent boundary conditions defined on the screen's midplane [1–3]. Such an approach is rigorous if the thickness of the screen does not exceed the penetration depth of the field. In this work, we consider the penetration of a low-frequency electric field through a thin-walled conducting cylinder in the presence of a thin unclosed ellipsoidal perfectly conducting sheath. Results obtained may be useful in designing screening systems.

STATEMENT OF THE SCREENING PROBLEM

Let a thin-walled infinitely long cylinder Γ of thickness Δ be placed in an isotropic space R^3 with a permittivity ε_0. Also, let an ideally thin perfectly conducting unclosed extended ellipsoidal sheath S be placed on the axis of the cylinder. The sheath covers an oblong ellipsoid of revolution S_1 (see figure). The cylinder Γ is filled with a medium of permittivity ε, permeability μ, and electrical conductivity γ. An electric charge q varying by the law $q\cos\omega t$, where ω is the circular frequency, is uniformly distributed over a circle of radius $l > d$.

The point O is taken to be the origin of the cylindrical, $\{\rho, \varphi, z\}$, and degenerate ellipsoidal, $\{\alpha, \beta, \varphi\}$, coordinates. In the coordinate system $\{\alpha, \beta, \varphi\}$, the sheath is described as

$$S = \left\{\alpha = \alpha_0 = \operatorname{arccosh}\frac{b}{c},\ 0 \le \beta \le \beta_0 < \pi,\ 0 \le \varphi \le 2\pi\right\},$$

where $c = \sqrt{b^2 - a^2}$ is half the focus spacing and a and

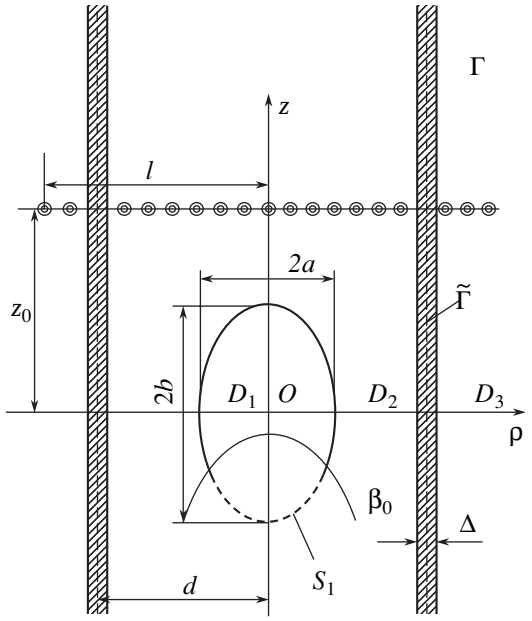

Figure.

1063-7842/03/4808-0952$24.00 © 2003 MAIK "Nauka/Interperiodica"

b are the major and minor axes of the ellipsoid, respectively.

Next, it is assumed that the surface of the ellipsoid S_1 and the midsurface $\tilde{\Gamma}$ of the cylinder Γ conventionally partition the entire space R^3 into three domains: D_1, interior of the ellipsoid S_1; D_3, domain outside the cylinder $\tilde{\Gamma}$; and $D_2 = R^3 \backslash (\bar{D}_1 \cup \bar{D}_2)$.

We consider the scattering of the primary electric field by the set of screens Γ and S with allowance for field penetration through the cylindrical layer Γ (the sheath S is assumed to be impenetrable to the field).

Let us denote the potentials of the primary and secondary fields in a domain D_j as U_d and U_j, respectively ($j = 1, 2, 3$). In the quasi-stationary approximation, the solution of the problem is reduced to finding electric potentials in domains D_j ($j = 1, 2, 3$). These potentials must satisfy

(i) the Laplace equation $\Delta U_j = 0$ (here, Δ is the Laplacian operator);

(ii) the boundary conditions at the midsurface $\tilde{\Gamma}$ [4, p. 86], which describe the penetration of the field through the thin-walled cylindrical layer Γ:

$$\frac{\partial}{\partial \rho}(U_3 + U_\mathrm{d} - U_2)\big|_{\tilde{\Gamma}} = -pF(U_3 + U_\mathrm{d} + U_2)\big|_{\tilde{\Gamma}}, \quad (1)$$

$$\frac{\partial}{\partial \rho}(U_3 + U_\mathrm{d} + U_2)\big|_{\tilde{\Gamma}} = qF(U_3 + U_\mathrm{d} - U_2)\big|_{\tilde{\Gamma}}, \quad (2)$$

where

$$p = \frac{\varepsilon'\delta}{2\varepsilon_0}, \quad q = \frac{2}{\omega^2 \delta \mu \varepsilon_0}, \quad \delta = \frac{2}{k}\tan\left(\frac{k\Delta}{2}\right),$$

$$k = \omega\sqrt{\mu\varepsilon'}, \quad 0 \le \arg k < \pi,$$

$$\varepsilon' = \varepsilon + i\frac{\gamma}{\omega}$$

is the complex permittivity, $\omega = 2\pi f$ is the circular frequency of the field, $F(U_j) = \mathbf{n} \cdot \nabla \times [\mathbf{n} \times \nabla U_j])$ is the boundary operator on the midsurface $\tilde{\Gamma}$ of the cylindrical layer Γ, and $\mathbf{n}$ is the unit vector to the surface $\tilde{\Gamma}$ directed inward to the domain D_3;

(iii) the boundary condition on the surface of the thin unclosed ellipsoidal perfectly conducting sheath S

$$U_2(M)\big|_{M \in S} = V = \mathrm{const}, \quad (3)$$

and (iv) the condition at infinity

$$U_j(M) \longrightarrow 0 \quad \text{for} \quad M \longrightarrow \infty; \quad j = 2, 3, \quad (4)$$

where M is an arbitrary point in a domain D_j.

We also require that the continuity conditions for the potential on the surface S_1 and for the field on the uncovered surface part $S_1 \backslash S$ of the ellipsoid be met:

$$U_1 = U_2, \quad \alpha = \alpha_0, \quad 0 \le \beta \le \pi, \quad (5)$$

$$\frac{\partial U_1}{\partial \alpha} = \frac{\partial U_2}{\partial \alpha}, \quad \alpha = \alpha_0, \quad \beta_0 < \beta \le \pi. \quad (6)$$

The boundary operator $F(U_j)$ in the cylindrical coordinate system is represented as [3]

$$F(U_j) = \frac{1}{\rho^2}\frac{\partial^2}{\partial \varphi^2}U_j + \frac{\partial^2}{\partial z^2}U_j. \quad (7)$$

SOLUTION OF THE PROBLEM

The primary field potential is represented as

$$U_\mathrm{d} = U_0 \int_{-\infty}^{\infty} f(\lambda)\frac{I_0(\lambda\rho)}{I_0(\lambda d)}\exp(i\lambda z)\,dz, \quad (8)$$

where

$$U_0 = \frac{q}{4\pi^2\varepsilon_0}; \quad f(\lambda) = K_0(|\lambda| l) I_0(\lambda d)\exp(-i\lambda z_0)$$

(z_0 is a distance to the origin).

The potentials U_j are sought as a superposition of cylindrical and ellipsoidal harmonic functions that satisfies condition at infinity (4):

$$U_1(\alpha, \beta) = \frac{U_0}{d}\sum_{n=0}^{\infty} \tilde{y}_n \frac{P_n(\cosh\alpha)}{P_n(\cosh\alpha_0)} P_n(\cos\beta) \text{ in } D_1,$$
$$U_2 = U_2^{(1)}(\alpha, \beta) + U_2^{(2)}(\rho, z) \text{ in } D_2, \quad (9)$$

where

$$U_2^{(1)}(\alpha, \beta) = \frac{U_0}{d}\sum_{n=0}^{\infty} y_n \frac{Q_n(\cosh\alpha)}{Q_n(\cosh\alpha_0)} P_n(\cos\beta), \quad (10)$$

$$U_2^{(2)}(\rho, z) = U_0 \int_{-\infty}^{\infty} Z(\lambda)\frac{I_0(\lambda\rho)}{I_0(\lambda d)}\exp(i\lambda z)\,d\lambda, \quad (11)$$

$$U_3(\rho, z) = U_0 \int_{-\infty}^{\infty} \tilde{Z}(\lambda)\frac{K_0(|\lambda|\rho)}{K_0(|\lambda| d)}\exp(i\lambda z)\,d\lambda \text{ in } D_3. \quad (12)$$

Here, $P_n(\cos\beta)$ are Legendre polynomials; $P_n(z)$ and $Q_n(z)$ are the Legendre functions of the first and second kinds, respectively; $I_\mathrm{m}(x)$ is the modified Bessel function of the first kind; and $K_\mathrm{m}(x)$ is the modified Bessel function of the second kind (Macdonald function) [5–8].

The unknown coefficients $\tilde{y}_n$ and y_n, as well as the functions $\tilde{Z}(\lambda)$ and $Z(\lambda)$, are found from the boundary conditions.

SATISFACTION OF THE BOUNDARY CONDITIONS

To meet boundary conditions (1) and (2), we express the potential $U_2^{(1)}(\alpha, \beta)$ through cylindrical harmonic functions, using relevant addition theorems [3, 9]. Then,

$$U_2^{(1)}(\rho, z) = U_0 \int_{-\infty}^{\infty} M(\lambda) K_0(|\lambda|\rho) \exp(i\lambda z) d\lambda, \quad (13)$$

where

$$M(\lambda) = \frac{c}{\pi d} \sum_{n=0}^{\infty} \frac{j_n(c\lambda)}{i^n Q_n(\cosh\alpha_0)} y_n, \quad (14)$$

and $j_n(z)$ is the spherical Bessel function of the first kind [5, 9].

Taking into account representation (8), representations (11)–(13), and representation (7) of the boundary operator $F(U_j)$ in the cylindrical coordinate system subject to boundary conditions (1) and (2), we obtain the set of equations

$$\begin{aligned}
&(K_0'(x)|\lambda| - \lambda^2 p K_0(x)) I_0(x) \tilde{Z}(\lambda) \\
&- (I_0'(x)|\lambda| + \lambda^2 p I_0(x)) K_0(x) Z(\lambda) \\
&= (K_0'(x)|\lambda| + \lambda^2 p K_0(x)) I_0(x) K_0(x) M(\lambda) \\
&+ (\lambda^2 p I_0(x) - |\lambda| I_0'(x)) K_0(x) f(\lambda), \\
&(K_0'(x)|\lambda| + \lambda^2 q K_0(x)) I_0(x) \tilde{Z}(\lambda) \\
&+ (I_0'(x)|\lambda| - \lambda^2 q I_0(x)) K_0(x) Z(\lambda) \\
&= (-K_0'(x)|\lambda| + \lambda^2 q K_0(x)) I_0(x) K_0(x) M(\lambda) \\
&- (\lambda^2 q I_0(x) + |\lambda| I_0'(x)) K_0(x) f(\lambda),
\end{aligned}$$

where $x = |\lambda|d$.

Solving this set of equations, we find

$$Z(\lambda) = Z_1(|\lambda|d) f(\lambda) + I_0(\lambda d) M(\lambda) Z_2(|\lambda|d), \quad (15)$$

where

$$Z_1(|\lambda|d) = \frac{(q+p)}{d} \frac{(\lambda d)^2}{\Delta(|\lambda|d)},$$

$$Z_2(|\lambda|d) = -\frac{2}{\Delta(|\lambda|d)} \Big[(\lambda d)^2 (K_1(|\lambda|d))^2 + \frac{pq}{d^2} (\lambda d)^4 (K_0(|\lambda|d))^2 \Big],$$

$$\Delta(|\lambda|d) = \frac{q-p}{d} \lambda d^2 - 2(\lambda d)^2 K_1(|\lambda|d) I_1(|\lambda|d) + 2\frac{pq}{d^2} (\lambda d)^4 K_0(|\lambda|d) I_0(|\lambda|d).$$

To meet boundary conditions (3), (5), and (6), we represent $U_2^{(2)}(\rho, z)$ through ellipsoidal harmonic functions, using a relevant addition theorem [3, 9]. Then,

$$U_2^{(2)}(\alpha, \beta) = U_0 \sum_{n=0}^{\infty} D_n P_n(\cosh\alpha) P_n(\cos\beta), \quad (16)$$

where

$$D_n = i^n (2n+1) \int_{-\infty}^{\infty} \frac{j_n(c\lambda)}{I_0(\lambda d)} Z(\lambda) d\lambda. \quad (17)$$

In view of representations (9), (10), and (16) and the orthogonality of the Legendre polynomials $P_n(\cos\beta)$ within the segment $[0, \pi]$, the continuity condition for the potential on the surface of the ellipsoid S_1 is equivalent to the condition

$$\tilde{y}_n = y_n + d D_n P_n(\cosh\alpha_0); \quad n = 0, 1, 2, \ldots. \quad (18)$$

Meeting boundary conditions (3) and (6) and taking into account representation (18) and Wronskian [7]

$$W\{P_n(\cosh\alpha), Q_n(\cosh\alpha)\} = -\frac{1}{\sinh^2\alpha},$$

we arrive at the paired summational equations

$$\begin{aligned}
&\sum_{n=0}^{\infty} y_n P_n(\cos\beta) = \sum_{n=0}^{\infty} (V_0 \delta_{0n} - d D_n P_n(\cosh\alpha_0)) P_n(\cos\beta), \\
&0 \le \beta < \beta_0, \\
&\sum_{n=0}^{\infty} \frac{y_n}{\sinh\alpha_0 P_n(\cosh\alpha_0) Q_n(\cosh\alpha_0)} P_n(\cos\beta) = 0, \\
&\beta_0 < \beta < \pi,
\end{aligned} \quad (19)$$

where δ_{0n} is the Kronecker symbol and $V_0 = V_d/U_0$.

We introduce new coefficients T_n by the formula

$$y_n = (2n+1) \sinh\alpha_0 P_n(\cosh\alpha_0) Q_n(\cosh\alpha_0) T_n \quad (20)$$

and a small parameter

$$\begin{aligned}
g_n &= 1 - (2n+1) \sinh\alpha_0 P_n(\cosh\alpha_0) Q_n(\cosh\alpha_0), \\
g_n &= O(n^{-2}) \quad \text{at} \quad n \longrightarrow \infty.
\end{aligned} \quad (21)$$

Then, paired equations (19) take the form

$$\sum_{n=0}^{\infty} (1 - g_n) T_n P_n(\cos\beta)$$

$$= \sum_{n=0}^{\infty} (V_0\delta_{0n} - dD_nP_n(\cosh\alpha_0))P_n(\cos\beta), \quad \beta < \beta_0,$$

$$\sum_{n=0}^{\infty} (2n+1)T_nP_n(\cos\beta) = 0, \quad \beta_0 < \beta.$$

The above paired summational equations can be transformed to an infinite set of linear algebraic equations (SLAEs) of the second kind for the coefficients $T_n \in l_2$ [8, 9]:

$$T_s - \sum_{n=0}^{\infty} g_nQ_{sn}T_n = V_0Q_{s0} - d\sum_{n=0}^{\infty} D_nP_n(\cosh\alpha_0)Q_{ns}, \quad s = 0, 1, 2, \ldots, \tag{22}$$

where

$$Q_{ns} = \frac{2}{\pi}\int_0^{\beta_0} \cos\left(n+\frac{1}{2}\right)x\cos\left(s+\frac{1}{2}\right)xdx$$

or

$$Q_{ns} = \frac{1}{\pi}\left[\frac{\sin(n-s)\beta_0}{(n-s)} + \frac{\sin(n+s+1)\beta_0}{(n+s+1)}\right],$$

$$\left.\frac{\sin(n-s)\beta_0}{(n-s)}\right|_{n=s} = \beta_0.$$

From representation (14) and (20), it follows that

$$M(\lambda) = \frac{c\sinh\alpha_0}{\pi d} \times \sum_{k=0}^{\infty} (-i)^k(2k+1)j_k(c\lambda)P_k(\cosh\alpha_0)T_k. \tag{23}$$

Using representations (15), (17) and (23), we rearrange the right of (22) to obtain the infinite SLAEs

$$T_s - \sum_{n=0}^{\infty} [g_nQ_{sn} - \alpha_{ns}]T_n = V_0Q_{s0} - f_s; \quad s = 0, 1, 2, \ldots, \tag{24}$$

where

$$\alpha_{ns} = \frac{\sinh\alpha_0}{\pi}(-1)^n(2n+1)P_n(\cosh\alpha_0) \times \sum_{p=0}^{\infty} i^{n+p}(2p+1)P_p(\cosh\alpha_0)Q_{ps}I_{np}, \tag{25}$$

$$I_{np} = 2\tau\int_0^{\infty} j_n(\tau t)j_p(\tau t)Z_2(t)dt, \quad \tau = \frac{c}{d} \quad \text{for even } n+p, \tag{26}$$

$$f_s = \sum_{n=0}^{\infty} (2n+1)P_n(\cosh\alpha_0)Q_{ns}J_n, \tag{27}$$

$$J_n = 2\int_0^{\infty} j_n(\tau t)Z_1(t)K_0(\sigma t)p_n(t)dt, \quad \sigma = \frac{l}{d},$$

$$p_n(t) = \begin{cases} (-1)^{\frac{n}{2}}\cos\left(\frac{z_0}{d}t\right) & \text{for even } n, \\ (-1)^{\frac{n+3}{2}}\sin\left(\frac{z_0}{d}t\right) & \text{for odd } n. \end{cases} \tag{28}$$

FIELD ATTENUATION (SCREENING) COEFFICIENT

In the absence of the screens, the primary field strength at an arbitrary point $M_0(\rho, z)$ of the space is given by

$$\mathbf{E}_d(M_0) = -\left(\frac{\partial U_d}{\partial\rho}\mathbf{e}_\rho + \frac{\partial U_d}{\partial z}\mathbf{e}_z\right)$$

$$= -U_0\left[\int_{-\infty}^{\infty} f(\lambda)\frac{I_0'(\lambda\rho)}{I_0(\lambda d)}\lambda e^{i\lambda z}d\lambda\mathbf{e}_\rho + \int_{-\infty}^{\infty} f(\lambda)\frac{I_0(\lambda\rho)}{I_0(\lambda d)}(i\lambda)e^{i\lambda z}d\lambda\mathbf{e}_z\right].$$

If the point $M_0(\rho, z)$ lies on the axis Oz, $\rho = 0$, $I_0(0) = 1$, and $I_1(0) = 0$. Therefore,

$$\mathbf{E}_d(0, z) = -U_0\int_{-\infty}^{\infty} f(\lambda)(i\lambda)e^{i\lambda z}d\lambda\mathbf{e}_z = \frac{2U_0}{d^2}\int_0^{\infty} K_0(\sigma t)I_0(t)t\sin\left[\frac{t(z-z_0)}{d}\right]dt\mathbf{e}_z. \tag{29}$$

The secondary field strength at an arbitrary point $M_0(\rho, z)$ on the axis Oz in the domain D_2 is given by

$$\mathbf{E}_2(M_0) = \mathbf{E}_2^{(1)}(M_0) + \mathbf{E}_2^{(2)}(M_0), \tag{30}$$

where

$$\mathbf{E}_2^{(2)}(M_0) = -\left(\frac{\partial U_2^{(2)}}{\partial \rho}\mathbf{e}_\rho + \frac{\partial U_2^{(2)}}{\partial z}\mathbf{e}_z\right)\Big|_{\rho=0}$$

$$= -U_0\int_{-\infty}^{\infty}\frac{Z(\lambda)}{I_0(\lambda d)}(i\lambda)e^{i\lambda z}d\lambda\mathbf{e}_z.$$

In view of representations (15) and (23), we obtain after rearrangements

$$\mathbf{E}_2^{(2)}(0, z) = -U_0[I_{12}(z) + I_{22}(z)]\mathbf{e}_z, \qquad (31)$$

where

$$I_{12}(z) = -\frac{2}{d^2}\int_0^\infty Z_1(t)K_0(\sigma t)t\sin\left(\frac{t(z-z_0)}{d}\right)dt,$$

$$I_{22}(z) = \frac{2c\sinh\alpha_0}{\pi d^3}\sum_{k=0}^{\infty}(2k+1)P_k(\cosh\alpha_0)T_kH_k(z),$$

$$H_k(z) = \int_0^\infty Z_2(t)j_k(\tau t)tW_k(z, t)dt,$$

$$W_k(t, z) = \begin{cases}(-1)^{\frac{3k+2}{2}}\sin\left(\frac{z}{d}t\right) & \text{for even } k\\ (-1)^{\frac{3k+2}{2}}\cos\left(\frac{z}{d}t\right) & \text{for odd } k.\end{cases}$$

According to representation (10),

$$\mathbf{E}_2^{(1)}(M_0) = -\frac{1}{c\sqrt{\sinh^2\alpha + \sin^2\beta}}\left[\frac{\partial U_2^{(1)}}{\partial\alpha}\mathbf{e}_\alpha + \frac{\partial U_2^{(1)}}{\partial\beta}\mathbf{e}_\beta\right],$$

where

$$\frac{\partial U_2^{(1)}}{\partial\alpha} = \frac{U_0\sinh\alpha}{d}$$

$$\times\sum_{n=0}^{\infty}\frac{y_n}{Q_n(\cosh\alpha_0)}\frac{d}{d\xi}Q_n(\xi)|_{\xi=\cosh\alpha}P_n(\cos\beta),$$

$$\frac{\partial U_2^{(1)}}{\partial\beta} = -\frac{U_0}{d}\sin\beta\sum_{n=0}^{\infty}\frac{y_n}{Q_n(\cosh\alpha_0)}$$

$$\times Q_n(\cosh\alpha)\frac{d}{d\xi}P_n(\xi)|_{\xi=\cos\beta}.$$

If the point is on the Oz axis, $|z| > b$ and $\beta = 0$ or π; therefore,

$$\mathbf{E}_2^{(1)}(0, z) = \begin{cases}\mathbf{E}_2^{(1+)}(0, z) = -\frac{1}{c\sinh\alpha}\frac{\partial U_2^{(1)}}{\partial\alpha}\mathbf{e}_z,\\ \text{if} \quad z > b,\ \beta = 0\\ \mathbf{E}_2^{(1-)}(0, z) = \frac{1}{c\sinh\alpha}\frac{\partial U_2^{(1)}}{\partial\alpha}\mathbf{e}_z,\\ \text{if} \quad z < -b,\ \beta = \pi,\end{cases}$$

where

$$\mathbf{E}_2^{(1+)}(0, z) = -U_0\frac{\sinh\alpha_0}{cd}\sum_{n=0}^{\infty}(2n+1)$$

$$\times P_n(\cosh\alpha_0)T_n\frac{d}{d\xi}Q_n(\xi)|_{\xi=\frac{z}{c}}\mathbf{e}_z,$$

$$\mathbf{E}_2^{(1-)}(0, z) = U_0\frac{\sinh\alpha_0}{cd}\sum_{n=0}^{\infty}(-1)^n(2n+1)$$

$$\times P_n(\cosh\alpha_0)T_n\frac{d}{d\xi}Q_n(\xi)|_{\xi=\frac{z}{c}}\mathbf{e}_z.$$

The coefficient of field screening (attenuation) at a point $M_0(0, z)$ located on the Oz axis in the domain D_2 is calculated by the formula

$$K_2^{(\pm)}(z) = \frac{\left|\mathbf{E}_2^{(1\pm)}(0, z) + \mathbf{E}_2^{(2)}(0, z)\right|}{\mathbf{E}_\mathrm{d}(0, z)}. \qquad (32)$$

The secondary field strength at an arbitrary point M_0 located on the Oz axis in the domain D_1 is given by

$$\mathbf{E}_1(0, z) = \begin{cases}\mathbf{E}_1^{(+)}(0, z) = -\frac{1}{c\sinh\alpha}\frac{\partial U_1}{\partial\alpha}\mathbf{e}_z,\\ \text{if} \quad 0 \le z < b,\ \beta = 0\\ \mathbf{E}_1^{(-)}(0, z) = \frac{1}{c\sinh\alpha}\frac{\partial U_1}{\partial\alpha}\mathbf{e}_z,\\ \text{if} \quad -b < z \le 0,\ \beta = \pi,\end{cases}$$

where

$$\mathbf{E}_1^{(+)}(0, z) = -\frac{U_0}{cd}\sum_{n=0}^{\infty}\frac{\tilde{y}}{P_n(\cosh\alpha_0)}\frac{d}{d\xi}P_n(\xi)|_{\xi=\frac{z}{c}}\mathbf{e}_z,$$

$$\mathbf{E}_1^{(-)}(0, z) = \frac{U_0}{cd}\sum_{n=0}^{\infty}(-1)^n\frac{\tilde{y}}{P_n(\cosh\alpha_0)}\frac{d}{d\xi}P_n(\xi)|_{\xi=\frac{z}{c}}\mathbf{e}_z.$$

From representations (15), (17), (18), (20), and (23), it follows that

$$\frac{\tilde{y}}{P_n(\cosh\alpha_0)} = (2n+1)\sinh\alpha_0Q_n(\cosh\alpha_0)T_n$$

Table

$\frac{z}{b}$	Vertex angle Θ_0 of the unclosed ellipsoidal sheath, deg		
	60	90	120
$\frac{2}{15}$	$\frac{0.956}{0.016}$	$\frac{0.943}{0.0078}$	$\frac{0.551}{0.00045}$
$\frac{3}{15}$	$\frac{0.695}{0.011}$	$\frac{0.694}{0.0047}$	$\frac{0.291}{0.00041}$
$\frac{4}{15}$	$\frac{0.429}{0.0089}$	$\frac{0.421}{0.0031}$	$\frac{0.173}{0.00039}$
$\frac{1}{3}$	$\frac{0.284}{0.0073}$	$\frac{0.274}{0.0021}$	$\frac{0.112}{0.00038}$
$\frac{7}{15}$	$\frac{0.137}{0.0051}$	$\frac{0.131}{0.0011}$	$\frac{0.05}{0.00037}$
$\frac{3}{5}$	$\frac{0.069}{0.0034}$	$\frac{0.067}{0.00056}$	$\frac{0.024}{0.00036}$
$\frac{11}{15}$	$\frac{0.039}{0.0021}$	$\frac{0.037}{0.00039}$	$\frac{0.013}{0.00035}$
$\frac{13}{15}$	$\frac{0.018}{0.00094}$	$\frac{0.016}{0.00028}$	$\frac{0.008}{0.00024}$

$$+ (2n+1)J_n + \frac{\sinh\alpha_0}{\pi}(2n+1)$$

$$\times \sum_{k=0}^{\infty} (-1)^k i^{n+k}(2k+1)P_k(\cosh\alpha_0)T_k I_{nk}.$$

The coefficient of field screening (attenuation) at a point $M_0(0, z)$ located on the Oz axis in the domain D_1 is calculated by the formula

$$K_1^{(+)}(z) = \frac{\left|\mathbf{E}_1^{(\pm)}(0, z)\right|}{\left|\mathbf{E}_\mathrm{d}(0, z)\right|}. \qquad (33)$$

COMPUTATIONAL EXPERIMENT

Using the MathCAD 2000 software package [10], we calculated the screening coefficient $K_1^+(z)$ in the domain D_1 by formula (33) for various geometries of the screen and various material parameters of the thin-walled cylinder Γ. Infinite sums (25) and (27) were calculated accurate to 10^{-6}. Infinite SLAEs (24) was solved by the truncation method [11] with an accuracy of 10^{-5}. The calculation was performed for the thin-walled cylinder Γ made of organic glass (relative permittivity $\varepsilon_r = 3.7$, $\gamma = 10^{-12}$ $(\Omega\,\mathrm{m})^{-1}$) [12] and of the PPV material ($\varepsilon_r = 5$, $\gamma = 0.1$ $(\Omega\,\mathrm{m})^{-1}$). Here, $\varepsilon_r = \varepsilon/\varepsilon_0$, $\varepsilon_0 = \frac{1}{\mu_0 c^2} \approx (1/36\pi) \times 10^{-9}$ F/m, and $\mu_0 = 4\pi \times 10^{-7}$ H/m.

The table lists the screening coefficient $K_1^+(z)$ versus vertex angle Θ_0 of the unclosed ellipsoidal sheath S and position of the point $M_0(0, z)$ for $b/a = 1.5$, $d/b = 2$, $d/l = 0.6$, $\Delta = 0.01d$, $V = 0$, $z_0 = 0$, and $f = 50$ Hz. In each of the rows, the upper and lower values correspond to the organic glass and PPV material, respectively.

Based on the computational experiment, one can draw the following conclusions.

(1) For the thin-walled cylinder Γ made of the PPV material, the screening coefficient $K_1^{(+)}(z)$ is virtually zero for any vertex angle Θ_0 of the ellipsoidal sheath S; in other words, the field does not penetrate into the domain D_1.

(2) The greater the angle Θ_0, the smaller $K_1^{(+)}(z)$.

(3) As z increases, the screening coefficient $K_1^{(+)}(z)$ decreases for any vertex angle Θ_0 of the ellipsoidal sheath S.

REFERENCES

1. S. V. Zhukov, Izv. Akad. Nauk SSSR, Énerg. Transp., No. 5, 54 (1983).
2. V. E. Shpitsberg, Izv. Akad. Nauk SSSR, Énerg. Transp., No. 1, 110 (1989).
3. V. T. Erofeenko, *Electromagnetic Fields in Screening Shells* (Minsk. Gos. Univ., Minsk, 1988).
4. S. M. Apollonskiĭ and V. T. Erofeenko, *Equivalent Boundary Conditions in Electrodynamics* (Bezopasnost, St. Petersburg, 1999).
5. N. N. Lebedev, *Special Functions and Their Applications* (Fizmatgiz, Moscow, 1963; Prentice-Hall, Englewood Cliffs, 1965).
6. V. Ya. Arsenin, *Methods of Mathematical Physics and Special Functions* (Nauka, Moscow, 1984).
7. *Handbook of Mathematical Functions with Formulas, Graphs, and Mathematical Tables*, Ed. by M. Abramowitz and I. A. Stegun (Dover, New York, 1972; Nauka, Moscow, 1979).
8. Ya. S. Uflyand, *Method of Paired Equations in Problems of Mathematical Physics* (Nauka, Leningrad, 1977).
9. G. Ch. Shushkevich, *Calculation of Electrostatic Fields by the Methods of Paired and Triple Equations Using Addition Theorems* (Grodnensk. Gos. Univ., Grodno, 1999).
10. G. Ch. Shushkevich and S. V. Shushkevich, *Introduction to MathCAD 2000* (Grodnensk. Gos. Univ., Grodno, 2001).
11. L. V. Kantorovich and V. I. Krylov, *Approximate Methods of Higher Analysis* (Fizmatgiz, Moscow, 1962; Wiley, New York, 1964).
12. A. S. Enokhovich, *Handbook of Physics* (Prosveshchenie, Moscow, 1990).

Translated by V. Isaakyan

Technical Physics, Vol. 48, No. 8, 2003, pp. 958–963. Translated from Zhurnal Tekhnicheskoĭ Fiziki, Vol. 73, No. 8, 2003, pp. 19–24.

THEORETICAL AND MATHEMATICAL PHYSICS

On Oscillatory Wave Processes on the Surface of Massive Bodies Nonuniform in Composition

S. O. Gladkov

Moscow State Regional University, ul. Radio 10a, Moscow, 105005 Russia

e-mail: Sglad@newmail.ru

Received December 25, 2002

Abstract—A set of interrelated nonlinear differential equations describing the simultaneous oscillations of material density (acoustic waves) and gravitational potential is derived in terms of Lagrangean formalism (taking into account the gravitational potential is necessary when massive bodies are considered). The natural frequencies of these oscillations are found. It is shown that, when interacting with the gravitational potential, the spectrum of the surface waves is greatly distorted and depends on the 2D surface wavevector not linearly (as a typical spectrum of phonons in a solid) but quadratically. The concept proposed in this work allows one to detect additional acoustic low-frequency signals due to internal disturbances. It is stated that a separate consideration of acoustic and gravitational waves is incorrect because of the strong correlation between them. *© 2003 MAIK "Nauka/Interperiodica".*

INTRODUCTION

The subject considered in this paper appertains to a class of purely theoretical problems. We will investigate surface oscillatory processes incident only to massive bodies. Although the investigation technique used is by no means new (the well-known least action method [1]), its efficiency and accuracy (repeatedly verified in practice) allow one to solve a variety of problems in any area of physics (ranging from the derivation of the Gilbert–Einstein equations to those encountered in the physics of combustion and explosion [2]), as well as synergetics problems [3–5].

This issue seems to be timely and topical, since such surface waves generate the natural noise background of massive bodies, any variation of which (that is, the occurrence of additional noise) may be considered as a prediction of some phenomena. It is clear that such an important issue cannot be ignored, and the objective of this communication is to fill this gap.

STATEMENT OF THE PROBLEM

Let a large plane area of the surface of a massive body have a characteristic linear size L^* such that $L^* \ll R_0$, where R_0 is the radius of the body. We assume that surface irregularities within an area $\sigma = L^{*2}$ have a linear size $|l^*| \ll L^*$ and the characteristic wavelengths of the oscillations satisfy the inequality $\lambda \gg |l^*|$. Note that the condition $|l^*| \ll L^*$ does not limit the generality of the subsequent analysis and may be considered only as a limitation imposed on the wavelength of nonuniform oscillations (see below). Indeed, let the wavevector of these oscillations obey the inequality $q_z|l^*| \ll 1$. Note that the modulus sign in this inequality merely means that we are dealing with either convex or concave surface areas. Later on, the modulus sign will be omitted.

As for transverse oscillations (relative to the z axis directed along the radius), we limit their wavevector by the inequality $q_{x,y}l^* \gg 1$. The density of the structure over the surface area σ and at depths of $h \geq l^*$ is defined by a function $\rho = \rho(\mathbf{x})$, where $\mathbf{x} = (x, y)$. The characteristic intervals δx of density variation $\delta\rho$ satisfy the inequality $\delta x \geq l^*$. Assume that the function $\rho(\mathbf{x})$ is monotone, differentiable, and is found by averaging a certain local density $\rho_1(\mathbf{x})$ over regions $v_0 < l^{*3}$ with a weight $G(\xi, \eta, z)$. This means that $\rho(\mathbf{x}) = \int \rho_1(x - \xi, y - \eta, z)G(\xi, \eta, z)d\xi d\eta dz$. The Newtonian potential $\varphi(r)$, as is well known [1], satisfies the Poisson equation $\Delta\varphi = 4\pi k\rho$ in the nonrelativistic limit, where k is the gravitation constant. The solution to this equation in the spherically symmetric case, when φ depends only on the radial coordinate r, is

$$\varphi(r) = \begin{cases} -mk/r & \text{at} \quad r \geq R_0 \\ (2\pi k\rho_0/3)(r^2 - 3R_0^2) & \text{at} \quad r \leq R_0, \end{cases} \tag{1}$$

where R_0 is the body mean radius and m is the body mass.

We emphasize that the density ρ varies only on the surface but not along the radius; that is, the density ρ is taken at $z = R_0$.

Next, since we consider regions near the surface (at $r \approx R_0$), the form of solution (1) is of no significance and we assume that $\varphi = -mk/R_0$.

1063-7842/03/4808-0958$24.00

We also assume that, like $\rho(\mathbf{x})$, the potential φ undergoes fluctuations with a characteristic range of argument variation $|\delta x| > |l^*|$.

BASIC EQUATIONS AND NATURAL FREQUENCIES OF JOINT OSCILLATIONS

In accordance with the aforesaid, we can write the following spatial-shifts- and time-inversion-invariant expression for the Lagrange function:

$$L\{\rho, \varphi\} = \int (L_1 + L_2 + L_3) d^3x, \tag{2}$$

where

$$L_1 = -a^2\{0.5\rho(\nabla\varphi)^2 + 4\pi k\rho^2\varphi\} + b^2\nabla\rho\nabla\varphi, \tag{3a}$$

$$L_2 = (1/2\rho_0)[(d^2 + l^4)(\nabla\varphi)^2/c^4] \times [(\partial\rho/\partial t)^2 - c_s^2(\nabla\rho)^2], \tag{3b}$$

$$L_3 = (\rho/2c^2)[a^2(\partial\varphi/\partial t)^2 - \varphi^2], \tag{3c}$$

and $\nabla\varphi = (\partial\varphi/\partial x, \partial\varphi/\partial y)$, $\nabla\rho = (\partial\rho/\partial x, \partial\rho/\partial y)$.

The phenomenological constant a has the dimension of time, and the constants b, d, and l have the dimension of length. Here, ρ_0 is the mean surface density, c_s is the mean speed of sound, c is the velocity of light, and t is time.

It is easy to see that expressions (3a)–(3c) yield correct and consistent results in various limiting cases. Indeed, in the absence of acoustic oscillations ($b = d = l = 0$) and in the nonrelativistic approximation under the condition $a \gg \delta x$, the minimization of the action $S = \int L\, d^3x dt$ in φ for expression (3a) leads to the Poisson equation $\Delta\varphi = 4\pi k\rho$. In another limiting case where the gravitational potential φ is neglected, the minimization of action (3b) in ρ gives the usual equation for density variation in an acoustic wave

$$\partial^2\rho'/\partial t^2 - c_s^2\Delta\rho' = 0, \tag{4}$$

where $\rho' = \rho - \rho_0$ at $\varphi = 0$ and Δ is the Laplacian. Interaction between acoustic and gravitational (long-wavelength) oscillations is described by all the three Lagrangeans. Other interactions including the parameters ρ and φ do not exist in nature (of course, without considering higher order terms of the expansions in powers of $\nabla\rho$, $\nabla\varphi$, $\partial\rho/\partial t$, and $\partial\varphi/\partial t$). Now, using all three Lagrangeans (3a), (3b), and (3c), we can find a desired set of linearized equations for small deviations $\delta\rho = \rho - \rho_0$ and $\delta\varphi = \varphi - \varphi_0$. Thus, minimizing the actions $S = \int (L_1 + L_2 + L_3) d^3x dt$ yields

$$\begin{cases} A^2(c_s^2\Delta\xi - \partial^2\xi/\partial t^2) + (b^2/a^2)\Delta\varphi - 8\pi k(ac)^2\rho_0\varphi_0\xi \\ -(8\pi k a^2\rho_0 + \varphi_0)\delta\varphi = \Gamma_1\{\delta\varphi, \xi\} \end{cases} \tag{5a}$$

$$\begin{cases} \Delta\varphi - c_s^{-2}\partial^2\varphi/\partial t^2 - \delta\varphi/(ac)^2 + (b/a)^2\Delta\xi \\ -(4\pi k\rho_0 + \varphi_0/(ac)^2)\xi = \Gamma_2\{\delta\varphi, \xi\}, \end{cases} \tag{5b}$$

where the functions on the right-hand sides are

$$\begin{cases} \Gamma_1\langle\delta\varphi, \xi\rangle = (ac)^2\{0.5(\nabla\varphi)^2 + 8\pi k\rho_0\xi\delta\varphi\} \\ + 0.5[\delta\varphi^2 - a^2(\partial\varphi/\partial)^2] \end{cases} \tag{6a}$$

$$\begin{cases} \Gamma_2\langle\delta\varphi, \xi\rangle = \xi\{(4\pi k\rho_0\xi - \Delta\delta\varphi) \\ - a^{-2}(\delta\varphi + a^2\partial^2\varphi/\partial t^2)\}, \end{cases} \tag{6b}$$

with $\xi = \delta\rho/\rho$, $A = c[d^2 + (l^4/c^4)(\partial\varphi/\partial R_0)^2]^{1/2}$.

The set of equations obtained describes nonlinear interactions between the density and gravitational potential fluctuations.

Equating the right-hand sides in Eqs. (5) to zero ($\Gamma_1 = \Gamma_2 = 0$), one readily finds the natural oscillation frequencies for the coupled system. Assuming that $\xi = \xi_0\exp(i\omega t - i\mathbf{qx})$ and $\delta\varphi = \delta\varphi_0\exp(i\omega t - i\mathbf{qx})$, where $\mathbf{q} = (q_x, q_y)$ and $\mathbf{x} = (x, y)$, and performing simple transformations, we obtain the dispersion relation

$$(\omega^2 - \omega_1^2)(\omega^2 - \omega_2^2) - \omega_3^4 = 0, \tag{7}$$

where the frequencies are

$$\begin{cases} \omega_1^2 = c_s^2q^2 + 8\pi k\rho_0\varphi_0/c^2d^{*2} \\ \omega_2^2 = c_s^2q^2 + 1/a^2 \\ \omega_3^2 = [8\pi k(ac)^2\rho_0 + \varphi_0 + c^2b^2q^2]/cad^*, \end{cases} \tag{7a}$$

and

$$d^{*2} = d^2 + (l^4/c^4)(\partial\varphi/\partial R_0)^2. \tag{7b}$$

The solutions to Eq. (7) are

$$\omega^{\pm 2}(q) = (\omega_1^2 + \omega_2^2)/2 \pm [(\omega_1^2 - \omega_2^2)^2/4 + \omega_3^4]^{1/2}. \tag{8}$$

From (8) and (7a) at $q = 0$, we find

$$\begin{cases} \omega_0^+ = 1/a, \\ \omega_0^- = (a/d^*)(8\pi k\rho_0\varphi_0)^{1/2}. \end{cases} \tag{9}$$

Let us estimate these frequencies. Setting $a = R_0 = 6.4 \times 10^8$ cm, $d^* = 100$ cm, $c = 3 \times 10^{10}$ cm/s, $\rho_0 = 5.5$ g/cm^3, and $k = 6.7 \times 10^{-8}$ cm^3/(g s^2) and assuming that $\varphi_0 = 4\pi k\rho_0 R_0^2/3$ in view of solution (1), we find the desired frequencies of natural surface oscillations:

$\omega_0^+ = 46.9$ Hz and $\omega_0^- = 0.51$ Hz. Thus, one of the frequencies (ω_0^+) is near the lower threshold of human perception, while the other is beyond the audibility limit (in the range of hypersonic frequencies). These frequencies determine the range of natural noise background; thus, their physical meaning becomes clear. Information about the frequencies of natural noise background may be useful in a number of applications. For example, if one detects additional oscillations (no matter whether acoustic or electromagnetic) on the background of natural noise, the reason for these oscillations and the distance to the noise source may be found by measuring the additional intensity. Acoustic transducers detecting noise effects should be placed at a certain depth under the surface.

Now let us evaluate additional contributions to the natural noise intensity from various disturbing factors. To do this, we turn to Eqs. (5) and assume that their right-hand sides ($\Gamma_{1,2}$) are other than zero putting $q = 0$, $\xi = \xi_0(t) + \xi'(t)$, and $\delta\varphi = \delta\varphi_0(t) + \delta\varphi'(t)$, where the functions $\delta\varphi_0(t)$ and $\xi_0(t)$ are known. Indeed,

$$\delta\varphi_0(t) = A_1\varphi_0\exp(i\omega_0^+ t), \quad \xi_0(t) = A_2\exp(i\omega_0^- t). \tag{10a}$$

We shall seek the corrections $\xi'(t)$ and $\delta\varphi'(t)$ in the form

$$\delta\varphi'(t) = A_3\varphi_0\exp(i\Omega_1 t), \quad \xi'(t) = A_4\exp(i\Omega_2 t). \tag{10b}$$

The constants $A_{1,2}$ in expressions (10) are the amplitudes of background oscillations; $A_{3,4}$ are the amplitudes of forced oscillations caused by a disturbing factor; and $\Omega_{1,2}$ are the frequencies of these oscillations, which may be complex.

Substituting expression (10) into Eqs. (5) yields

$$\begin{aligned} d^2\xi/dt^2 + (\omega_0^-)^2\xi &= -[(\omega_0^-)^2/\varphi_0] \\ \times\{A_2A_3\exp(i\omega_0^- \pm \Omega_1)t + A_1A_4\exp(i\omega_0^+ \pm \Omega_2)t\} &- \{(A_1A_3/A^2)(1 \pm \Omega_1/2\omega_0^+)\exp(i\omega_0^+ \pm \Omega_1)t\}, \end{aligned} \tag{11}$$

$$\begin{aligned} d^2\delta\varphi/dt^2 + (\omega_0^-)^2\delta\varphi &= -8(\omega_0^+)^2\pi k\rho_0 a^2 A_2A_4\exp(i\omega_0^- \pm \Omega_2)t \\ &+ \varphi_0[(\omega_0^+)^2 - \Omega_1^2]A_2A_3\exp(\omega_0^- \pm \Omega_1)t. \end{aligned} \tag{12}$$

Note that we neglect commutative products of type $\xi\delta\varphi$, which, strictly speaking, must be involved in Eqs. (11) and (12). Solving the equations with the disturbing factors on the right-hand sides, we find for the relative density fluctuations

$$\begin{aligned} \xi_f(t) &= B_1(\Omega_1)\exp[i(\omega_0^- + \Omega_1)t] \\ &+ B_1(-\Omega_1)\exp[i(\omega_0^- - \Omega_1)t] + B_2(\Omega_2)\exp[i(\omega_0^+ + \Omega_2)t] \\ &+ B_2(-\Omega_2)\exp[i(\omega_0^+ - \Omega_2)t] + B_3(\Omega_1)\exp[i(\omega_0^+ + \Omega_1)t] \\ &+ B_3(-\Omega_1)\exp[i(\omega_0^+ - \Omega_1)t], \end{aligned} \tag{13}$$

where the coefficients are given by

$$\begin{cases} B_1(\Omega_1) = A_2A_3(\omega_0^-)^2[\Omega_1^2 + 2\Omega_1\omega_0] \\ B_2(\Omega_1) = A_1A_4(\omega_0^-)^2/[(\Omega_2 + \omega_0^+)^2 - (\omega_0^-)^2] \\ B_3(\Omega_1) = (A_1A_3/A^2)(1 + \Omega_1/2\omega_0^+)/[(\Omega_1 + \omega_0^+)^2 - (\omega_0^-)^2]. \end{cases} \tag{14}$$

For the fluctuations of the potential φ, we obtain in a similar way

$$\begin{aligned} \delta\varphi_f(t) &= \varphi_0\{B_4(\Omega_2)\exp[i(\omega_0^- + \Omega_2)t] \\ &+ B_4(-\Omega_2)\exp[i(\omega_0^- - \Omega_2)t] + B_5(\Omega_1)\exp[i(\omega_0^- + \Omega_1)t] \\ &+ B_5(-\Omega_1)\exp[i(\omega_0^- - \Omega_1)t]\}, \end{aligned} \tag{15}$$

where

$$\begin{aligned} B_4(\Omega_2) &= 8\pi k\rho_0 a^2(\omega_0^+)^2 A_2A_4/\varphi_0[(\Omega_2 + \omega_0^-)^2 - (\omega_0^+)^2], \\ B_5(\Omega_1) &= A_2A_3[\Omega_1^2 - (\omega_0^+)^2]/[(\Omega_1 + \omega_0^-)^2 - (\omega_0^+)^2]. \end{aligned} \tag{16}$$

Thus, knowing the solutions to inhomogeneous Eqs. (11) and (12), one can also evaluate a relative increase in the background energy that is caused by a disturbing factor. For this purpose, one must consider the ratio

$$\eta = \overline{\delta\varepsilon'}/\overline{\delta\varepsilon_0}, \tag{17}$$

where

$$\begin{cases} \overline{\delta\varepsilon_0} = \int\Lambda dV = -(\rho_0 d^2V/2)[\overline{(d\xi_0/dt)}^2 + \overline{(d\xi_f/dt)}^2] \\ \overline{\delta\varepsilon'} = -(\rho_0 d^2V/2)\overline{(d\xi_f/dt)}^2. \end{cases} \tag{18}$$

The bar here means time averaging. Eventually, we have

$$\eta = \overline{(d\xi_f/dt)}^2/[\overline{(d\xi_0/dt)}^2 + \overline{(d\xi_f/dt)}^2], \tag{19}$$

where $\xi_0(t) = A_2\exp(i\omega_0^- t)$ and $\xi_f(t)$ is defined by formula (13).

It is obvious that, when $|\xi_f| \ll |\xi_0|$, transducers detecting hypersonic disturbances must be very sensitive in order to sense even very weak density oscillations. One can always suppose that a disturbance is accompanied by some electromagnetic processes. This

means that there must be a relation between the electromagnetic field and density fluctuations. This relation must show up in dispersion laws for electromagnetic and acoustic waves. We will see that this actually takes place; however, the effect, as expected, turns out to be very weak.

The interaction between density fluctuations $\delta\rho$ and a magnetic field H can be represented in the form

$$L_4 = \int \rho H^2 d^3x/8\pi\rho_0. \quad (20)$$

Setting $\mathbf{H} = \mathbf{H}_0 + \mathbf{h}$, where $\mathbf{H}_0$ is a certain static field and $\mathbf{h}$ is a weak disturbance-related variation of the field, and assuming that $\rho = \rho_0 + \delta\rho$, we obtain the variation of the Lagrangean in the form $dL_4 = \int \delta\rho\, \mathbf{H}_0\mathbf{h} d^3x/4\pi\rho_0$. Next, putting $\mathbf{h} = \mathrm{curl}\mathbf{A}$, we arrive at an expression for the action variation:

$$\delta S_4 = \int \xi \mathbf{H}_0 \cdot \mathrm{curl}\mathbf{A} d^3x dt/4\pi. \quad (21)$$

In view of (2) and (21), the joint equations for ξ and $\mathbf{A}$ can be represented as

$$\begin{cases} \partial^2\xi/\partial t^2 - c_s^2\Delta\xi + (\bar{\omega_0})^2\xi + \mathbf{H}_0 \cdot \mathrm{curl}\mathbf{A}/d^{*2}\rho_0 = 0 \\ \partial^2\mathbf{A}/\partial t^2 - c^2\Delta\mathbf{A} - c^2[\mathbf{H}_0 \times \nabla\xi] = 0. \end{cases} \quad (22)$$

Now we immediately derive the desired dispersion relation

$$(\omega^2 - c^2k^2)[\omega^2 - (\omega_k)^2] - [\mathbf{H}_0 \times \mathbf{k}]^2 c^2/d^{*2}\rho_0 = 0, \quad (23)$$

where the frequency $\bar{\omega_k} = [c_s^2 k^2 + (\bar{\omega_0})^2]$.

An interesting physical case is realized when $k < k^*$, where $k^* = H_0/d^* c\rho_0^{1/2}$. In this case, the natural frequency of such oscillations is

$$\omega^* = \{|[\mathbf{H}_0 \times \mathbf{k}]|c/d^*\rho_0^{1/2}\}^{1/2}. \quad (24)$$

Let us evaluate this frequency. At $H_0 = 10^4$ Oe, $\rho_0 = 5.5$ g/cm^3, $d^* = 100$ cm, and $k^* = 10^{-8}$ cm^{-1}, we have $\omega < 100$ Hz, which is a well detectable value. Note that the frequency obtained corresponds in order of magnitude to that of gravitational waves with a wavelength of approximately 300 km.

SPATIAL VARIATION OF THE DENSITY OF A MASSIVE BODY DUE TO SELF-GRAVITY

Putting $b = 0$ in expressions (2) yields a set of nonlinear differential equations from which one can find the extremals of the functional $S(\rho, \varphi)$:

$$\begin{cases} \Delta\varphi = 4\pi k\rho + \varphi/c^2a^2, & (25) \\ (\nabla\varphi)^2 + 16\pi k\rho\varphi + \varphi^2/c^2a^2 = (dc_s/a)^2\Delta\rho/\rho_0. & (26) \end{cases}$$

Let us find at least one physically meaningful solution of this set of equations. Assuming that $r < a$ and considering the spherically symmetric case, that is, $\rho = \rho(r)$ and $\varphi = \varphi(r)$, we find from (25)

$$\varphi(r) = (2\pi k/r)\int_0^r \rho(r')r'^2 dr'. \quad (27)$$

Then, substituting (27) into (26) gives the equation

$$xy''' + 3y'' = 2(xy'')^{1/2}(xy' + 3y), \quad (28)$$

where $x = r/r_0$, $r_0 = (dc_s/2\pi ak\rho_0)^{1/2}$, $y = x\rho(r)/\rho_0$, and $y' = dy/dx$ with the boundary condition $e = R_0/r_0$ at $r = R_0$ (here, r_0 can be identified with a certain radius).

Equation (28) is rather difficult to solve analytically; therefore, we restrict ourselves to the asymptotic behavior of $y(x)$ in two limiting cases: $x \ll 1$ and $x \gg 1$. After simple mathematical manipulation, we come to

$$y(x) = \begin{cases} C_1 + C_2x^3 & \text{for } x \ll 1 \\ C_5x + C_4^2/x + C_3C_4x^2 + C_3x^5/20 & \text{for } x \gg 1, \end{cases} \quad (29)$$

where C_i are constants of integration ($i = \overline{1, 5}$).

In terms of the density, we obtain, respectively,

$$\rho(r) = \begin{cases} \rho_0[C_1r_0/r + C_2(r/r_0)^2] & \text{for } r < r_0 \\ \rho_0[C_5 + C_4^2(r_0/r)^2 \\ + C_3C_4r/r_0 + (C_3^2/20)(r/r_0)^4] & \text{for } r > r_0. \end{cases} \quad (30)$$

It is clear that a real physical case corresponds to only the following set of constants: $C_3 = 0$ and $C_1 = C_5 = 1$. Then, the density is given by

$$\rho(r) = \begin{cases} \rho_0[r_0/r + C_2(r/r_0)^2] & \text{for } r < r_0 \\ \rho_0[(1 + C_4r_0/r)] & \text{for } r > r_0. \end{cases} \quad (31)$$

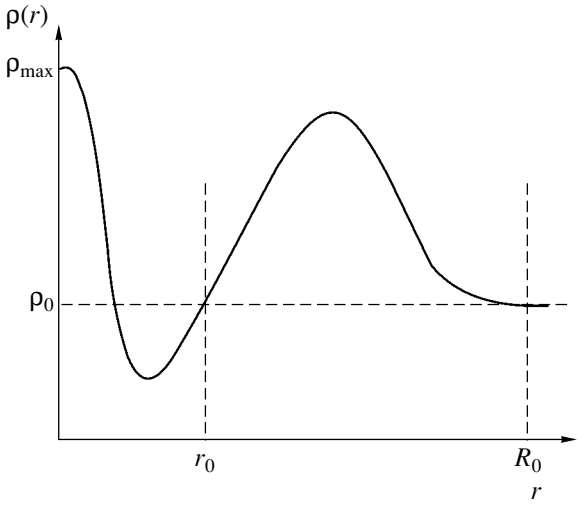

Fig. 1. Steady-state density distribution due to the gravitational potential.

When the density is a continuous function, one must put $C_2 = C_4$. The function $\rho(r)$ is shown in Fig. 1. The constant C_2 can be evaluated as follows. The total mass M is the sum of two masses M_1 and M_2. Then, we may write

$$M = M_1 + M_2 = 4\pi\int_0^{r_0}\rho(r)r^2dr + 4\pi\int_{r_0}^{R_0}\rho(r)r^2dr. \quad (32)$$

Solving this equation gives C_2.

The function $\rho(r)$, shown in Fig. 1, reflects the specific behavior of the density ρ, in particular, near the core. Indeed, at $r < r_0$, the case $\rho \sim 1/r$ is possible. This means that the major part of the mass concentrates in a relatively small range $r < r_{cr}$, where r_{cr} is a certain critical radius. The rest of the mass (in the given example) must be distributed over the remaining volume as a loose substance.

Now consider the case when the density $\rho(r)$ deviates weakly from its mean value ρ^*. Assume that $\rho(r) = \rho^* + \delta\rho(r)$. Turning back to Eqs. (25) and (26) and substituting $\rho(r) = \rho^* + \delta\rho(r)$ into them, we find

$$\varphi(r) = 2\pi k\rho^* r^2/3 + (2\pi k/r)\int_0^r \delta\rho(r')r'^2dr', \quad (33)$$

$$\Delta\xi = r_0^{-4}\left\{(20/3r)\int_0^r \xi(r')r'^2dr' + (2r/a^2)\int_0^r \xi(r')r'^2dr' + 8\xi r^2/3 + 28r^2/9 + r^4/a^2\right\}. \quad (34)$$

Recall that $\xi = \delta\rho/\rho_0$.

Reducing Eq. (34) to dimensionless form and introducing a new function $y = x\xi$, where $x = r/r_0$, we obtain

$$y'' = (20/3)\int_0^x y(x')x'^2dx' + 2x^2\kappa\int_0^x y(x')x'^2dx' + 8x^2y/3 + 28x^2/9 + \kappa x^4, \quad (35)$$

where $\kappa = (r_0/a)^2$ is a parameter.

To make sure that the condition $\kappa \ll 1$ is fulfilled, we evaluate the radius r_0. Turning back to its definition (see formula (28)) we put $c = 3 \times 10^{10}$ cm/s, $c_s = 10^5$ cm/s, $ac = R_0 = 6.4 \times 10^8$ cm, $\rho_0 = 5.5$ g/cm^3, $k = 6.7 \times 10^{-8}$ cm^3/(g s^2), and $d = 100$ cm. Then, $r_0 = 200$ km.

Thus, omitting terms in (35) that are proportional to κ and differentiating with respect to x, we arrive at

$$y''' = 12xy + 8x^2y'/3 + 56x/9. \quad (36)$$

Let us find asymptotic solutions of this equation.

If $x \ll 1$,

$$y(x) = 7x^4/27. \quad (37)$$

Assuming that $y = C/x^n$ with $x \gg 1$ and substituting this expression into (36), we have $n = 4.5$; that is,

$$y(x) = C/x^{4.5}. \quad (38)$$

Hence, the density variation is described as follows:

$$\delta\rho(r) = \rho_0\begin{cases}(7/27)(r/r_0)^3 & \text{for} \quad r \ll r_0\\ (7/27)(r_0/r)^{11/2} & \text{for} \quad r \gg r_0.\end{cases} \quad (39)$$

From the joining condition for the solutions at $r = r_0$, we find that $C = 7/27$. For this case, the function $\delta\rho(r)$ is depicted in Fig. 2.

Substituting the asymptotic expression for $\delta\rho(r)$ into formula (34) yields an expression for the gravitational potential:

$$\varphi(r) = (2\pi k\rho_0 r^2/3) \times \begin{cases}1 + (7/54)(r/r_0)^3 & \text{for} \quad r \ll r_0\\ 1 - (14/45)(r_0/r)^{11/2} & \text{for} \quad r \gg r_0.\end{cases} \quad (40)$$

As is seen from (40), the potential φ decreases when $r > r_0$. This indicates that density fluctuations in massive bodies weaken, though insignificantly, the gravitational potential. The decrease is the least at $r_0 = R_0$. Note that solution (39) implies the continuous variation of density fluctuations, whereas solution (40) describes a discontinuity of the gravitational potential at $r \sim r_0$. Thus, the radius r_0 should be identified with the radius of an imaginary sphere with a discontinuity of the potential $\varphi(r)$ at its boundary.

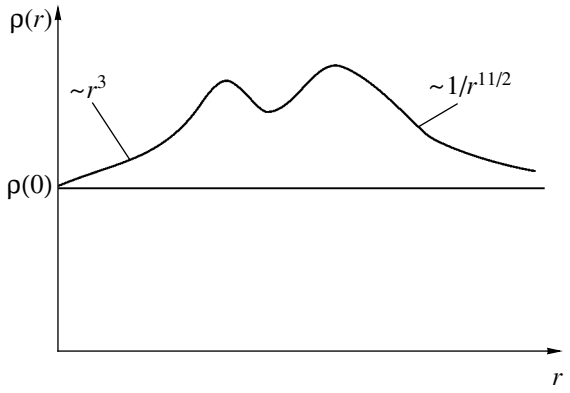

Fig. 2. Density variation about a certain mean value ρ^*.

Let us evaluate the variation of the free-fall acceleration at $r = R_0$. According to (40), we find

$$\varphi(R_0) \equiv (kM_0/R_0)[1 - (14/45)(r_0/R_0)^{11/2}], \quad (41)$$

where $M_0 = V_0\rho_0$ is the body's mass.

Hence, the acceleration is

$$g = g_0 - \delta g, \quad (42)$$

where $\delta g = g_0[(77/45)(r_0/R_0)^{11/2}]$.

Putting $g_0 = 9.81$ m/s^2, $r_0 = 200$ km, and $R_0 = 6400$ km, we obtain $\delta g \approx 10^{-9}$ m/s^2. This estimate shows that the variation of the free-fall acceleration on the surface of a massive body is small. However, for experimental investigation of gravitational phenomena and, in particular, for experiments on detecting gravitational waves, this prediction should be taken into account when performing numerical evaluations of fine effects.

CONCLUSIONS

The basic results are as follows.

(1) Joint oscillations of the density and gravitational potential at the surface of a massive body have been predicted.

(2) It has been shown that the effect considered is appreciable and the natural frequencies of the oscillations are low.

(3) A set of differential equations derived has made it possible to predict the existence of structures where the mass concentrates largely near a certain core, while the rest of the structure is a loose substance kept near the core by attractive forces.

(4) A relation between density fluctuations and gravitational potential fluctuations, on the one hand, and the electromagnetic field, on the other, has been indicated.

REFERENCES

1. L. D. Landau and E. M. Lifshitz, *The Classical Theory of Fields* (Nauka, Moscow, 1973; Pergamon, Oxford, 1975).
2. S. O. Gladkov and A. M. Tokarev, Fiz. Goreniya Vzryva **25** (1), 30 (1990).
3. A. Yu. Loskutov and A. S. Mikhaĭlov, *Introduction to Synergism* (Nauka, Moscow, 1990).
4. S. O. Gladkov, Perspekt. Mater., No. 1, 50 (2000).
5. S. O. Gladkov, *Physics of Composites: Thermodynamic and Dissipative Properties* (Nauka, Moscow, 1999).

Translated by N. Mende

Technical Physics, Vol. 48, No. 8, 2003, pp. 964–968. Translated from Zhurnal Tekhnicheskoĭ Fiziki, Vol. 73, No. 8, 2003, pp. 25–29.

ATOMS, SPECTRA, RADIATION

Elastic Scattering of Low-Energy Electrons by Cadmium Atoms

J. E. Kontros, I. V. Chernyshova, and O. B. Shpenik

Institute of Electron Physics, National Academy of Sciences of Ukraine, Uzhgorod, 88000 Ukraine

e-mail: an@zvl.iep.uzhgorod.ua

Received July 15, 2002; in final form, January 28, 2003

Abstract—Experimental results on the differential cross sections of 180° elastic electron scattering and the total cross section of electron scattering by cadmium atoms in the energy range 0–6 eV are reported for the first time. Distinct shape resonances with the $(5s^25p)^2P^0$ and $5s5p^2$ configurations are revealed in the near-threshold range and at $E \approx 4$ eV. In the range 3.0–3.7 eV, the differential cross section exhibits extra singularities that are probably related to the *d*-wave shape resonance. The resonance contribution to the backscattering cross section near 4 eV is found to be about 20%. *© 2003 MAIK "Nauka/Interperiodica".*

INTRODUCTION

A cadmium atom, which has a complex electron configuration (the electron configuration of krypton plus ten electrons in the 4*d* subshell and two electrons in the 5*s* subshell [1]), is an attractive object for investigating a variety of collision processes, such as elastic electron scattering, excitation, ionization, etc. Yet the number of experimental and theoretical works concerning the elastic scattering of slow electrons by cadmium atoms is very scarce [2].

The pioneering experimental investigation into elastic scattering of low-energy electrons (0–7 eV) by cadmium atoms was performed by Burrow *et al.* [3], who observed the ^2P shape resonance at an energy close to zero. They also discovered a well-defined wide singularity when the electron energy slightly exceeded the excitation threshold (≈4 eV) for the $(5s5p)^3P$ atomic level and a cusp in the excitation threshold for the $(5s5p)^1P_1$ atomic level. The differential cross sections of elastic scattering at 60°, 90°, and 120° in the interval 3–5 eV were studied with a 127° electrostatic energy analyzer [4]. The scattering of electrons through angles in the range 20°–120° was measured using a semispherical energy analyzer equipped with a set of electrostatic lenses [5]. Marinkovic *et al*. [1] used a semispherical energy analyzer to measure the differential cross sections of elastic electron scattering over a wide range of energies (from 3.4 to 85 eV) and angles (from 0° to 150°), as well as the excitation cross section for 16 levels of a cadmium atom.

^2P shape resonances in elastic scattering of electrons by Cd atoms have been predicted in terms of the horizontal extrapolation method [6] and the Dirac–Fock semirelativistic approximation [7]. A detailed description of relevant experimental and theoretical techniques is available elsewhere [2, 8]. However, as far as we know, published data for the differential cross sections of elastic electron backscattering (at 180° relative to the primary electron beam direction) by cadmium atoms are lacking, presumably because conducting such experiments is a challenging problem.

It is known [9] that measuring large-angle elastic electron scattering is of significance in determining phase shifts of partial waves involved in the process. Upon 180° scattering, all partial waves making a contribution to the process (the greater the atomic number of the target, the greater the contribution) are of the same magnitude as their associated Legendre polynomials in the partial wave expansion of the scattering amplitude. Furthermore, upon backscattering, the polarization- and exchange-related contributions are expected to be much greater than the contribution from the electric dipole moment. Of no less importance for experimentalists is the possibility of maximal signal acquisition from the area of beam interaction upon detecting backscattered electrons [10].

In this work, we study the energy dependences of the differential (180°) and total cross sections of slow electron elastic scattering by cadmium atoms and analyze the correlation between singularities in these sections. It is expected that results obtained will make up for missing data on elastic electron scattering at 180°.

A hypocycloidal electron spectrometer was used to generate a monoenergetic electron beam and analyze the spectrum of backscattered electrons. It is capable of operating at extremely low (close to zero) energies, offering a high transmission (up to 95%) [11].

1063-7842/03/4808-0964$24.00

EXPERIMENTAL

Electron and atomic beams intersect at a right angle. The experimental setup consists of a vacuum chamber with a hypocycloidal electron spectrometer inside, a small-size atomic beam source, a quartz lamp to heat the spectrometer, a power supply unit of the spectrometer, and a system for recording the primary and scattered electron currents.

The small-size effusive source of the cadmium atom beam is made of stainless steel. It is heated to a desired temperature with a bifilar molybdenum heater. The source temperature is selected in such a way that the atom concentration in the beam is lower than the critical value for double atomic scattering. An atomic beam is formed with a stainless steel microchannel plate mounted at the exit from the source. Combined with the mechanical modulation of the beam, such a design of the atomic source provides a high density of the atomic beam and suppresses the background scattering of electrons by residual gases.

The hypocycloidal electron spectrometer, which was used to generate a monoenergetic beam and analyze the backscattered electron spectrum, is schematically shown in Fig. 1. It is composed of two hypocycloidal electron energy analyzers placed in tandem [11], one of which (the electrodes K, A_1, A_2, A_3, B_1, and B_2) serves as a primary electron beam monochromator and the other (the electrodes A_4, A_5, B_3, and B_4), as a backscattered electron analyzer.

The cylindrical capacitors B_1, B_2 and B_3, B_4 generate transverse electric fields in the monochromator and analyzer, respectively. The electrode A_7 and the Faraday cup F_c are used to detect the primary electron beam and suppress the backscattered electron background. The backscattered electron spectrometer uses a characteristic feature of the charged particle motion in crossed $\mathbf{F} \times \mathbf{B}$ fields [12]: electrons or ions deviate in the same direction irrespective of the direction of their motion along the spectrometer axis. Thus, in our instrument, electrons backscattered by the atoms move toward the analyzer and, having passed the drift region, turn out to be displaced by a distance that is equal to the double drift of the primary electron beam. Their detection is accomplished by a special collector F_b of backscattered electrons, which is placed on the electrode A_4. The spectrometer is placed in a uniform magnetic field of 1.6×10^{-2} T. The design and operation of the spectrometer are detailed in [13].

The basic parameters of the primary electron beam in the spectrometer are as follows: the current is $\sim 10^{7}$ A; the diameter, ≈ 0.5 mm; and the FWHM Γ, no more than 0.15 eV. Prior to the measurements, the electron spectrometer was heated to $T = 500$ K under a pressure of $\sim 10^{-5}$ Pa for 30–40 h to degas the electrode surfaces.

The energy dependence of the differential backscattering cross section was taken with certain potentials applied to the monochromator and analyzer electrodes.

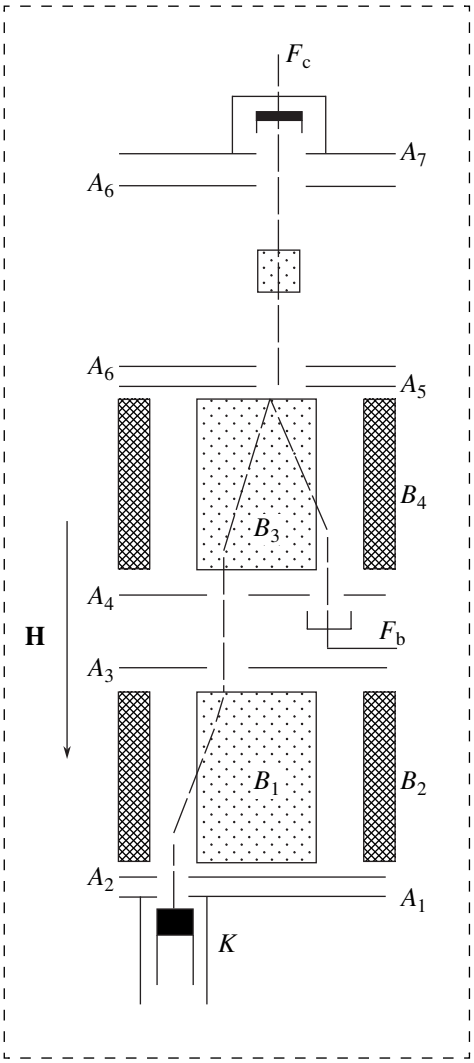

Fig. 1. Schematic of a hypocycloidal backscattered electron spectrometer.

These potentials were optimized so as to provide the maximal current to collector F_b. Provided that the electron beam is sufficiently monoenergetic, the current to the backscattered electron collector F_b is measured by varying the electron energy, which is specified by the potential difference across the electrodes K and A_6 (for details, see [14]). In taking the energy dependence of the total cross section, the scattered electron current to the electrode A_6 of the collision chamber was measured. A mechanical chopper of the atomic beam makes it possible to measure the scattered electron current both with and without the atomic beam present in the collision chamber. The scattered electron current was measured with a digital electrometric picoamperemeter.

The absolute energy scale was calibrated with an accuracy of ±0.05 eV from the position of the electron energy distribution peak.

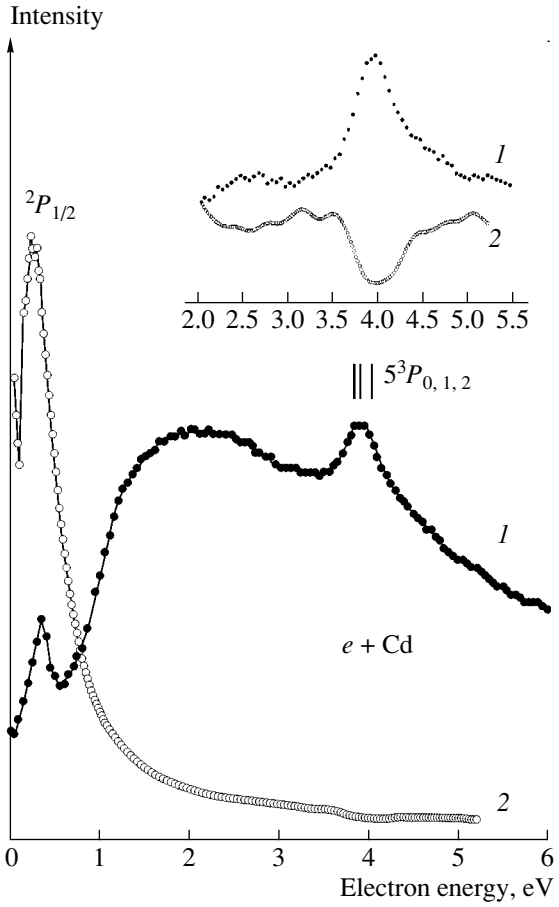

Fig. 2. Cross sections of the elastic electron scattering by Cd atoms versus electron energy.

RESULTS OF MEASUREMENTS

Figure 2 shows the energy dependences of the total (curve *1*) and differential (180°, curve *2*) cross sections of elastic electron scattering in the energy range 0–6 eV. The short vertical straight lines show the energy position of the lowest excited 5^3P state of a Cd atom. It is seen that we succeeded in getting very low collision energies. The curves depicted in Fig. 2 are the energy dependences of the electron scattering intensities normalized to the beam current. Both the total and differential cross section of elastic scattering exhibits a maximum near zero (which is more pronounced for the differential cross section). The maxima are attained at E = 0.33 eV ($\Gamma \approx 0.33$ eV, curve *1*) and E = 0.285 eV ($\Gamma \approx$ 0.29 eV, curve *2*). The slight discrepancy in the resonance energies may be explained by a strong variation of the primary electron beam current in the range 0–6 eV. The maxima observed are apparently related to the shape resonance associated with unexcited levels of a Cd atom. As is known [12, 15], shape resonances arise when electrons with nonzero angular moments are scattered in the central force field. Therefore, it seems that the above singularities may be attributed to the *p*-wave resonance due to the formation and decay of the $(5s^25p)^2P_{1/2}$ state of Cd^-. This is also indicated by a deep minimum observed in the differential cross section of 90° elastic electron scattering by Cd atoms [4]. It is remembered that *p*-wave resonances at E = 0.33 and 0.25 eV were first observed in transmission experiments [3] and [4], respectively. These values agree well with our data. The energy position of the singularity observed in this work also correlates well with the calculated values: E = 0.28 [7] and 0.34 eV [16]. However, the value E = 0.78 eV, which was obtained by horizontal extrapolation [6], disagrees with our data and data obtained by other authors.

Below the excitation threshold of the first energy levels of the atom, the differential cross section exhibits singularities at 2.74 ($\Gamma \approx 0.27$ eV), 3.12 ($\Gamma \approx 0.21$ eV), and 3.5 eV ($\Gamma \approx 0.19$ eV) (see inset to Fig. 2). In the curve of the total scattering cross section, singularities are not so distinct. These singularities were revealed by the polynomial interpolation of the slowly varying cross section. Curves *1* and *2* in the inset to Fig. 2 display the behavior of the resonance structure separated. Each of the singularities was fitted by the least-squares method using the Fano–Cooper formula [15].

Singularities like the last two were previously observed in [4] at 3.02 and 3.5 eV in the differential cross section of 90° elastic electron scattering. It is likely that here we are dealing either with a wide *d*-wave resonance or with two narrow Feshbach resonances. The presence of a resonance in the *d* wave was predicted earlier in [13]. It should be noted that the singularity at ≈3.6 eV is attributed to the $(5s5p^2)^4P_{1/2}$ state of Cd^- [8].

Slightly above the excitation threshold for the 5^3P state of a neutral atom at $E \approx 3.98$ eV, the total scattering cross section shows a distinct maximum (curve *1*) and the differential cross section, a minimum (curve *2*) (in the inset, curves *1* and *2* between 2 and 5.5 eV are shown close to each other for convenience). This singularity is a shape resonance originating from the 5^3P level of the atom (E = 3.73–3.95 eV), as indicated by its considerable width and position relative to the parent state.

The electron configuration of a cadmium atom (ns^2) is similar to that of a mercury atom, which features a large spin–orbit split because of the presence of the heavy atomic nucleus. In the excitation range for the lower 6^3P level of a mercury atom, five resonances corresponding to the $^4P_{1/2,\,3/2,\,5/2}$ and $^2D_{3/2,\,5/2}$ terms are observed [17]. One could expect five similar resonances corresponding to the $5s5p^2$ electron configuration of a cadmium atom at energies near 4 eV. In a cadmium atom, unlike a mercury atom, spin–orbit terms degenerate, causing a substantial overlap of resonance singularities [8]; therefore, they are hard to resolve.

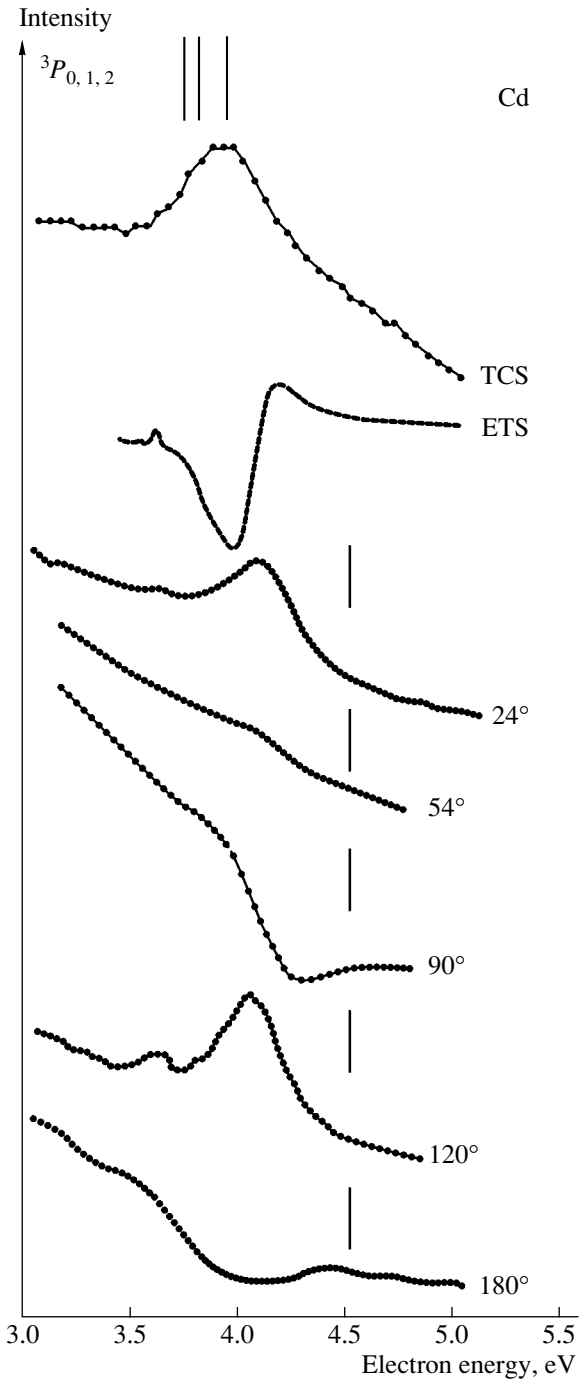

Fig. 3. Our energy dependence of the total cross section (TCS) and differential (180°) cross section of elastic electron scattering near the excitation range of the 5^3P state of a Cd atom, the energy dependences of the differential cross sections of elastic electron scattering for different angles of observation, and the electron transmission spectrum (ETS) [8].

Figure 3 demonstrates the energy dependences of the total and differential backscattering cross sections measured in the range 3–5 eV together with data taken from [8]. The vertical segments near each of the curves outline a 20% intensity interval at $E = 4.5$ eV. It is seen that the shape of the $(5s5p^2)$ Cd^- resonance strongly depends on the angle of observation because of the interference between potential (Coulomb) and resonance scatterings. The vanishing intensity of the resonant minimum at scattering at an angle of 54° implies that the resonant states of a Cd^- negative ion decay largely through the self-detachment of the *d* electron. From Fig. 3 it also follows that the resonant contribution to the cross section of 180° scattering is significant (about 20%).

CONCLUSION

With the use of a hypocycloidal electron spectrometer, the elastic scattering of low-energy (0–6 eV) electrons at an angle of 180° and the total cross section of elastic electron scattering by Cd atoms are investigated in detail for the first time. Near zero energy, both the total and differential cross sections exhibit distinct resonant singularities due to the formation and decay of the short-lived $(5s^25p)^2P^0$ state of Cd^- (which is assigned to the *p*-wave shape resonance), as well as a singularity at ≈4 eV. The energy dependence of the backscattering cross section in the range 3.0–3.7 eV has additional singularities, which are presumably associated with the *d*-wave shape resonance. It is shown that the resonance contribution to the differential cross section of elastic electron scattering at 180° near 4 eV is significant (about 20%).

ACKNOWLEDGMENTS

This work was partially supported by the CRDF (Award no. UP2-2118).

REFERENCES

1. B. Marinkovic, V. Pejcev, D. Filipovic, *et al.*, J. Phys. B **24**, 1817 (1991).
2. S. J. Buckman and C. W. Clark, Rev. Mod. Phys. **66**, 539 (1994).
3. P. D. Burrow, J. A. Michejda, and J. Comer, J. Phys. B **9**, 3225 (1976).
4. S. M. Kazakov, Pis'ma Zh. Tekh. Fiz. **7**, 900 (1981) [Sov. Tech. Phys. Lett. **7**, 386 (1981)].
5. J. P. Sullivan, M. Moghbelalhossein, and S. J. Buckman, in *Proceedings of the 20th International Conference on the Physics of Electronic and Atomic Collisions (XX ICPEAC), Vienna, 1997*, p. TH014.
6. R. J. Zollweg, J. Chem. Phys. **50**, 4251 (1969).
7. L. T. Sin Fai Lam, J. Phys. B **14**, L437 (1981).
8. S. J. Buckman, D. T. Alle, M. J. Brennan, *et al.*, Aust. J. Phys. **52**, 473 (1999).

9. F. H. Read, *Supercomputing, Collision Processes, and Applications*, Ed. by K. L. Bell *et al.* (Kluwer, New York, 1999), pp. 9–14.
10. P. D. Burrow and L. Sanche, Phys. Rev. Lett. **28**, 333 (1972).
11. N. I. Romanyuk, O. B. Shpenik, I. A. Mandy, *et al.*, Zh. Tekh. Fiz. **63** (7), 138 (1993) [Tech. Phys. **38**, 599 (1993)].
12. G. J. Schulz, Rev. Mod. Phys. **45**, 378 (1973).
13. O. B. Shpenik, N. M. Erdevdy, N. M. Romanyuk, *et al.*, Prib. Tekh. Éksp. **1**, 109 (1998).
14. N. I. Romanyuk, I. V. Chernyshova, and O. B. Shpenik, Zh. Tekh. Fiz. **54**, 2051 (1984) [Sov. Phys. Tech. Phys. **29**, 1204 (1984)].
15. H. S. W. Massey, *Negative Ions* (Cambridge University Press, Cambridge, 1976; Mir, Moscow, 1979).
16. H. A. Kurtz and K. D. Jordan, J. Phys. B **14**, 4361 (1981).
17. P. D. Burrow, J. A. Michejda, D. R. Lun, *et al.*, J. Phys. B **31**, L1009 (1998).

Translated by V. Isaakyan

Technical Physics, Vol. 48, No. 8, 2003, pp. 969–971. Translated from Zhurnal Tekhnicheskoĭ Fiziki, Vol. 73, No. 8, 2003, pp. 30–33.

ATOMS, SPECTRA, RADIATION

Absolute Populations of Argon Metastable States in an RF Discharge Plasma

B. T. Baĭsova, V. I. Strunin, N. N. Strunina, and G. Zh. Khudaĭbergenov

Omsk State University, Omsk, 644077 Russia

Received October 31, 2002

Abstract—Absolute populations of argon metastable states in the plasma of an rf discharge in pure argon and an argon–silane mixture are determined. © *2003 MAIK "Nauka/Interperiodica".*

In recent years, rf discharge monosilane plasma, which is widely used in plasmochemistry to produce hydrogenated amorphous silicon films, has become the subject of intensive theoretical and experimental studies [1, 2]. High-quality films in a pure-silane plasma (SiH_4) can be produced only at low input powers, in which case the deposition rate is unacceptably low (1 Å/s). At high powers, the deposition process is faster but is accompanied by the formation of the condensed disperse phase (CDP) because of the increased number of gas-phase reactions, which adversely affects the quality of the deposited film [3]. Dilution of silane with a noble gas (e.g., Ar, He, or Kr) under the same decomposition conditions substantially suppresses the CDP production and increases the deposition rate to 10 Å/s [4]. The mechanism for silane dissociation in argon and the role of argon metastable states in silane decomposition have become the subject of detailed studies [5, 6].

The aim of this paper is to determine the absolute populations of argon metastable states in the plasma of an rf discharge in pure argon and an Ar(95%)–SiH_4(5%) mixture.

Long radiative lifetimes of metastable states ensure the relatively high density of the excited particles produced in a weakly ionized or excited gas.

Since the radiative lifetimes of atomic metastable states are several orders of magnitude longer than the characteristic collision times, metastable atoms can be accumulated in abundance in a low-temperature plasma.

Argon metastable atoms in the $^3P_0$ and $^3P_2$ states play an important role in a number of secondary processes occurring in the plasma of gas discharges in pure argon and mixtures of argon with other gases. The discharge kinetics can substantially depend on the populations of the $^3P_0$ and $^3P_2$ states because various step processes proceed via these states. Therefore, the development of reliable methods for determining the populations of the argon metastable states is of great interest for the diagnostics of argon-containing plasmas.

In this study, an rf discharge was ignited between stainless-steel electrodes in a quartz tube 30 mm in diameter and 50 mm in length. The discharge was supplied from an rf oscillator with a frequency of 13.56 MHz. The pressure in the system was measured by a PMT-2 gauge.

The discharge emission was focused in a narrow beam and directed onto the 8-μm slit of an ISP-30 spectrograph equipped with a three-lens slit-illumination system. The system allowed us to measure the radiation spectrum over the wavelength range 2000–6000 Å. The exposure time was 45 min. To measure the absolute intensities of spectral lines, the system was calibrated using a C-8-200V reference lamp.

In the experiments, we observed three spectral lines corresponding to the $3p^55p \longrightarrow 3p^54s$ radiative transitions, which are responsible for the decay of metastable states (Table 1).

The populations of the $3p^55p$ levels were deduced from the intensities of the corresponding spectral lines, whose wavelengths are given in Table 1.

The populations of these levels were calculated by the formula [8]

$$N = \frac{4\pi GSI(\lambda)\dfrac{d\lambda}{dx}}{Ah\nu l}\frac{t_1}{t_2}, \qquad (1)$$

where G is the spectrograph magnification, S is the width of the microphotometer slit, $d\lambda/dx$ is the inverse dispersion, l is the tube diameter, t_1 is the exposure time

Table 1. Transition probabilities and oscillator strengths for the spectral lines of an argon atom [7]

λ, Å	$f_{12} \times 10^3$	g_1	g_2	A, 10^6 s^{-1}
4164.18	0.46	5	3	0.278
4181.88	4.6	3	3	0.587
4200.67	3.8	5	7	1.031

1063-7842/03/4808-0969$24.00

Table 2. Populations of the $3p^5 5p$ levels

λ, Å	Pressure, torr	Ar		Ar + SiH_4	
		$\bar{N}$, 10^5 cm^{-3}	ΔN, 10^5 cm^{-3}	$\bar{N}$, 10^5 cm^{-3}	ΔN, 10^5 cm^{-3}
4164.18	0.02	78.92	7.56	65.72	5.08
	0.03	47.31	4.15	48.39	4.21
	0.05	48.46	4.21	46.64	4.11
	0.065	47.19	4.15	44.39	3.99
	0.095	44.19	3.98	43.65	3.95
4181.88	0.02	80.21	4.28	40.75	2.73
	0.03	47.35	3.02	30.37	2.25
	0.05	39.04	2.56	22.84	1.77
	0.065	37.54	2.50	21.42	1.71
	0.095	32.96	2.28	21.13	1.70
4200.67	0.02	184.42	7.53	54.27	6.23
	0.03	105.36	4.37	48.02	2.56
	0.05	63.12	2.97	25.83	1.79
	0.065	61.56	2.92	16.86	1.39
	0.095	19.93	1.49	13.55	1.22

of the lamp spectrum, and t_2 is the time during which the discharge spectrum was observed.

The spectral intensity $I(\lambda)$ was calculated by the formula

$$I(\lambda) = \frac{2\pi c^2 h}{\lambda^5}\frac{1}{\exp\left(\frac{hc}{k\lambda T}\right)}\varepsilon_{\lambda, T}, \quad (2)$$

where $\varepsilon_{\lambda, T}$ is the spectral coefficient of thermal radiation and T is the lamp temperature for which the radiation doses absorbed by the photoemulsion (the absorbed energy) from the lamp and the discharge are the same (equal absorbed radiation doses correspond to the same photoemulsion blackening).

The average populations $\bar{N}$ of the $3p^5 5p$ levels and the confidence intervals ΔN for them are given in Table 2.

The absolute populations of the $^3P_0$ and $^3P_2$ argon metastable states in pure argon were found from the balance equation

$$k_1 n n_e - k_2 n^* n_e - k_3 n^* n_e - k_4 n^* n_e - k_5 n^* n - k_7 n^{*2} - D\frac{n^*}{\Lambda^2} + \sum_i A_i n_i = 0, \quad (3)$$

and, for an argon–silane mixture, these populations were found from equation

$$k_1 n n_e - k_2 n^* n_e - k_3 n^* n_e - k_4 n^* n_e - k_5 n^* n - k_7 n^{*2} - k_9 n^* n_{SiH_4} - k_{10} n^* n_{SiH_4} - D\frac{n^*}{\Lambda^2} + \sum_i A_i n_i = 0. \quad (4)$$

Here, n^* is the population of a metastable state; n is the density of atoms in the ground state; n_{SiH_4} is the density of silane molecules; A_i is the transition probability; n_i is the density of atoms at the $3p^5 5p$ levels from which radiative transitions to a metastable level occur; D is the diffusion coefficient; Λ^2 is the characteristic diffusion length; n_e is the electron density; and k_1, k_2, k_3, k_4, k_5, k_7, k_9, and k_{10} are the rate coefficients of the processes listed in Table 3.

Table 3. Main channels for the population and deexcitation of metastable argon states

Process	Rate constant, k_i
$Ar(^1S_0) + e \longrightarrow Ar(^3P_{0,1,2}) + e$	3.1×10^{-11} cm^3 s^{-1}
$Ar(^3P_{0,2}) + e \longrightarrow Ar(^1S_0) + e$	$2–5 \times 10^{-10}$ cm^3 s^{-1}
$Ar(^3P_{0,2}) + e \longrightarrow Ar(i) + e$	$3–5 \times 10^{-7}$ cm^3 s^{-1}
$Ar(^3P_{0,2}) + e \longrightarrow Ar^+ + 2e$	10^{-13} cm^3 s^{-1}
$Ar(^3P_{0,2}) + e \longrightarrow Ar(^1S_0) \longrightarrow 2Ar(^1S_0)$	3×10^{-15} cm^3 s^{-1}
$Ar(^3P_{0,2}) \longrightarrow Ar(^1S_0)$	$[360/(PR^2)](T/300)^{12}$ s^{-1}
$2Ar(^3P_{0,2}) \longrightarrow Ar^+ + Ar + e$	10^{-9} cm^3 s^{-1}
$Ar(i) \longrightarrow Ar(^3P_{0,2}) + h\nu$	10^6 s
$Ar(^3P_{0,2}) + SiH_4 \longrightarrow Ar + SiH_3 + H$	1.4×10^{-10} cm^3 s^{-1}
$Ar(^3P_{0,2}) + SiH_4 \longrightarrow Ar + SiH_2 + 2H$	2.6×10^{-10} cm^3 s^{-1}

Table 4. Populations of metastable states

Metastable state	Pressure, torr	Ar		Ar + SiH_4	
		$\bar{N}$, 10^5 cm^{-3}	ΔN, 10^5 cm^{-3}	$\bar{N}$, 10^5 cm^{-3}	ΔN, 10^5 cm^{-3}
$^3P_2$	0.02	12.23	0.21	16.55	0.09
	0.03	11.05	0.12	16.28	0.08
	0.05	10.47	0.09	15.69	0.06
	0.065	10.45	0.09	15.45	0.05
	0.095	9.85	0.05	15.35	0.04
$^3P_0$	0.02	10.05	0.07	15.30	0.04
	0.03	9.78	0.05	15.15	0.03
	0.05	9.72	0.04	15.04	0.03
	0.065	9.70	0.04	15.02	0.03
	0.095	9.67	0.04	15.01	0.03

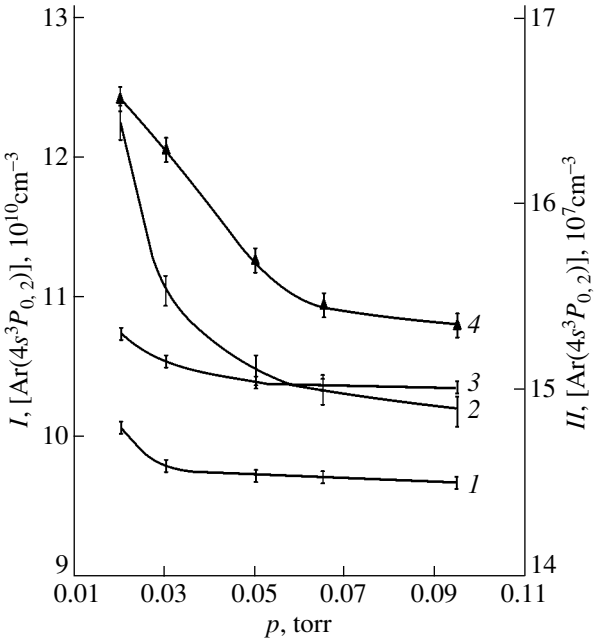

Populations of the $^3P_{0,2}$ states vs. pressure (I) in pure argon: (*1*) Ar($4s^3P_0$), (*2*) Ar($^3P_2$) and (II) in an argon–silane mixture: (*3*) Ar($4s^3P_0$), (*4*) Ar($^3P_2$).

The rate coefficients of the processes k_2, k_3, and k_5 are taken from [9] and are applicable to a nonequilibrium electric discharge. The rate coefficients k_1, k_4, k_7, k_9, and k_{10} were calculated in [6] at a gas pressure of 0.124 torr, a gas temperature of 500 K, and an rf field frequency of 13.56 MHz.

The calculated populations of the $^3P_0$ and $^3P_2$ metastable states are presented in Table 4 and the figure.

The results of calculations show that the populations of the argon metastable states decreases with increasing pressure. The reason is that, as the pressure increases, the frequency of collisions between argon atoms in the metastable and ground states increases.

The populations of the metastable states in the argon–silane mixture are lower than in pure argon. This result indicates a fairly high rate of decomposition of silane molecules due to their collisions with argon metastable atoms.

CONCLUSIONS

(i) The absolute populations of the $3p^55p$ argon levels in pure argon and an argon–silane mixture have been measured by emission spectroscopy. The populations are found to be in the range 19.93×10^5–184.42×10^5 cm^{-3} in pure argon and 13.55×10^5–65.72×10^5 cm^{-3} in the argon–silane mixture.

(ii) The populations of the $^3P_2$ and $^3P_0$ argon metastable states in pure argon and an argon–silane mixture have been determined using the balance equations. The population of the $^3P_2$ state is found to be 9.85×10^{10}–12.23×10^{10} cm^{-3} in pure argon and 15.35×10^7–16.55×10^7 cm^{-3} in the argon–silane mixture. The population of the $^3P_0$ state is found to be 9.67×10^{10}–10.05×10^{10} cm^{-3} in pure argon and 15.01×10^7–15.30×10^7 cm^{-3} in the argon–silane mixture.

(iii) The populations of the argon metastable states in pure argon and an argon–silane mixture have been studied as functions of pressure within the pressure range from 0.02 to 0.095 torr.

REFERENCES

1. M. J. Kushner, J. Appl. Phys. **63**, 2532 (1988).
2. A. J. Flewitt, J. Robertson, and W. Milne, J. Appl. Phys. **85**, 8032 (1999).
3. M. A. Childs and A. Gallagher, J. Appl. Phys. **87**, 1076 (2000).
4. J. C. Knights, R. A. Lujan, *et al.*, Appl. Phys. Lett. **38**, 331 (1985).
5. M. C. M. van de Sanden, R. J. Severens, *et al.*, J. Appl. Phys. **84**, 2426 (1998).
6. V. I. Strunin, A. A. Lyakhov, *et al.*, Zh. Tekh. Fiz. **72** (6), 109 (2002) [Tech. Phys. **47**, 760 (2002)].
7. G. A. Kasabov and V. V. Eliseev, *Spectroscopic Tables for Low-Temperature Plasmas* (Moscow, 1973).
8. *Applied Spectroscopy: Proceedings of the 16th Workshop on Spectroscopy*, Ed. by R. N. Rubinshteĭn (Moscow, 1969), Vol. 1.
9. D. I. Slovetskiĭ, *Mechanisms for Chemical Reactions in Nonequilibrium Plasma* (Moscow, 1980).

Translated by E. Satunina

Technical Physics, Vol. 48, No. 8, 2003, pp. 972–977. Translated from Zhurnal Tekhnicheskoĭ Fiziki, Vol. 73, No. 8, 2003, pp. 34–39.

GASES AND LIQUIDS

Kinematic Structure of Electrohydrodynamic Flow in "Wire–Wire" and "Wire over Plane" Electrode Systems Placed in a Liquid

A. V. Buyanov and Yu. K. Stishkov

Research Institute of Radiophysics, St. Petersburg State University, St. Petersburg, 198504 Russia

e-mail: stishkov@paloma.spbu.ru

Received December 24, 2002

Abstract—A specially designed program package is used for the visualization of experimental data for 2D electrohydrodynamic flows in geometrically symmetric (wire–wire) and asymmetric (wire over plane) electrode systems. The velocity and acceleration distributions in the flows are obtained. The influence of the passive electrode on the kinematic and dynamic structures of the electrodynamic flows is revealed by comparing the results obtained for both electrode systems. A recombination zone is separated and studied. © *2003 MAIK "Nauka/Interperiodica".*

INTRODUCTION

The distributions of the electrical parameters (field strength and potential) in a system of two parallel wires (electrodes) are easy to derive in the electrostatic approximation (in the absence of space charge) by using the mirror images if similar distributions in the "wire over plane" (below referred to as wire–plane) electrode system are known. Such an approach is common in solving electrostatics problems. When the effect of the space charge on the electric field distribution is insignificant, two opposing electrohydrodynamic streams of equal intensities arise in a system of two parallel wires. The structure of either of them must be similar to that of the electrohydrodynamic flow in the wire–plane electrode system. In the presence of the space charge, the actual distribution of the electrical parameters differs from the one calculated in the electrostatic approximation. If, however, the charge production conditions at the electrodes are the same, it could be expected that the structure of the opposing streams approaches the structure of the electrohydrodynamic flow in the wire–plane system, except for the area where the streams meet. This area will be given special attention.

The kinematic and dynamic structures of electrohydrodynamic flows in geometrically asymmetric electrode systems (wire–plane and edge–plane) were studied at length in [1–3]. In these systems, the flow is directed from the wire (edge) toward the planar electrode. The former electrode is usually called active and the latter, passive. Several basic zones of the electrohydrodynamic flow can be distinguished [3]: (i) dead (boundary) zones near either of the electrodes, where an electric charge is injected into the liquid; (ii) the zone where the electric energy is converted into kinetic energy via the energization of the flow by the electric field; (iii) the braking zone near the plane electrode, where the flow velocity magnitude decreases sharply, the flow direction changes, and the central jet bifurcates; and (iv) the transition (steady-state) zone between the energization and braking zones, where the velocity varies insignificantly. Basically, the zone structure does not depend on the process conditions (the voltage across the electrodes, the material and geometry of the active electrode, and the low-voltage conductivity of the liquid): only the shape and dimension of some of the zones change.

In a system of two parallel wires made of dissimilar materials, the contact areas between the electrodes and liquid, as well as the electric field distributions at the electrodes that are derived in the electrostatic approximation, are the same. If the reaction rates at both electrodes are equal, the general electrohydrodynamic flow takes the form of two streams that are symmetric about the plane passing through the center of the interelectrode space parallel to the electrodes. If the liquid is a good insulator, the electrode reaction rate is governed by impurity atoms that are effective donors or acceptors. The ion production rate at the cathode can be controlled over wide limits by varying the impurity concentration. It should be noted that the charge production rate at the electrodes depends not only on the impurity concentration but also on other process parameters, i.e., the potential difference. The complete symmetry of the opposing streams is therefore hardly probable, since it breaks when the voltage or concentration changes. Stable opposing streams are usually observed when the diameter of the electrodes is small.

1063-7842/03/4808-0972$24.00

In this work, we perform a comparative analysis of the electrodynamic flow structure in the wire–plane and wire–wire systems. The latter structure is of interest in that, with opposing streams, the electrode (and, hence, charge injection) in the symmetry plane is absent, unlike in the wire–plane system. As a result, only the recombination of counterions takes place. This allows the separation and analysis of the effective recombination zone, which was not clearly defined in the previous analysis of the flow in the wire–plane system and thus remained poorly understood. Also, one can estimate the influence of the planar electrode on the flow structure in an asymmetric electrode system.

EXPERIMENTAL

The electrohydrodynamic flows were detected with a setup similar to that used in [4]. The only difference is that the flows were filmed, rather than photographed, in order to take a closer look into the flow velocity fields and decrease the error in determining the local velocities and accelerations. Visualization was accomplished by introducing tiny, $(10–20) \times 10^{-6}$ m across, gas bubbles into the liquid with a special capillary. The bubble-producing device made it possible to introduce individual bubbles of a desired size. The volume fraction of the bubbles was about 0.001% and did not noticeably affect the basic properties of the liquid (electrical conductivity, viscosity, and permittivity). The program for processing steady 2D electrodynamic flow data was thoroughly described in [5, 6]. The procedure was applied to bubble paths that follow flow streamlines with an accuracy of no worse than 2–3%. The correspondence of the bubble paths to streamline equations is checked for each path being processed. The program generates vector fields of the flow velocity and acceleration, plots of the velocity and acceleration magnitudes on the surface, and maps of velocity and acceleration isolines. Experiments were carried out in TM-40 transformer oil. The ion production conditions at the cathode were modified by adding butyl alcohol (butanol). It contains the OH group, which has a high electron affinity. By varying the butanol concentration, one can easily control the flow rate from the cathode.

FLOW IN THE WIRE–PLANE SYSTEM

As was noted, the flow structure in this electrode system was carefully examined in [1–3]. Here, we will briefly recall the characteristic features of the flow in this system. Figure 1 shows the (a) velocity and (b) acceleration isolines for the electrohydrodynamic flow with the following process parameters: active electrode diameter d = 0.5 mm, low-voltage conductivity $\sigma = 10^{-11}$ $(\Omega\,\mathrm{m})^{-1}$, electrode spacing L = 15 mm, and voltage across the electrodes U = 6 kV.

Electrochemical reactions at the active electrode produce ions of the same sign as the electrode. Within the boundary layer, the ions move relative to the quiescent liquid with a velocity depending on their low-voltage mobility and form a solvation sheath around themselves. In the acceleration zone, the ions subjected to the electric field are accelerated together with their molecular environment. The acceleration is significant, varying from 1 to 10 m/s^2 according to the applied voltage, so that adjacent liquid layers are also involved in the process. A vortical region forms near the active

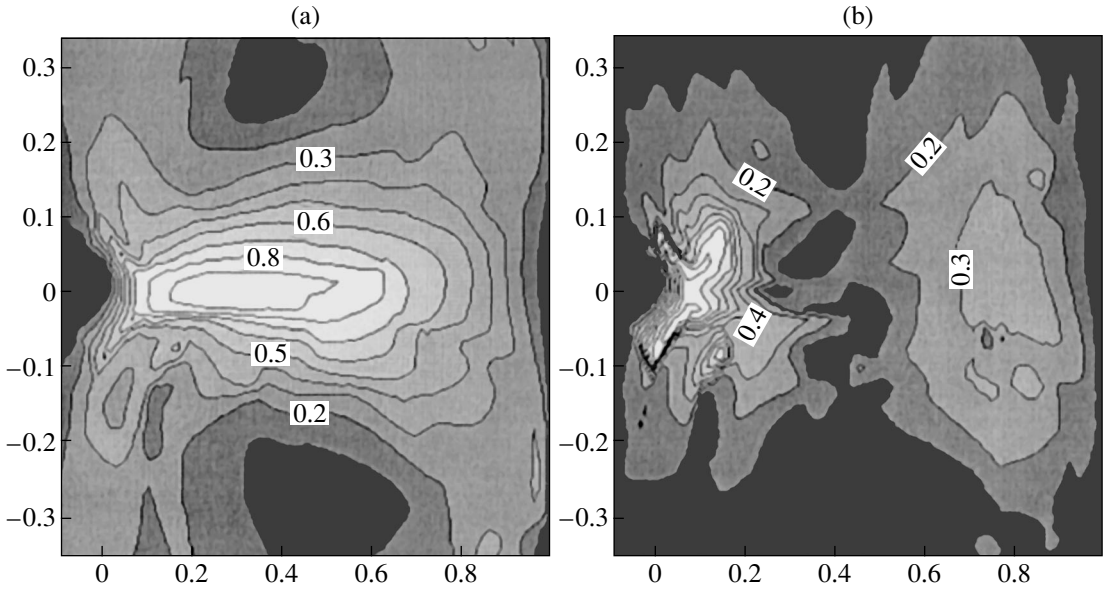

Fig. 1. Maps of (a) velocity and (b) acceleration isolines for the electrohydrodynamic flow in the wire–plane electrode system.

electrode, as is clearly seen in Fig. 1a. The acceleration zone, where the electric field energy is converted into the kinetic energy of the liquid, occupies a rather limited space (Fig. 1b).

For electrohydrodynamic flow with allowance for Coulomb forces, the Navier–Stokes equation has the form

$$\gamma\left[\frac{\partial \mathbf{V}}{\partial t} + (\mathbf{V}\cdot\nabla)\mathbf{V}\right] = -\nabla P + \eta\Delta\mathbf{V} + \rho\mathbf{E},$$

where γ is the liquid density, $\mathbf{V}$ is the liquid velocity, P is the pressure, η is the viscosity, ρ is the space charge density, and $\mathbf{E}$ is the electric field strength.

This equation implies that the liquid is under the action of electrical, viscous, and internal pressure forces. In the steady-state zone, viscous and electrical forces are balanced and internal pressure forces are small; therefore, the flow velocity varies (decreases or increases) insignificantly. In Fig. 1b, the steady-state zone appears as a dip between two acceleration maxima. Here, the flow velocity reaches a maximum.

The structure of the braking zone is the most interesting. Figure 2a shows the velocity isolines with the vector acceleration field superposed and Fig. 2b, isolines of the acceleration projections onto the velocity direction. Both figures were obtained under the same conditions as Fig. 1 but at a larger magnification. The braking zone is seen to have a complicated structure. It begins from a level of (0.4–0.5)L (sometimes 0.3L), ends up in the immediate vicinity of the planar electrode, and has the form of a triangle one vertex of which faces the active electrode (Fig. 1b). The liquid stagnates when subjected to viscous and internal pressure forces. The stagnation forces are maximum at a distance of (0.75–0.80)L. It is reasonable to assume that the inter-

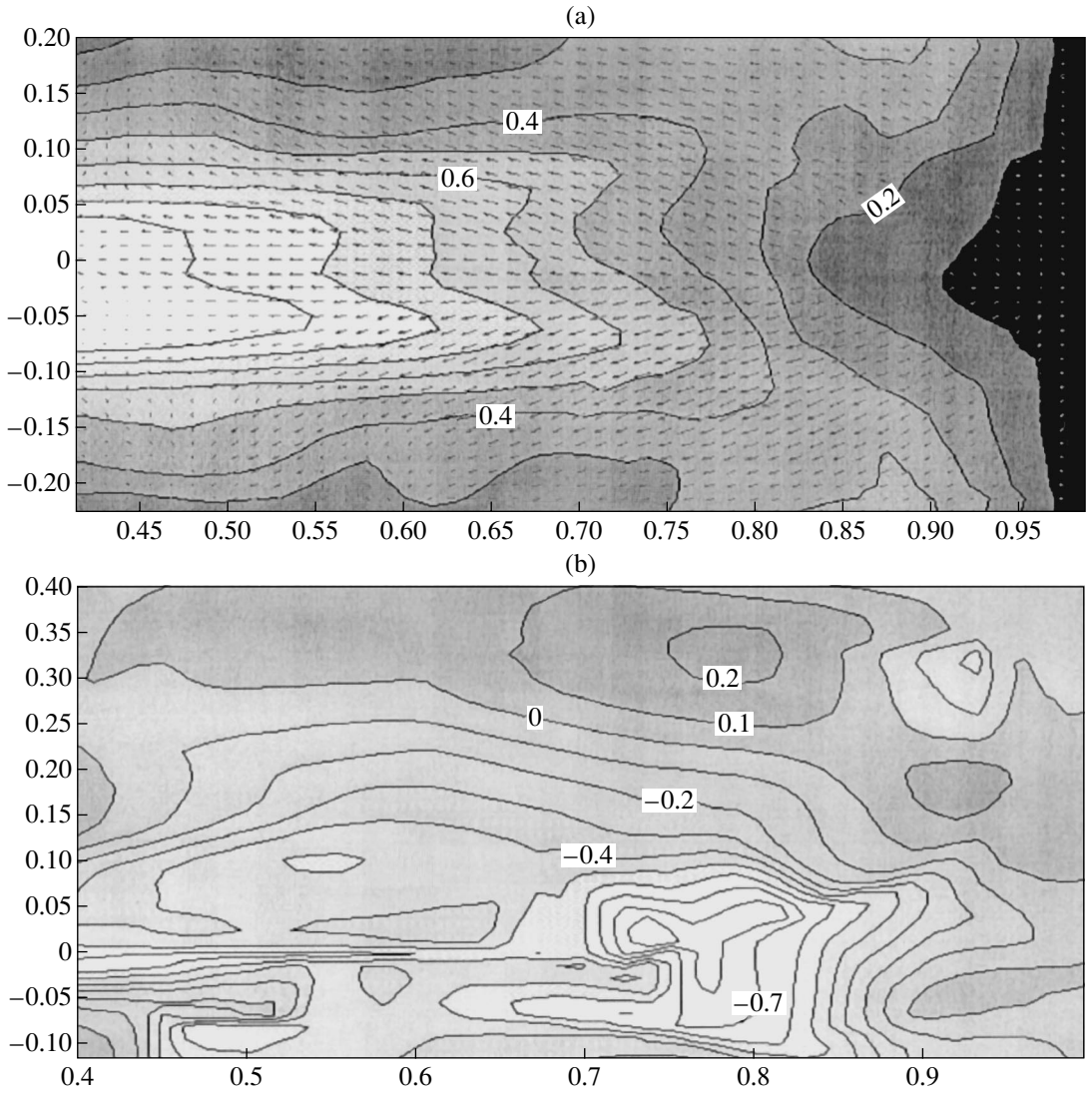

Fig. 2. Maps of (a) velocity isolines and (b) isolines of the force projections onto the velocity direction in the braking zone.

nal pressure also reaches a maximum in this area. The vector acceleration field pattern supports this assumption. In fact, Fig. 2 shows that the liquid is accelerated when running out of the braking zone. The flow bifurcates. It is distinctly seen (Fig. 2b) that the liquid has a positive acceleration in the direction of lateral streams. The space charge adds complexity to the situation. The charge on the active electrode accumulates in the dead zone near the planar electrode. Accordingly, the electric field at the metal–liquid interface grows. This is substantiated by the measurement of the electric field distribution in the electrode spacing [4, 6]. The rise in the electric field enhances the injection of the charge from planar electrode (positive in our case) and initiates the recharge of the liquid.

The liquid charged like the planar electrode flows in the lateral streams. The space charge distorts the electrode-induced electric field. The charge of the initial electrohydrodynamic flow and that of the lateral streams produce an electric field that is normal (and sometimes even opposite) to the external field. The former field greatly complicates the flow structure in the braking zone. Apparently because of this, the braking zone is as wide as (0.5–0.7)L at a velocity level of 0.1, while the acceleration zone at the same velocity level has transverse dimensions of (0.3–0.5)L. The secondary acceleration of the liquid in return streams, which is clearly demonstrated in Fig. 2b, is direct evidence of the liquid recharge at the planar electrode surface.

FLOWS IN THE SYMMETRIC AND ASYMMETRIC SYSTEMS

Figure 3 demonstrates the velocity and acceleration isolines for the wire–wire system with $d = 0.07$ mm, $\sigma = 10^{-11}$ $(\Omega\,\mathrm{m})^{-1}$, and $U = 10$ kV. For convenience, the patterns are cut at the place of meeting with the second flow from the counterelectrode. At this place, there exists a narrow (about 0.04L) region where the flow velocity is negligible. It is clearly seen at a distance of 0.65L from the anode (Fig. 3a). For the totally symmetric conditions of electrode charging, this region is in the middle of the electrode spacing.

The flows in the wire–plane and wire–wire electrode systems share a number of traits. The central flowing stream, as well as the energization, steady-state, and braking zones, are distinctly seen. Structurally, the acceleration zones are the closest to each other. In both cases, the vortical region forms near the active electrode. It is distinctly seen that the liquid speeds up before it reaches the lower edge of the active electrode, where the injection is supposedly the most intense. The extent of the acceleration zone in the symmetric and asymmetric systems is, respectively, (0.28 ± 0.03)L and (0.30 ± 0.03)L. The most noticeable difference between the systems is that the bifurcation of the acceleration maximum in the symmetric system is more obvious than in the asymmetric one. Thus, one can infer that, in the acceleration zones of both systems, the formation of charges due to electrochemical reactions, the formation of their molecular environment, and the acceleration of

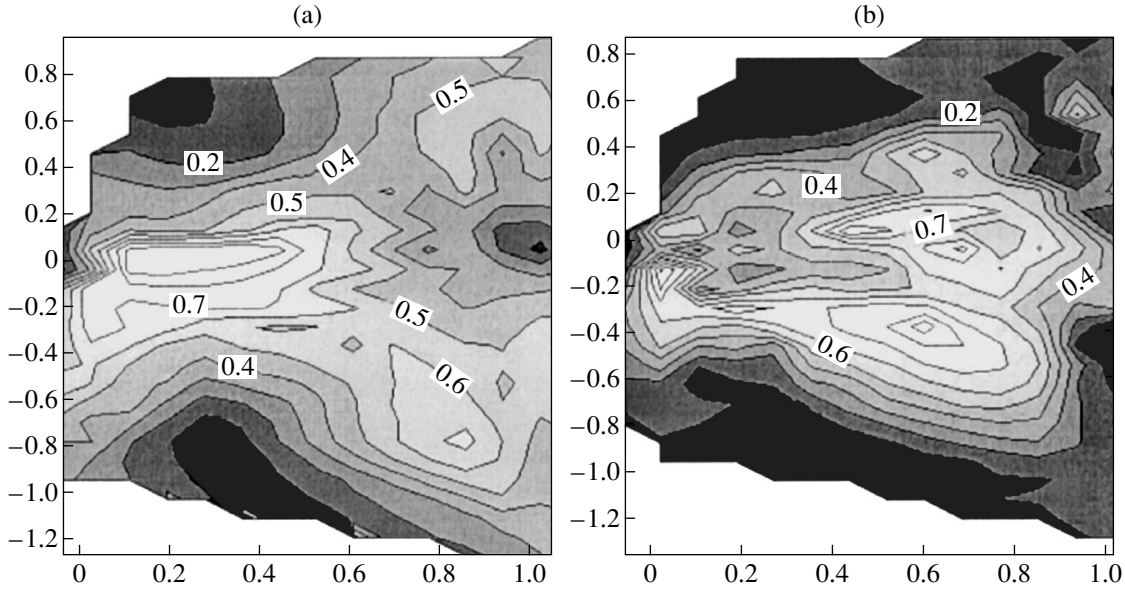

Fig. 3. Maps of (a) velocity and (b) force isolines for the electrodynamic flow in the system of two parallel wires.

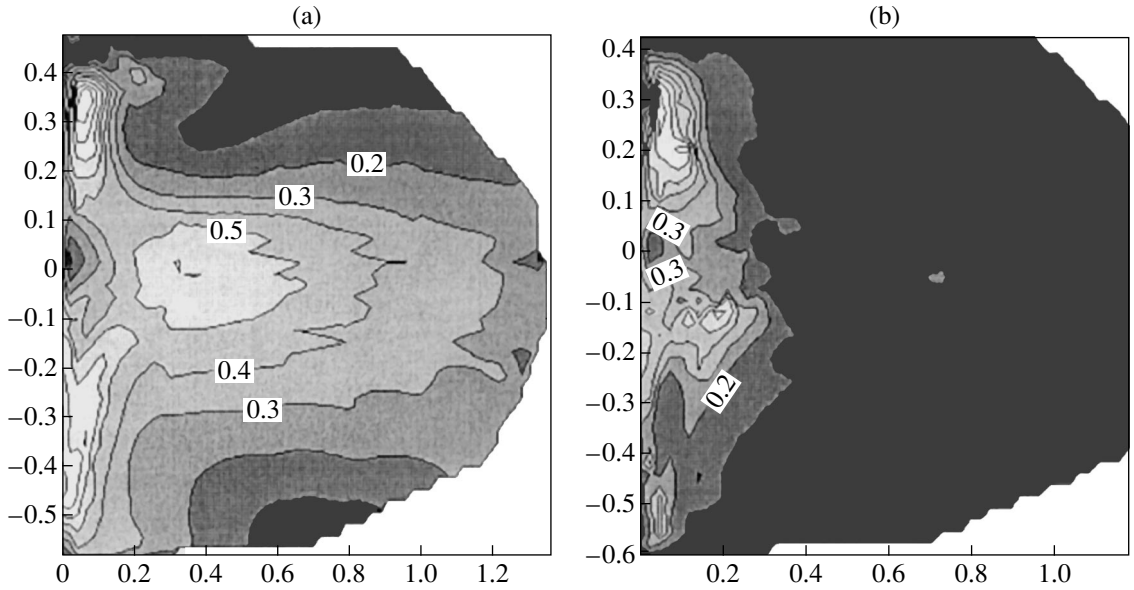

Fig. 4. (a) Velocity isolines and (b) isolines of the force projections onto the velocity direction for the lateral streams of the electrohydrodynamic flow in the symmetric electrode system.

the liquid by the electric field follow the same mechanisms.

In a system of two parallel wires, the steady-state zone of the electrohydrodynamic flow is very short: the acceleration zone passes into the braking zone almost immediately. The structure and transverse dimensions of the latter differ radically from those in the wire–plane configuration because of the absence of the counterelectrode. In the wire–plane system, the liquid flow, as was noted above, is recharged at the surface of the counterelectrode, acquires a velocity component in the direction from the counterelectrode, and slightly speeds up in the lateral streams (Fig. 2b). In the wire–wire system, the counterelectrode is absent and the liquid cannot be recharged. Here, two unlikely charged streams meet and then flow parallel to each other (without mixing) and normally to an imaginary straight line connecting the electrode axes. Between the streams, a field induced by their self-space charges and directed normally to the flow arises. Counterions may approach each other only by drift (migration) in the transverse field. This process is slow, since the flow velocity far exceeds the ion drift velocity. To recombine, the ions must come within the Debye length R_D. The value of R_D is evaluated by the formula

$$R_D = \sqrt{\frac{kT}{e}\frac{b_i\varepsilon_0\varepsilon}{\sigma}}.$$

For our experiment, $kT/e = 0.25$ mV, $b_i \sim 10^{-8}$ m/s, $\varepsilon_0 = 8.8 \times 10^{-12}$, $\varepsilon = 2$, and $\sigma \approx 10^{-11}$ $(\Omega\,\mathrm{m})^{-1}$; hence, we find that R_D is 3×10^{-5} m.

The unlikely charged lateral streams are attracted together and run parallel to each other until most of the charges recombine. Because of this, the lateral streams are markedly longer than the electrode spacing.

To study the flow velocity distribution in the lateral streams in more detail, they were processed with a higher resolution (Fig. 4). The origin here coincides with the center of the dead zone. The electrodes are at the upper left and lower left corners of the figure. Both central streams of the return flow are seen at the left of the figure. It is seen (Fig. 4b) that weak forces speeding up the liquid along the flow direction are present in the lateral streams. They are presumably associated with an increased pressure in the dead zone. After a short acceleration time, the liquid velocity declines slowly over a distance of (3–5)L. Within this length, the velocity varies insignificantly (Fig. 4b). The lateral streams are rather wide in the direction normal to the velocity direction: 0.4L and 0.6L for velocity levels of 0.4 and 0.2, respectively.

Thus, the planar electrode and processes in its vicinity greatly affect the flow structure in the asymmetric electrode system. This fact is, as a rule, ignored in most simulations of electrohydrodynamic flows, where emphasis is given on processes near the active electrode.

CONCLUSIONS

Our comparative analysis of the kinematic and dynamic structure of electrohydrodynamic flows in wire–wire and wire–plane systems revealed that the planar electrode also injects charge. This has an effect on the structure of return flows. The braking zone structures in the systems differ. In the wire–wire system, the liquid is not recharged: charges coming from both elec-

trodes recombine. The recombination zones are lateral streams, which have a bipolar structure and a length depending on the recombination rate.

REFERENCES

1. Yu. K. Stishkov, M. A. Pavleyno, and A. V. Buyanov, in *Proceedings of the 6th International Scientific Conference "Modern Problems of Electrophysics and Electrodynamics of Fluids," St. Petersburg, 2000,* pp. 87–92.
2. Y. K. Stishkov and M. A. Pavleyno, in *Proceedings of the 2nd International Workshop "Electrical Conduction, Convection, and Breakdown in Fluids," Grenoble, 2000,* pp. 186–189.
3. A. V. Buyanov, M. A. Pavleyno, and Yu. K. Stishkov, Vestn. St. Peterb. Univ., Ser. 4: Fiz., Khim., 109 (2001).
4. Yu. K. Stishkov and A. A. Ostapenko, *Electrohydrodynamic Flows in Insulating Fluids* (Leningr. Gos. Univ., Leningrad, 1989).
5. Yu. K. Stishkov and M. A. Pavleyno, Élektron. Obrab. Mater., No. 1, 14 (2000).
6. Yu. M. Rychkov and Yu. K. Stishkov, Kolloidn. Zh. **40**, 1204 (1978).

Translated by V. Isaakyan

Technical Physics, Vol. 48, No. 8, 2003, pp. 978–982. Translated from Zhurnal Tekhnicheskoĭ Fiziki, Vol. 73, No. 8, 2003, pp. 40–44.

GASES AND LIQUIDS

Engineering Physical Model of Gas Flows in a Medium Vacuum

Yu. M. Pechatnikov

St. Petersburg State Polytechnical University, St. Petersburg, 195297 Russia

e-mail: yiriy@mail.ru

Received December 24, 2002

Abstract—The development of techniques for simulating gas flows in vacuum units in going from the molecular to viscous flow is hampered by the lack of adequate physical concepts of a medium vacuum. We offer an engineering physical model to simulate gas flows in vacuum units. Based on this model, a probabilistic method of simulation is worked out, and the gas flows in the molecular–viscous regime are evaluated. The paradox observed in the molecular–viscous regime is accounted for. The model is verified by experiments. © *2003 MAIK "Nauka/Interperiodica".*

In accordance with Monte Carlo statistical methods, a gas flow Q passing through a vacuum unit is calculated as

$$Q = Q_0 P, \quad (1)$$

where Q_0 is the gas flow at the inlet, $P = N_2/N_1$ is the probability that gas molecules will pass through the unit, and N is the number of molecules at the inlets ($N = N_1$) or at the outlets ($N = N_2$).

The number N_2 is found from numerical experiments where the motion of molecules between the inlet and outlet is traced. The absence of a generally accepted model of gas flow in moderate-vacuum units is the main difficulty in simulating the molecular–viscous flow of a rarefied gas by direct Monte Carlo techniques without solving kinetic equations at any step [1, 2]. Nevertheless, at present, there are a number of methods that are well developed on the conceptual level [3, 4], such as (1) the method of simulating probable paths for $0.01 < \mathrm{Kn} < 100$ [5], where Kn is the Knudsen number, and (2) the direct simulation method for $0.1 < \mathrm{Kn} < 100$ [6].

Calculations are used for solving specific problems [7–10]; however, the use of numerical experiment in vacuum technology, instead of expensive full-scale measurements, is limited [11]. The fact is that the former method (of those listed above) is poorly known [12–14] and the latter is conceptually developed only to solve special problems of space technology [6]. Furthermore, the engineering physical model elaborated in [6] has an essential restriction: only pair collisions are considered. The application of this model causes an uncertainty, which is associated with the fact that a finite number of molecules (N) is simulated simultaneously and that a rarefied gas does not obey strictly the Boltzmann statistics. In engineering practice, one faces difficulties when specifying physical constants in molecular collisions under certain conditions. It should also be noted that the Berd method [6] requires considerable computational resources [15].

Unlike the Berd model, the method of simulating probable molecule trajectories consistently allows for physical processes occurring in the steady flow of a rarefied gas in vacuum systems. In this method, (i) the molecular–viscous flow obeys the Boltzmann statistics and the velocities and free path lengths of molecules are distributed according to the Maxwell statistics; (ii) the path of a molecule is described by a piecewise linear function that is a polygonal line with segments equal to the molecule free path; (iii) boundary conditions for the velocity distribution and the distribution of molecule motion directions become diffuse after collisions with the stainless steel wall of a vacuum unit according to the cosine law throughout the range of molecular–viscous flow; (iv) intermolecular interactions inside the gas flow are governed by the collective effect of the molecular ensemble according to the dynamic theory of kinetic equations; (v) since the number of molecules in the volume of the vacuum unit is large, it is reasonable and sufficient to consider the collective effect of molecule interaction inside the gas flow as a probabilistic process.

The distribution of the molecule motion directions after molecular collisions inside the flow is viewed as a result of the collective interaction of the molecular ensemble based on the following concepts of medium vacuum physics.

(1) As was shown [16], when heat exchange processes are neglected and only forces of molecular interaction are considered, similarity inside the steady flow of a certain rarefied gas can be achieved in vacuum systems with the same Knudsen similarity number (Kn).

(2) According to the dynamic theory of kinetic equations, a gas flow (Q) is represented by an ensemble of N

1063-7842/03/4808-0978$24.00

statistically independent identical molecules, which are characterized by effective diameters and masses.

(3) If quantum effects are neglected, a molecular ensemble is assumed to be a complex mechanical system consisting of molecules, each of which is a complex mechanical system composed of atoms.

(4) Since the flow is assumed to be steady, we can, without considering the time factor [5], sequentially trace the trajectories of N statistically independent individual molecules in the volume of a vacuum unit from inlets (N_1) to outlets (N_2).

(5) We assume that the entire molecular–viscous flow of a rarefied gas simulates the conversion of the random molecule motion (according to the Boltzmann statistics for the molecular regime) to the laminar flow (according to the ideas of continuum mechanics, which are applicable to the viscous regime).

(6) Since the random motion of molecules in the molecular regime changes to the laminar flow in the viscous regime, there exists a force (Φ) that alters the type of molecule motion in the gas flow and specifies the motion direction for each molecule in the flow of a rarefied gas.

(7) In accordance with the dynamic theory of kinetic equations, the force Φ is assumed to be governed by the collective effect of intermolecular interactions in the molecular ensemble and its value depends on the molecule concentration in the flow: $\Phi = \Phi(Kn)$.

(8) In accordance with the dynamic theory of kinetic equations, molecules are statistically independent at spacings greater than the effective range of interaction; hence, the collective effect of intermolecular interactions shows up only at the moment of collision, relaxation, and energy redistribution over degrees of freedom.

(9) Under intermolecular collisions, first the energy is redistributed over degrees of freedom and the collective effect of the molecular ensemble ($\Phi(Kn)$) arises. Then, molecules bounce off each other and freely move in the vacuum unit. In the local spherical coordinate system with the origin at the point of collision, the molecule trajectory is expressed as

$$\frac{x - x_1}{\sin\gamma\cos\varphi} = \frac{y - y_1}{\sin\varphi\sin\gamma} = \frac{z - z_1}{\cos\gamma}, \qquad (2)$$

where (x_1, y_1, z_1) and (x, y, z) are the initial and running coordinates of a molecule, respectively (the distance between the points with coordinates (x_1, y_1, z_1) and (x, y, z) is the free path of a molecule); γ is the angle the path makes with the coordinate axis directed along the flow, $\gamma \in [0, \pi]$; and φ is the angle lying in the plane perpendicular to the flow direction, $\varphi \in [0, 2\pi]$.

The distribution of the angle φ is assumed to be uniformly random:

$$\varphi = 2\pi R_1, \qquad (3)$$

where R_1 is a random number evenly distributed in the closed interval [0, 1].

The distribution of the angle γ is based on the following reasoning. Since the trajectory of each isolated molecule is affected by intermolecular interaction in the molecular ensemble ($\Phi(Kn)$), the direction angle γ of a trajectory can be described as a probability function of the argument $\Phi(Kn)$: $\gamma = \gamma(\Phi(Kn))$. Thus, the angle $\gamma = \gamma(\Phi(Kn))$ relates the effect of molecular interaction forces on the motion of an individual molecule [5]. To determine this angle, one must know its probability distribution as a function of the molecule concentration in a microvolume of the vacuum unit characterized by a Knudsen number. Evidently, such quantitative estimations should be applied to a large number of molecules.

The dependence $\gamma = \gamma(\Phi(Kn))$, which describes the collective effect of molecule interaction during the transformation of the chaotic motion into the laminar flow, is found based on the above-postulated laws of intermolecular interaction and molecule relaxation under collisions. Note that the dependence obtained should be refined experimentally because of the uncertain definition of physical constants in engineering calculations of molecular interaction. This is made by comparing analytical results and full-scale measurements for the capacity of a long pipeline with a round cross section. Experimental results for air can be expressed as

$$\gamma = \pi R_2(1 - P_f(\delta)), \qquad (4)$$

where R_2 is a random number evenly distributed in the [0, 1] interval and $P_f(\delta)$ is the probability distribution of the angle γ, which specifies the molecule trajectory after intermolecular interaction ($\delta = 1/Kn$) (Fig. 1) [5].

The dependence $P_f(\gamma) = P_f(\gamma(Kn))$ can be approximated as

$$P_f(\mathrm{Kn}) = 0.021\delta^{0.84}. \qquad (5)$$

Note the experimental results that are most interesting from the viewpoint of the physics of rarefied gas. Initial intermolecular collisions are observed at $\delta \cong 0.01$ sr, where $\delta = 1/Kn$ (Fig. 1). The direction of the molecule trajectory after molecular collisions remains equiprobably within a complete solid angle of 4π sr ($P_f = 0$) for $\delta < 0.5$ (Fig. 1). This fact indicates that the collective effect of the molecular ensemble (Φ) has no influence and collisions between molecules can be regarded as pair events. In essence, the range $\delta < 0.5$ is the applicability domain for the Berd model. For $\delta > 0.5$, the motion direction of a molecule is additionally affected by the force field due to the interaction between surrounding molecules. However, for $0.5 < \delta < 10$, this effect is rather weak (P_f varies from 0 to 0.1) and the Berd model still holds. For lower Knudsen numbers, most collisions involve more than two molecules and the collective effect should be taken into

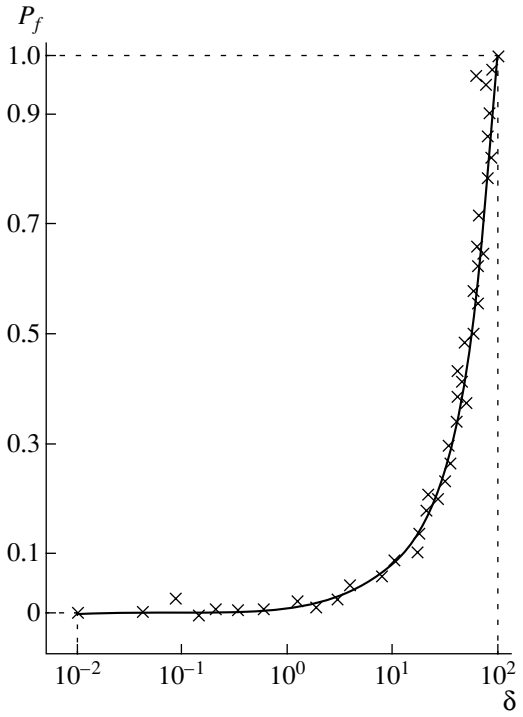

Fig. 1. Distribution of the direction angle γ after intermolecular interaction inside a gas flow.

account. For $\delta \cong 100$, molecules are entrained by the rarefied gas flow.

Using the adopted model of rarefied gas flow, we developed a method conventionally called the method of simulating probable directions [5].

(1) The configuration of vacuum unit components is mathematically represented as a set of connected surfaces in three-dimensional space. Each of these surfaces is described by one analytical equation and a system of inequalities.

(2) The molecule coordinates at the inlet section are assumed to be equiprobably distributed over the cross section.

(3) The trajectory of a separate molecule between collisions is described in the local spherical coordinate system with the origin placed at the point of collision and the axes changing their direction according to the site of collision (inside or at the boundary of the flow) and the "internal" flow direction.

(4) When a rarefied gas molecule strikes the surface of the vacuum unit at the boundary of the flow, the trajectory is determined from Eq. (2). In this case, the local spherical coordinate system has its origin at the point of collision; γ is the angle between the trajectory and the coordinate axis directed perpendicularly to the surface that is tangent to the vacuum element surface at the point of collision, $\gamma \in [0, \pi]$; and φ is the angle lying in this surface ($\varphi \in [0, 2\pi]$, $\varphi = 2\pi R_1$, $\gamma = \arcsin\sqrt{R_2}$).

(5) When collisions take place inside the gas flow, the postcollision trajectory is determined from Eq. (2) in the local spherical coordinate system with the origin at the point of collision, and the direction angles φ and γ are calculated with (3) and (4), respectively.

(6) The number N of independent experiments that is necessary to provide a sufficient accuracy of calculations is determined from the normal distribution law of a random quantity when estimating the expectation.

According to this method, we simulate the walk of a molecule in the vacuum unit using the probability distribution of the trajectory directions and fix the number of molecules going out through the outlet (N_2) in N separate experiments. Then, we find the gas flow from expression (1). The experimental results are shown in dimensionless coordinates as the dependence $J_{MB} = J_{MB}(L/D; \delta)$, where J_{MB} is the ratio of the calculated capacity of the vacuum pipeline to its capacity in the molecular regime (Figs. 2, 3). Experimental tests and the estimation of computational resources needed to calculate P in (1) lead us to conclude that standard computing facilities suffice to implement this method in engineering practice.

From Figs. 2 and 3, it follows that, as the length-to-diameter ratio (L/D) decreases, the minimum of the capacity smooths out and shifts to higher Knudsen numbers. For $L/D < 4$, the curve $J_{MB}(L/D; \delta)$ does not have a minimum (Figs. 2, 3). The presence of a capacity minimum (the Knudsen paradox) in long pipelines ($L/D > 8$) can be accounted for as follows. As the Knudsen number decreases from 100 to 1, the number of pair molecular collisions greatly increases and they are no longer compensated for by the collective effect of intermolecular interaction forces at the initial stage of formation of the directed flow velocity (which is close to zero in this range of Knudsen numbers). Such a situation makes the motion of molecules along a pipeline still more difficult, and, hence, the probability that they will pass through the pipeline drops. This drop is not made up by an increase in the capacity at the inlet section. As a result, the capacity of pipelines with geometrical sizes $L/D > 8$ declines when the Knudsen number decreases from 100 to 1.

It is also noteworthy that the length dependence of the pipe capacity weakens when the molecular flow changes to the molecular–viscous and viscous regimes (Fig. 2). In terms of our model, this fact can be explained as follows. For $Kn = 0.01$, $P_f = 1$ (Fig. 1) and all molecules are directed along the flow ($\gamma = 0$ according to Eq. (5)); therefore, $N_2 \longrightarrow N$ and hence $P \longrightarrow 1$ and $Q \longrightarrow Q_0$ (see (1)). Another explanation can be given from the theory of a boundary layer in a continuum. Since the flow velocity of a rarefied gas in real vacuum systems is small, the viscosity of the gas and the Reynolds number at the boundary between the molecular–viscous and viscous regimes, where the molecule free path is comparable with the pipeline diameter, do not influence the pipeline capacity. Under

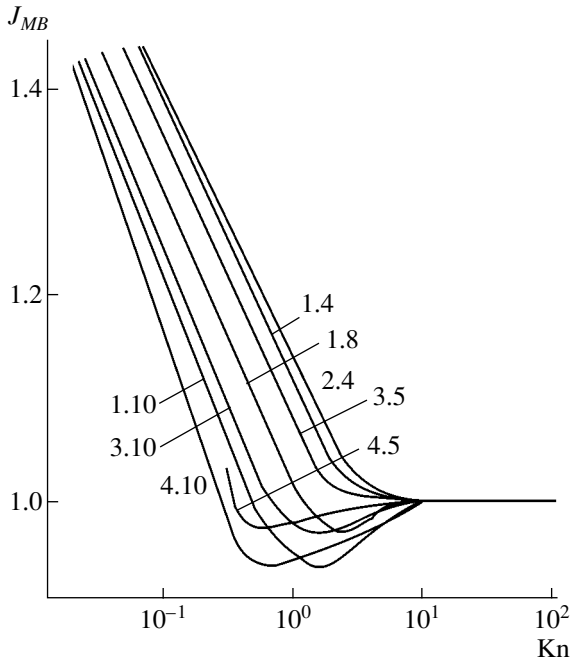

Fig. 2. Data calculated (1.4, 1.8, 1.10) by the method of probable directions [5] for L/D = 4, 8, and 10, respectively; (3.5, 3.10) by solving the linearized Boltzmann equation for L/D = 5 and 10; and (4.5, 4.10) by the method of direct simulation for L/D = 5 and 10 [9]. (2.4) Full-scale experiments for L/D = 4 [3].

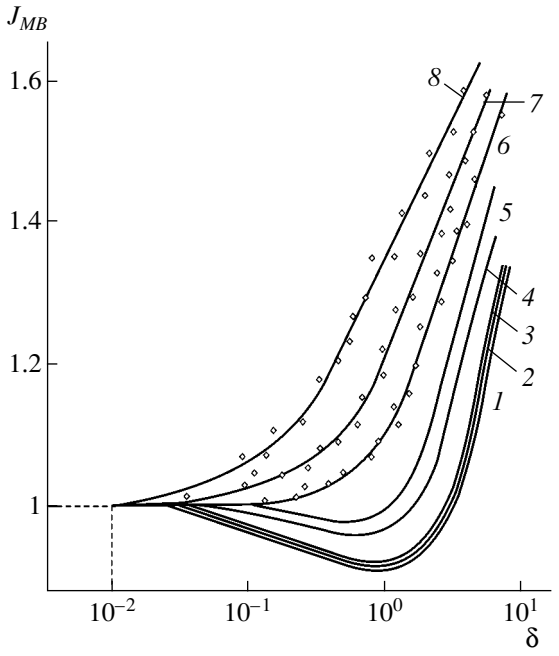

Fig. 3. Data calculated by the method of probable directions [5]: (*1*) long rectangular pipeline; (*2*) long elbow round pipeline; and (*3*–*8*) round pipelines with L/D = 40, 10, 8, 4, 2, and 0.1, respectively. (◇) Full-scale experiments [3].

these conditions, vacuum pipelines of the same diameter with L/D varying from 0.01 to 40 can be considered as long channels and corrections may be disregarded, as demonstrated by the investigations of the viscous regime [3].

Thus, our model is consistent with the models of molecular and viscous flows, accounts for the Knudsen paradox, and explains the independence of the pipeline capacity from the length in going from the molecular–viscous to viscous regime. The results of this work allow one to critically revise the current notions of the influence of a solid wall under conditions where the molecule free path is comparable to the pipeline diameter.

To conclude, our engineering physical model of a rarefied gas flow and the method of probable directions are based on scientific concepts and are validated by comparing with results obtained by the method of direct simulation and by solving the linearized Boltzmann equation (Fig. 2). The model and method are also substantiated by full-scale measurements carried out by the author and other researchers (Fig. 3).

For engineering purposes, the experimental results for air at room temperature can be generalized as

$$J_{MB} = \frac{1 + 202G + 2653G^2}{1 + 236G},$$

where

$$G = \frac{4.7 \times 10^{-3}}{Kn}\left(1 + 2.1Kn^{0.25}\frac{D}{L}\right).$$

When introduced into engineering practice, the method of probable directions will make expensive experiments considerably cheaper.

REFERENCES

1. V. V. Kuz'min, *Vacuum Physics* (St. Peterb. Gos. Tekh. Univ., St. Petersburg, 2000).
2. R. G. Livesey, *Foundations of Vacuum Science and Technology*, Ed. by J. M. Lafferty (Wiley, New York, 1998).
3. Yu. M. Pechatnikov, Vak. Tekh. Tekhnol. **6** (2), 5 (1996).
4. V. N. Gusev, I. V. Egorov, A. I. Erofeev, *et al.*, Izv. Ross. Akad. Nauk, Mekh. Zhidk. Gaza, No. 2, 128 (1999).
5. Yu. M. Pechatnikov, Inzh.-Fiz. Zh., No. 6, 673 (1992).
6. J. N. Moss and G. A. Berd, Aerospace America, No. 3, 11 (1989).
7. V. A. D'yachenko, V. Ya. Krasnoslobodtsev, and V. Yu. Skvortsov, Vak. Tekh. Tekhnol., No. 2, 34 (1996).
8. G. Scherer-Abreu and R. A. Abreu, Vacuum, Nos. 8–10, 863 (1995).
9. A. I. Erofeev, M. N. Kogan, and O. G. Frilender, Izv. Ross. Akad. Nauk, Mekh. Zhidk. Gaza, No. 5, 193 (1999).

10. Yu. M. Pechatnikov and V. V. Shchenev, in *Proceedings of the Scientific and Technical Conference on Vacuum Science and Technology* (Mosk. Inst. Élektron. Mashinostroeniya, Moscow, 2002), pp. 48–51.

11. Yu. M. Pechatnikov, Nauchn.-Tekh. Vedomosti St. Peterb. Gos. Tekh. Univ., No. 1, 80 (2002).

12. Yu. M. Pechatnikov, in *Proceedings of the International Symposium on Vacuum Technologies and Equipment, Kharkov, 2001*.

13. Yu. M. Pechatnikov, in *Proceedings of the Scientific Meeting "Vacuum Equipment and Technology," St. Petersburg, 2002* (UNIVAK, St. Petersburg, 2002), pp. 18–21.

14. Yu. M. Pechatnikov, in *Proceedings of the Scientific and Technical Conference on Vacuum Science and Technology* (Mosk. Inst. Élektron. Mashinostroeniya, Moscow, 2002), pp. 51–54.

15. V. V. Zakharov, G. A. Luk'yanov, and G. O. Khanlarov, *Parallel Algorithms for Direct Monte Carlo Simulation in Molecular Gas Dynamics* (Inst. Vysokoproizvodit. Vychisl., St. Petersburg, 1999).

16. Yu. M. Pechatnikov, *Complex Vacuum Units Designed for Viscous Molecular Gas Flow* (Svetlana, St. Petersburg, 2002).

Translated by M. Astrov

Technical Physics, Vol. 48, No. 8, 2003, pp. 983–994. Translated from Zhurnal Tekhnicheskoĭ Fiziki, Vol. 73, No. 8, 2003, pp. 45–55.

GAS DISCHARGES, PLASMA

Substantiation of the Two-Temperature Kinetic Model by Comparing Calculations within the Kinetic and Fluid Models of the Positive Column Plasma of a DC Oxygen Discharge

E. A. Bogdanov*, A. A. Kudryavtsev*, L. D. Tsendin, R. R. Arslanbekov***, V. I. Kolobov***, and V. V. Kudryavtsev******

** St. Petersburg State University, Universitetskaya nab. 7/9, St. Petersburg, 199034 Russia*
e-mail: akud@ak2138.spb.edu
*** St. Petersburg State Technical University, ul. Politekhnicheskaya 29, St. Petersburg, 195251 Russia*
**** CFDRC, 215 Wynn Drive, Huntsville, AL, USA*
***** CFD-Canada, 45 English Ivyway, Toronto*
Received December 23, 2002

Abstract—Results from kinetic and fluid simulations of the positive column plasma of a dc oxygen discharge are compared using commercial CFDRC software (http://www.cfdrc.com/~cfdplasma), which enables one to perform numerical simulations in an arbitrary 3D geometry with the use of both the fluid equations for all the components (fluid model) and the kinetic equation for the electron energy distribution function (kinetic model). It is shown that, for both the local and nonlocal regimes of the formation of the electron energy distribution function (EEDF), the non-Maxwellian EEDF can satisfactorily be approximated by two groups of electrons. This allows one to take into account kinetic effects within the conventional fluid model in the simplest way by using the proposed two-temperature approximation of the nonequilibrium and nonlocal EEDF (2T fluid model).

The increased interest in discharges in molecular (first of all, electronegative) gases stems from their wide use in modern plasma technologies [1]. The parameters of a gas-discharge plasma can only be determined by employing self-consistent models with allowance for the transport processes and volume plasmochemical reactions involving a great number of atomic and molecular components in different excited and ionization states. To date, the most frequently used model is the hydrodynamic (fluid) model, which has been widely used to describe various plasmochemical facilities (see, e.g., [1–3]). To make an express estimate of the plasma parameters, a simplified version of the model, namely, space-averaged (global) model [4, 5] is also used. In those models, the rate constants K_j of the reactions with the participation of electrons are expressed in Arrhenius form via the ratio of the activation energy to the electron temperature: $K_j \sim \exp(-E_j/T_e)$. In fluid models, the temperature T_e in the exponential dependence $K_j(T_e)$ is deduced from the mean energy $\bar{\varepsilon} = 3T_e/2$ using the energy balance equation for the electron gas.

In order for such a description to be adequate, the electron energy distribution function (EEDF) must be Maxwellian. However, it is well known (see, e.g., [6]) that the electron distribution differs considerably from Maxwellian (with the only exception of the Langmuir paradox in the collisionless (free-fall) regime, when the EEDF can be well approximated by a Maxwellian distribution [7]). Generally, when the degree of ionization is not too high ($n_e/N < 10^{-3}$), the EEDF is highly nonequilibrium and is depleted of electrons in the energy range corresponding to inelastic collisions ($\varepsilon > \varepsilon_j$). Depending on the relation between the characteristic diffusion length Λ (e.g., $\Lambda = R/2.4$ for a cylinder) and the electron energy relaxation length λ_ε, the EEDF is either local (at $\Lambda > \lambda_\varepsilon$) or nonlocal (at $\Lambda < \lambda_\varepsilon$) [8]. The procedure of calculating Λ in discharges with different geometrical configurations is described, for example, in [1]. Thus, for plane-parallel geometry ($x = 0, L$), we have $\Lambda = L/\pi$. Let us remember that, in the first approximation, any discharge geometry can be approximately reduced to the plane–parallel geometry by introducing the effective length $L = V/S$, where V is the volume and S is the surface area. The local EEDF is determined by the plasma parameters at a given spatial point and is factorized in the form of the product $f_0(w, r) = n_e(r) f_0^0(w)$, where $n_e(r)$ is the electron density at the point r and w is the kinetic energy. In contrast, the nonlocal EEDF is determined by the physical parameters (primarily, electric field) in the region with a size on the order of the electron energy relaxation length $\lambda_\varepsilon \gg \lambda$ (the electron mean free path), rather than those at a given spatial point. In the case of $\lambda_\varepsilon \gg \Lambda$, the EEDF is a function of the total electron energy $\varepsilon = w + e\phi(r)$ (the

kinetic energy plus the potential energy) and the Boltzmann equation should be averaged over the entire discharge volume [8]. Hence, the characteristics of all the processes with the participation of electrons are determined by this space-averaged EEDF $f_0(\varepsilon)$, which can significantly differ from that calculated in the local approximation. Under such conditions, which occur at low pressures ($p\Lambda \le (0.1–1.0)$ cm torr), attempts to improve the fluid model by refining rate constants obtained with the help of an EEDF calculated in the local approximation are not guaranteed to be free of faults and unacceptable inaccuracy.

Since, for a real nonequilibrium EEDF, the calculations of the rate constants under the assumption of a Maxwellian distribution hardly have any physical sense, it is difficult to even qualitatively estimate the inaccuracy of data thus obtained. An analysis of the transport processes also shows [9] that, for a weakly ionized plasma with a nonlocal EEDF, a closed system of fluid transport equations can only be written for the local regime ($\Lambda > \lambda_\varepsilon$). In this case, however, the equation of energy for the electron gas does not provide additional information and appears to be redundant. At the same time, in the nonlocal regime with $\Lambda < \lambda_\varepsilon$, the electron fluid model itself is not physically justified.

In order to self-consistently calculate the parameters of a multicomponent plasma, it is desirable to have a procedure that, on one hand, take into account the nonequilibrium and nonlocal character of the EEDF and, on the other hand, is less time-consuming than the full-scale solution of the Boltzmann equation with allowance for the spatial transport processes. Therefore, it is important to develop a simplified kinetic description based on a physically justified modification of the fluid model for a non-Maxwellian EEDF.

For this purpose, in this paper we compare the kinetic and fluid approaches to the modeling of the plasma of the positive column of a dc oxygen discharge. It is shown that, in accordance with the analysis of [10], the non-Maxwellian distribution function in the fluid model (in both the local and nonlocal regimes of the EEDF formation) can satisfactorily be approximated by two groups of electrons, each of which has its own temperature (mean energy). The temperature T_{et} of the fast electrons determines the rate constants for excitation and ionization. In a steady-state discharge, the ionization frequency (the inverse lifetime) for a given gas species is a function of the only parameter $p\Lambda$ and depends slightly (logarithmically) on it. Hence, at a constant $p\Lambda$ value, the temperature T_{et} is almost the same for different types of gas discharges [10]. The temperature T_{eb} of the low-energy part of the EEDF determines the plasma ambipolar fields. In some important cases (see below), this temperature depends only on the gas species. To adapt the classical fluid model in order to determine the parameters of a gas-discharge plasma, we propose a 2T fluid model in which the rate constants of the processes with the participation of electrons are found with the help of a proper EEDF approximation (see Eqs. (1), (2)).

We chose the positive column of a dc discharge because it is a very suitable test object and has been intensely studied for both atomic and molecular gases. In turn, among the electronegative gases, most of the studies and calculations within different approximations have been made for oxygen (see, e.g., [11–15]).

To calculate the discharge parameters, we used commercial software developed by the CFD Research Corporation, Huntsville, AL, USA [16, 17]. The self-consistent model of a discharge plasma, the numerical iteration scheme, and the technique for solving the set of equations are described in detail in [16, 17]. In simulations, the main model parameters are the discharge geometry, the pressure and composition of the gas, and the specific power W deposited in the discharge. A specific feature of the dc discharge is that we can specify the current density j instead of W using the simple relation $W = jE$. The self-consistent electric field was found from Poisson's equation. Heavy particles were described in the fluid model. The parameters of the electron gas could be found both by using the fluid equations for the balance of the electron density and energy and by solving the kinetic equation for the EEDF. Since this study is aimed at comparing the fluid and kinetic descriptions of the electron component, all other factors being the same, some problems that are not directly related to the electron kinetics were not analyzed in detail. In particular, we did not take into account the heating of the heavy components [12, 15], because the physical consequence of this effect is of minor importance when calculating the EEDF. This issue will be considered in a separate paper. Here, the gas and ion temperatures were assumed to be constant over the discharge cross section and equal to room temperature.

The accounted volume plasmochemical processes with the participation of various atomic and molecular oxygen states are listed in Table 1. In the fluid model, the rate constants of the processes with the participation of electrons were obtained by convoluting the corresponding cross sections with a Maxwellian EEDF, whereas in the kinetic model, they were obtained by convoluting these cross sections with an EEDF calculated with the help of the CDFRC Kinetic Module [16, 17].

For definiteness, we considered conditions corresponding to the positive column of a dc discharge in a 12-mm-diameter glass tube at gas pressures of 0.05–3 torr and discharge currents of 5–200 mA. These conditions correspond to those investigated in [12, 18], in which, in our opinion, the most detailed experimental and theoretical studies of the positive column of a dc oxygen discharge were performed.

Typical EEDFs obtained by self-consistently simulating the dc discharge plasma at gas pressures of $p = 1$ and 0.15 torr are shown in Figs. 1 and 2. It can be seen

Table 1. Volume plasmochemical processes involved in simulations

No.	Reaction	Δε, eV	Rate constant
	Elastic electron scattering		
1	$e + O_2 \longrightarrow e + O_2$	0	Cross section (CS) [1]
2	$e + O_2(a^1\Delta) \longrightarrow e + O_2(a^1\Delta)$	0	CS (copy of 1)
3	$e + O_2(b^1\Sigma) \longrightarrow e + O_2(b^1\Sigma)$	0	CS (copy of 1)
4	$e + O_2(v_1) \longrightarrow e + O_2(v_1)$	0	CS (copy of 1)
5	$e + O_2(Ry) \longrightarrow e + O_2(Ry)$	0	CS (copy of 1)
6	$e + O \longrightarrow e + O$	0	CS [3]
7	$e + O(^1D) \longrightarrow e + O(^1D)$	0	CS (copy of 6)
8	$e + O(^1S) \longrightarrow e + O(^1S)$	0	CS (copy of 6)
9	$e + O_3 \longrightarrow e + O_3$	0	CS [5]
	Inelastic processes with the participation of electrons		
10	$e + O_2 \longrightarrow O_- + O$	3.637	CS [1]
11	$e + O_2 \longrightarrow e + O_2(v_1)$	0.19	CS [1]
12	$e + O_2(v_1) \longrightarrow e + O_2$	–0.19	CS [1]
13	$e + O_2 \longrightarrow e + O_2(v_2)$	0.38	CS [1]
14	$e + O_2 \longrightarrow e + O_2(v_3)$	0.57	CS [1]
15	$e + O_2 \longrightarrow e + O_2(v_4)$	0.75	CS [1]
16	$e + O_2 \longrightarrow e + O_2(a^1\Delta)$	0.97	CS [1]
17	$e + O_2(a^1\Delta) \longrightarrow e + O_2$	–0.97	Obtained from a detailed balance with c 16
18	$e + O_2 \longrightarrow e + O_2(b^1\Sigma)$	1.63	CS [1]
19	$e + O_2(b^1\Sigma) \longrightarrow e + O_2$	–1.63	Obtained from a detailed balance with c 18
20	$e + O_2 \longrightarrow e + 2O$	5.12	CS [1]
21	$e + O_2 \longrightarrow e + O + O(^1D)$	7.1	CS [1]
22	$e + O_2 \longrightarrow 2e + O_{2+}$	12.6	CS [1]
23	$e + O_2 \longrightarrow 2e + O + O_+$	18.8	CS [1]
24	$e + 2O_2 \longrightarrow O_2 + O_{2-}$	–5.03	$k_{24} = 3.6E - 43\,T_e^{-0.5}$ m^6/s
25	$e + O_{2+} \longrightarrow 2O$	–6.96	Cross section (CS) from 2
26	$e + O_{2+} \longrightarrow O + O(^1D)$	–5.0	CS [2]
27	$e + O_2(a^1\Delta) \longrightarrow 2e + O_{2+}$	–11.63	CS [3]
28	$e + O_2(b^1\Sigma) \longrightarrow 2e + O_{2+}$	–10.97	$k_{28} = 1.3E - 15\,T_e^{-1.1}\exp(-10.43/T_e)$ m^3/s
29	$e + O_3 \longrightarrow O_- + O_2$	–0.42	CS [5]
30	$e + O_3 \longrightarrow O + O_{2-}$	0.60	CS [5]
31	$e + O \longrightarrow e + O(^1D)$	1.97	CS [4]
32	$e + O \longrightarrow e + O(^1S)$	4.24	CS [4]
33	$e + O(^1S) \longrightarrow e + O$	–4.24	Obtained from a detailed balance with c 32
34	$e + O \longrightarrow 2e + O_+$	13.67	CS [4]
35	$e + O(^1D) \longrightarrow e + O$	–1.97	CS [4]
36	$e + O(^1D) \longrightarrow 2e + O_+$	11.7	CS [4]
37	$e + O(^1S) \longrightarrow 2e + O_+$	9.43	$k_{37} = 6.6E - 15\,T_e^{0.6}\exp(-9.43/T_e)$ m^3/s
38	$e + O_- \longrightarrow 2e + O$	1.53	$k_{38} = 1.95E - 18\,T_e^{0.5}\exp(-3.4/T_e)$ m^3/s
39	$e + O_+ \longrightarrow O(^1D)$	–11.7	$k_{39} = 5.3E - 19\,T_e^{-0.5}$ m^3/s
40	$2e + O_+ \longrightarrow e + O(^1D)$	–11.7	$k_{40} = 5.12E - 36\,T_e^{-4.5}$ m^6/s
41	$e + O \longrightarrow e + O(3s^5S_0)$	9.15	CS [4]
42	$e + O \longrightarrow e + O(3s^3S_0)$	9.51	CS [4]
43	$e + O \longrightarrow e + O(3p^5P)$	10.73	CS [4]
44	$e + O \longrightarrow e + O(3p^3P)$	10.98	CS [4]
45	$e + O_2 \longrightarrow e + O_2(Rot)$	0.02	CS [1]
46	$e + O_2 \longrightarrow e + O_2(v_5)$	0.19	CS [1]
47	$e + O_2 \longrightarrow e + O_2(v_6)$	0.38	CS [1]
48	$e + O_2 \longrightarrow e + O_2(^1\Pi_g)$	8.4	CS [1]

Table 1. (Contd.)

No.	Reaction	Δε, eV	Rate constant
49	$e + O_2 \longrightarrow e + O_2(a^1\Sigma_u^+)$	10.0	CS [1]
50	$e + O_2 \longrightarrow e + O_2 + h\nu$ (130 nm)	9.547	CS [1]
51	$e + O_2(a^1\Delta) \longrightarrow e + O_2(b^1\Sigma)$	0.65	CS [1]
52	$e + O_2(b^1\Sigma) \longrightarrow e + O_2(a^1\Delta)$	–0.65	CS [2]
53	$e + O_2 \longrightarrow e + O_2(Ry)$	4.47	CS [1]
54	$e + O_2(Ry) \longrightarrow e + O_2$	–4.47	CS [2]
55	$e + O_2(a^1\Delta) \longrightarrow e + O_2(Ry)$	3.45	CS [2]
56	$e + O_2 \longrightarrow e + O + O(^1S)$	9.36	CS [2]
57	$e + O_2(a^1\Delta) \longrightarrow O + O_-$	2.57	CS [2]
58	$e + O_{2+} \longrightarrow O_2(Ry)$	–7.66	CS [2]
59	$e + O_2 + O_3 \longrightarrow O_2 + O_{3-}$	–0.679	$4.6E-40$ m^3/s
60	$e + O_{2+} \longrightarrow O + O(^1S)$	–2.73	$2.42E-13\,T_e^{-0.55}$ m^3/s
61	$e + O_{4+} \longrightarrow 2O_2$	–0.8	$2.42E-11\,T_e^{-0.5}$ m^3/s
62	$e + O_{4+} \longrightarrow O_2 + O_2(Ry)$	3.68	$2.425E-12\,T_e^{-0.5}$ m^3/s
	Reactions involving heavy particles		
63	$O_- + O_{2+} \longrightarrow O + O_2$		$k_{63} = 5.96E-11\,T_g^{-1}$ m^3/s
64	$O_- + O_{2+} \longrightarrow 3O$		$k_{64} = 1E-13$ m^3/s
65	$O_- + O_+ \longrightarrow 2O$		$k_{65} = 5.96E-11\,T_g^{-1}$ m^3/s
66	$O_{2-} + O_{2+} \longrightarrow 2O_2$		$k_{66} = 5.96E-11\,T_g^{-1}$ m^3/s
67	$O_{2-} + O_{2+} \longrightarrow O_2 + 2O$		$k_{67} = 1E-13$ m^3/s
68	$O_+ + O_{2-} \longrightarrow O_2 + O$		$k_{68} = 5.96E-11\,T_g^{-1}$ m^3/s
69	$O_{2+} + O_{3-} \longrightarrow O_2 + O_3$		$k_{69} = 5.96E-11\,T_g^{-1}$ m^3/s
70	$O_{2+} + O_{3-} \longrightarrow 2O + O_3$		$k_{70} = 1E-13$ m^3/s
71	$O_+ + O_{3-} \longrightarrow O + O_3$		$k_{71} = 5.96E-11\,T_g^{-1}$ m^3/s
72	$O_- + O_{2+} + O_2 \longrightarrow O + 2O_2$		$k_{72} = 3.066E-31\,T_g^{-2.5}$ m^6/s
73	$O_- + O_+ + O_2 \longrightarrow 2O + O_2$		$k_{73} = 3.066E-31\,T_g^{-2.5}$ m^3/s
74	$O + O_- \longrightarrow O_2 + e$		$k_{74} = 1.159E-17\,T_g^{0.5}$ m^3/s
75	$O_- + O_2(a^1\Delta) \longrightarrow O_3 + e$		$k_{75} = 1.738E-17\,T_g^{0.5}$ m^3/s
76	$O_- + O_2(b^1\Sigma) \longrightarrow O_2 + O + e$		$k_{76} = 4E-17\,T_g^{0.5}$ m^3/s
77	$O_- + O_2 \longrightarrow O_3 + e$		$k_{77} = 2.896E-22\,T_g^{0.5}$ m^3/s
78	$O_- + O_3 \longrightarrow 2O_2 + e$		$k_{78} = 1.744E-17\,T_g^{0.5}$ m^3/s
79	$O_- + O_3 \longrightarrow O + O_{3-}$		$k_{79} = 1.153E-17\,T_g^{0.5}$ m^3/s
80	$O_- + O_3 \longrightarrow O_2 + O_{2-}$		$k_{80} = 5.909E-19\,T_g^{0.5}$ m^3/s
81	$O + O_{2-} \longrightarrow O + O_{2-}$		$k_{81} = 8.69E-18\,T_g^{0.5}$ m^3/s
82	$O + O_{2-} \longrightarrow O_3 + e$		$k_{82} = 8.69E-18\,T_g^{0.5}$ m^3/s
83	$O_2(a^1\Delta) + O_{2-} \longrightarrow 2O_2 + e$		$k_{83} = 1.159E-17\,T_g^{0.5}$ m^3/s
84	$O_{2-} + O_3 \longrightarrow O_2 + O_{3-}$		$k_{84} = 3.746E-17\,T_g^{0.5}$ m^3/s
85	$O + O_{3-} \longrightarrow O_2 + O_{2-}$		$k_{85} = 1.448E-17\,T_g^{0.5}$ m^3/s
86	$O + O_+ + O_2 \longrightarrow O_2 + O_{2+}$		$k_{86} = 5.793E-43\,T_g^{0.5}$ m^6/s

Table 1. (Contd.)

No.	Reaction	Δε, eV	Rate constant
87	$O_+ + O_2 \longrightarrow O + O_{2+}$		$k_{87} = 1.953E-16\,T_g^{-0.4}$ m^3/s
88	$O_+ + O_3 \longrightarrow O_2 + O_{2+}$		$k_{88} = 1E-16$ m^3/s
89	$O(^1D) + O \longrightarrow 2O$		$k_{89} = 8E-18$ m^3/s
90	$O(^1D) + O_2 \longrightarrow O + O_2(b^1\Sigma)$		$k_{90} = 2.56E-17\exp(+67/T_g)$ m^3/s
91	$O(^1D) + O_2 \longrightarrow O + O_2(a^1\Delta)$		$k_{91} = 1.6E-18\exp(+67/T_g)$ m^3/s
92	$O(^1D) + O_2 \longrightarrow O + O_2$		$k_{92} = 4.8E-18\exp(+67/T_g)$ m^3/s
93	$O(^1D) + O_3 \longrightarrow 2O + O_2$		$k_{93} = 1.2E-16$ m^3/s
94	$O(^1D) + O_3 \longrightarrow 2O_2$		$k_{94} = 1.2E-16$ m^3/s
95	$O(^1S) + O_2 \longrightarrow O(^1D) + O_2$		$k_{95} = 3.2E-16\exp(-850/T_g)$ m^3/s
96	$O(^1S) + O_2 \longrightarrow O + O_2$		$k_{96} = 1.6E-18\exp(-850/T_g)$ m^3/s
97	$O(^1S) + O_2(a^1\Delta) \longrightarrow O + O_2$		$k_{97} = 1.1E-16$ m^3/s
98	$O(^1S) + O_2(a^1\Delta) \longrightarrow O(^1D) + O_2(b^1\Sigma)$		$k_{98} = 2.9E-17$ m^3/s
99	$O(^1S) + O_2(a^1\Delta) \longrightarrow 3O$		$k_{99} = 3.2E-17$ m^3/s
100	$O(^1S) + O \longrightarrow O(^1D) + O$		$k_{100} = 1.67E-17\exp(-300/T_g)$ m^3/s
101	$O(^1S) + O \longrightarrow 2O$		$k_{101} = 3.33E-17\exp(-300/T_g)$ m^3/s
102	$O(^1S) + O_3 \longrightarrow 2O_2$		$k_{102} = 5.8E-16$ m^3/s
103	$O_2(a^1\Delta) + O \longrightarrow O_2 + O$		$k_{103} = 2E-22$ m^3/s
104	$O_2(a^1\Delta) + O_2 \longrightarrow 2O_2$		$k_{104} = 3E-24\exp(-200/T_g)$ m^3/s
105	$2O_2(a^1\Delta) \longrightarrow 2O_2$		$k_{105} = 9E-23\exp(-560/T_g)$ m^3/s
106	$2O_2(a^1\Delta) \longrightarrow O_2 + O_2(b^1\Sigma)$		$k_{106} = 9E-23\exp(-560/T_g)$ m^3/s
107	$2O_2(a^1\Delta) + O_2 \longrightarrow 2O_3$		$k_{107} = 1E-43\exp(-560/T_g)$ m^3/s
108	$2O_2(a^1\Delta) + O_2 \longrightarrow 2O_3$		$k_{108} = 1.709E-28T_g$ m^3/s
109	$O_2(a^1\Delta) + O_3 \longrightarrow 2O_2 + O$		$k_{109} = 5.2E-17\exp(-2840/T_g)$ m^2/s
110	$2O_2(b^1\Sigma) \longrightarrow O_2(a^1\Delta) + O_2$		$k_{110} = 2.085E-24\,T_g^{0.5}$ m^3/s
111	$O_2(b^1\Sigma) + O_2 \longrightarrow O_2(a^1\Delta) + O_2$		$k_{111} = 2.085E-25\,T_g^{0.5}$ m^3/s
112	$O_2(b^1\Sigma) + O_2 \longrightarrow 2O_2$		$k_{112} = 2.317E-28\,T_g^{0.5}$ m^3/s
113	$O_2(b^1\Sigma) + O \longrightarrow O_2(a^1\Delta) + O$		$k_{113} = 4.171E-21\,T_g^{0.5}$ m^3/s
114	$O_2(b^1\Sigma) + O \longrightarrow O_2 + O$		$k_{114} = 4.634E-22\,T_g^{0.5}$ m^3/s
115	$O_2(b^1\Sigma) + O_3 \longrightarrow 2O_2 + O$		$k_{115} = 4.246E-19\,T_g^{0.5}$ m^3/s
116	$O_2(b^1\Sigma) + O_3 \longrightarrow O_2(a^1\Delta) + O_3$		$k_{116} = 4.246E-19\,T_g^{0.5}$ m^3/s
117	$O_2(b^1\Sigma) + O_3 \longrightarrow O_2 + O_3$		$k_{117} = 4.246E-19\,T_g^{0.5}$ m^3/s
118	$O_2(v_1) + O \longrightarrow O_2 + O$		$k_{118} = 5.793E-22\,T_g^{0.5}$ m^3/s
119	$O_2(v_1) + O_2 \longrightarrow 2O_2$		$k_{119} = 5.793E-22\,T_g^{0.5}$ m^3/s
120	$2O + O_2 \longrightarrow 2O_2$		$k_{120} = 9.268E-45\,T_g^{-0.63}$ m^6/s
121	$3O \longrightarrow O + O_2$		$k_{121} = 3.334E-44\,T_g^{-0.63}$ m^6/s
122	$2O + O_2 \longrightarrow O_2(a^1\Delta) + O_2$		$k_{122} = 6.987E-46\,T_g^{-0.63}$ m^6/s
123	$3O \longrightarrow O_2(a^1\Delta) + O$		$k_{123} = 2.509E-45\,T_g^{-0.63}$ m^6/s
124	$O + 2O_2 \longrightarrow O_3 + O_2$		$k_{124} = 5.081E-39\,T_g^{-2.8}$ m^6/s
125	$2O + O_2 \longrightarrow O + O_3$		$k_{125} = 3.166E-43\,T_g^{-1.2}$ m^6/s
126	$O + O_3 \longrightarrow 2O_2$		$k_{126} = 8E-18\exp(-2060/T_g)$ m^3/s
127	$O_2 + O_3 \longrightarrow O + 2O_2$		$k_{127} = 1.56E-15\exp(-11490/T_g)$ m^3/s

Table 1. (Contd.)

No.	Reaction	Δε, eV	Rate constant
128	$O_2(Ry) \longrightarrow O_2$	$k_{128} = 0.015\ s^{-1}$	
129	$O_2 + O_2(Ry) \longrightarrow O_2 + O_2(a^1\Delta)$	$k_{129} = 1.86E-19\ m^3/s$	
130	$O_2 + O_2(Ry) \longrightarrow O_2 + O_2(b^1\Sigma)$	$k_{130} = 1.86E-19\ m^3/s$	
131	$O(^1D) + O_2(a^1\Delta) \longrightarrow O_2 + O$	$k_{131} = 1E-17\ m^3/s$	
132	$O(^1S) + O_2 \longrightarrow O + O_2(a^1\Delta)$	$k_{132} = 1.5E-18\exp(-850/T_g)\ m^3/s$	
133	$O(^1S) + O_2 \longrightarrow O + O_2(b^1\Sigma)$	$k_{133} = 7.3E-19\exp(-850/T_g)\ m^3/s$	
134	$O(^1S) + O_2 \longrightarrow O + O_2(Ry)$	$k_{134} = 7.3E-19\exp(-850/T_g)\ m^3/s$	
135	$O(^1S) + O_2(a^1\Delta) \longrightarrow O + O_2(Ry)$	$k_{135} = 1.3E-16\ m^3/s$	
136	$O_2(b^1\Sigma) + O_3 \longrightarrow O_2(a^1\Delta) + O_3$	$k_{136} = 7.1E-18\ m^3/s$	
137	$O + O_2 + O_2(a^1\Delta) \longrightarrow O_2(b^1\Sigma) + O_3$	$k_{137} = 1.56E-40\,T_g^{-1.5}\ m^6/s$	
138	$O + O_2 + O_2(a^1\Delta) \longrightarrow O + 2O_2$	$k_{138} = 3E-44\ m^6/s$	
139	$O + O_3 \longrightarrow O_2 + O_2(a^1\Delta)$	$k_{139} = 2.4E-19\exp(-2060/T_g)\ m^3/s$	
140	$O + O_3 \longrightarrow O_2 + O_2(b^1\Sigma)$	$k_{140} = 8E-20\exp(-2060/T_g)\ m^3/s$	
141	$2O_3 \longrightarrow O + O_2 + O_3$	$k_{141} = 1.65E-15\exp(-11435/T_g)\ m^3/s$	
142	$2O + O_2 \longrightarrow O_2 + O_2(Ry)$	$k_{142} = 1.2E-46\ m^6/s$	
143	$2O + O_2 \longrightarrow O_2 + O_2(b^1\Sigma)$	$k_{143} = 7.6E-44\,T_g^{-1}\exp(-170/T_g)\ m^6/s$	
144	$O + O_2 + O_3 \longrightarrow 2O_3$	$k_{144} = 1.3E-41\,T_g^{-2}\ m^6/s$	
145	$2O_2 + O_{2+} \longrightarrow O_2 + O_{4+}$	$k_{145} = 1.25E-38\,T_g^{-1.5}\ m^6/s$	
146	$O_2(a^1\Delta) + O_{4+} \longrightarrow 2O_2 + O_{2+}$	$k_{146} = 1E-16\ m^3/s$	
147	$O_2(b^1\Sigma) + O_{4+} \longrightarrow 2O_2 + O_{2+}$	$k_{147} = 1E-16\ m^3/s$	
148	$O + O_{4+} \longrightarrow O_{2+} + O_3$	$k_{148} = 3E-16\ m^3/s$	
149	$O_2 + O_{4+} \longrightarrow 2O_2 + O_{2+}$	$k_{149} = 0.02673\,T_g^{-4}\exp(-5030/T_g)\ m^3/s$	
150	$O_- + O_2(a^1\Delta) \longrightarrow O + O_{2-}$	$k_{150} = 3.3E-17\ m^3/s$	
151	$O_- + O_2 \longrightarrow O + O_{2-}$	$k_{151} = 1E-20\ m^3/s$	
152	$O_- + O_2(a^1\Delta) \longrightarrow O + O_2 + e$	$k_{152} = 2E-16\exp(-15\,000/T_g)\ m^3/s$	
153	$O_- + 2O_2 \longrightarrow O_2 + O_{3-}$	$k_{153} = 3.3E-40\,T_g^{-1}\ m^6/s$	
154	$O_{2-} + O_2 \longrightarrow 2O_2 + e$	$k_{154} = 2E-16\exp(-5338/T_g)\ m^3/s$	
155	$O_- + O_+ \longrightarrow O_2$	$k_{155} = 2.7E-13\ m^3/s$	
156	$O_- + O_{4+} \longrightarrow O_2 + O_3$	$k_{156} = 6.9E-12\,T_g^{-0.5}\ m^3/s$	
157	$O_- + O_2 + O_{2+} \longrightarrow O_2 + O_3$	$k_{157} = 2E-37\ m^6/s$	
158	$O_{2-} + O_{2+} + O_2 \longrightarrow 3O_2$	$k_{158} = 2E-37\ m^6/s$	
159	$O_{2-} + O_{4+} \longrightarrow 3O_2$	$k_{159} = 1E-13\ m^3/s$	
160	$O + O_{3-} \longrightarrow 2O_2 + e$	$k_{156} = 3E-16\ m^3/s$	
161	$O_2 + O_{3-} \longrightarrow 2O_2 + O_-$	$k_{161} = 1.62E-6\,T_g^{-2}\exp(-18260/T_g)\ m^3/s$	
162	$O_{3-} + O_{4+} \longrightarrow 3O_2 + O$	$k_{160} = 1E-13\ m^3/s$	
163	$O_2 + O_{2-} + O_{4+} \longrightarrow 4O_2$	$k_{161} = 4E-38\ m^6/s$	
164	$O_2 + O_{3-} + O_{4+} \longrightarrow 4O_2 + O$	$k_{162} = 4E-38\ m^6/s$	

Note: T_e is the electron temperature in eV; T_g is the gas temperature in K; O and O_2 are the $O(^3P)$ and $O_2(X^3\Sigma_g^-)$ ground states of an oxygen atom and molecule, respectively; $O_2(Ry)$ is the electronically excited $O_2(A^1\Sigma_u^-)$ state with an energy of 4.47 eV; $O_2(v_k)$ ($k = 1, 2, \ldots$) are the vibrationally excited states; $O_2(Rot)$ is the first rotational level of an O_2 molecule; and Δε is the electron energy loss in the output channel (Δε < 0 for impacts of the second kind). The cross sections for reactions 12, 17, 19, and 33 (impacts of the second kind) are calculated from the cross sections of corresponding direct processes using the detailed balance relation. The rate constants shown in Arrhenius form are taken from [6].

1. A. V. Phelps, JILA Report, No. 28, 1985 (ftp://jila.colorado.edu/collision data/).
2. Y. Itikawa and A. Ichimura, Phys. Chem. Ref. Data. **19**, 637 (1990).
3. S. Matejcik, A. Kiender, P. Cicman, *et al.*, Plasma Sources Sci. Technol. **6**, 140 (1997).
4. I. A. Kossyi, A. Y. Kostinsky, A. A. Matveyev, and V. P. Silakov, Plasma Sources Sci. Technol. **1**, 207 (1992).
5. V. V. Ivanov, K. S. Klopovsky, D. V. Lopaev, *et al.*, IEEE Trans. Plasma Sci. **5**, 1279 (1999).
6. www.kinema.com

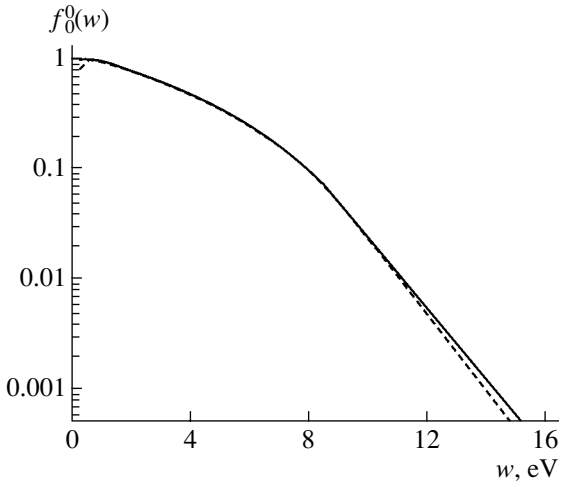

Fig. 1. Local EEDFs for p = 1 torr and i = 50 mA. The solid curve shows the results of self-consistent calculations for the radius r varying from 0 to R with a step of R/5. The dashed curve shows the local EEDF $f_0^0(w)$.

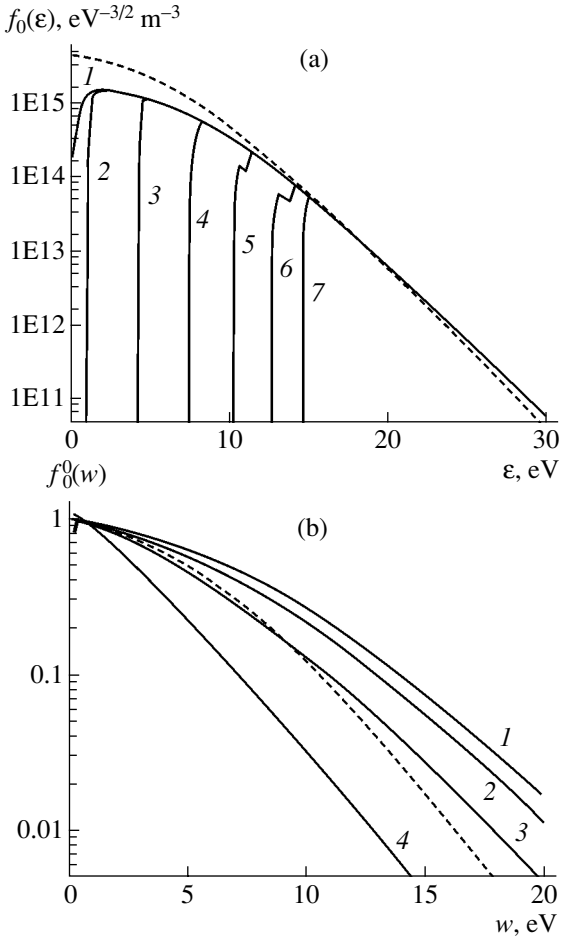

Fig. 2. Nonlocal EEDFs for p = 0.15 torr and i = 50 mA. (a) The solid curves show the results of self-consistent calculations for the radii r = (*1*) 0, (*2*) 0.6R, (*3*) 0.8R, (*4*) 0.69R, (*5*) 0.95R, (*6*) 0.98R, and (*7*) R. The dashed curve shows the local EEDF $f_0^0(w)$. (b) The solid curves show the results of self-consistent calculations for the radii r = (*1*) 0, (*2*) 0.6R, (*3*) 0.8R, and (*4*) R. The dashed curve shows the local EEDF $f_0^0(w)$.

that all the EEDFs are strongly nonequilibrium. For this reason, the rate constants of many plasmochemical processes differ significantly from those obtained in the fluid model, which deals with the temperature T_{ef} (the same for all the electrons). In turn, this leads to a difference in the plasma parameters that significantly depend on these rate constants.

At high pressures, the EEDF is local; i.e., the function $f_0^0(w)$ is independent of r (Fig. 1). At low pressures, the EEDF is not only nonequilibrium but also nonlocal. In this case, the values of $f_0(\varepsilon)$ represented as a function of the total energy $\varepsilon = w + e\phi(r)$ (i.e., without normalizing and shifting by the space potential) coincide at different radii (Fig. 2a). The same EEDFs $f_0(\varepsilon)$ plotted using the conventional local representation as functions of the kinetic energy w (similar to Fig. 1) differ for different radii r (Fig. 2b). In oxygen, the energy loss due to inelastic collisions is dominant over almost the entire energy range. Hence, using the equality $\lambda_\varepsilon = \sqrt{\lambda\lambda^*}$ [8] and the total cross sections for elastic and inelastic collisions ($\sigma = 5 \times 10^{-16}$ cm^2 and $\sigma^* = 5 \times 10^{-17}$ cm^2, respectively), we obtain the estimate $\lambda_\varepsilon \simeq 0.2/p$ (in cm), where p is in torr. It follows from the above estimates that, for oxygen, the criterion for the EEDF to be nonlocal ($\lambda_\varepsilon > \Lambda$) is $p\Lambda < 0.2$ cm torr, which agrees with the results of our simulations and the data from [12, 18]. Note that, at $\lambda_\varepsilon > \Lambda$, the thermal conductivity equalizes the electron temperature over the discharge cross section. This circumstance justifies the use of the space-averaged (global) model [4, 5]. However, due to the unavoidable non-Maxwellian character of the EEDF, the correct application of the space-averaged description is only possible in the frame of the 2T global model [10].

For rapid self-consistent estimates of the plasma parameters, it is desirable to have a procedure that takes into account the nonequilibrium and nonlocal character of the EEDF and is less time-consuming than the full-scale (4D) solution of the Boltzmann equation. To date, the most developed and widespread method is the solution of the local kinetic equation with known initial parameters, i.e., with a given reduced field E/N, degree of ionization n_e/N, and degree of excitation n^*/N. This approach can be implemented using available commercial software (e.g., the 0D Boltzmann Solver CFDRC [16, 17], BOLSIG [19], etc.). For comparison, the dashed curves in Figs. 1 and 2 show the EEDF $f_0^0(w)$ determined by solving the local Boltzmann equation (using the 0D Boltzmann Solver [16, 17]) with the same input parameters as in self-consistent calcula-

tions. As was expected, this EEDF is almost the same as that obtained for the pressure $p = 1$ torr (Fig. 1) but significantly differs from that obtained at a lower pressure (Fig. 2b). This means that, in the local regime ($\Lambda > \lambda_\varepsilon$), one can use any version of the hybrid model with an EEDF determined by solving the local kinetic equation [19]. In particular, Lookup Tables [16, 17] can be used in such a situation. At lower pressures, when the EEDF forms in the nonlocal regime, the EEDFs represented as a function of the kinetic energy are different at different radii and the corresponding local calculation of the EEDF is no longer justified (Fig. 2b). This is also confirmed by the results of directly comparing the local and nonlocal approaches when modeling the positive column of a dc discharge in noble gases (see, e.g., [20]). Under nonlocal conditions of EEDF formation, direct attempts to modernize the fluid model (see, e.g., [21]) seem to be unpromising.

In our opinion, the approach of [10] is more attractive. It was shown in that paper that, for a given value of the parameter $p\Lambda$, the fast part of the EEDF does not depend on the EEDF formation regime (local or nonlocal). Indeed, if we match the fast parts of the EEDFs calculated in the local ($f_0^0(w)$) and nonlocal ($f_0(\varepsilon)$) models (e.g., by joining them at an energy close to the ionization threshold), then the tails of both EEDFs will coincide (Fig. 2a). This, at first sight paradoxical result reflects the nature of the discharge as a self-organizing system: to enable its steady-state operation, electron reproduction with a rate depending on the electron loss rate is required. Note that the latter rate is slightly sensitive to the shape of the EEDF.

The aforesaid explains the fact that a real EEDF in a gas-discharge plasma can be, as a rule, satisfactorily approximated by two (or three) electron groups. In [10], the more common approximation by the two exponents was used:

$$f_0(\varepsilon) = c_n e^{-\frac{\varepsilon}{T_{eb}}} - c_n e^{-\frac{\varepsilon_1}{T_{eb}}}(1 - T_{et}/T_{eb}), \quad \varepsilon \le \varepsilon_1,$$

$$f_0(\varepsilon) = c_n \frac{T_{eb} e^{\frac{\varepsilon_1}{T_{et}} - \frac{\varepsilon_1}{T_{eb}}}}{T_{eb}} e^{-\frac{\varepsilon}{T_{et}}}, \quad \varepsilon \ge \varepsilon_1, \qquad (1)$$

$$c_n \simeq 2n_e/\sqrt{\pi T_{eb}^3}.$$

Here, T_{eb} is the temperature of slow (bulk) electrons with $\varepsilon < \varepsilon_1$ and T_{et} is the temperature of fast (tail) electrons with $\varepsilon > \varepsilon_1$. In writing approximation (1), it was taken into account that, to ensure the continuity of the energy flux, one should join both the EEDFs themselves and their derivatives at the threshold energy ε_1. For an oxygen plasma, the energy $\varepsilon_1 \simeq 10$ eV corresponds to the energy threshold for the most efficient processes of dissociative excitation of the high-lying electronic states of an oxygen molecule [22] and is close to the ionization energy $\varepsilon_i = 12$ eV (Figs. 1, 2). Since the behavior of the EEDF tail is close to exponential (see, e.g., Figs. 1, 2), the temperature T_{et} is defined as

$$T_{et} = -(d \ln f_0(\varepsilon)/d\varepsilon)^{-1}. \qquad (2)$$

As a rule, when the electron–electron collision frequency is low, the energy dependence of the distribution function of the bulk electrons ($\varepsilon < \varepsilon_1$) is nonexponential (Figs. 1, 2). This is related to the fact that the energy balance in low- and moderate-pressure gas discharges is usually determined by inelastic processes with high energy thresholds ($\sim\varepsilon_1$). At $w \le \varepsilon_1$, the energy dependence of the EEDF is determined by the behavior of the cross section $\sigma(w)$ for elastic collisions [8]

$$f_0(w) \sim \int_w^{\varepsilon_1} (\sigma(w)/w)dw + f_0(\varepsilon_1). \qquad (3)$$

It seems that such EEDFs are more suitable to approximate by power-law (rather than exponential) functions of energy. These EEDFs depend slightly on the electric field (mainly via the matching constant $f_0(\varepsilon_1)$). Since the electrons with energies $\varepsilon \le \varepsilon_1$ insignificantly contribute to the total energy balance of the electron gas, their mean energy also slightly depends on the electric field. These electrons acquire the energy from the field in the energy range $(0, \varepsilon_1)$ and provide the required electron energy flux toward the EEDF tail [8]. In other words, the low-energy part of the EEDF ($\varepsilon < \varepsilon_1$) acts as a kind of pipeline from a source at low energies to a sink in the EEDF tail ($\varepsilon > \varepsilon_1$). The electron density profile along this pipeline does not depend on the energy flux and is only determined by the condition that the energy acquired by low-energy electrons is almost entirely transferred to high-energy electrons. In such a situation, attempts to find the electron temperature from the energy balance equation (see, e.g. [23–25]) seem to be unpromising. However, approximation (1) requires knowledge of the temperature T_{eb} of the slow electrons. The problem can be somewhat simplified because the temperature T_{eb} is only needed to find the characteristics that are slightly sensitive to its value (the plasma ambipolar field; the rate constants of reactions with low energy thresholds, $\varepsilon_j \le T_{eb}$; etc.). Taking this fact into account and assuming that $\sigma(w)$ in formula (3) grows monotonically, we can propose the following approximation for the EEDF (2T EEDF):

$$f_0(\varepsilon) = c_n\left(1 - \frac{\varepsilon}{\varepsilon_1 + T_{et}}\right), \quad \varepsilon \le \varepsilon_1,$$

$$f_0(\varepsilon) = c_n \frac{T_{et}}{(\varepsilon_1 + T_{et})} e^{-\frac{(\varepsilon - \varepsilon_1)}{T_{et}}}, \quad \varepsilon \ge \varepsilon_1, \qquad (4)$$

$$c_n \simeq 15n_e/(4\varepsilon_1^{3/2}),$$

which also ensures the conservation of the energy flux at $\varepsilon = \varepsilon_1$ and depends explicitly only on the temperature T_{et} of the fast electrons. The temperature of the low-energy part ($\varepsilon \le \varepsilon_1$) of the EEDF (4) is

$$T_{eb} = 2\bar{\varepsilon}_{eb}/3 \simeq 0.3(\varepsilon_1 + T_{et}).$$

Table 2 presents the characteristic effective temperatures T_j for typical conditions under study, namely, the local regime at $p = 1$ torr and the nonlocal regime at $p = 0.15$ torr. The temperature T_{ef} was found using the fluid model, whereas the temperatures T_{et}, T_{eb}, and T_e were obtained using the kinetic model with allowance for Eq. (2) and formulas

$$T_{eb} = 2\int_0^{\varepsilon_1} f_0(w)w^{3/2}dw \Big/ \left(3\int_0^{\varepsilon_1} f_0(w)w^{1/2}dw\right), \quad (5a)$$

$$T_e = 2\int_0^{\infty} f_0(w)w^{3/2}dw \Big/ \left(3\int_0^{\infty} f_0(w)w^{1/2}dw\right). \quad (5b)$$

As was expected, the temperatures T_e and T_{eb} turned out to be close to each other ($T_e \simeq T_{eb}$). At first glance, the temperature T_{ef}, which is found in the fluid model from the energy balance for the entire electron gas, should also be close to T_e and T_{eb}, because it seems that the energy balance for all the electrons would yield the energy of the "average" electron. It happens, however, that the temperature obtained by fluid simulations is significantly lower than the average EEDF temperature ($T_{ef} < T_e$) and is close to the temperature of the EEDF tail ($T_{ef} \simeq T_{et}$). On one hand, this fact indicates that the fluid description of electrons is inapplicable to the simulations of a weakly ionized gas-discharge plasma. On the other hand, it explains why the use of the conventional fluid model proved to be surprisingly successful in calculating the main plasma parameters. For electropositive plasma, this is explained by the fact that both the energy loss due to inelastic collisions with high energy thresholds and the ionization processes are determined by the EEDF tail [10]. Hence, roughly speaking, the energy balance and the particle balance are determined by the same temperature T_{et}. Indeed, for a simple plasma, it follows from the condition of steady-state discharge operation that the ionization rate and the loss rate associated with diffusion toward the wall are equal to each other (Schottky condition):

$$\nu_i \tau_{dp} = 1. \quad (6)$$

This condition determines the eigenvalue $\nu_i(T_{et})$ of the boundary-value problem for the density of charged particles with $n_e = n_p$. The characteristic time τ_{dp} is determined by the discharge geometry and depends slightly on the EEDF shape. It can be estimated by the interpolation formula (see, e.g., [14])

$$\tau_{dp} = \tau_{ap} + \tau_{bp}. \quad (7)$$

Here, $\tau_{ap} = \Lambda^2/D_{ap}$ is the characteristic time of ambipolar diffusion ($D_{ap} = D_p T_{eb}/T$) and $\tau_{bp} = a\Lambda/V_b$ is the Bohm time, where $V_b = \sqrt{T_{eb}/M}$ and a is a numerical factor on the order of unity. As is seen from Eq. (7), the characteristic time τ_{dp} is determined by the discharge geometry and depends slightly on the EEDF shape. Nevertheless, the ionization frequency depends strongly on the temperature. For example, for a Maxwellian EEDF and the commonly used approximation for the energy dependence of the ionization cross section, $\sigma_i(\varepsilon) = \sigma_{0i}(\varepsilon/\varepsilon_i - 1)$, with the threshold $\varepsilon_i \gg T_{et}$, the ionization frequency can be represented in Arrhenius form:

$$\nu_i = N\int_{\varepsilon_i}^{\infty} \sigma_i(w)\sqrt{\frac{2w}{m}} f_0(w)\sqrt{w}dw \approx N\sigma_{0i}\sqrt{\frac{8T_e}{\pi m}} e^{-\frac{\varepsilon_i}{T_e}}. \quad (8)$$

For an oxygen plasma with a Maxwellian EEDF, we propose the following approximation for the ionization rate constant:

$$k_i \approx 4\times 10^{-15}\sqrt{T_e}\exp(-12.06/T_e) \approx 3\times 10^{-15} T_e \exp(-12.06/T_e)\ \mathrm{m}^3/\mathrm{s}. \quad (8a), (8b)$$

Condition (6) allows one to reliably calculate the ionization frequency ν_i, which is equal to the diffusion loss rate $1/\tau_{dp}$. Since this rate depends slightly (logarithmically) on T_{eb}, it follows from Eqs. (6)–(8) that, for a given gas species, the temperature T_{et} depends only on the parameter $p\Lambda$ [10]. It should be stressed that any EEDF (not necessarily a Maxwellian or Druyvesteyn one) that sharply (exponentially) depends on energy gives more or less close values of the effective temperature of the high-energy part of the EEDF (note that this temperature depends logarithmically on the discharge parameters). On the other hand, if inelastic losses with a high energy threshold ε_1 (comparable with the ionization energy ε_i) are dominant in the energy balance of the entire electron gas, then we have $T_{ef} \simeq T_{et}$. In gas dis-

Table 2. Characteristic temperatures in the positive column of a dc oxygen discharge

No.	Regime	T_{ef}, eV	T_e, eV	T_{eb}, eV	T_{et}, eV	T_t, eV
1	150 mtorr–5mA	3.2	3.9	3.1	2.9	2.7
2	150 mtorr–50 mA	2.9	4.1	3.4	2.8	2.7
3	150 mtorr–500 mA	2.9	3.9	3.1	2.9	2.7
4	1 torr–5 mA	1.7	2.6	2.6	1.3	1.5
5	1 torr–50 mA	1.7	2.6	2.6	1.3	1.5
6	1 torr–200 mA	1.7	2.6	2.6	1.4	1.5

charges, inelastic energy losses usually exceed elastic ones. Hence, the surprising fact that fluid simulations, as a rule, quite fairly describe the main plasma parameters can be explained by the insensitivity of the calculated results (some kind of "self-healing") to the shape of the high-energy part of the EEDF. At the same time, the errors in determining the plasma characteristics that are governed by the low-energy part of the EEDF with the temperature T_{eb} (which is different from T_{et}) can be rather large.

To generalize the data of [10] on electronegative gases, we will use scaling laws [14] based on the classification of the regimes of charged particle transport in a discharge.

The main channel for the production of negative ions is dissociative attachment. In the low-pressure range under study ($p\Lambda \le 1$ cm torr), the processes involving three-body collisions are of minor importance. Hence, the main negative ions are O^- ions, whereas the densities of O_2^- and O_3^- ions are low and do not affect the balance of charged particles. The main ionization mechanism is the direct ionization of O_2 molecules; consequently, the main positive ions are O_2^+ ions, whereas the density of O^+ ions is significantly lower.

At $p\Lambda < 1$ cm torr and the degrees of ionization considered in this study ($n_e/N < 10^{-4}$), the recombination loss rate of positive ions is smaller than the loss rate associated with diffusion toward the wall (the latter can be again estimated using Eq. (7)).

It is known (see, e.g., [9]) that the plasma of electronegative gases is characterized by the presence of an outer electron–ion plasma shell ("skin"), in which negative ions are practically absent. Although the skin is usually very thin, its presence is of principal importance because it confines the negative ions inside the volume. Discharges in electronegative gases are characterized by an extra degree of freedom, namely, the degree of electroneutrality. In a simple model that describes the processes of attachment, detachment, ionization, and recombination with the help of phenomenological coefficients K_a, K_d, K_i, and K_r [9, 14], the parameters of an electronegative-gas plasma depend on the relation between the attachment time $1/\nu_a$ and diffusion time τ_{an} (which is determined by the electron temperature T_{eb}) of the negative ions, i.e., on the parameter $\nu_a\tau_{an}$. The dependences obtained in [9, 14] allow one to find the temperature T_{et} using the following simple considerations. Since the flux of negative ions toward the wall is zero, from the balance of negative and positive ions, we obtain the following relationships for the densities $\bar{n}$ averaged over the discharge cross section:

$$\nu_a\bar{n}_e = \nu_d\bar{n}_n + K_r\bar{n}_n\bar{n}_p, \tag{9}$$

$$\nu_i\bar{n}_e = \bar{n}_p/\tau_{dp}, \tag{10}$$

where ν_a is the attachment frequency, ν_d is the detachment frequency, and K_r is the rate constant for ion–ion recombination. The positive ion density n_p is equal to the sum of the negative ion density n_n and the electron density n_e: $n_p = n_n + n_e$.

At low pressures ($\tau_{an}\nu_a < 1$), the negative ions obey a Boltzmann distribution and their density profile is parabolic, whereas the electron density profile is flat. In this regime, the ionization rate exceeds the attachment rate [9, 14] and, at the discharge periphery (in the electron–ion skin), the equality $n_e = n_p$ is satisfied. At low pressures, the skin thickness is smaller than the particle mean free path; hence, using Eqs. (7) and (10), we obtain the simple expression

$$\nu_i\tau_{bp} = 1, \tag{11}$$

which can be used to find the temperature T_{et}.

Using approximation (8a) for the ionization rate constant in oxygen, we obtain the analytic expression for T_{et}:

$$T_t = \varepsilon_1/(\ln 2286 p\Lambda), \tag{12}$$

which depends only on the parameter $p\Lambda$ (here, the pressure p is in torr and Λ is in cm).

Expression (11), which is similar to Eq. (6) for an ordinary plasma, can be used to find the temperature T_e in an electronegative plasma (see [1]). This expression has been widely used when analyzing the plasmas of electronegative gases (see, e.g., [2, 3–5, 13, 15]). However, we note that expression (11) is only applicable when $\nu_a\tau_{an} < 1$, which, in the case of oxygen, corresponds to the condition $p\Lambda < 0.1$ cm torr. In [26], it was shown that the approach of [1], which is based on the assumption that not only the electrons but also the ions obey a Boltzmann distribution, cannot be extended to the higher pressure range.

At elevated pressures ($p\Lambda > 0.1$ cm torr), the condition $\nu_a\tau_{an} > 1$ is satisfied and the ionization rate is less than the attachment rate [9, 14]. In this case, the situation substantially depends on the volume loss of negative ions. In oxygen, the inequality $\tau_{an}\nu_a > 1$ means the occurrence of the detachment regime; i.e., the loss of negative ions is governed by detachment (rather than recombination). In this case, various types of flat-top profiles of the electron and ion densities can be established (see [9, 14, 26] for details). Hence, from Eqs. (9) and (10) we have

$$\nu_i\tau_{ap}/(1 + \bar{n}_n/\bar{n}_e) = \nu_i\tau_{ap}/(1 + \nu_a/\nu_d) = 1, \tag{13}$$

which, with allowance for Eq. (8a), gives a simple analytic estimate for the temperature T_{et}:

$$\begin{aligned} T_t &= \varepsilon_1/[2\ln(182 p\Lambda) - \ln(1 + \nu_a/\nu_d)] \\ &\approx \varepsilon_1/(2\ln(182 p\Lambda)), \end{aligned} \tag{14}$$

where pressure p is in torr and Λ is in cm.

The results of calculating T_t by formulas (12) and (14) are also presented in Table 2. These simple expressions are seen to agree well with both the EEDF tail temperature T_{et} obtained by the kinetic model and the average electron temperature T_{ef} obtained by fluid simulations.

From the kinetic equation for the temperature of the high-energy part of the EEDF, we have the simple estimate

$$T_{et} = \sqrt{\sum_j \nu_j / D_E}, \quad (15)$$

where $D_E = 2(eE\lambda)^2\nu/3$ is the energy diffusion coefficient in an electric field (see, e.g., [8] for details). Since it is the electric field that delivers energy to electrons, the temperature T_{et} and, consequently, the ionization frequency ν_i are governed by the heating electric field, which is either the longitudinal field (in the positive column under study) or the averaged high-frequency field $\langle E_{eff} \rangle$ (in rf and microwave discharges). For this reason, when analyzing the EEDF (see, e.g., [27]) or developing user's software for computing the EEDF (see, e.g., [19]), the electric field is usually assumed to be given. However, in any problem of plasma physics, neither fields nor particle motion can be treated as given, because the fields are specified not only by the external conditions, but also by the charged particle motion, which, in turn, is governed by the fields. Hence, all the problems are self-consistent: the plasma allows only those fields in the discharge volume that are required for this plasma to exist. The ionization rate is specified by the EEDF shape (the T_{et} temperature), which is determined by the fields in the plasma. On the other hand, it is necessary that the production of the charged particles balances their losses, which depend mainly on the discharge geometry and the pressure ($p\Lambda$). As a result, the heating field, which can be obtained from expression (15) using the temperature T_{et} deduced from Eqs. (6)–(14), is also governed by the parameter $p\Lambda$ [10]. We note in this context that the spatial distribution of the self-consistent fields in the plasma volume is not known *a priori* and, in contrast to the case of the positive column of a dc discharge, which has been considered in this study, the problem of determining the field profiles in the plasmas of various discharges (ECR, ICP, SW, etc.) is a difficult problem by itself. In such discharges, attempts to find T_{et} as a function of the average effective heating field $\langle E_{eff} \rangle$ via relations similar to expression (15) are very laborious and lead to rather sophisticated expressions that are difficult to handle (see, e.g., [28]).

Let us now consider the reasons why the mean electron energy $\bar{\varepsilon}_{ef} = 3T_{ef}/2$, which was obtained in fluid simulations from the energy balance equation for all the electrons, turned out to be close to the temperature T_{et} of the high-energy part of the EEDF, rather than to the mean energy of the electron gas $\bar{\varepsilon}_e = 3T_e/2$. An analysis of the energy balance equation for all the electrons shows that, for an oxygen dc discharge, the most efficient channels of energy losses are the reactions of dissociative excitation of the high-lying electronic states of an oxygen molecule with energy thresholds of 7–10 eV ($\varepsilon_1 \simeq 10$ eV) and ionization ($\varepsilon_i = 12$ eV). Since the efficiency of these processes is determined by the high-energy part of the EEDF, then, for a Maxwellian EEDF, we have $T_{ef} \simeq T_{et}$. We note that, for steady-state low-pressure discharges, both the electron energy balance and ionization are almost always (especially in atomic gases) determined by the processes with high thresholds. Hence, the results obtained in this study apply to all these cases. If the energy balance is determined by elastic processes or inelastic processes with low thresholds (quasi-elastic processes), then the situation changes insignificantly. In this case, only the shape of the low-energy part of the EEDF changes, whereas the high-energy part of the EEDF and its temperature T_{ef} are again governed by the balance between ionization and diffusion losses (see Eqs. (6)–(14)). The energy balance equation, as well as calculations by the fluid model, give the temperature T_{eb} of the low-energy part of the EEDF, and the dc (or rf) discharge current is expressed in terms of the specific power W deposited in the discharge (or the longitudinal electric field in the case of a dc discharge). Such a situation occurs, in particular, in gases in which the energy loss due to vibrational excitation is dominant (e.g., in nitrogen, carbon oxide, etc.), provided that the gas pressure is not too low. Particular features of such discharges can easily be taken into account by applying the 2T fluid model proposed here.

The increase in the degree of ionization caused by an increase in the discharge current (an increase in the specific power W deposited in the discharge) leads to the Maxwellianization of the EEDF due to electron–electron collisions. According to Eqs. (6)–(14), with given external conditions and given ionization and loss mechanisms, the temperature T_{et} of the high-energy part of the EEDF remains almost unchanged. Therefore, as the electron–electron collision frequency increases, the temperature T_{et} of the low-energy part of the EEDF changes and approaches the constant temperature T_{et} of the EEDF tail. This process is accompanied by a decrease in D_E (and, consequently, in the electric field). In other words, the paradigm of the problem changes radically because, in the literature, the change of the EEDF with increasing electron density at a constant electric field is usually considered; in this case, both the body and the tail of the distribution function vary with increasing degree of ionization. However, according to [10] and the above analysis, in a steady-state discharge occupying a fixed volume, the temperature T_{et} of the high-energy part of the EEDF remains nearly constant. For this reason, the increase in the electron–electron collision frequency with increasing deposited power

(current) leads to a change of only the low-energy part of the EEDF; i.e., the temperature T_{eb} of the low-energy part of the EEDF approaches the constant temperature T_{et} of the EEDF tail.

In all the discharges, as the degree of ionization and the electron–electron collision frequency increase further ($n_e T_e \nu_e \gg W$), the EEDF becomes Maxwellian with a single temperature that coincides with the temperature of fast electrons and depends only on $p\Lambda$.

Thus, using commercial CFDRC software (http://www.cfdrc.com/~cfdplasma), we compared the kinetic and fluid approaches to modeling the plasma of the positive column of a dc oxygen discharge. It is shown that for both local and nonlocal regimes of EEDF formation, the non-Maxwellian EEDF can be adequately approximated by two groups of electrons. The condition of steady-state discharge operation allows one to determine the temperature T_{et} of the fast electrons as an eigenvalue of the problem. For a given gas species, this temperature is a function of the parameter $p\Lambda$ and weakly (logarithmically) depends on the external conditions. The energy balance for the entire electron gas does not allow one to find the characteristic temperatures that are of practical interest. To calculate the parameters of a gas-discharge plasma, we propose the 2T fluid model, which allows one to incorporate the main characteristics of a nonequilibrium and nonlocal EEDF into the conventional fluid model.

ACKNOWLEDGMENTS

One of the authors (L.D. Tsendin) acknowledges the support of the Russian Foundation for Basic Research (project no. 01-02-16874) and NATO SfP (grant no. 974354).

REFERENCES

1. M. Lieberman and A. Lichtenberg, *Principles of Plasma Discharges and Materials Processing* (Wiley, New York, 1994).
2. I. G. Kouznetsov, A. J. Lichtemneberg, and M. A. Lieberman, Plasma Sources Sci. Technol. **5**, 662 (1996).
3. J. D. Bukowski, D. B. Graves, and P. J. Vitello, Appl. Phys. **80**, 2614 (1996).
4. C. Lee and M. A. Lieberman, J. Vac. Sci. Technol. A **13**, 368 (1995).
5. J. T. Gudmindsson, I. G. Kouznetsov, K. K. Patel, *et al.*, J. Phys. D **34**, 1100 (2002).
6. I. P. Shkarofsky, T. W. Johnson, and M. P. Bachynski, *The Particle Kinetics of Plasmas* (Addison–Wesley, Reading, 1966).
7. A. A. Kudryavtsev and L. D. Tsendin, Zh. Tekh. Fiz. **69** (11), 34 (1999) [Tech. Phys. **44**, 1290 (1999)].
8. L. D. Tsendin, Plasma Sources Sci. Technol. **4**, 200 (1995).
9. A. V. Rozhansky and L. D. Tsendin, *Transport Phenomena in Partially Ionized Plasma* (Taylor & Francis, London, 2001).
10. A. A. Kudryavtsev and L. D. Tsendin, Pis'ma Zh. Tekh. Fiz. **28** (20), 7 (2002) [Tech. Phys. Lett. **28**, 841 (2002)].
11. G. Gousset, C. M. Ferreira, M. Pinheiro, *et al.*, J. Phys. D **24**, 290 (1991).
12. V. V. Ivanov, K. S. Klopovsky, D. V. Lopaev, *et al.*, IEEE Trans. Plasma Sci. **27**, 1279 (1999).
13. J. T. Gunmindsson, A. M. Marakhtanov, K. K. Patel, *et al.*, J. Phys. D **33**, 1323 (2000).
14. E. A. Bogdanov, V. I. Kolobov, A. A. Kudryavtsev, *et al.*, Zh. Tekh. Fiz. **72** (8), 13 (2002) [Tech. Phys. **47**, 946 (2002)].
15. M. W. Kiehlbauch and D. B. Graves, J. Appl. Phys. **91**, 3539 (2002).
16. *CFD–PLASMA: User's Manual* (CFD, Huntsville, 1999–2002).
17. http://www.cfdrc.com/~cfdplasma.
18. V. V. Ivanov, K. S. Klopovsky, D. V. Lopaev, *et al.*, J. Plasma Phys. **26**, 970 (2000).
19. http://www.siglo-kinema.com/BOLSIG: Boltzmann Solver for the SIGLO-series.
20. J. Behnke, Yu. Golobovsky, S. U. Nisimov, *et al.*, Contrib. Plasma Phys. **36** (1), 75 (1996).
21. J. H. Ingold, Phys. Rev. E **56**, 5932 (1997).
22. B. Eliassen and V. Kogelsschalz, J. Phys. B **19**, 1241 (1986).
23. W. L. Morgan and L. Vriens, J. Appl. Phys. **51**, 5300 (1980).
24. J. T. Dakin, J. Appl. Phys. **60**, 563 (1986).
25. A. Harters and J. A. M. van der Mullen, J. Phys. D **34**, 1907 (2001).
26. R. N. Franklin and J. Snell, J. Phys. D **32**, 2190 (1999).
27. V. L. Ginzburg and V. L. Gurevich, Usp. Fiz. Nauk **70**, 201 (1960) [Sov. Phys. Usp. **70**, 115 (1960)].
28. T. Kimura and K. Oke, J. Appl. Phys. **89**, 4240 (2001).

Translated by N. Ustinovskiĭ

Technical Physics, Vol. 48, No. 8, 2003, pp. 995–1000. Translated from Zhurnal Tekhnicheskoĭ Fiziki, Vol. 73, No. 8, 2003, pp. 56–61.

SOLIDS

Monte Carlo Simulation of the Dielectric Response from Ferroelectrics

P. N. Yudin, M. A. Nikol'sky, and S. P. Zubko

St. Petersburg State Electrotechnical University, ul. Prof. Popova 5, St. Petersburg, 197376 Russia

e-mail: mwlab@eltech.ru

Received December 23, 2002

Abstract—The simulation of the response of a ferroelectric film as a part of a plane capacitor or any other nonlinear element is of particular importance for designing microwave ferroelectric devices. Models required for the description of the dielectric response and the capacitance of the plane ferroelectric capacitor are given. These models are used to develop a mathematical algorithm that finds the model parameters of the dielectric response of a ferroelectric material from experimental data. © *2003 MAIK "Nauka/Interperiodica".*

INTRODUCTION

Interest in ferroelectrics and related microwave devices has grown in recent years [1–8]. Dielectric nonlinearity and low microwave losses in ferroelectrics allow for designing electrically controlled high-Q microwave devices, such as tunable filters and phase shifters.

To date, $SrTiO_3$ (STO) and $KTaO_3$ ferroelectrics, which are well compatible with high-temperature superconductors (HTSCs) and can be applied at liquid nitrogen temperature, as well as $Ba_xSr_{1-x}TiO_3$ (BSTO) ferroelectric of variable composition, have come to the forefront in microwave technology [1, 2, 5–8, 9]. The unique feature of the last-listed compound is the high room-temperature controllability of devices based on it because of the relatively high temperature of the ferroelectric transition.

Ferroelectric microwave devices are usually fabricated by planar technology. A plane capacitor with the capacitance controlled by an electric field is of special interest [6, 10].

The application of ferroelectrics for designing microwave devices requires elaborate models of their ferroelectric element. These models can then be used as a basis for the computer-aided design (CAD) of microwave devices based on ferroelectrics. At present, there are several reliable approaches that take into account the ferroelectric properties of the material: the phenomenological model, which includes the permittivity of a ferroelectric as a function of the temperature and applied field [1–4], and the methods of conformal mapping and partial capacitances, which allow the calculation of the capacitance of a plane capacitor with a ferroelectric film [10].

To choose model parameters that fit experimental data is a challenge. A mathematical algorithm for searching model parameters that is considered in this work makes it possible to perform optimization in terms of several model parameters simultaneously and to substantially shorten the data processing time, which is important for the CAD of ferroelectric microwave devices.

In [9], we simulated the dielectric response of ferroelectrics and proposed the use of the known models to study microwave losses in ferroelectrics and increase the switching quality factor (SQF) of a ferroelectric component at microwaves [6]. This work extends this idea in order to find model parameters from experimental temperature and field dependences of the ferroelectric permittivity or the capacitance of a plane capacitor.

CALCULATION OF THE PLANE CAPACITOR CAPACITANCE BY THE METHOD OF PARTIAL CAPACITANCES

The method of partial capacitances, as applied to layered structures, was first used in [15, 16]. This method implies the assignment of zero boundary conditions to the field normal components at the interface between media ("magnetic walls") with the subsequent correction of the permittivity values in either medium.

According to the method of partial capacitances [10], the capacitance of a plane capacitor (Fig. 1) can be expressed as the sum of the capacitances of its parts: the capacitance of stray fields in the environment (air) with the permittivity $\varepsilon_1 = 1$, the capacitance of the ferroelectric layer h_2 thick with a permittivity ε_2, and the capacitance of the substrate h_3 thick with a permittivity ε_2.

Thus, the composite capacitor (Fig. 1) is divided into three plane uniformly filled capacitors (Fig. 2) connected in parallel:

$$C = C_1 + C_2 + C_3. \quad (1)$$

1063-7842/03/4808-0995$24.00

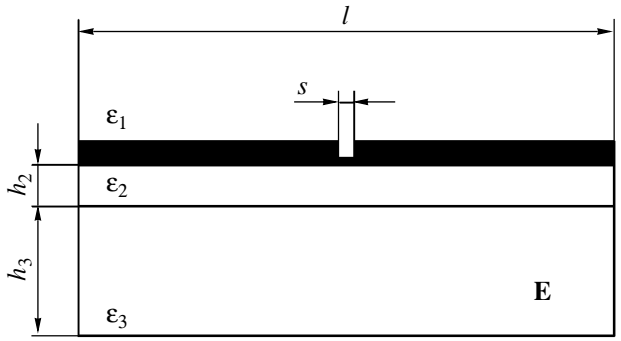

Fig. 1. Plane capacitor consisting of a dielectric substrate, a thin ferroelectric layer, and conducting electrodes spaced *s* apart.

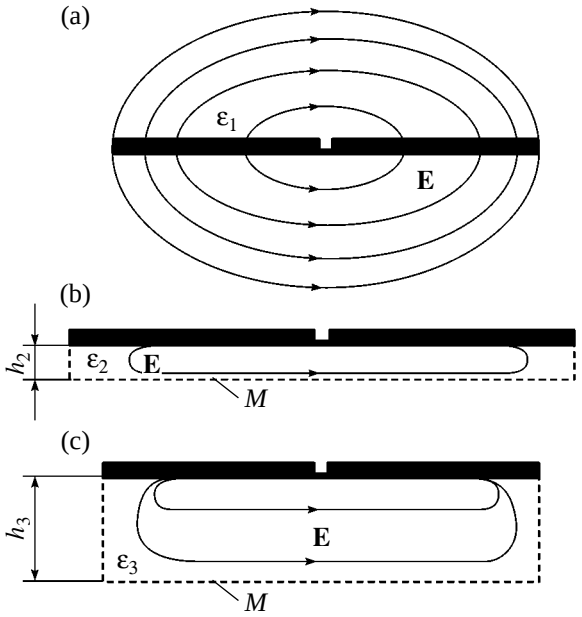

Fig. 2. Partition of the planar capacitor (Fig. 1) into partial capacitors used in the calculation: (a) electrodes in "air," (b) thin ferroelectric layer, and (c) substrate. *M* is the magnetic wall.

Introducing the permittivities

$$\varepsilon_2^* = \varepsilon_2 - \varepsilon_3; \quad \varepsilon_3^* = \varepsilon_3 - 1 \tag{2}$$

and using the simplifications adopted in [10], we obtain the easy-to-use formulas

$$C_1 = w\varepsilon_0 \frac{2}{\pi}\ln\left(4\frac{l}{s}\right) \quad \text{at} \quad s \le 0.25l, \tag{3}$$

$$C_2 = \frac{w\varepsilon_0\varepsilon_2^*}{s/h_2 + (4/\pi)\ln 2} \quad \text{at} \quad s \ge h_2, \tag{4}$$

$$C_3 = w\varepsilon_0\varepsilon_3^* \frac{1}{\pi}\ln\left(16\frac{h_3}{\pi s}\right), \quad \text{at} \quad s \le 0.5h_3, \tag{5}$$

where *w* is the capacitor gap.

The reliability of the method of partial capacitances was checked by a numerical calculation carried out in [17]. The applicability domains of Eqs. (1)–(5) were found in [10].

PHENOMENOLOGICAL DESCRIPTION OF A FERROELECTRIC

In the general case, the permittivity of a ferroelectric is a complex quantity. It is a function of the temperature *T*, applied field strength *E*, frequency *w*, parameter of structural quality ξ_s, and barium content *x* (in the case of BSTO) [9–14]:

$$\varepsilon(T, E, x, \xi_s, \omega) = \frac{\varepsilon_{00}(x)}{G^{-1}(T, E, x, \xi_S) + i\sum_{q=1}^{4}\Gamma_q(T, E, x, \xi_s, \omega)}, \tag{6}$$

where $G(T, E, x, \xi_s)$ is the real part of the Green's function for the dielectric response of a ferroelectric [9–14, 18].

The sum in the denominator of (6) describes four loss mechanisms observed in ferroelectrics [11–14, 18]. At frequencies $\omega \ll \omega_{ei}$ (where ω_{ei} is the eigenfrequency of the soft ferroelectric mode [19]) or at $f \le 100$ GHz, the real part of the Green's function $G(T, E, x, \xi_s)$ is independent of frequency. We will consider only the real part of the Green's function, that is, assume that the ferroelectric is loss less. Then, Eq. (6) takes the form

$$\varepsilon(T, E, x, \xi_s) = \varepsilon_{00}(x)G(T, E, x, \xi_s). \tag{7}$$

To describe the real part of the Green's function, we use the repeatedly verified model [11–14]:

for the paraelectric phase $[a(T, E, x, \xi_s) \ge 0]$,

$$G(T, E, x, \xi_s) = \frac{1}{\left(a(T, E, x, \xi_s)^{1/2} + \xi(E, x, \xi_s)\right)^{2/3} + \left(a(T, E, x, \xi_s)^{1/2} - \xi(E, x, \xi_s)\right)^{2/3} - \eta(T, x)}; \tag{8}$$

for the ferroelectric phase $[a(T, E, x, \xi_s) < 0]$,

$$G(T, E, x, \xi_s) = \frac{1}{\frac{1}{4}a(T, E, x, \xi_s)\xi(E, x, \xi_s)^{1/3} + \xi(E, x, \xi_s)^{2/3} - 2\eta(T, x)} \tag{9}$$

where

$$\eta(T, x) = \frac{\Theta_f}{T_C(x)}\sqrt{\frac{1}{16} + \left(\frac{T}{\Theta_f}\right)^2} - 1,$$

$$\xi(E, x, \xi_s) = \frac{\sqrt{[\xi_s E_N(0)]^2 + E^2}}{E_N(x)}, \quad (10)$$

$$a(T, E, x, \xi_s) = \xi(E, x, \xi_s)^2 \eta(T, x)^3.$$

Here, we use five model parameters [9, 11–14]:

$$(1)\ \varepsilon_{00}(x) = \frac{C}{T_C(x)}$$

is an analog of the Curie–Weiss constant, where C is the Curie–Weiss constant and $T_C(x)$ is the Curie temperature. In the general case, $T_C(x)$ is a function of the barium concentration x for $Ba_xSr_{1-x}TiO_3$ samples [9] and is given by

$$T_C(x) = 42 + 439x - 96x^2;$$

(2) Θ_f is the effective Debye temperature for crystal sublattices that are responsible for ferroelectric polarization;

(3) $E_N(x)$ is the normalizing field strength:

$$E_N(x) = \frac{2D_N}{\varepsilon_0(3\varepsilon_{00}(x))^{3/2}};$$

(4) ξ_s is the coefficient characterizing the amount of defects in the material (ξ_s = 0.01–0.05 for single crystals and 0.1–1.5 for films [11–14]);

(5) x is the barium concentration.

For virtual ferroelectrics, the real part of the Green's function is described by Eq. (8). In the case of a $Ba_xSr_{1-x}TiO_3$ ferroelectric, the material may be both in the ferroelectric phase and in the paraelectric phrase; therefore, both Eqs. (8) and (9) can be used to describe the temperature dependence of the permittivity.

Expressions (8) and (9) are the solutions to a cubic equation that can be derived by the normalization of the Ginzburg–Devonshire equation for spontaneous polarization [11–14]:

$$\frac{P^3}{D_N^2} + \frac{1}{\varepsilon(T, E, x, \xi_s)}P = \varepsilon_0 E. \quad (11)$$

The roots of the equation obtained were comprehensively analyzed in [13]. In particular, when the material is in the paraphase ($a(T, E, x, \xi_s) \geq 0$), the Cardano formula is used for solving Eq. (11). In the case of the ferroelectric phase ($a(T, E, x, \xi_s) < 0$), Eq. (11) has three real roots, one of which can be represented by approximation (9) [12].

EXTRACTION OF MODEL PARAMETERS FOR A THIN FERROELECTRIC FILM FROM EXPERIMENTAL CHARACTERISTICS

The model parameters of a thin ferroelectric film are found by the Monte Carlo method [20] based on the properties of Halton pseudorandom sequences [21, 22]. Using Halton sequences, one probes the space of model parameters to be optimized. These sequences are chosen because their uniformity characteristics are the best among the quasi-uniformly distributed sequences known.

The choice of the Monte Carlo method is dictated by the global search for an extremum of the objective function $Q(\mathbf{X})$:

$$Q_1(\mathbf{X}) = \sum_{k=1}^{n} ((C_{exp} - C_{calc}(\mathbf{X}_k))^2 / C_{exp}^2),$$
$$Q_2(\mathbf{X}) = \sum_{k=1}^{n} ((\tan\delta_{exp} - \tan\delta_{calc}(\mathbf{X}_k))^2 / \tan\delta_{exp}^2). \quad (12)$$

Here, Q_1 is the real part of the objective function; Q_2 is the imaginary part of the objective function; C_{exp} and C_{calc} are the experimental and calculated characteristics of the capacitance of the plane capacitor, respectively; $\tan\delta_{exp}$ and $\tan\delta_{calc}$ are the experimental and calculated values of the loss tangent of the ferroelectric, respectively; n is the number of capacitance measurements; m is the number of loss tangent measurements; and $\mathbf{X} = (\xi_S, \Theta_f, D_N, x, C)$ is the vector of the parameters to be optimized.

To find the model parameters from the experimental dependences of the permittivity of a ferroelectric film on the temperature and applied electric field, we use the objective function

$$Q_1(\mathbf{X}) = \sum_{k=1}^{n} ((\varepsilon_{3exp} - \varepsilon_{3calc}(\mathbf{X}_k))^2 / \varepsilon_{3exp}^2). \quad (13)$$

Here, $\varepsilon_{3\,exp}$ and $\varepsilon_{3\,calc}$ are the experimental and calculated permittivities, respectively, and q is the number of permittivity measurements. To find the vector of optimal parameters, it is necessary to find a minimum of the objective function $Q(\mathbf{X})$,

$$\min_{x \in D} Q = Q(\mathbf{X}^*) = Q^*, \quad (14)$$

with regard for the parametric constraints

$$x_j^- \leq x_j \leq x_j^+; \quad j = 1, 2, \ldots, N, \quad (15)$$

where $\mathbf{X}^* = (x_1^*, x_2^*, \ldots, x_N^*)$ is the vector of optimal parameters corresponding to the minimum of the objective function $Q(\mathbf{X})$ and N is the number of the parameters being optimized.

To construct Halton sequences, which are used to probe the space of the model parameters being optimized, it is necessary to define numerical sequences $p_r(i)$ as

$$i = \sum_{S=1}^{N} a_S r^{S-1}, \quad p_r(i) = \sum_{S=1}^{N} a_S r^{-S}, \quad (16)$$

where a_S are rth integers.

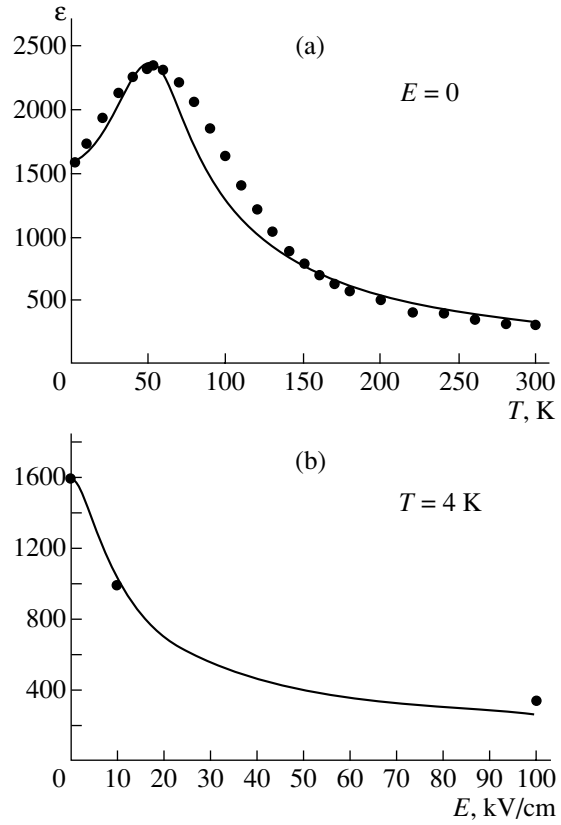

Fig. 3. Measured (●) and calculated (solid line) values of the permittivity of the STO film as functions of (a) temperature and (b) field strength [25]. The model parameters of the ferroelectric are given in the table.

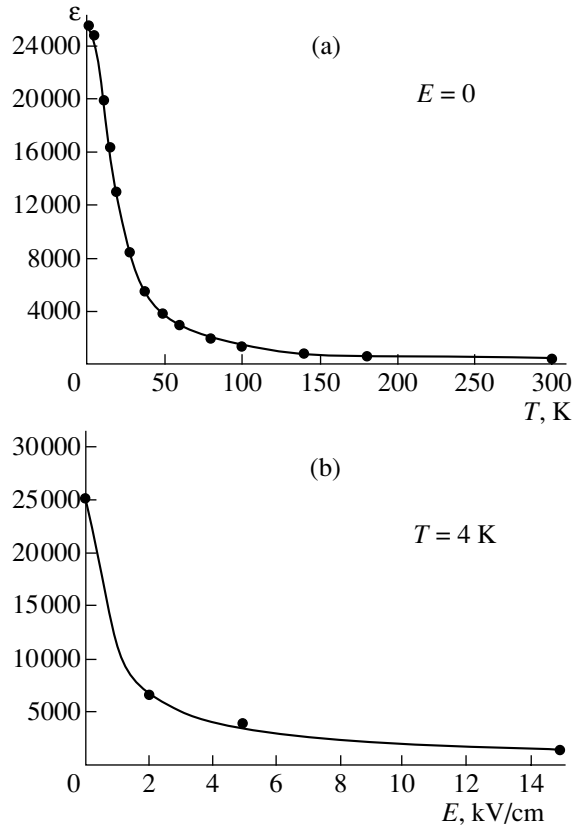

Fig. 4. The same as in Fig. 3 but for the STO single crystal [23].

In practice, r is taken to be a prime integer.

The above formulas for the generation of Halton sequence points are related to the unit hypercube. To calculate the sequences of points uniformly distributed in a given hyperparallelepiped with sides parallel to the coordinate faces, we use the linear transformation

$$\alpha_{i,j} = x_j^- + (x_j^+ - x_j^-)p_r(i). \qquad (17)$$

An extremum of the objective function $Q(\mathbf{X})$ is found as follows:

(1) A point of the Halton sequence that is uniformly distributed in the unit hypercube is mapped to a point in the domain of solutions D via linear transformation (17).

(2) Parametric constraints (15) are formally checked. If they are not satisfied, this point is excluded from further consideration. Otherwise, the point is retained as a sampling point in the domain D.

(3) At the sampling point, the value of the objective function $Q(\mathbf{X})$ is calculated.

(4) Items 1–3 are repeated for each point obtained, and the minimum values of the objective function $Q(\mathbf{X})$ and corresponding parameter vector $\mathbf{X}$ are found.

(5) After the generation of Halton sequence points has been completed, the domain of solutions D is contracted by changing the parametric constraints.

(6) Items 1–5 are repeated until a given accuracy of the minimum value of the objective function $Q(\mathbf{X})$ and corresponding vector $\mathbf{X}$ is achieved.

Model parameters calculated by the program

Dependence	Model parameters				
	ξ_s	Θ_f, K	D_N, C/m^2	C	x
Fig. 3 [25]	0.58	134	2.6	0.87×10^5	–
Fig. 4 [23]	0.013	181	4.1	1×10^5	–
Fig. 5 [24]	0.15	200	10	2.09×10^5	0.5
Fig. 6	2.42	199.5	3.42	1.02×10^5	0.46

COMPARISON OF THE EXPERIMENTAL DATA WITH THE SIMULATION RESULTS

The algorithm mentioned above was implemented as a program extracting five model parameters of a ferroelectric film (Eqs. (12) and (13)) from the tempera-

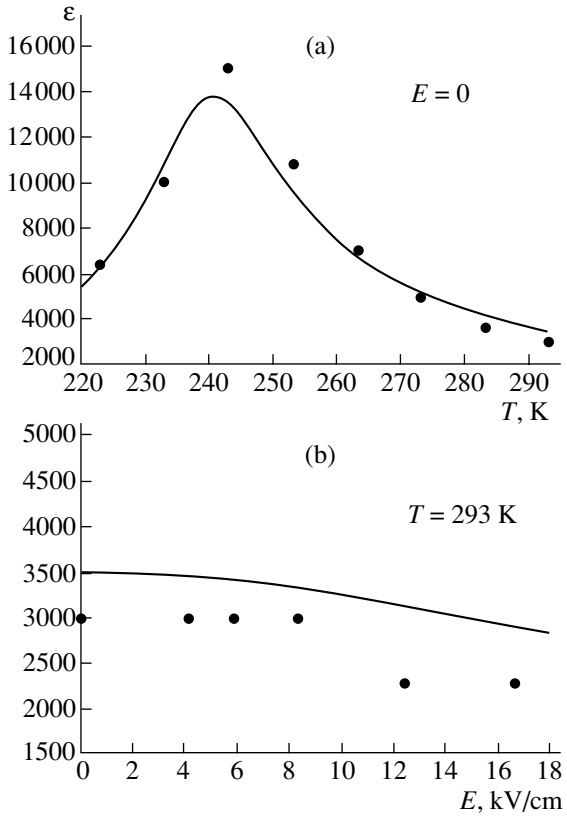

Fig. 5. The same as in Fig. 3 but for BSTO ceramic [24].

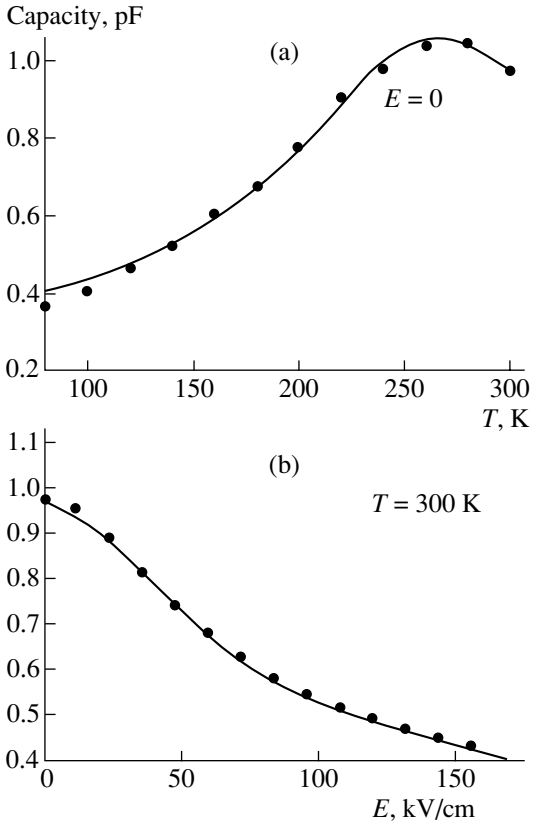

Fig. 6. Measured (●) and calculated (solid line) values of the capacitance of the plane capacitor with the STO film as functions of (a) temperature and (b) field strength. The model parameters of the ferroelectric are given in the table. The geometrical parameters of the plane capacitor are h_2 = 0.8 μm, h_3 = 500 μm, s = 5 μm, l = 1800 μm, w = 0.71 mm, and ε_3 = 9.8.

ture and field dependences of the permittivity and from the capacitance of the plane ferroelectric capacitor measured as a function of the temperature and applied field. The program was tested for both cases. Experimental dependences of the permittivity were taken from [23–25], and the plane ferroelectric capacitor was made of BSTO.

Figures 3–6 show the experimental and simulated temperature and field dependences of the permittivity for the ferroelectric single crystals and films, as well as of the capacitance of the plane capacitor. In data processing, the geometry of the plane capacitor (h_3, l, w, h_2, and s (Fig. 1)) and the permittivity of the substrate ε_3 are taken to be reliably known and do not need optimization.

In addition, the program allows one to process the dependences of the ferroelectric loss tangent on the temperature and field according to objective function (12). In this work, losses in the ferroelectric material are not considered.

As is seen from Figs. 3–6, the calculated and experimental characteristics agree well at certain model parameters (see table) [7, 10–14]. The values of the Curie temperature T_C for the BSTO samples are given for a barium concentration x found by optimization. The discrepancy between the calculated and experimental characteristics is explained by both the roughness of model (6)–(10) and the experimental error.

CONCLUSIONS

The method of partial capacitances in combination with the phenomenological description of a ferroelectric allows the calculation of the capacitance of a plane ferroelectric capacitor, given the geometrical sizes of the planar structure and the parameters of the ferroelectric film. The mathematical algorithm for searching for model parameters provides optimization in terms of several parameters subject to the constraints imposed and finds all five model parameters used for the description of the dielectric response of a ferroelectric. Our method simplifies substantially the processing of experimental data for a plane ferroelectric capacitor and significantly cuts the computation time. This can be useful for the statistical processing of experiments aimed at refining the deposition technology and improving the properties of ferroelectric films and related devices, such as the SQF of a ferroelectric and the reproducibility of the device characteristics (the lat-

ter factor is of importance for mass production). Moreover, the models involved in the program may serve as a basis for the CAD of microwave devices with ferroelectrics.

ACKNOWLEDGMENTS

We are grateful to I.B. Vendik and O.G. Vendik for fruitful discussions and useful comments and to S.F. Karmanenko for submitting the ferroelectric materials.

This work was supported by the Ministry of Industry, Science, and Technology of the Russian Federation (project no. 40.012.1.11.46) and the Ministry of Education of the Russian Federation (project no. PD02-2.7-130).

REFERENCES

1. R. Romanofsky, J. Bernhard, G. Washington, *et al.*, IEEE MTT-S Int. Microwave Symp. Dig. **3**, 1351 (2000).
2. V. Sherman, K. Astafiev, N. Setter, *et al.*, IEEE Microwave Wireless Comp. Lett. **11**, 407 (2001).
3. O. Vendik, L. Vendik, V. Pleskachev, *et al.*, Int. Microwave Symp. Dig. **3**, 1461 (2001).
4. O. G. Vendik, I. B. Vendik, V. Pleskachev, *et al.*, Integr. Ferroelectr. **43** (1–4), 153 (2002).
5. D. Kim, Y. Choi, M. Allen, *et al.*, in *Proceedings of the IEEE MTT-S International Microwave Symposium (IMS 2002), Seattle, 2002*, pp. 1471–1474.
6. O. G. Vendik and S. P. Zubko, Integr. Ferroelectr., part 5 **34** (1–4), 215 (2001).
7. O. G. Vendik and S. P. Zubko, J. Appl. Phys. **88**, 5343 (2000).
8. O. G. Vendik, S. P. Zubko, S. F. Karmanenko, *et al.*, J. Appl. Phys. **91**, 331 (2002).
9. O. G. Vendik, S. P. Zubko, and M. A. Nikol'sky, J. Appl. Phys. (2003) (in press).
10. O. G. Vendik, S. P. Zubko, and M. A. Nikol'sky, Zh. Tekh. Fiz. **69** (4), 1 (1999) [Tech. Phys. **44**, 349 (1999)].
11. O. G. Vendik and S. P. Zubko, J. Appl. Phys. **82**, 4475 (1997).
12. O. G. Vendik and S. P. Zubko, Integr. Ferroelectr., part 5 **34**, 215 (2001).
13. O. G. Vendik and S. P. Zubko, J. Appl. Phys. **88**, 5343 (2000).
14. O. G. Vendik, L. T. Ter-Martirosyan, and S. P. Zubko, J. Appl. Phys. **84**, 993 (1998).
15. É. S. Kochanov, Radiotekhnika (Moscow) **22** (7), 82 (1967).
16. É. S. Kochanov, Radiotekhnika (Moscow) **30** (1), 92 (1975).
17. A. N. Deleniv, Zh. Tekh. Fiz. **69** (4), 8 (1999) [Tech. Phys. **44**, 356 (1999)].
18. A. K. Tagantsev, Appl. Phys. Lett. **76**, 1182 (2000).
19. V. G. Vaks, *Introduction to the Microscopic Theory of Ferroelectrics* (Nauka, Moscow, 1973).
20. I. M. Sobol', *Numerical Monte-Carlo Methods* (Nauka, Moscow, 1973).
21. J. H. Halton, Appl. Numer. Math. **2** (2), 84 (1960).
22. J. H. Halton, SIAM Rev. **12** (1), 1 (1970).
23. K. Bethe, Philips Res. Rep. Suppl. **2**, 1 (1970).
24. *Ferroelectrics in Microwave Technology*, Ed. by O. G. Vendrik (Sov. Radio, Moscow, 1979).
25. D. Galt and J. Price, Appl. Phys. Lett. **63**, 3078 (1993).

Translated by K. Shakhlevich